

UNIVERSITÀ DEGLI STUDI DI NAPOLI FEDERICO II



FACOLTÀ DI INGEGNERIA

DIPARTIMENTO DI INGEGNERIA AEROSPAZIALE

**DOTTORATO DI RICERCA IN INGEGNERIA AEROSPAZIALE,
NAVALE E DELLA QUALITÀ**

XXIV CICLO

PHD THESIS

**THE MEDUSA AND MICROMED EXPERIMENTS
FOR THE EXOMARS SPACE PROGRAMME
TO PERFORM IN SITU ANALYSIS OF MARTIAN DUST**

Tutors

Prof. Luigi Colangeli

Dr. Francesca Esposito

Coordinator

Prof. Antonio Moccia

PhD Student

Sergio Ventura

2011

SUMMARY

ACKNOWLEDGEMENTS	6
INTRODUCTION	8
1 MARS	11
1.1 The Mars Planet.....	11
1.2 Mars Atmosphere	14
1.2.1 Composition, Temperature, and Pressure	15
1.2.2 Winds	17
1.2.3 Dust.....	18
1.2.4 Water.....	29
1.3 The Mars Exploration	33
1.3.1 Missions to Mars	33
1.3.2 Some Key Scientific Objectives of the Future Mars Exploration.....	34
2 EXOMARS PROGRAMME	38
2.1 Aurora Programme and ExoMars Programme	38
2.2 ExoMars Programme Evolution	39
2.3 ExoMars 2016 Mission	40
2.3.1 Mission Architecture.....	40
2.3.2 ExoMars EDM	42
2.4 ExoMars 2018 Mission	46
2.4.1 Mission Architecture.....	46
2.4.2 ExoMars Rover	48
2.4.3 ExoMars Rover Pasteur Payload	52
2.4.4 ExoMars Rover Scientific Payload Requirements.....	54
2.4.5 ExoMars Rover Reference Surface Mission.....	54
3 AEROSOL ANALYSIS	67
3.1 Fluid Dynamics Models.....	67
3.1.1 Fluid Phase.....	67
3.1.2 Particles Dynamics.....	80
3.1.3 Numerical Methods for Aerosol Dynamics	89
3.2 Particles Measurement.....	93
3.2.1 Aerosol Measurements in Planetary Research.....	93
3.2.2 Optical Detection Principle.....	99

3.2.3	Aerosol Sampling and Transport	108
4	MEDUSA FOR THE EXOMARS LANDER.....	113
4.1	MEDUSA Concept.....	113
4.2	MEDUSA Scientific Objectives and Measurements.....	113
4.3	MEDUSA System.....	115
4.3.1	Laser Diode Assembly (LDA)	121
4.3.2	Optical Stage (OS)	124
4.3.2.1	Inlet Duct and Outlet Duct.....	126
4.3.2.2	Objective System.....	126
4.3.2.3	Forward (FW) and Backward (BW) Collecting Mirrors	127
4.3.2.4	Sampling Volume (SV)	128
4.3.2.5	Light Trap.....	130
4.3.2.6	Detectors	131
4.3.2.7	Proximity Electronics (PE).....	132
4.3.3	Pump	133
4.4	MEDUSA for the ExoMars Humboldt Payload (HPL)	135
4.4.1	MEDUSA Requirements	135
4.4.2	MEDUSA Engineering Budgets	137
4.4.3	MEDUSA Operations and Maintenance.....	139
4.5	Analysis of the MEDUSA Breadboard	140
4.5.1	Computational Fluid Dynamics Analysis	140
4.5.2	Test and Verification of the Laser Diode.....	157
4.5.3	Stray Light Analysis	158
4.5.4	Theoretical Scattering Analysis	158
4.5.5	Experimental Tests on the Detection System	161
4.5.6	Procedure for the Optical System Calibration of MEDUSA	172
4.6	Conclusions about MEDUSA	175
5	MICROMED AND DREAMS FOR THE EXOMARS EDM 2016.....	177
5.1	DREAMS.....	177
5.1.1	DREAMS Proposal.....	177
5.1.2	DREAMS Scientific Investigation.....	178
5.1.3	DREAMS System Architecture	182
5.1.4	DREAMS Operations	184
5.1.5	DREAMS Final Arrangement.....	186
5.2	MicroMED for the DREAMS Proposal.....	186
5.2.1	The MicroMED Scientific Objectives and Measurements	186
5.2.2	The MicroMED System.....	187
5.2.3	MicroMED Requirements.....	190
5.2.4	MicroMED Engineering Budgets	190

5.2.5 MicroMED Operations	191
5.3 Fluid Dynamics Design.....	191
5.3.1 Basic Guidelines	191
5.3.2 Computational Fluid Dynamics Analysis	194
5.4 Optical Design	223
5.4.1 Basic Guidelines	223
5.4.2 Test and Verification of the Laser Diode.....	228
5.5 Conclusions about MicroMED	231
CONCLUSIONS.....	234
ACRONYMS AND ABBREVIATION.....	239
SYMBOLS.....	243
BIBLIOGRAPHY.....	245
TECHNICAL DOCUMENTS	256

***No Exploration
without Collaboration***

ACKNOWLEDGEMENTS

Thanks very much and *summa cum laude* to my parents, *Assia* and *Gianni*, which have been always confident and encouraging without any interruptions and doubts.

Thanks to my tutors, Prof. *Luigi Colangeli* and Dr. *Francesca Esposito*, for their advice and the opportunity to work on an ambitious project for the exploration of the Solar System, and thanks to the *Istituto Nazionale di Astrofisica (INAF) - Osservatorio Astronomico di Capodimonte (OAC)*, Naples, Italy.

Thanks to *Jorge L. Vago*, who was my mentor for the ExoMars Programme at *European Space Agency (ESA)*. Thanks to all the ESA Staff people with which I collaborated at ESA-ESTEC.

Thanks to the *University of Naples "Federico II"* and *Agenzia Spaziale Italiana (ASI)*, which supported and funded my PhD. In particular, thanks to Prof. *Leonardo Lecce*, whose suggestions were very precious, and to Prof. *Antonio Moccia* for being excellently the Chairman of the PhD course in *Aerospace, Naval and Total Quality Management Engineering*.

Thanks to the wide community orbiting around the *INAF-OAC*, which shared pleasant and constructive moments during the PhD years: Michele Zusi, Stavro Ivanosky, Simone De Angelis, Nella Ferrigno, Katia Biazzo, Vincenzo Della Corte, Alessandra Rotundi, Cesare Molfese, Fabio Cozzolino, Pasquale Palumbo, Mario Accolla, Davide Perna, Alessandro Aronica, Ciprian Popa, Alessia Albanese, Ernesto Zona, Fausto Cortecchia, Ilda Cozzolino, Elena Mazzotta Epifani, Alessandra Ciucci, Gaetano Di Achille, Vito Mennella, Vincenza Mastascusa, Marco Ferrari, Valentina Galluzzi, and many others. Thanks to the ESA-ESTEC community and The Netherlands, where I spent a fundamental step for my career in space engineering.

Thanks to all my friends, which both in agree or in disagree, gave me useful and sincere contributions to understand the world and correct my mistakes. Thanks to all the people that I really had the pleasure and honour to meet in these years, and to those ones who could do in the future.

Finally, but not least, thanks to my own obstinacy and eclecticism that allow me to face challenges with determination and motivation.

INTRODUCTION

The subject of this PhD thesis is the study and development of scientific instrumentation for *in situ detection* and *monitoring* of *dust* and *water vapour* in the Martian atmosphere at surface level. The activities have been developed within the *MEDUSA* and *MicroMED* projects, which are, respectively, the original device and its miniaturized version proposed for the *ESA-NASA ExoMars Programme*.

The work was mainly developed at the *National Institute of Astrophysics (INAF) - Astronomical Observatory of Capodimonte (OAC)*, Naples, Italy, for what concerns the *MEDUSA* and *MicroMED* design, development and tests, and at the *European Space Agency (ESA) - European Space and Technology Research Centre (ESTEC)*, in Science and Robotic Exploration Directorate, Research and Scientific Support Department, Solar System Missions Division (SRE-SM), Noordwijk, The Netherlands, for what concerns the *ExoMars Programme*.

MEDUSA and *MicroMED* are scientific instruments designed to perform *in situ* measurements of dust grain size and to derive dust size distribution and concentration on a local scale in the Martian atmosphere, at ground level.

Airborne dust particles are constantly present in the Martian atmosphere with abundance variable with seasons. They have a relevant impact on the radiative-convective equilibrium of the troposphere by absorbing and scattering radiation. Moreover, wind and windblown dust are the most important modifying agents currently active on the surface of Mars. They are responsible for erosion, redistribution of dust on the surface and weathering. These processes are driven by wind intensity and grain properties (primarily size). Beside its scientific interest, the study of atmospheric Martian dust is relevant in the context of analysing hazard conditions connected to the contamination and/or failure of payloads (e.g., solar panels, mechanisms, optical systems) and to the environmental risks for human exploration. Measuring *in situ* the amount and the mass and/or size distribution of solid particles in the Martian atmosphere, as a function of time, is a fundamental step to shed light on the airborne dust evolution, in particular, and on climatic processes, more in general.

MEDUSA was proposed and accepted to be accommodated on the rover/lander of the first *ESA ExoMars* mission concept (2009). *MicroMED*, a lightweight version

derived from MEDUSA, has been, instead, proposed in 2011 as part of the *DREAMS* payload package for the ESA-NASA *ExoMars EDM 2016* mission.

The PhD work performed within these projects is described in the following chapters.

Chapter 1 (*Mars*) gives a summary of the current knowledge about the planet Mars from past missions, ground observations, and model simulations, with emphasis on the Mars environment and meteorology. This information gives the context for the scientific investigation on Mars and provides the boundary conditions for the operations of the MEDUSA and MicroMED sensors and the DREAMS package. The main parameters to be considered are atmospheric (composition, temperature, pressure, density, wind speed and direction) and airborne dust grain (size, density, concentration, refractive index) properties.

Chapter 2 (*ExoMars Programme*) describes the ESA-NASA ExoMars Programme for the exploration of Mars. The MEDUSA and MicroMED instruments and the DREAMS package were designed in different phases of the ExoMars Programme evolution. The work of this thesis also includes the support to the definition of the scientific payload for the *ExoMars Entry Descent and Landing Demonstrator Module (EDM) 2016* mission, and of the scientific payload requirements and reference surface mission for the *ExoMars Rover 2018*. These tasks were accomplished at ESA-ESTEC, SRE-SM, in 2010 under the supervision of the ExoMars Project Scientist Jorge L. Vago, and collaborating with the ESA Payload and Assembly, Integration and Verification (AIV) team and ExoMars Rover System Engineers.

Chapter 3 (*Aerosol Analysis*) is aimed at introducing theoretical models and techniques applied to develop the MEDUSA and MicroMED instruments. Fluid dynamics and optical concepts needed to cope with aerosol measurements are summarized.

Chapter 4 (*MEDUSA for the ExoMars Lander*) describes the tasks accomplished on the MEDUSA instrument to characterize from a fluid dynamics point of view the detection system designed to perform scattering analysis of dust particles.

Chapter 5 (*MicroMED and DREAMS for the ExoMars EDM 2016*) deals with the activities for the design of the MicroMED instrument and its integration within the DREAMS package for the EDM payload.

Conclusions summarizes the research path, the scientific and engineering contribution and the results obtained within the work of this thesis.

1 MARS

1.1 The Mars Planet

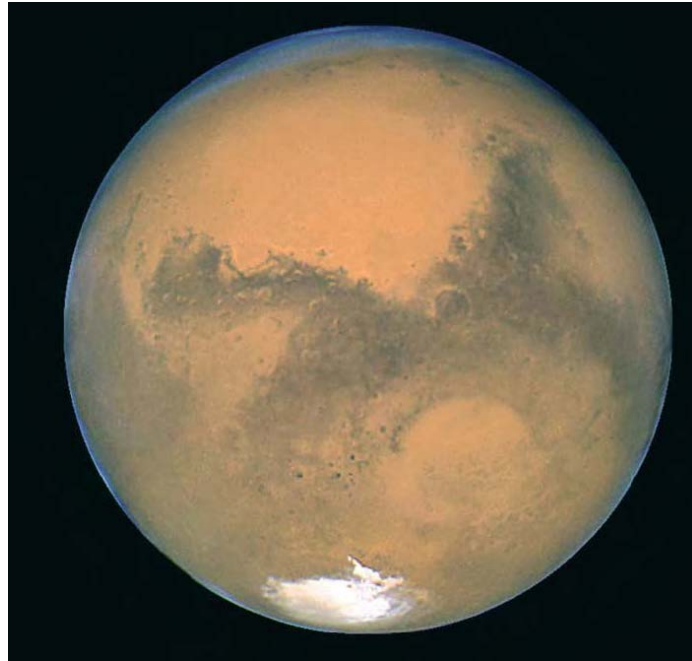


Fig. 1.1: Mars (Hubble Space Telescope, 26/08/2003, NASA).

Mars is the fourth planet far from the Sun in the Solar System (Fig. 1.1). It is typically called the Red Planet due to its reddish appearance with an average albedo¹ of 0.25, which is mainly caused by the presence of iron oxide on the surface. The Martian surface has several large morphological features, such as impact craters, volcanoes, valleys, deserts, and polar ice caps. Its atmosphere is thin, dry and dusty. Mars has two smaller and irregularly shaped natural satellites, *Phobos* and *Deimos*.

Bulk Parameters	Mars	Earth
Mass	$0.64185 \cdot 10^{24}$ kg	$5.9736 \cdot 10^{24}$ kg
Volume	$16.318 \cdot 10^{10}$ km ³	$108.321 \cdot 10^{10}$ km ³
Equatorial radius	3396.2 km	6378.1 km
Polar radius	3376.2 km	6356.8 km
Volumetric mean radius	3389.5 km	6371.0 km
Core radius	1700 km	3485 km
Ellipticity	0.00648	0.00335
Mean density	3933 kg/m ³	5515 kg/m ³
Gravity at pole	3.758 m/s ²	9.823 m/s ²
Gravity at equator	3.711 m/s ²	9.7801 m/s ²
Escape velocity	5.03 km/s	11.19 km/s
Mean solar flux	588.98 W/m ²	1367 W/m ²

Tab. 1.1: Comparison between Mars and Earth bulk parameters.

¹ Albedo: ratio of the reflected radiation from a surface and the incident radiation upon it.

Orbital Parameters	Mars	Earth
Sideral rotation period	24.6229 h	23.9345 h
Mean day	24.6597 h = 1 sol	24.00 h
Axial tilt (obliquity to orbit)	25.19°	23.45°
Semimajor axis	227.92·10 ⁶ km = 1.524 AU	149.60·10 ⁶ km = 1.000 AU
Eccentricity	0.0933941	0.0167
Inclination to ecliptic	1.84969142°	0.00°
Longitude of the ascending node	49.55953891°	348.73936°
Argument of perihelion	286.537°	114.20783°
Sideral orbital period	686.980 Earth days	365.256 Earth days
Tropical orbital period	686.973 Earth days	365.242 Earth days
Synodic orbital period	779.94 Earth days	-
Perihelion distance	206.62·10 ⁶ km = 1.381 AU	147.09·10 ⁶ km = 0.9832 AU
Aphelion distance	249.23·10 ⁶ km = 1.662 AU	152.10·10 ⁶ km = 1.017 AU
Mean orbital velocity	24.13 km/s	29.78 km/s
Max orbital velocity	26.50 km/s	30.29 km/s
Min orbital velocity	21.97 km/s	29.29 km/s
Min distance from Earth	55.7·10 ⁶ km = 0.3723 AU	-
Max distance from Earth	401.3·10 ⁶ km = 2.682 AU	-

Tab. 1.2: Comparison of Mars and Earth motion parameters (NASA, Epoch J2000).

In Tab. 1.1 and Tab. 1.2 are reported the main bulk and motion parameters of Mars compared to the Earth, respectively. The Mars eccentric orbit implies not homogeneous seasons between the hemispheres (Fig. 1.2). A Martian day (*sol*) due to the planet rotation around its axis lasts $24^{\text{h}}39.6^{\text{m}}$. The planet motion is also characterised by periodical oscillations ($\sim 10^5$ years), which cause variations of the inclination of the rotation axis up to $\sim 60^\circ$ (obliquity).

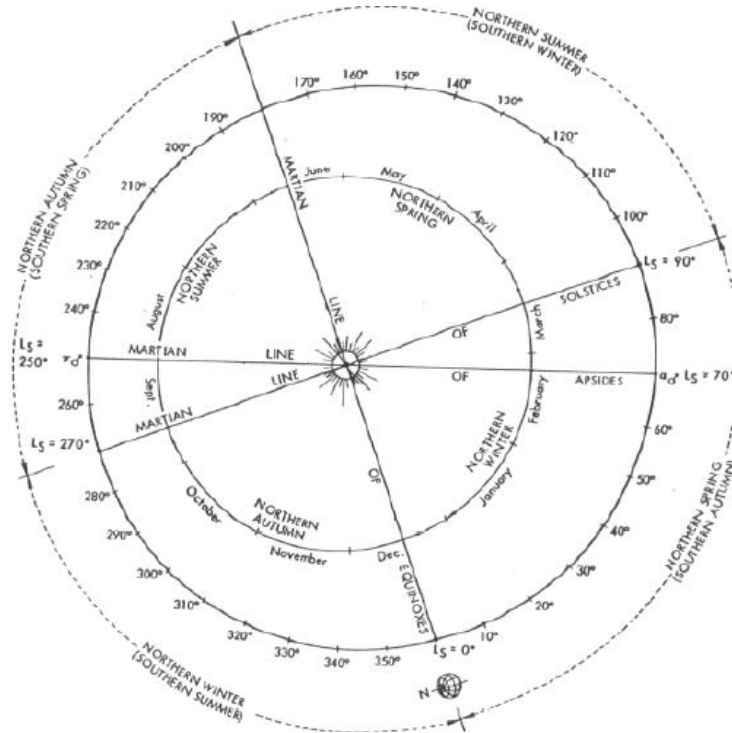


Fig. 1.2: The Martian seasons defined by the aerocentric solar longitude (L_S) (Michaux, C.M., Newburn, R.L., 1972): $L_S = 0^\circ$ at northern spring equinox; $L_S = 90^\circ$ at northern summer solstice; $L_S = 180^\circ$ at northern autumn equinox; $L_S = 270^\circ$ at northern winter solstice.

Although the Mars mass is 11% smaller and its distance from the Sun is 50% larger than for the Earth, its climate evolution has important similarities with our planet, such as the polar ice caps formation, seasonal changes, and weather patterns, but also significant differences such as the lack of liquid water and much lower thermal inertia.

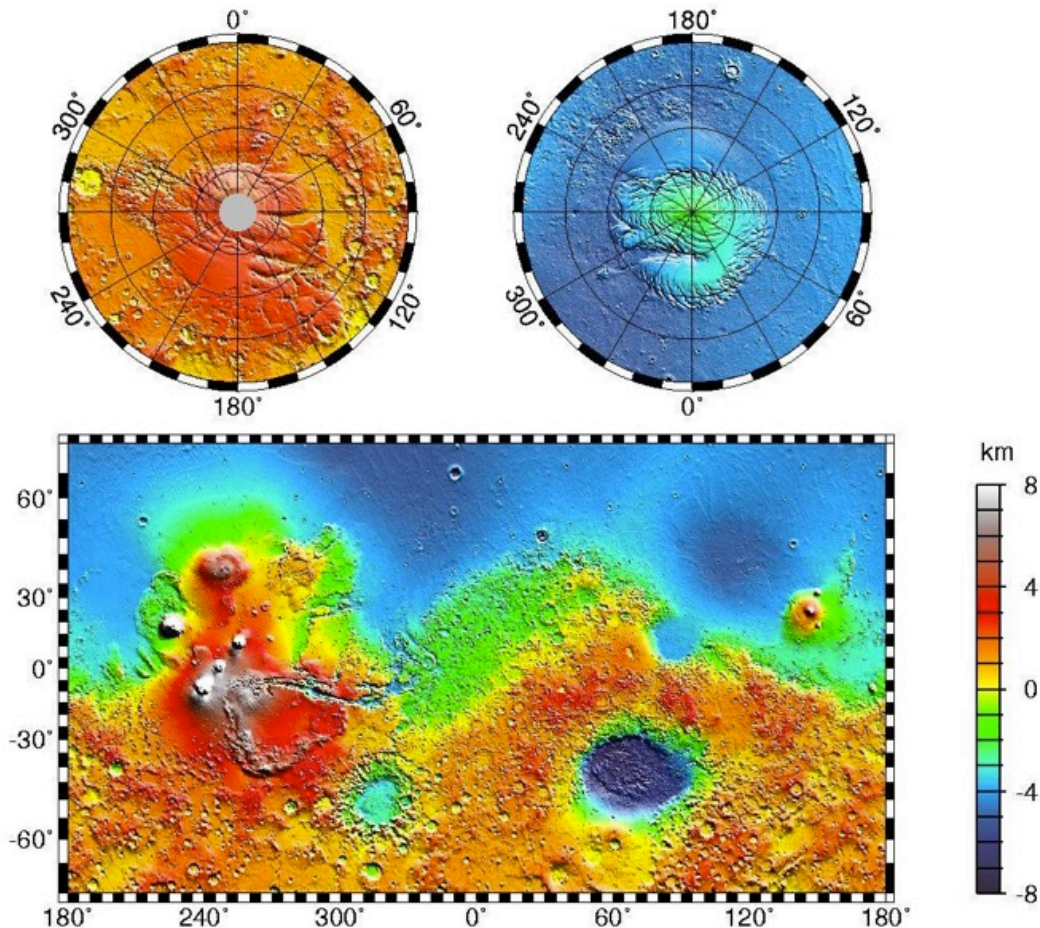


Fig. 1.3: Mars topography from the MOLA instrument on board Mars Global Surveyor (NASA/MOLA Science Team). The southern (top left) and northern (top right) hemispheres, and the global map (bottom) are represented.

Mars is now geologically inactive and it does not seem to have tectonic activities. The most plausible hypothesis is that the structure of Mars is characterised by a central metallic core, a mantle, and a crust. Two main kinds of regions are identified on the surface of Mars, which determine a global dichotomy (Fig. 1.3): the northern hemisphere is characterized by lower abundance of impact craters and mountains and has a higher albedo than the southern hemisphere, which implies that the northern hemisphere is relatively younger than the southern one.

The two Martian *Polar Caps* are deposits of volatile ice (H_2O , CO_2) and dust sediments. They have a thickness of about 1.2-3 m and a width of about 1,000 km. In

winter, due to the very low temperature, CO_2 condensates and caps spread down to a latitude of 60° , while in summer the ices sublimate and the caps retreat. CO_2 sublimation creates winds that sweep off the poles at velocity up to 400 m/s, transporting large amounts of dust and water vapour and giving rise to large cirrus clouds (Forget, F., et al., 2006).

1.2 Mars Atmosphere

The study of the Martian atmosphere improves continuously thanks to the analysis of data coming from space missions and the elaboration of theoretical models. The most relevant parameters of the Martian environment are reported in Tab. 1.3. Generally, they vary with location, season and depend on special events, as discussed in this section.

Composition (volume fraction)	95.32% CO_2 , 2.70% N_2 , 1.60% Ar^{40} , 0.13% O_2 , 0.07% CO , 0.03% H_2O , 0.013% NO , 5.3 ppm Ar^{36+38} , 2.5 ppm Ne , 0.3 ppm Kr , 0.13 ppm CH_2O , 0.08 ppm Xe , 0.04-0.02 ppm O_3 , 10.5 ppb CH_4
Isotopic ratios	$90 \pm 5 C^{12}/C^{13}$, $170 \pm 15 N^{14}/N^{15}$, $490 \pm 25 O^{16}/O^{18}$, $5.5 \pm 1.5 Ar^{36}/Ar^{38}$, $3000 \pm 500 Ar^{40}/Ar^{36}$, $2.5 Xe^{129}/Xe^{132}$, $(7.7 \pm 0.3) \cdot 10^{-4} D/H$
Mean Molecular Mass	43.49 g/mole
Degree of Freedom of Gas Molecules	6
Gas Constant	192 J/kg/K
Ratio between Heat Capacities	1.33
Specific heat capacity at constant pressure	860 J/kg/K
Mean Free Molecular Path	$4.74 \cdot 10^{-6}$ m
Sutherland constant	222 K
Pressure	6.1 mbar (average) - 0.2-12 mbar (range)
Temperature	215 K (average) - 140-310 K (range)
Density	0.020 kg/m^3 (average) - $0.010\text{-}0.020 \text{ kg/m}^3$ (range)
Temperature gradient (Troposphere)	-4.5 K/km
Viscosity ($T = 293.15$ K)	$1.4673 \cdot 10^{-5}$ Pa·s
Mean scale height ($T = 210$ K)	10.8 km
Average columnar mass	150 kg/m^2
Wind Speed	0-30 m/s
Albedo	0.25
Atmospheric visible optical depth	0.1-10
Atmospheric dust mass density	$1\text{-}100 \cdot 10^3 \text{ kg/m}^3$
Atmospheric dust particle number density	$1\text{-}100 \text{ cm}^{-3}$
Atmospheric dust grain size	0.010-10 μm
Water vapour total mass	$1\text{-}2 \cdot 10^{15}$ g
Water vapour total volume	1-2 km^3
Water vapour average volume fraction	220 ppm
Water vapour mass concentration	$1.2 \cdot 10^{-9}\text{-}4.5 \cdot 10^{-6} \text{ kg/m}^3$
Water vapour column density	5-90 pr- μm
Water vapour partial pressure	$1.4 \cdot 10^{-4}\text{-}3.0 \cdot 10^{-2}$ mbar

Tab. 1.3: Martian surface atmosphere.

To have global, local and temporal predictions of the Martian atmosphere parameters, nowadays the most updated models are: the *Martian Global Climate Model (GCM)*, developed by the Laboratoire de Meteorologie Dynamique of CNRS (France), the Department of Atmospheric, Oceanic and Planetary Physics of Oxford University (UK), the Institute of Astrophysics of Andalusia (Spain), and the Open University (UK) with CNES (France) and ESA fundings, whose results are stored in the *European Martian Climate Database (EMCD)*; and the *Mars General Circulation Model (MGCM)* developed by NASA.

1.2.1 Composition, Temperature, and Pressure

The Mars atmosphere is thin, cold, dry, and dominated by *carbon dioxide* (95.3% by volume). The main atmospheric layers are (Fig. 1.4): *troposphere* (at altitude of 0-50 km, where temperature decreases with altitude); *mesosphere* (at altitude of 50-110 km, which is approximately isothermal); *thermosphere* (at altitude of more than 110 km, where temperature increases due to extreme UV solar radiation).

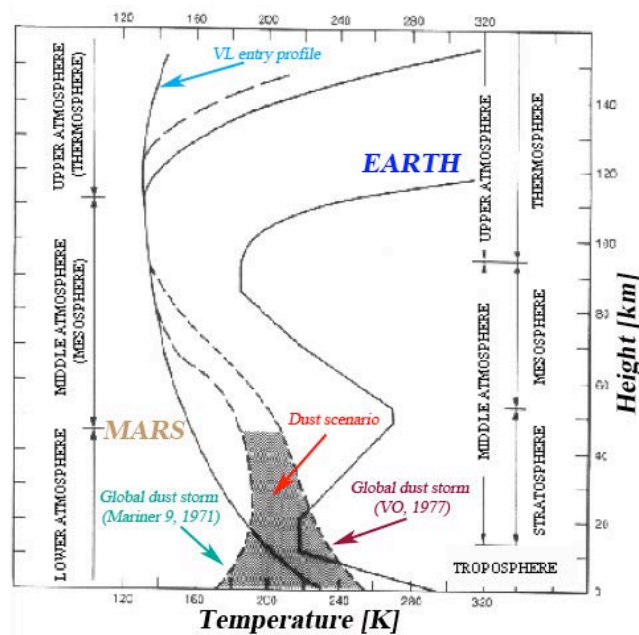


Fig. 1.4: Atmospheric temperature-height profile on Earth and Mars (Zurek, R.W., 1992).

The atmospheric gas (above all CO_2 and H_2O) concentrations depend on season, latitude and surface temperature. During winter, the poles are cold, which causes 25% of atmospheric CO_2 to condense into solid CO_2 ice (*dry ice*), while in summer CO_2 ice sublimates back into atmosphere. Noble gases, e.g., argon, do not condense, and their

total amount is constant (Forget, F., 2004). Traces of methane, which could have a great importance as biomarker (Sect. 1.3.2), are uniformly distributed in the atmosphere (10 ± 5 ppb by volume). Moreover, the instrument PFS on board the Mars Express Orbiter suggested higher concentrations (up to 30 ppb by volume) nearby some areas on the surface (Formisano, V., et al., 2004), whose possible origin is currently under study.

The vertical temperature profiles, among other factors, depends on solar light absorbance by suspended dust, often highly concentrated at lower altitudes, while oxygen (O_2) and ozone (O_3), mainly present at 40 km, play a minor role unlike on Earth. In fact, dust grains absorb and scatter thermal and solar radiation, so contributing to the troposphere heating, while in dust-clear conditions, temperature in the lower atmosphere declines with altitude at a rate of about 4.5 K/km (Zurek R.W., et al. 1992). Moreover, the high atmospheric transparency to solar UV radiation is responsible for the presence of atomic hydrogen due to the photodecomposition of H_2O .

The surface temperature varies due to seasonal and geographical effects; it may fall to 140 K at the poles in winter, and reaches 310 K at low latitudes in summer. Day/night excursion can reach even 100 K with time-rate faster in the morning than in the afternoon (Fig. 1.5).

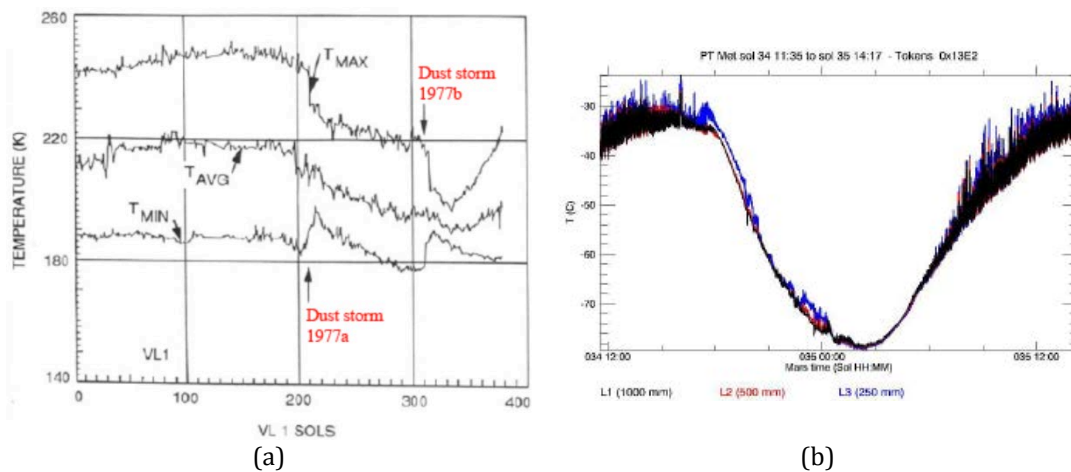


Fig. 1.5: (a) Seasonal temperature variation by the Viking Lander 1 (Golden Plain, 22.70°N 48.22°W) (Ryan J.A., Henry R.M., 1979). (b) Daily temperature variation by MET on board Phoenix (Green Valley, 68°N 126°W, sol 34/34) (Taylor, P.A., et al., 2008).

The mean atmospheric pressure at surface level is about 6-7 mbar with local extremes from ~ 0.2 mbar (e.g., Olympus Mons, 18°N 133°W, 27 km above the Martian Surface Level (MSL)) to ~ 13 mbar (Hellas Planitia, 42.7°S 70°E, -7 km MSL). Considerable pressure variations ($\sim 30\%$) are caused by seasonal effects due to the Mars

axial inclination with respect to the ecliptic plane, and the resulting variation of the abundance of atmospheric gases due to condensation/sublimation of CO_2 and H_2O at the poles. In fact, in summer, pressure increases in one hemisphere, while part of the atmospheric gases condense in the opposite hemisphere. Moreover, due to the orbital eccentricity, summer lasts more in the northern hemisphere than in the southern one. Therefore, the extension of the Polar Cap and the quantity of condensed CO_2 is larger in the southern hemisphere than in the northern one. Pressure cyclic variations up to 10% also occur twice a day, due to strong thermal tides produced by solar heating and amplified by dust presence (Fig. 1.6).

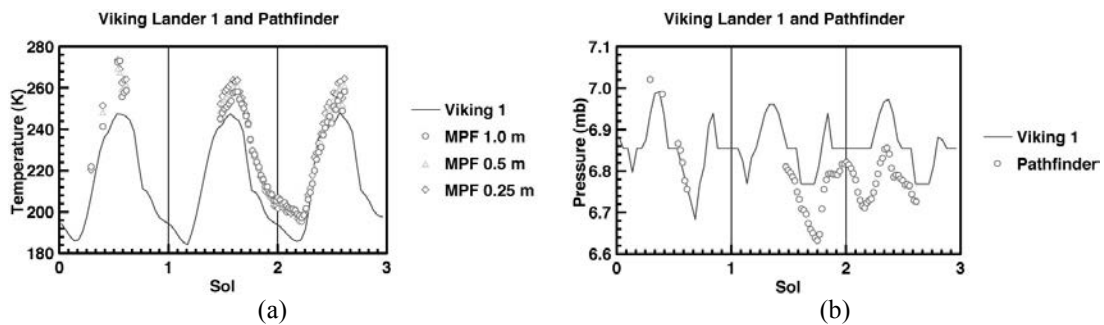


Fig. 1.6: Temperature (a) and pressure (b) daily variations measured *in situ* by Viking Lander 1 (Golden Plain, 22.70°N 48.22°W) and Mars Pathfinder rover (Ares Vallis, 19.13°N 33.22°W) missions (NASA/JPL).

1.2.2 Winds

Pressure and temperature gradients produce winds, which are particularly intense and on average locally omnidirectional (Fig. 1.7). Typical wind intensities are 2-7 m/s in summer, 5-10 m/s in autumn, and 17-40 m/s during dust storm events. Winds play a fundamental role in the dust cycle as it will be discussed in Sect. 1.2.3.

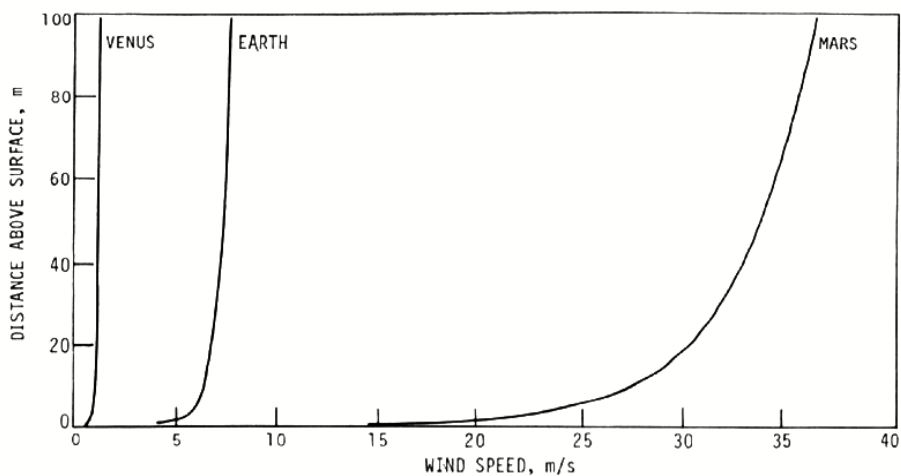


Fig. 1.7: Logarithmic wind speed profiles for Mars, Earth and Venus.

The global Martian atmosphere dynamics is ruled by the Hadley circulation (Fig. 1.8). Over warmer regions (near the equator), warmer air raises, cools at higher altitudes, flows towards the poles, and then closes the circulation along the equatorial surface. Moreover, the rotation of the planet causes the Coriolis effect, i.e., meridional (South-North) movements of air create strong lateral zonal winds (East-West). A large Hadley cell forms, involving both hemispheres and straddling the equator, and vertical movements are not prevented due to the lack of a stratosphere.

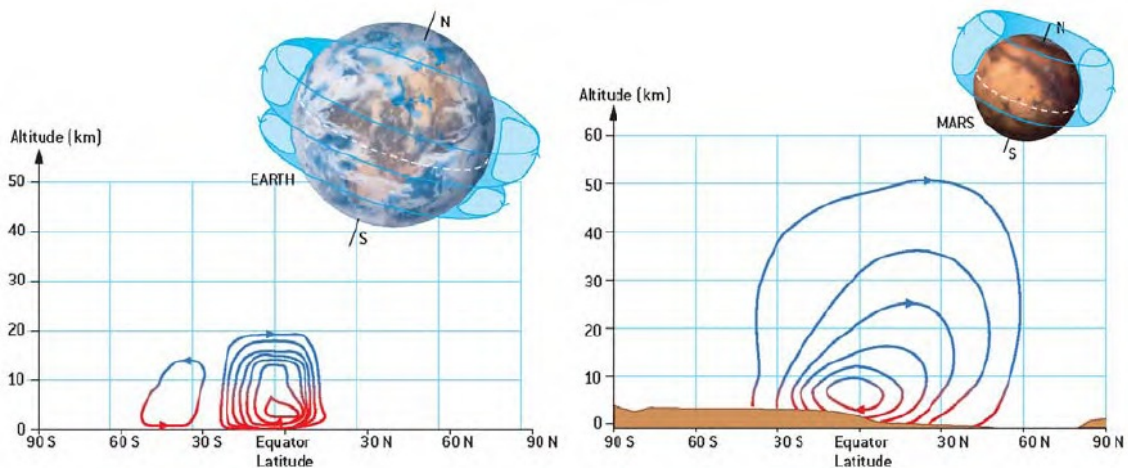


Fig. 1.8: Meridional winds and Hadley circulation on Earth and on Mars (Forget, F., et al., 2006).

Small-scale features, even at boulders levels, may greatly influence the wind behaviour in the *Planetary Boundary Layer (PBL)* up to a height of ~ 1 km. The dynamics of such layer determine dust removal from and settling onto the surface, and transportation within the atmosphere (Sect. 1.2.3).

1.2.3 Dust

Dust is widespread in the Martian atmosphere. It has a variable concentration depending on season, place and special meteorological events as *dust storms* and *dust devils* (Fig. 1.9, Fig. 1.10). Dust plays a fundamental role on the planet climate due to its interaction with solar and thermal radiation and its role in gas condensation and evaporation processes (Pollack, J.B., 1977, 1982).

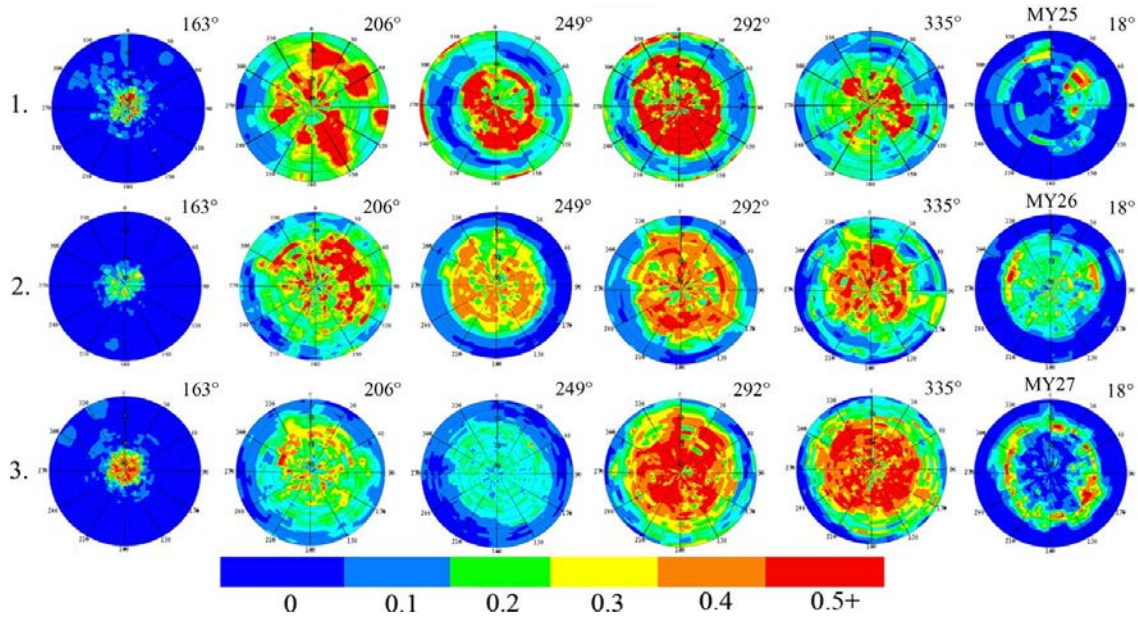


Fig. 1.9: Spatial distribution of dust (optical depth) during Martian years (MY) and seasons (L_S) in the northern hemisphere by TES/MGS (Horne, D., Smith, M.D., 2009).

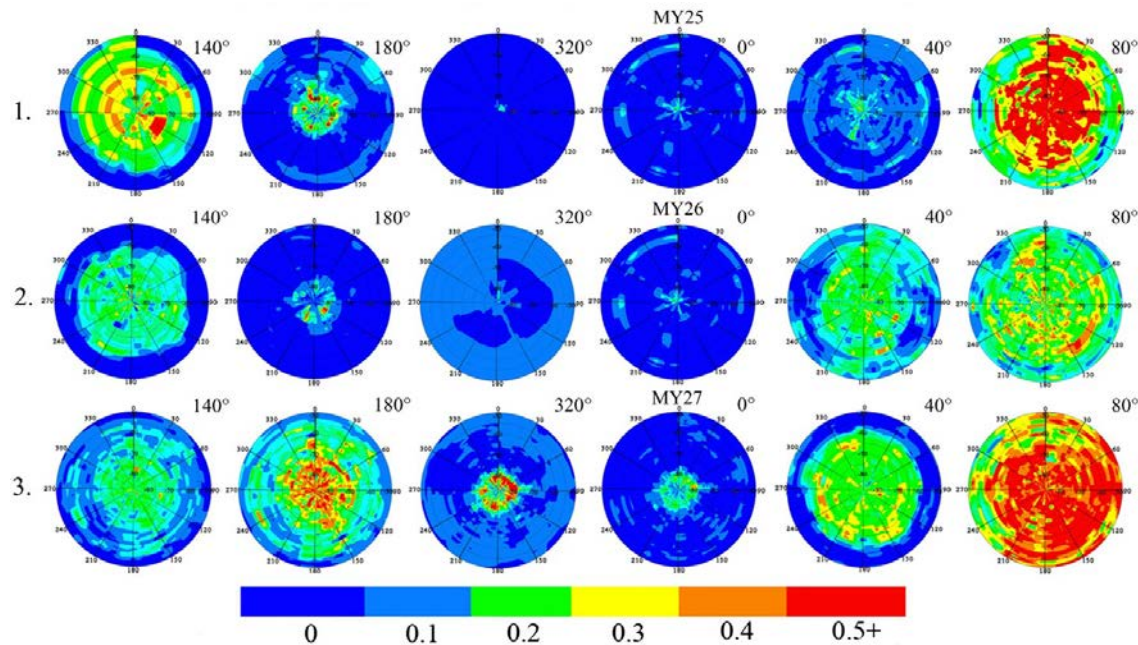


Fig. 1.10: Spatial distribution of dust (optical depth) during Martian years (MY) and seasons (L_S) in the southern hemisphere by TES/MGS (Horne, D., Smith, M.D., 2009).

The current knowledge about the Martian dust has been mainly gained by remote sensing measurements of the atmospheric *optical depth* (τ). This is a measurement of atmospheric transparency corresponding to the vertical path from surface (or a specific altitude) to outer space:

$$\tau = -\ln\left(\frac{I}{I_0}\right) \quad (1.1)$$

where I_0 is the intensity of the radiation at the source, I is the observed intensity after a given path. It expresses the quantity of radiation removed from a light beam by aerosol's scattering or absorption during its path through the atmosphere. The optical properties of dust depend on its chemical and physical characteristics. The clearest evidence of dust is the colour of the Martian sky, which changes from yellowish-brown at high opacity ($\tau \sim 1$) to bluish-black or black if dust free ($\tau \sim 0$) (Bell III, J.F., et al., 2006). Nevertheless, remote measurements can be biased by haze, fog and suspended water ice grains (Pollack, J.B., et al., 1977; Colburn, D., et al., 1989; Leovy, C.B., et al., 1972; Anderson, E.M., Leovy, C.B., 1978; Jaquin, F., et al., 1986; Kahn, R.A., 1990), while *in situ* measurements, currently very poor, should overcome such limitations.

Atmospheric and surface dust is globally distributed with a similar mineralogical composition over the entire planet (Pollack, J.B., et al., 1977, 1979), as a result of the so-called *dust cycle* (Fig. 1.11).

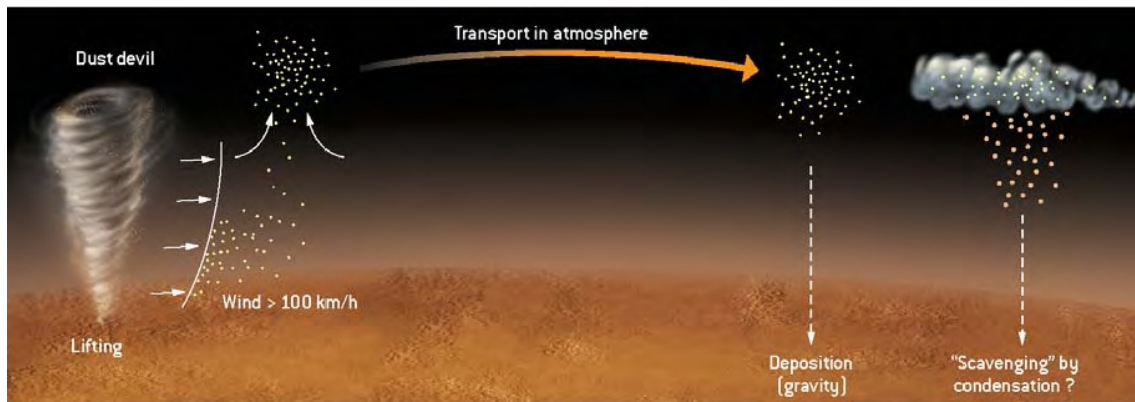


Fig. 1.11: A dust cycle in the Martian atmosphere (Forget, F., et al., 2006).

The dust cycle is characterized by *lifting*, *transport* in the atmosphere, *deposition* and eventual *scavenging* by clouds and *precipitation*. Winds cause grains (size $\sim 1 \mu\text{m} - 1 \text{cm}$) to lift off from surface. The smaller particles ($d_p < 10 \mu\text{m}$) go in suspension in the atmosphere, while the larger ones are lifted but do not go in suspension carried down by winds to surface, where they bounce back into flight (*saltation*). Average saltation trajectories are about 1 m long and 10-20 cm high (White, F.M., 1979). Saltating sand and grains may strike larger grains ($d_p < 1 \text{cm}$) and push them along the surface (*creep*). Saltation may also trigger the injection of much smaller particles (*suspension*) via

impacts. The physical boundary between the saltation and suspension phenomena is not well defined, so, commonly, it is assumed that particles with *settling velocity*² quite lower than the *threshold friction velocity*³ are ruled by suspension, while particles with settling velocity higher than the threshold friction velocity are ruled by saltation. Sand-sized aggregated particles can be raised and then broken down into much smaller particles by collisions (*sandblasting*). Finally, surface volatile outgassing, dust storms and dust devils, and planetary baroclinic⁴ waves are also responsible of injection and transport of particles in the atmosphere.

Wind profiles (U) with respect to height from surface (y) in the PBL are mathematically described with the threshold friction velocity (u_τ) (Eq. (1.2)):

$$u_\tau = \sqrt{\frac{\tau_w}{\rho}} \quad (1.2)$$

$$y^+ = \frac{\rho u_\tau y}{\mu} \quad (1.3)$$

where y^+ is the dimensionless wall distance, τ_w is the tangential wall stress, ρ is the fluid density, μ is the fluid viscosity. A general relationship between soil particle size and threshold velocity was studied in experimental simulations in wind tunnels (Bagnold, R.A., 1941, Peabody, S.A., 1982, Greeley, R., Iversen, J.D., 1985, Shao, Y., et al., 1996, Batt, R.G.) obtaining the following empirical expressions (Iversen, J.D., White, B.R., 1982):

$$u_\tau = A \left(\frac{\rho_p - \rho}{\rho} g d_p \right)^{1/2} \quad (1.4)$$

$$u_\tau = \begin{cases} \left[\frac{0.1666681 \rho_p g d_p}{-1 + 1.928 \text{Re}_\tau^{0.0922}} \left(1 + \frac{6 \cdot 10^{-7}}{\rho_p g d_p^{2.5}} \right) \right]^{1/2} \rho^{-1/2} & 0.03 \leq \text{Re}_\tau \leq 10 \\ \left[0.0144 \rho_p g d_p \left(1 - 0.0858 e^{-0.0617(\text{Re}_\tau - 10)} \right) \left(1 + \frac{6 \cdot 10^{-7}}{\rho_p g d_p^{2.5}} \right) \right]^{1/2} \rho^{-1/2} & \text{Re}_\tau > 10 \end{cases} \quad (1.5)$$

² Settling velocity: the particle speed at equilibrium in a fluid (Sect. 3.1.2).

³ Threshold friction velocity: the velocity above which particles can be dragged by atmosphere against gravity.

⁴ Baroclinic condition: the atmospheric density depends both on temperature and pressure in contrast with a barotropic condition for which the atmospheric density depends only on pressure.

$$Re_\tau = \frac{\rho u_\tau d_p}{\mu} \quad (1.6)$$

where ρ_p is the particle density, d_p is the particle diameter, g is the gravity acceleration, A is an empirical constant, and Re_τ is the Reynolds number. As an example, on Mars, $u_\tau \sim 1.5$ m/s for $\rho_p = 2.73 \cdot 10^3$ kg/m³ and $d_p = 100$ μ m.

PBLs are turbulent and wind profiles are mathematically modelled from the surface to the asymptotic height with: a *viscous sublayer*, i.e., where viscous effects prevail on convective effects, computable with the *Prandtl's linear law* (Prandtl, L., 1925, Eq. (1.7)); a *buffer layer*, i.e., an intermediate region, computable with interpolation functions as the *Spalding's law of the wall* (Spalding, D.B., 1961, Eq. (1.8)); a *log-law region*, i.e., where convective effects become more important, computable with the *Von Karman's log-law* (Von Karman, T., 1930, Eq. (1.9)).

$\frac{U}{u_\tau} = y^+$	$y^+ < 5$	(1.7)
$y^+ = \frac{U}{u_\tau} + e^{-kB} \left[e^{\frac{kU}{u_\tau}} - 1 - k \frac{U}{u_\tau} - \frac{1}{2} k^2 \left(\frac{U}{u_\tau} \right)^2 - \frac{1}{6} k^3 \left(\frac{U}{u_\tau} \right)^3 \right]$	$10 < y^+ < 30$	(1.8)
$\frac{U}{u_\tau} = \frac{1}{k} \ln y^+ + B$	$5 < y^+ < 30$	(1.9)
$k = 0.41 \quad B = 5.2$ (Pope, S.B., 2000)		
$k = 0.41 \quad B = 5.0$ (Coles, D.E., Hirst, E.A., 1968)		
$k = 0.40 \quad B = 5.5$ (Nikuradse, J., 1930)		

When dust particles are larger than the thickness of the viscous sublayer, i.e., ~ 9 mm (White, F.M., 1981), the surface roughness cannot be neglected and the log-law is modified as in Eq. (1.10):

$$\frac{U}{u_\tau} = \frac{1}{k} \ln \left(\frac{y}{y_0} \right) \quad (1.10)$$

where y_0 is the *equivalent roughness height*, which depends on surface properties, e.g., for uniform layers composed by spherical particles with diameter of 60-2000 μ m, y_0 is equal to 1/30 of the grains diameter (Bagnold, R.A., 1941).

Experimental simulations by Greeley, R. et al., 1980 show that grains need threshold velocities (u_τ) larger than on Earth due to the lower atmospheric density (Fig. 1.12). For

instance, on Mars for $\rho_p = 2.73 \cdot 10^3 \text{ kg/m}^3$ and $d_p = 100 \text{ }\mu\text{m}$, $u_\tau = 1.5 \text{ m/s}$, which needs a wind velocity at 1.5 m above surface of 20 m/s if $z_0 = 1 \text{ cm}$ and 30 m/s if $z_0 = 0.1 \text{ cm}$, while on Earth $u_\tau = 0.3 \text{ m/s}$. The trends of the curves in Fig. 1.12 can be explained with the following considerations (a more detailed study of the physical models of the aerosol dynamics will be done in Chapter 3):

- The minimum point is ruled by the ballistic coefficient⁵ of the particles, as the most relevant phenomena determining the particle dynamics are the aerodynamic drag and the mass inertia.
- Smaller particles have smaller frontal size and higher Cunningham correction factors (Sect. 3.1.2), hence their drag is lower, and, although their mass inertia is also lower, higher wind velocity is required to accelerate them.
- At lower atmospheric density (i.e., low pressure and/or high temperature), a higher wind velocity is required to move particles.

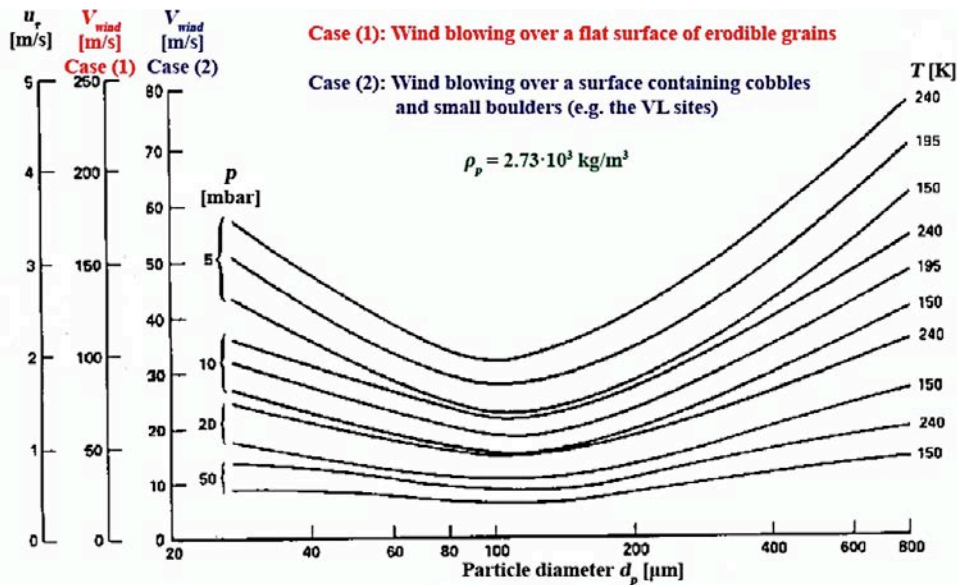


Fig. 1.12: Threshold velocity (u_τ) and wind velocity (V_{wind}) required to move dust grains ($\rho_p = 2.73 \cdot 10^3 \text{ kg/m}^3$) on Mars surface (Greeley, R., et al., 1980).

As said before, Martian climate and dust cycle are influenced by special events as dust storms and dust devils. They are the most common and energetic atmospheric phenomena on Mars (Fig. 1.13), which redistribute dust lifted by winds on a local scale

⁵ Ballistic coefficient: the ratio of the mass of a body/particle and its reference surface and drag coefficient ($m_p/(S_p C_D)$).

or on a global scale (e.g., from the southern to northern hemisphere, where dust can be partly incorporated in the polar caps).

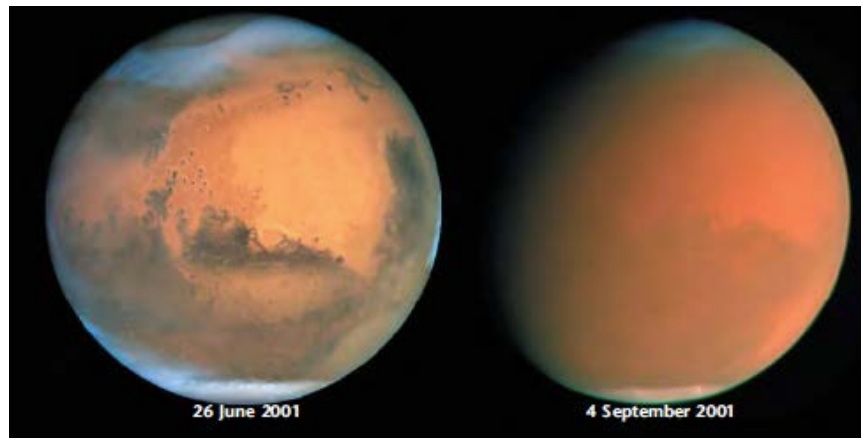


Fig. 1.13: Dust storms occurrence on Mars (NASA, JPL, Malin Space Science Systems, 2001).

Dust storms arise when a gust front blows loose sand and dust from a dry surface. Particles are transported by saltation and suspension causing soil erosion from one place (causing soil erosion) and deposition in another. These particles and those up to tens of microns that precipitate faster, fall over most of the planet, and contribute to a dust layer that covers all surface, if not removed later by wind. Aeolian processes and windblown particles over many years determine large accumulation of dust producing bright albedo areas (~ 0.27), vast dune fields, eroded hills, drifts of fine grains, and influencing formation and structure of cratered uplands and smooth terrain in the polar regions. Deposits of windblown particles may be important reservoirs for volatiles and may influence climate changes via variation of regional albedo. Dust storms can be thousands of meters wide and tens of kilometers high, tracing innumerable dark graffiti on the surface (Thomas, P., Gierasch, P.J., 1985; Biener, K.K., et al., 2002). In some years, one or two local dust storms at southern hemisphere can grow into exceptional events (*planet-wide dust storms*), which cover the entire planet of dust, like a veil for many months (Fig. 1.13).

Dust devils are thermally driven atmospheric vortices filled with loose sand and dust. The particles are raised from the surface by the low-pressure core within the dust devil (Sinclair, P.C., 1969; Greeley, R., 2003; Ferri, F., et al., 2003; Balme, M., Hagermann, A., 2006). The masses of air sucked towards the dust devil axis of rotation are strongly accelerated, resulting in violent transverse winds. In combination with the vertical aspiration at the center of the dust devil, these winds succeed in lifting large quantities

of dust. Dust devils strongly contribute to Martian weather by dust entrainment, which influences atmospheric temperature, and lead to surface changes by removing thin layers of dust, causing albedo changes (Malin, M.C., Edgett, K.S., 2001). HRSC on board Mars Express demonstrated the great influence of the Hadley circulation ascending branch for the increase in dust devil activity, especially during southern summer at latitude of 50°-60°S (Stanzel, C., et al., 2008).

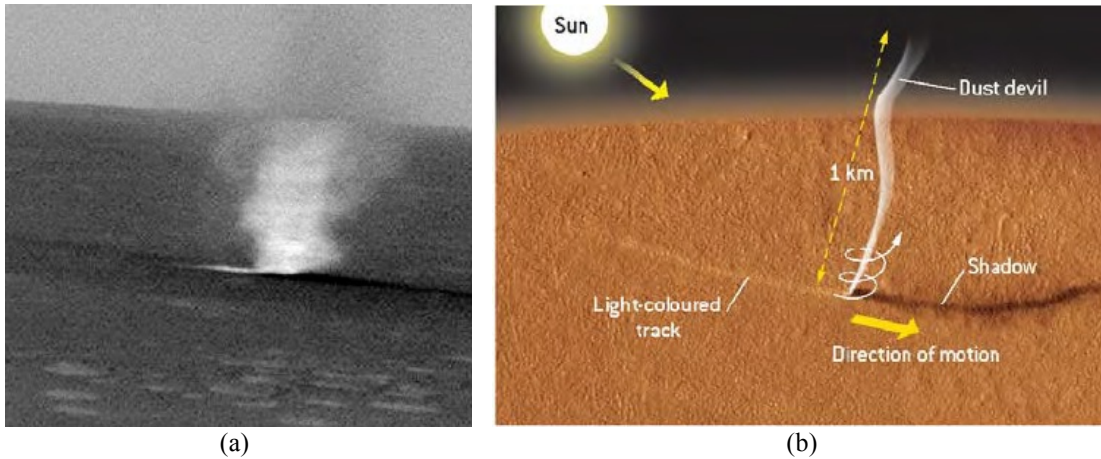


Fig. 1.14: (a) A dust devil from Navcam on board MER-A Spirit (Greeley, R., et al., 2006). (b) A dust devil scheme (Forget, F., et al., 2006).

Dust devils were first seen by VIS/Viking Orbiter and Camera/Viking Lander (Thomas, P., Gierasch, P.J., 1985; Ryan, J.A., Lucich, R.D., 1983; Ringrouse, T.J., et al., 2003) and several occurrences were observed by Mars Pathfinder (Metzer, S.M., et al., 1999; Ferri, F., 2003), MER-A and MER-B (Greeley, R., et al., 2006), Mars Express (Stanzel, C., et al. 2008), Mars Global Surveyor (Cantor, B.A., et al., 2006), showing height up to 5000 m, diameter up to 1700 m and dust flux up to $5 \cdot 10^{-4} \text{ kg/m}^2/\text{s}$ (Fig. 1.14). Dust devils and dust storms are very common in northern autumn and winter as confirmed by the high dust opacity (Fig. 1.15).

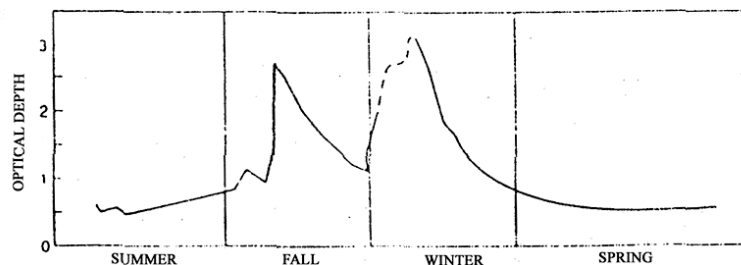


Fig. 1.15: Atmospheric opacity during a Martian year (Viking landing site, Haberle, R.M., 1986).

The Martian year is, therefore, marked in two periods with respect to dusty activities (Fig. 1.16):

- *Clear season*: during northern spring and summer, with only few dust storms and a low content of suspended dust in the atmosphere.
- *Dust season*: during northern autumn and winter with global and/or regional dust storms occurrence, which mostly grow up from the southern hemisphere (southern spring, i.e., Mars at perihelion) and can last several days.

In fact, when Mars is closer to perihelion (northern autumn and winter), dust, which in the former period was locally distributed in various regions, is, then, carried from the southern (where dust storms originate) to the northern hemisphere. Here part of the dust is incorporated into the Polar Cap. When storms are absent, dust transportation is driven by baroclinic planetary waves. These are synoptic-scale disturbances of $\sim 10^2$ - 10^3 km, which grow at mid-latitudes due to baroclinic instability, arising from the existence of meridional temperature gradients in quasi-geostrophic equilibrium⁶.

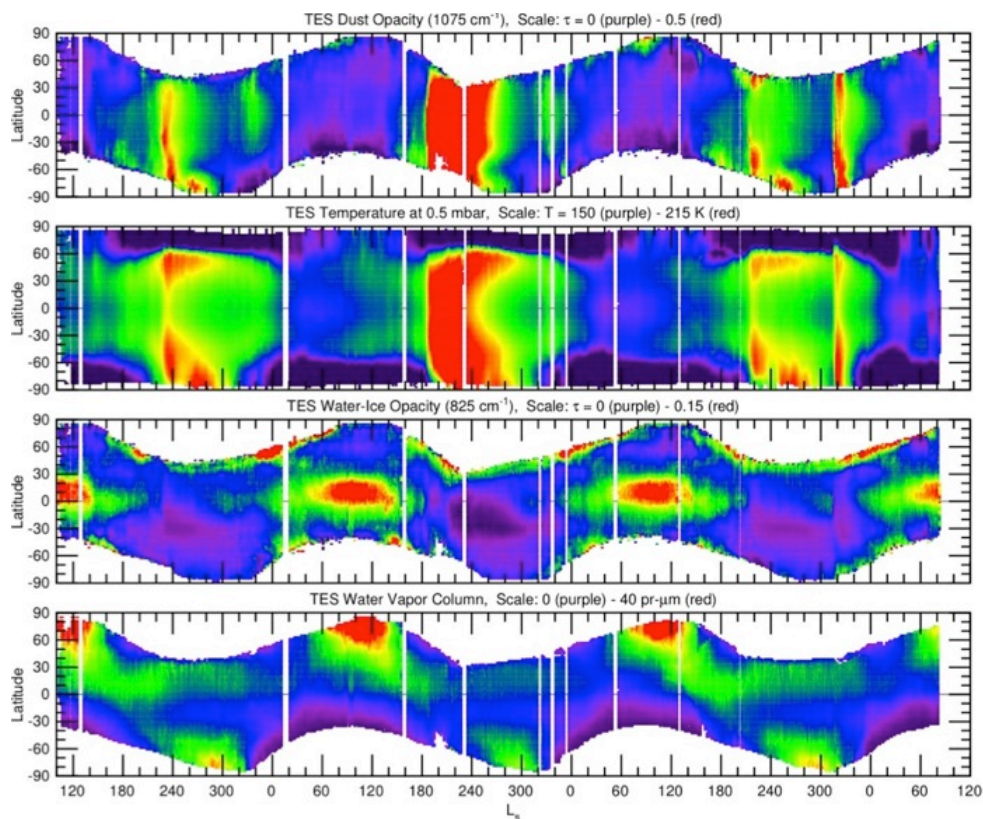


Fig. 1.16: Mars maps of dust opacity, temperature, water-ice opacity and water vapour column density by TES/MGS (NASA/JPL/Arizona State University).

The dust cycle is interconnected and anti-correlated with the H_2O and CO_2 concentration (Zurek, R.W., 1992). In fact, dust content in the seasonal polar caps may

⁶ Geostrophic equilibrium: atmospheric equilibrium between the Coriolis force and the pressure gradient force.

influence CO_2 and water vapour fluxes, as suspended grains act as condensation nuclei for H_2O and CO_2 . Therefore, when dust concentration is higher, H_2O and CO_2 concentration is lower. Moreover, dust storms occurrence depends on the long-term variations of CO_2 abundance, as the capability of injecting dust in suspension depends on the atmospheric pressure. Vapour or ice grains (H_2O) transportation depends on condensation winds and other agents of atmospheric circulation, such as those related to the variation of suspended dust content.

Finally, dust near Mars surface is also susceptible to *triboelectric charging*: when dust particles come in contact, charge can be transferred between them. Electrical potential of few hundreds Volts in an atmosphere with CO_2 at low pressure (6-10 mbar) can produce discharges from 1 mm to 1 cm length. The *Paschen breakdown voltage*⁷ is close to 100 V and the electric field can be ~ 200 kV/m (Haberle, R.M., Greeley, R., 1991). Due to low humidity, the dry Martian environment maintains charge separation.

Dust spectra acquired by remote sensing measurements show silicon dioxide (SiO_2) structures and ferric oxide (Fe_2O_3) and Aluminium oxide (Al_2O_3) traces for the dust grain composition. Possible terrestrial analogues are basalts, clay minerals composed in part of poorly crystalline ferric mineral, such as maghemite with a volume percentage of about 1.2% of magnesite, nontronite and palagonite (Toon, O.B., et al., 1977; Bell III, J.F., et al., 2006; Korablev, O.I., et al. 1993). Moreover, dust grains covered by icy layers may also be found.

The *dust particle size distribution* in the Martian atmosphere has been mainly retrieved by measurements of light scattering. Data collected from past missions provided some estimations of the dust particles' *effective radius* ($r_{eff} = 0.50-2.75 \mu m$) and *effective variance* ($v_{eff} = 0.2-0.5$) (Tab. 1.4) considering dust particle distributions based on the gamma and gamma-modified function (Fig. 1.17) (see Sect. 3.2.2 for definitions). The proposed size distributions have a range of diameter $d_p < 20 \mu m$ with maxima concentration for $d_p = 1-5 \mu m$ and lower concentration for very smaller particles, which suggested that the dispersion of particles in the atmosphere is both ruled on gravitational settling and mainly on turbulent intake by winds (Conrath, B.J., 1975; Toon, O.B., et al., 1977). Anyway, a size distribution estimated from *in situ* data

⁷ Paschen breakdown voltage: the minimum voltage that causes the medium to become electrically conductive.

acquisition by directly detecting and counting single grains dispersed in the atmosphere without assuming *a priori* distribution functions has not been made yet on the Martian ground.

r_{eff} (μm)	v_{eff}	Boundary Conditions	Mission (Instrument), Year [Reference]
2.75	0.42	$L_S = 143.5^\circ$ Dust storm	Mariner 9 (IRIS), 1971 [Toon, O.B., et al., 1977]
1.8	0.44	$L_S = 295^\circ\text{-}350^\circ$	Mariner 9 (IRIS), 1971 [Clancy, R.T., et al., 1995]
0.53	0.023	$L_S = 343^\circ\text{-}348^\circ$	Mariner 9 (IRIS), 1972 [Santee, M., Crisp, D., 1993]
2.7	0.38	$L_S = 143.5^\circ$ Mie Crater (48.27°N 134.01°E)	Viking 2 Lander, 1977 [Pollack, J.B., et al., 1979; Colburn, D., et al., 1989]
1.85±0.3	0.5±0.2	$L_S = 143.5^\circ$ Mie Crater (47. 7°N 134.01°E)	Viking 2 Lander, 1977 [Pollack, J.B., et al., 1995]
1.52±0.3	0.5±0.2	$L_S = 208.1^\circ$ Golden Plain (22.70°N 48.22°W) Dust storm	Viking 1 Lander, 1977 [Pollack, J.B., et al., 1995]
0.1-0.4		$L_S = 169^\circ\text{-}185^\circ$	Viking Orbiter (IRTM), 1977-1979 [Clancy, R.T., Lee, S.W., 1991]
1.25	0.25	$L_S = 2^\circ\text{-}18^\circ$	Phobos 2 Orbiter (ISM), 1989 [Drossart, P., et al., 1991]
1.26±0.2	0.2	$L_S = 2^\circ\text{-}18^\circ$ Height 12-35 km MSL	Phobos 2 Orbiter (KRFM, ISM), 1989 [Korablev, O.I., et al., 1993; Drossart, P., et al., 1991; Moroz, V.I., et al., 1993]
1.8	0.4	$L_S = 2^\circ\text{-}18^\circ$ Height 12 km MSL	Phobos 2 Orbiter (KRFM, ISM), 1989 [Korablev, O.I., et al., 1993; Drossart, P., et al., 1991; Moroz, V.I., et al., 1993]
1.6±0.15	0.2-0.5	$L_S = 145^\circ$ Ares Vallis (19.3°N 33.22°W)	Mars Pathfinder (IMP), 1997 [Tomasko, M.G., et al., 1999]
1.71±0.29	0.25±0.1	$L_S = 145^\circ$ Ares Vallis (19.3°N 33.22°W)	Mars Pathfinder (IMP), 1997 [Markiewicz, W.J., et al., 1999; Smith, P.H., Lemmon, M., 1999]
1.5-1.8		$L_S = 200^\circ$ Northern hemisphere	Mars Global Surveyor (TES), 1999-2000 [Clancy, R.T., et al. 2001]
1.0±0.29		$L_S = 130^\circ\text{-}160^\circ$ 40°-45°N	Mars Global Surveyor (EPF TES), 1999-2000 [Clancy, R.T., et al., 2003]
0.5-1.0	0.3-0.5	$L_S = 130^\circ\text{-}160^\circ$ 40°-60°N	Mars Express (SPICAM), 2003 [Fedorova, A.A., et al., 2009]
1.7	0.3	Gusev Crater (14.57°S 175.48°E) $L_S = 330^\circ\text{-}150^\circ$	MER-A (Mini-TES), 2003 [Wolff, M.J., et al., 2006]
1.9±0.4	0.3	$L_S = 350^\circ$ Meridiani Planum (1.95°S 354.47°E)	MER-B (Mini-TES), 2003 [Wolff, M.J., et al., 2006]
1.6	0.2	$L_S = 84^\circ$ Green Valley (68°N 126°W) Height = 2 km	Phoenix (MET/Lidar), 2008 [Dickinson, C., et al. 2010]

Tab. 1.4: Dust size parameters obtained by past measurements.

The particle size distributions obtained by remote measurements (Fig. 1.17) are based on some simplifying hypotheses about distribution, optical properties and morphology of the particles. In fact, the light scattering for non-spherical particles, which should be the most expected on Mars, is quite complex to be modelled (Sect. 3.2.2). Moreover, in polydisperse samples, the number of variables to be considered for modelling the asphericity is very high such that to make quite difficult to obtain results from remote measurements.

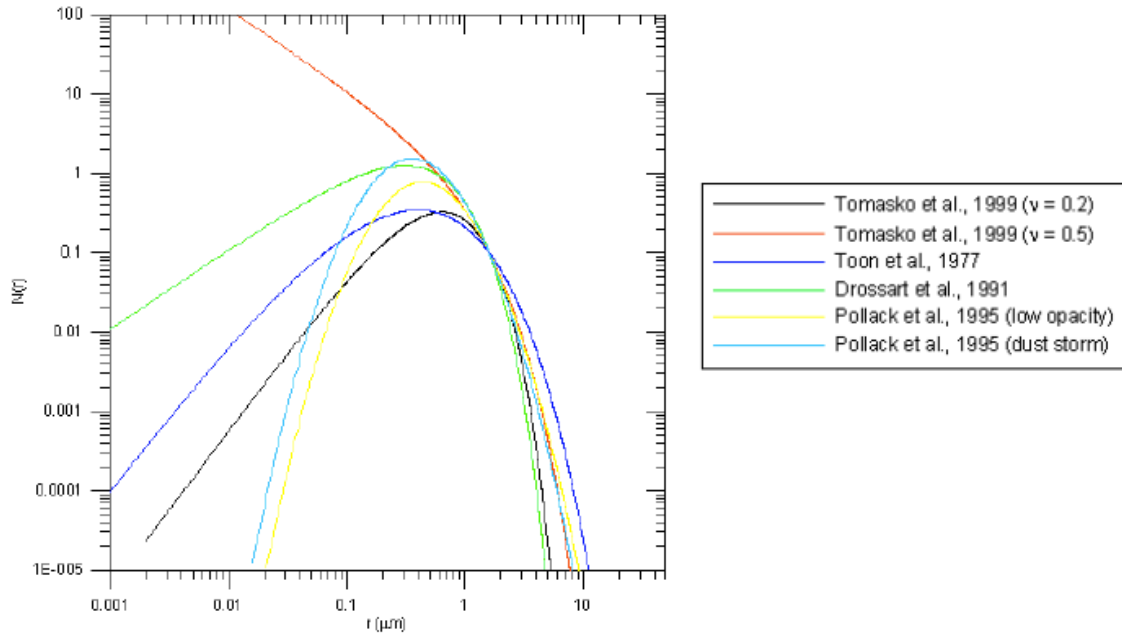


Fig. 1.17: Particle size distributions ($N(r)$) as a function of particle radius (r) as derived by remote measurements. The curves were scaled to have $N = 0.1$ for $r = 1.6 \mu\text{m}$.

1.2.4 Water

On Mars, water is much less abundant than on Earth. Most of it is locked in the cryosphere (permafrost and polar caps), and no liquid water has been found yet. Only a small amount of water vapour is present in the atmosphere with seasonal and daily variations (on average about $1\text{-}2 \cdot 10^{12}$ kg with a volume of $\sim 1\text{-}2 \text{ km}^3$ and a concentration of ~ 200 ppm by volume) (Smith, M.D., 2002, 2009, Fig. 1.18). To have an idea of the total amount of water on Mars, one can think that if all precipitated out, the water would form a uniform layer of $\sim 10^{-6}$ m.

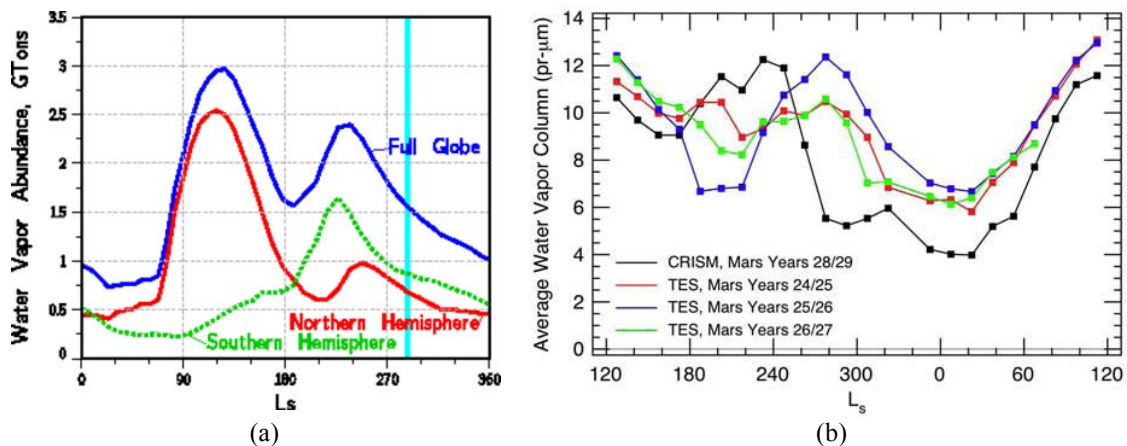


Fig. 1.18: (a) Annual cycle of water vapour in the Martian atmosphere (MGCM) and (b) column abundance of water vapour as a function of season (L_s) (Smith, M.D., et al., 2009).

Since the typical atmospheric pressure and temperature at the surface level are close to the *water triple point* ($T = 273 \text{ K}$, $p = 6.1 \text{ mbar}$, Fig. 1.19), water condenses/sublimates directly to/from the solid state; hence, most of H_2O is found as ice or vapour, but not in liquid form. Nevertheless, low liquid quantities of water could be found in favourable conditions.

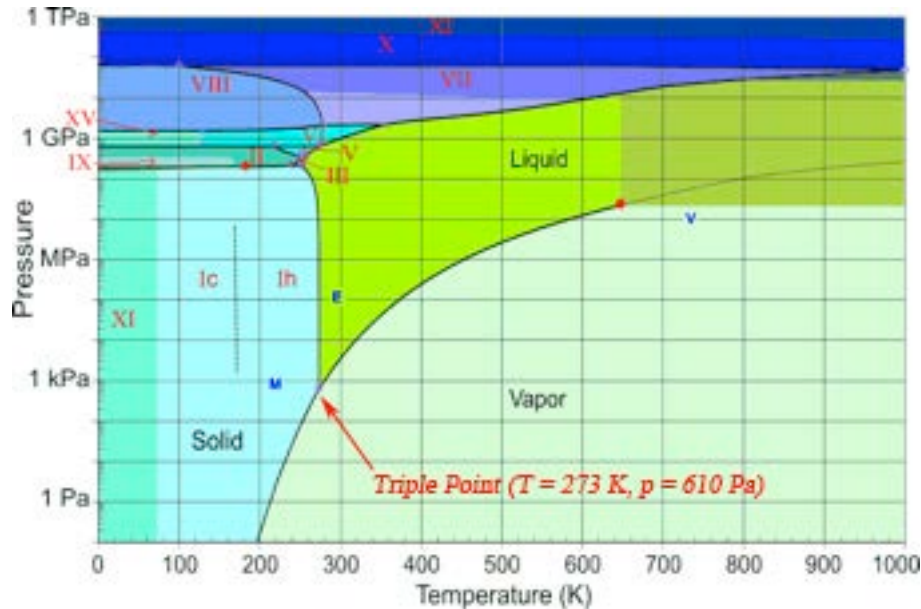


Fig. 1.19: (a) Water (H_2O) phase diagram (London South Bank University).

Measurements of the water vapour content in the atmosphere have been performed mainly via remote sensing and on global and/or wide scale as by the instrument MAWD on board the Viking Orbiter (Jakosky, B.M., Haberle, R.M., 1992; Melchiorri, R., et al., 2007; Tamppari, L.K., et al., 2009), TES on board Mars Global Surveyor (Smith, M.D., 2002, 2004; Melchiorri, R., et al., 2007), OMEGA and SPICAM on board Mars Express (Melchiorri, R., et al., 2007; Encrenaz, T., et al., 2008; Fedorova, A.A., 2009), CRISM on board Mars Reconnaissance Orbiter (Tamppari, L.K., et al., 2009; Smith M.D., et al., 2009). Results show the higher water content of 90-100 $\text{pr-}\mu\text{m}$ ($\sim 4.5 \cdot 10^{-6} \text{ kg/m}^3$) in northern summer ($L_S = 93^\circ\text{-}126^\circ$) at high latitudes, and minima content of 1-10 $\text{pr-}\mu\text{m}$ ($\sim 1.2 \cdot 10^{-9} \text{ kg/m}^3$) in northern winter ($L_S = 330^\circ\text{-}40^\circ$) at northern and southern middle and high latitudes, which determine a global average amount over the year of 10 $\text{pr-}\mu\text{m}$ in the northern hemisphere and 9.5 $\text{pr-}\mu\text{m}$ in the southern hemisphere (Fig. 1.20).

Nevertheless, remote sensing measurements are not able to observe the eventual presence of liquid water since its little amount, hence, the need to perform local *in situ*

measurements. Up to now, the only *in situ* measurement was performed by the instrument IMP on board Mars Pathfinder, which found a local annual average amount of water vapour of 6 ± 4 pr- μm (Titov, D.V., et al., 1999).

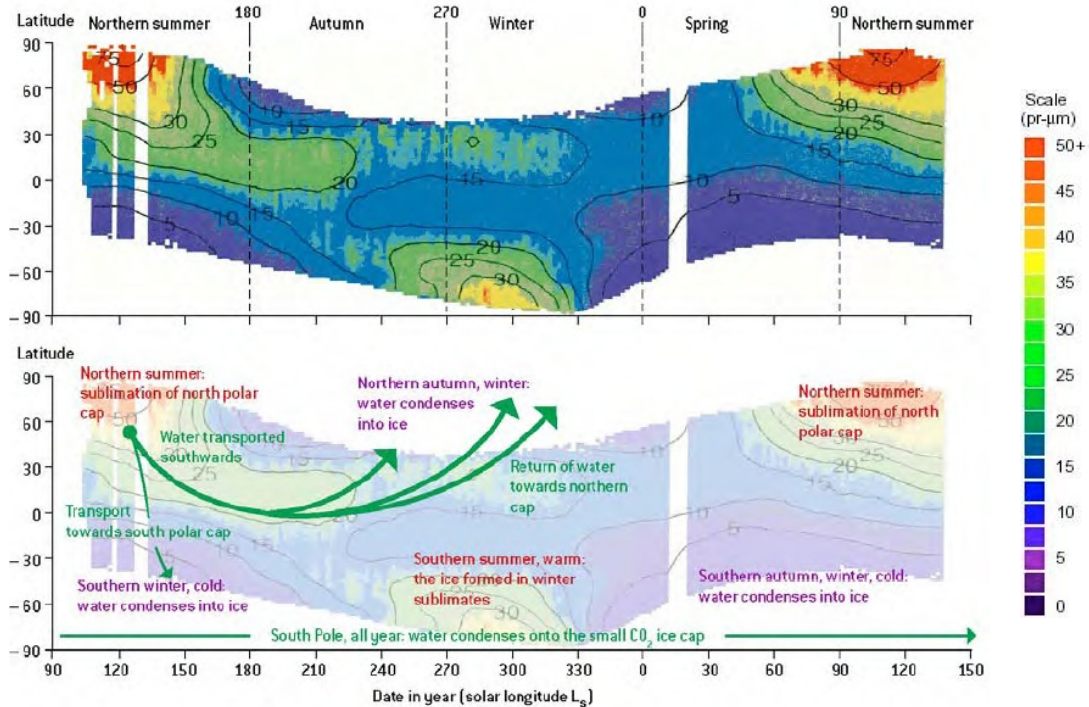


Fig. 1.20: The annual water vapour cycle observed by the TES/MGS (Smith, M.D., 2002).

If the water vapour abundance is referred to a surface isobar level of 6.1 mbar pressure, the latitudinal and longitudinal annually averaged water vapour column abundance is independent from topography: the annually average of water vapour becomes 17 pr- μm in the latitude band 10°S - 40°N , and 12 pr- μm elsewhere (Smith, D., 2002).

Polar regions are undoubtedly the most suitable places to observe water vapour variability because they are the main permanent and seasonal water reservoir of the planet (Melchiorri, R., et al., 2009). Almost every year from the end of northern spring through the northern summer, water vapour girdles the equator. From the North cap, vast quantities of water vapour are released into the cold atmosphere; this water vapour, transported to tropical latitudes, is rapidly borne aloft in the ascending branch of the Hadley cell; as it raises, it encounters colder atmospheric layers, until it reaches a level at the limit of saturation, where it condenses; when autumn and winter come to the polar regions, the mass of carbon dioxide moving towards the poles condenses, and many different cloud forms are created (*polar hood*).

OMEGA on board Mars Express monitored the water vapour over high and large volcanoes on the Tharsis Plateau, i.e., Olympus Mons (18°N, 133°W, 27 km MSL, Fig. 1.21), Ascraeus Mons (11.3°N, 104.5°W, 18 km MSL), Pavonis Mons (0.8°N, 113.4°W, H 14 km MSL), Arsia Mons (9.5°S, 120°W, 16 km MSL) evidencing clouds in northern summer and founding an increase of water vapour mixing ratio from the valley to the summit (Maltagliati, L., et al., 2006).



Fig. 1.21: Clouds around the Olympus Mons (18°N, 133°S, 27 km MSL, Viking Orbiter reconstructed image, NASA).

Due to the low temperature, pressure and water vapour amount, fine ice crystals (size of 1-5 μm) forming the clouds will sublime before ever reaching the ground, so raining cannot happen on Mars.

In every season, water vapour content is maximum during the day and minimum at night, varying by a factor of 2 in anti-correlation with dust opacity (Formisano, V., et al., 2001; Titov, D.V., et al., 1994; Böttger, H.M., et al., 2005). Daily variability of atmospheric water vapour depends on many causes:

- Regolith or other components *breathing*, i.e., the exchange process of gas by a solid rock, forced by temperature changes, gather water from the atmosphere, adsorbing it into the surface during the night and desorbing it as soon as the Sun warms the ground (Titov, D., 2002; Melchiorri, R., et al., 2009).
- Formation of night-time hazes removes some water vapour from the night column (Jakosky, B.M., 1985).
- Frost, formed during the night, reduces the water vapour column density (Jones, K.L., 1979).

1.3 The Mars Exploration

1.3.1 Missions to Mars

Several missions to Mars were done up to now (2011), including probes, orbiters, landers and robotic rovers, which made important contributions to understand the Mars planet (Tab. 1.5).

Mission	Agency	Launch	Arrival	End	Platform(s)	Landing Site (Lander/Rover)
Mariner 4	NASA	28/11/1964	14/07/1967	21/12/1967	Flyby probe	
Mariner 6	NASA	25/02/1969	31/07/1969	31/08/1969	Flyby probe	
Mariner 7	NASA	27/03/1969	05/08/1969	31/08/1969	Flyby probe	
Mars 2	USSR	19/05/1971	27/11/1971	22/08/1972	Orbiter	
Mars 3	USSR	28/05/1971	02/12/1971	22/08/1972	Orbiter	
Mariner 9	NASA	30/05/1971	13/11/1971	27/10/1972	Orbiter	
Viking 1 (VL1 + VO1)	NASA	20/08/1975	20/07/1976	17/08/1980	Orbiter + Lander	Golden Plain, Chryse Planitia (22.70°N, 48.22°W)
Viking 2 (VL2 + VO2)	NASA	09/09/1975	03/09/1976	25/07/1978	Orbiter + Lander	Mie Crater, Utopia Planitia (48.27°N, 134.01°E)
Phobos 2	USSR	12/07/1988	29/01/1989	27/03/1989	Orbiter	
Mars Global Surveyor (MGS)	NASA	07/11/1996	11/09/1997	05/11/2006	Orbiter	
Mars Pathfinder (MPF)	NASA	04/12/1996	04/07/1997	27/09/1997	Lander + Rover	Ares Vallis (19.13°N, 33.22°W)
Mars Odyssey (MOd)	NASA	07/04/2001	24/10/2001	Operative	Orbiter	
Mars Express (MEx)	ESA	02/06/2003	25/12/2003	Operative	Orbiter	
Mars Exploration Rover Spirit (MER-A)	NASA	10/06/2003	04/01/2004	25/05/2011	Rover	Gusev Crater (14.57°S, 175.48°E)
Mars Exploration Rover Opportunity (MER-B)	NASA	07/07/2003	24/01/2004	Operative	Rover	Meridiani Planum (1.95°S 5.43° W)
Mars Reconnaissance Orbiter (MRO)	NASA	12/08/2005	10/03/2008	Operative	Orbiter	
Phoenix (PHX)	NASA	04/08/2007	25/05/2008	10/11/2008	Lander	Green Valley, Vastitas Borealis (68.22°N, 125.75°W)

Tab. 1.5: The successful missions to Mars.

In particular, in Fig. 1.22 a schematic summary of the measurements done and/or related to the closest upcoming scheduled missions to investigate the Martian PBL is provided. The ExoMars Programme (2016-2018) and its following Mars Sample Return mission (2018-2020) have not been included yet in the list of Fig. 1.22. The ExoMars Programme is widely discussed in detail in Chapter 2 as strongly connected to the work of this thesis.

Mission	Instrument	Observation platform		Surface										Observed variables								Subsurf. H ₂ O								
		Landers	Orbiters	Lander		Orbiter		Surface		Topography		Temperature		Pressure		Wind		H ₂ O content		Dust			Clouds		PBL indirect					
		in-situ	imaging	Remote sens.	radar	limb	radio occ.	stellar occ.	α	I	topography	T _s	T ₀	T	P	V	w	H ₂ O content	z	hyg	T(0)	dT/dz	dq/dz	dust devils	dust	clouds	$\tau_{0.5}$	hcz		
Past and current	VO			x	x				x	x	x								x											
				x	x																									
VL	IRTM MAWD VIS			x	x														x	x						x	x			
Phobos 2	VMIS Imager	x	x											x	x	x					x ¹				x	x	x	x		
MGS	Auguste			x				x														x	x		x	x	x			
	MOC			x	x																				x	x	x			
	MOLA RS TES			x	x		x		x	x	x			x					x	x		x				x	x			
MPF	ASU/MET	x		x	x	x			x	x	x			x	x	x ²					x ¹					x	x			
MOd	IMP		x																					x						
	THEMIS GRS, HEND			x	x			x	x		x																x			
MER	mini-TES			x							x			x						x ³	x									x
MEx	ParCam HRSC OMEGA	x	x					x																x	x	x				
	PFS			x	x						x				x												x	x		
	RS SPICAM			x	x		x									x				x		x				x	x			
	SSI RAC		x																								x	x		
PHX	MET TECP	x		x								x	x	x	x	x ⁴														
	LIDAR	x																												
	HIRISE			x	x																					x	x	x	x	
MRO	HIRISE			x	x																					x	x	x		
	MCS			x		x																x								
Confirmed																														
MSL	REMS MastCam	x	x	x							x			x	x	x	x	x												
MetNet Precursor	MET																													
	MetSIS, dust ParCam	x	x					x																						

¹ Entry profile

² Only wind direction information is of satisfactory quality, magnitude information is not

³ H₂O column abundance

⁴ Telltale observed via the imaging system

Fig. 1.22: Overview of the past and some next missions relevant to study the Martian Planetary Boundary Layer.

A list of the next expected missions, which will probe the Martian exobiology, geology and/or environment, is reported in Tab. 1.6. Some of them are not yet confirmed and/or are expected to be replanned. The trend is that collaboration between the most important space agencies and the widest scientific community will be essential in the coming years. Finally, in Sect. 1.3.2, a brief summary of the most important investigation objects on Mars will follow.

Mission	Agency	Launch	Arrival	Platform(s)
Mars Science Laboratory (MSL)	NASA	11/2011	08/2012	Rover
Phobos-Grunt	Russia, China	11/2011	?	Orbiter + Lander (Phobos) + Sample Return
MAVEN	NASA	12/2013	2014	Orbiter
MetNet	Finland, Russia, Spain	2014-19	2014-20	Lander
ExoMars TGO and EDM	ESA-NASA	01/2016	10/2016	Orbiter + Lander
ExoMars Rover(s)	ESA-NASA	2018	2019	Rover
Mars Sample Return	ESA-NASA	2018	2020-22	Orbiter + Lander + Rover + Sample Return

Tab. 1.6: The next missions for Mars exploration.

1.3.2 Some Key Scientific Objectives of the Future Mars Exploration

Among the most relevant scientific objectives of the next exploration of Mars *exobiological research*, *geological characterization*, and *atmospheric characterization* are certainly interconnected main subjects.

Exobiology studies the origin, evolution and distribution of life searching for *biomarkers* of extant and extinct life. For organisms to have emerged and evolved, liquid water is the main requirement. Hence, the search for extinct or extant life translates into a search for liquid water-rich environments, past or present.

The present environment on Mars is extremely hostile for the widespread proliferation of surface extant life. Nevertheless, basic organisms might still flourish in protected places, e.g., deep underground, shallow depths, or within rock cracks and cavities. In fact, Martian-like environments on Earth as the desert of the Antarctic dry valleys, where temperature is -15°C ... 0°C in summer and -60°C in winter with a relative humidity of 16-75%, hosts photosynthetic endolithic microbial communities, dominated by cryptoendolithic lichens. The search methodology should in particular focus on investigations in protected niches in the subsurface and within surface outcrops.

Life could have existed when Mars was warmer and wetter in the first billion years following planetary formation. Those conditions were similar to those when microbes gained a foothold on the young Earth. This needs to identify geologically suitable and life-friendly locations, currently unknown, where liquid water still exists, at least for short periods. Another hypothesis under study is the transport of terrestrial organisms embedded in meteoroids, delivered from Earth to Mars.

Biomarkers as compounds synthesised by living organisms are relatively stable and can be preserved for more than one billion year after the parent cells have died, even if only in backbone of carbon atoms (e.g., amino acids, lipids that comprise cell walls, pigments as bacteriochlorophyll and chlorophyll that absorb light to power photosynthesis in bacteria and plants).

A useful clue for extinct life may be the isotopic signature of carbon as many life processes favour the assimilation of the light isotope ^{12}C over ^{13}C . For instance, the enzymatic uptake of carbon during photosynthesis can result in a $^{12}\text{C}/^{13}\text{C}$ ratio significantly higher than the one used as standard for terrestrial abiotic material (Van Zuilen, M., 2008).

Homochirality, i.e., the property which involves molecules without an internal plane of symmetry that have a non-superimposable mirror image, is probably the most reliable biomarker (Bada, J.L., 2004). In fact, two of life's most important molecular building

blocks, amino acids and sugars, can exist in left-handed and right-handed configurations (i.e., enantiomers), which, like a pair of gloves, are mirror images of one another. Key life processes such as protein synthesis and gene transcription, rely on amino acids and sugar having the correct spatial conformation to “shake hands” at molecular level with their counterparts.

A major problem with the study of biomarkers is that many decompose when exposed to temperatures greater than 200°C. On Earth, high-temperature metamorphic processes and plate tectonics have resulted in the reformation of most ancient terrains. It is very difficult to find accessible rocks on Earth that are older than 3 billion years and in good conditions. Mars has not suffered such widespread tectonic activity. Therefore, rocks from the earliest period, which have not been exposed to high temperature recycling, are likely to exist. Consequently, well-preserved, ancient biomarkers may still be accessible for analysis.

Geological studies are mainly focused on studying surface and/or subsurface evidence of water and trace gases activity, soil characterization and relationship with atmospheric phenomena.

Trace gases, e.g., H_2O , HO_2 , H_2O_2 , NO_2 , N_2O , CH_4 , C_2H_2 , C_2H_4 , C_2H_6 , H_2CO , HCN , H_2S , OCS , SO_2 , HCl , CO , O_3 , are relevant as signature of geological and biological activity on Mars (Lefère, F., and Forget, F., 2010). Observations from the instrument PFS on board Mars Express and by very high spectral resolution spectrometers using Earth-based telescopes, have detected variable amounts of methane (CH_4) in the atmosphere of Mars (Zureck, R.W., Chicarro, M.A., et al., 2009; Mumma, M.J., et al., 2009; Atreya, S.K., Mahaffy, P.R., Wong, A.-S., 2007; Formisano, V., et al., 2004; Krasnopolsky, V.A., Mallaird, J.P., Owen, T.C., 2004). Based on photochemical models and on the current understanding of the composition of the Martian atmosphere, methane has a chemical lifetime of ~ 300-600 years, which is very short on geological time scales. Thus, its presence indicates a subsurface source that has recently (geologically) released methane into the atmosphere. There are both geochemical and biochemical processes that could produce methane in the subsurface, even if its presence is not sufficient to establish the nature of the source. Current photochemical models cannot explain the reported rapid space and time variations in atmospheric methane concentration. Whether geochemical or biochemical in origin, methane

observations indicate a dynamically active Mars subsurface today. Moreover, some studies suggest that large electric fields in windblown sand and dust storms (Melnik, O., Parrot, M., 1998; Farrell, W.M., et al., 2003; 2006) could produce energetic electrons that could directly dissociate methane (Delory, G.T., et al., 2006) and/or catalyze the production of H_2O_2 (Atreya, F.S., et al., 2006), which is a strong oxidant of organic matter and thus of CH_4 .

As seen in Sect. 1.2, most of the processes that control the current Martian weather and climate happen in the near surface. Dust lifting is one of the most obvious examples of mechanisms still suffering from the absence of relevant data (Newman, C.E., et al., 2002; Kok, J.F., 2010). Airborne dust grains are known to have a large impact on the radiative/convective equilibrium of the troposphere by absorbing and scattering radiation (Leovy, C., et al., 2001; Bougher, S.W., et al., 1999). Moreover, wind and windblown dust are the most important currently active surface modifying agents on Mars as they are responsible for erosion, redistribution of dust on the surface and weathering. Major improvements on Mars climate models requires, in addition to standard meteorological parameters (pressure, temperature, humidity, opacity), quantitative information about dust lifting, transport and removal mechanisms, i.e., the dust cycle (Farrell, W.M., et al., 2004; Kok, J.F. and Renno, N.O., 2009). A special focus should also be on environmental electric field effects on the dust cycle for lightning activity (Renno, N.O., et al., 2003; 2004). Finally, soil characterization, above all porosity and cohesion, is also relevant to study the dust dynamics (Mehta, K.T., et al., 2009).

2 EXOMARS PROGRAMME

2.1 Aurora Programme and ExoMars Programme

The *Aurora Programme* of the European Space Agency (ESA) included several missions with the aim of creating a European long-term plan for the exploration of the Solar System, above all Mars, the Moon, and asteroids, which also implies robotic spacecraft, human spaceflight, and search for life beyond the Earth. The Aurora Programme was endorsed by the European Union Council of Research and the ESA Council in 2001, involving European and Canadian industries and academia. The programme has experienced various modifications during years, as a result of technical and management considerations. Nowadays, the tasks scheduled within the Robotic Exploration program are:

- Remote sensing of the Martian environment
- Robotic exploration and surface analysis
- Mars sample return mission(s).

The first two steps are part of the *ExoMars Programme*. Nowadays, it foresees two missions to be carried on in cooperation with NASA:

- ExoMars 2016 mission: *Trace Gas Orbiter (TGO)* and *Entry, Descent and Landing Demonstrator Module (EDM)*;
- ExoMars 2018 mission: ESA-led *ExoMars Rover* for astrobiology exploration joint with NASA-led caching system for sample return preparation.

The ExoMars Programme will demonstrate essential flight and *in situ* enabling technologies that are necessary for future exploration missions (e.g., an international *Mars Sample Return* mission):

- *Entry, Descent and Landing (EDL)* of a payload on the surface of Mars;
- Surface mobility with a Rover;
- Access to the subsurface to acquire samples;
- Sample acquisition, preparation, distribution and analysis;
- Collection and packaging of samples to be returned to Earth in a future mission.

The scientific investigations of the ExoMars missions will be:

- To search for signs of past and present life on Mars;
- To investigate the water/geochemical environment as a function of depth in the shallow subsurface;
- To study Martian atmospheric trace gases and their sources.

The final goal of a Mars Sample Return mission is to collect rock and dust samples from Mars and to return them to Earth for laboratory analyses.

2.2 ExoMars Programme Evolution

The ESA *ExoMars Programme* was established by the ESA Directorate of Human Spaceflight, Microgravity and Exploration, and, then, committed to the ESA Directorate of Science and Robotic Exploration (SRE), and approved by European space ministers in December 2005 in order to perform an exobiology mission to Mars. During its development, the ExoMars Programme was subjected to many changes and reviews due to technical issues and costs.

The original architecture of the ExoMars mission (2003-2006) was based on a single robotic rover able to probe the subsurface and equipped with a 16.5 kg-mass analytical laboratory included in the so-called *Pasteur Payload (PPL)*. In the 2006-2009 period, it was established to equip the lander with the 8.5 kg mass *Geophysical and Environmental Payload (GEP)*, later renamed *Humboldt Payload (HPL)*. The ExoMars spacecraft consisted of a Carrier Module (CM) and a Descent Module (DM).

The DM, carrying the rover (210 kg) and the lander, would have separated from the CM in orbit around Mars and descended into the atmosphere of the planet. The launch by Ariane 5 or Proton launcher was firstly scheduled for 2011 and then shifted to 2013. The mission profile employed a direct injection into fast interplanetary trajectory to Mars resulting in a cruise phase duration of 10 months. The DM and CM would have been injected into orbit around Mars (November 2014), then, separated, and, subsequently, entered the atmosphere individually. The DM would have landed on Mars and deployed the rover, while the CM would have burned up in the atmosphere. The rover and lander surface mission would have nominally lasted 180 sols avoiding the global dust storm season.

In 2009 the ExoMars Programme entered a first reformation phase, descoping the Humboldt Payload and some Rover instruments. In July 2009, NASA and ESA agreed upon a *Joint Mars Exploration Programme (JMEP)*. The mission was split into two parts: the *Entry Descent and Demonstrator Module (EDM)* and the *Trace Gas Orbiter (TGO)* mission in 2016, and a two *Rovers* mission in 2018. In August 2010, the scientific payload for the ExoMars Trace Gas Orbiter was selected after an Announcement of Opportunity. In June 2011 the DREAMS package and the Entry and Descent Science program were selected for the ExoMars EDM 2016, after an Announcement of Opportunity released in November 2010.

In May 2011, ESA and NASA have started discussing about a single rover for the 2018 mission, accommodating the Pasteur payload and including a NASA provided caching system. This configuration shall preserve the exobiology goals of the European mission and prepare for returning samples to Earth.

2.3 ExoMars 2016 Mission

2.3.1 Mission Architecture



Fig. 2.1: ESA Spacecraft Composite.

The ExoMars 2016 mission is scheduled to be launched in January 2016 and arrive on Mars after approximately 9 months, in October 2016. It consists of the *Trace Gas Orbiter (TGO)* and the *Entry, Descent and Landing Demonstrator Module (EDM)*, carried in a mated configuration by an ESA Spacecraft Composite (Fig. 2.1). The main objectives of the mission are to search for evidence of methane and other trace gases in the Martian atmosphere (TGO), and to test key technologies for future international missions (EDM). The Spacecraft Composite, which has a mass of about 4,200 kg, will

be launched by NASA with an Atlas V 431 rocket. The spacecraft will perform a direct injection onto a Mars T2 transfer trajectory.

The EDM will be separated from the Spacecraft Composite along a hyperbolic trajectory. It will perform the Entry, Descent, and Landing (EDL) phases, beginning at the Entry Interface Point (EIP), i.e., the conventional Martian atmosphere edge at 120 km above the planet surface, and taking about 400 s to land. During the EDL phases, the sub-modules will be separated and jettisoned such that the *EDM Surface Platform (ESP)* can land safely (Fig. 2.2). The EDM scientific operations will be supplied by a primary battery, which will determine the EDM lifetime on Mars as no solar arrays are foreseen. Atmospheric surveys will be performed during the descent along the atmospheric entry profile and environmental measurements will be performed on the Martian surface, in a site in *Terra Meridiani*, within an ellipse centred at 1.9°S, 6.1°W with approximated major axis of 100 km, soon after landing in northern autumn ($L_S \approx 240^\circ\text{-}260^\circ$) for 2-4 sols during the Martian dust storm season.

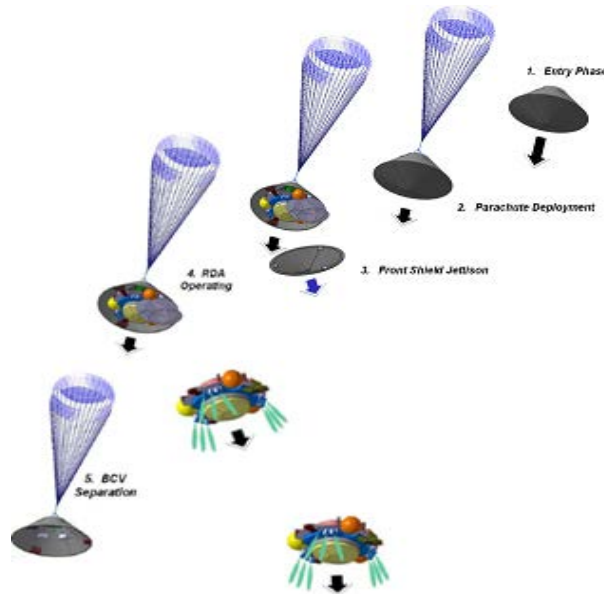


Fig. 2.2: EDM descend and landing phases.

3 days after the EDM separation, the TGO will enter the Mars Orbit Injection (MOI), which involves a 4 sol elliptical orbit around Mars and a series of manoeuvres and aerobraking operations to change the orbit inclination to 74° and reduce the apoapses down to a 1 sol orbit. Further reductions of the apoapses will be performed using aerobraking techniques over a period of about 6 to 9 months followed by a final

circularisation manoeuvre to arrive at the science and communications orbit (circular orbit, 400 km altitude, 74° inclination, 120 mins period).

The TGO scientific operations consist in spectroscopic and radiometric measurements, atmospheric monitoring and planetary mapping with US and European instruments focused to search for trace gases (Fig. 2.3); they will begin in May 2017 and last one Martian year. The TGO will include fuel to provide communications support and science operations until end 2022.

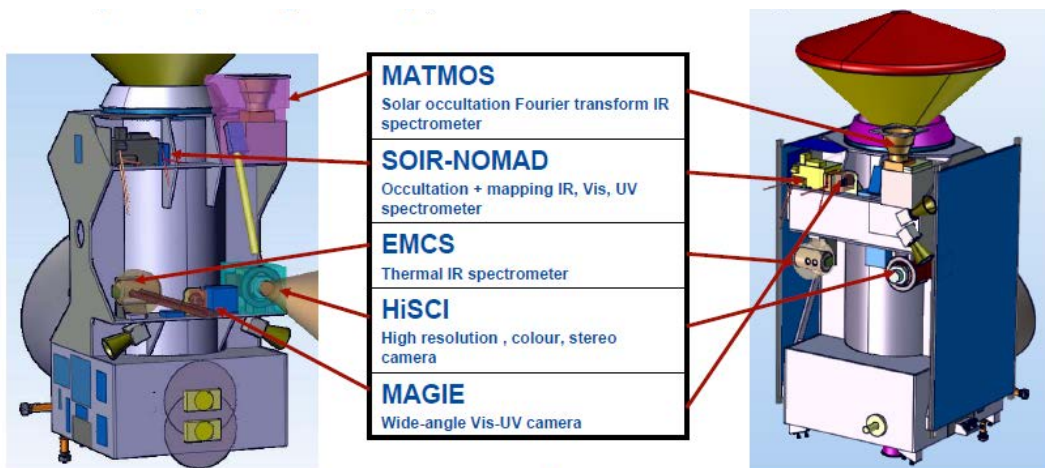


Fig. 2.3: TGO payload (ESA).

After separation the TGO will attempt to monitor the UHF transmission from the EDM during the EDL phase and surface operations, even if other ESA or NASA orbiters will be deputed to perform the communications with the EDM. Furthermore, ground-based communication arrays will track the UHF signal during the EDL phase. Planning and technical support activities will be performed jointly by ESA and NASA.

2.3.2 ExoMars EDM

The EDM is the Entry, Descent, and Landing Demonstrator Module. It has a mass of 600 kg. The EDM technologies for landing on the surface of Mars are: *Heat Shield* based on ablative materials for thermal protection; *Supersonic Parachute System* (Disk Gap Band canopy); velocity and slant range measurements sensor (using a Radar Doppler Altimeter); liquid propulsion controlled final braking; semi-soft landing; crushable structure (Fig. 2.4). The EDM scientific payload, named *Surface Payload (SPL)*, will have a mass of 3 kg for a maximum lifetime of 4 sols, depending on landing site. The total data volume rate, transmitted to Earth via a NASA relay orbiter, or the TGO if available, will not exceed 50 Mb.

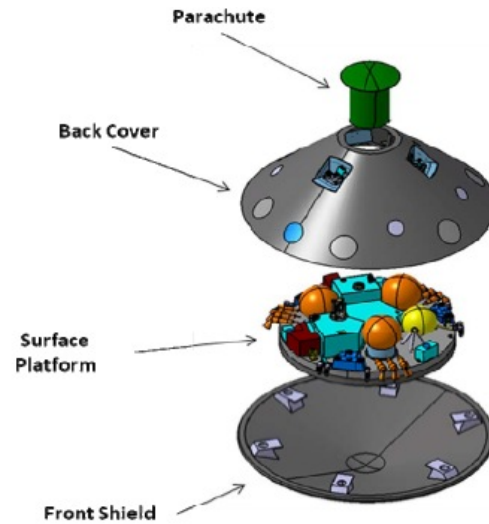


Fig. 2.4: EDM exploded view (ESA, TAS-I).

The EDM is being to be designed and manufactured by Thales Alenia Space - Italy (TAS-I). The structure is mainly made of Aluminium sandwich Carbon Fibre Reinforced Polymer skin. It is characterized by the following modules: the *Back Shell (BSH)*, which consists of the *Back Cover* plus all the EDM items physically installed, including the DM-OM (Demonstrator Module - Orbiter Module) separation mechanism, the ablative thermal protection material and the parachute system; the *Front Shield (FS)*, which is made of Norcot-Liege (i.e., a flight proven cork powder and phenolic resin ablator) and has a diameter of 2.4 m in order to sustain mechanical and thermal loads at entry; the *Surface Platform (SP)*, which consists of a primary structure accommodating the EDM propulsion system, the *Central Terminal Power Unit (CTPU)*, batteries, the *Surface Payload* plus crushable material to ensure the platform structural integrity at touchdown on Mars terrain (Fig. 2.5).

After entering the Martian atmosphere the module will deploy a single-stage Disk Gap Band parachute and will complete its landing by using a closed-loop Guidance, Navigation and Control (GN&C) system based on a Radar Doppler Altimeter sensor and on board *Inertial Measurement Units (IMU)*, that will guide a liquid propulsion system by the actuation of 3 clusters of thrusters operated in pulsed on-off mode.

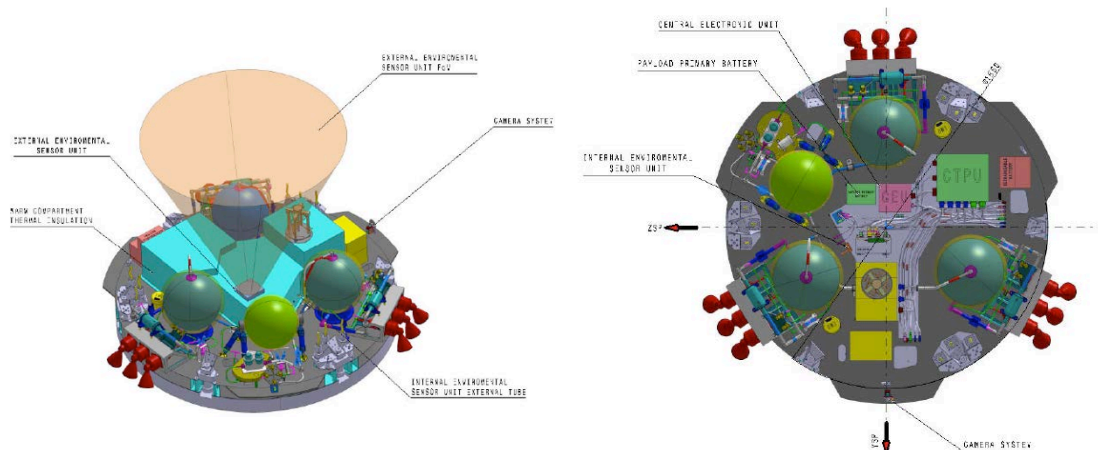


Fig. 2.5: EDM Surface Platform (ESP) showing a baseline configuration for the payload (ESA E-PIP).

The EDM scientific payload has been chosen after a selection among several proposals responding to the Announcement of Opportunity (AO) released in 2011. The definition of the AO was part of the work of this thesis. The work performed at ESA premises (ESTEC, Noordwijk, The Netherlands) in support to the Project Scientist of the EDM mission, has been finalized to harmonize the engineering constraints versus the scientific objectives (*Announcement of Opportunity: ExoMars Entry, Descent, and Landing Demonstrator Module (EDM) Science; ExoMars EDL Demonstrator Module Surface Payload Experiment Proposal Information Package - EXM-DM-IPA-ESA-00001 (E-PIP)*).

The EDM scientific calls defined in the AO were:

- *EDM Surface Payload (SPL)*: a variety of brief scientific measurements to be performed using small sensors housed within the lander’s Warm Compartment, and, possibly, with a camera mounted on the exterior.
- *EDM Entry and Descent Science*: data from the EDM Engineering Sensors (accelerometers, gyroscopes, radar altimeter, radio link, spacecraft sensors aimed at monitoring heat shield and parachute performance), and other auxiliary information (e.g., landing site ellipse, probe aerodynamic parameters, etc.) to be used to derive atmospheric profiles for density, temperature, pressure, and maybe wind along the entry and parachute descent trajectory.

The most critical requirements defined in the AO and E-PIP for the scientific payload proposal were the maximum allowed payload mass below 3 kg and the maximum data volume for the entire mission within 50 Mb. The call was open both to single sensors to

be included in a wider selected package, and to fully integrated payloads, containing a *Central Electronic Unit (CEU, i.e., analogue and digital electronics, power distribution, timer, memory, data processing and interface)*, an autonomous Power Source (*Primary Battery*), and interconnecting harness.

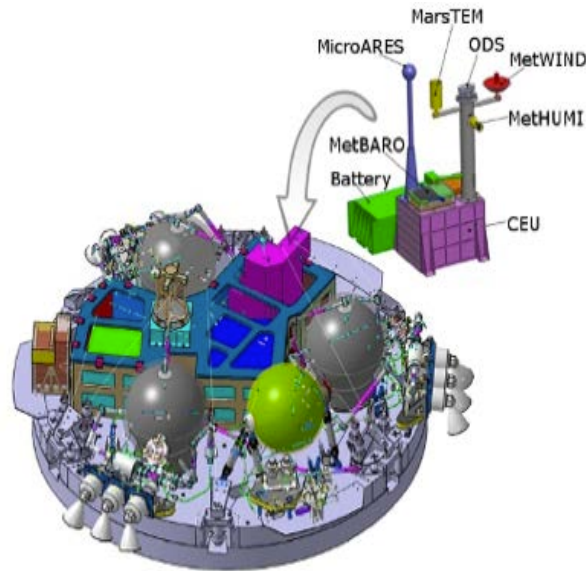


Fig. 2.6: The EDM DREAMS package in the EDM Surface Platform (ESA).

ESA-NASA selected the DREAMS package (Fig. 2.6) for the EDM Surface Payload and the *AMELIA* proposal for the EDM Entry and Descent Science.

DREAMS (Dust characterization, Risk assessment, and Environmental Analyzer on the Martian Surface) is a suite of environmental sensors led by the PI Francesca Esposito (INAF-OAC, Naples, Italy) including:

- *MetWind*, a hot film anemometer to measure horizontal wind speed and direction (Lead Co-I Colin Wilson, University of Oxford, UK);
- *MetHumi*, a capacitive atmospheric humidity sensor (Lead Co-I Ari-Matti Harri, FMI, Finland);
- *MetBaro*, a capacitive atmospheric pressure sensor (Lead Co-I Ari-Matti Harri, FMI, Finland);
- *MarsTem*, a thermometer (Lead Co-I Giacomo Colombatti, University of Padua, Italy);
- *ODS (Optical Depth Sensor)*, a sensor for the measurement of dust opacity (Lead Co-I Jean-Pierre Pommereau, LATMOS, France);

- *MicroARES*, a sensor for the measurement of atmospheric electrical field and conductivity (Lead Co-I Franck Montmessin, LATMOS, France).

DREAMS will provide the first measurement of the electric field on the surface of Mars with MicroARES. Combined with measurements of concentration of atmospheric dust (ODS) and wind speed, DREAMS will also provide new insights into the role of electrical forces on dust lifting, and on dust storms formation. In addition, the MetHumi sensor will complement MicroARES measurements with critical data about humidity, which will enable better understanding of dust electrification processes.

The DREAMS package will be discussed in Chapter 5 together with the MicroMED instrument, which was initially included in the original proposal for the EDM payload.

The *AMELIA* (*Atmospheric Mars Entry and Landing Investigation and Analysis*) team, is led by the PI Francesca Ferri (University of Padua, Italy) and the Co-PIs François Forget (LMD, France), Özgür Karatekin (Royal Observatory of Belgium, Belgium) and Stephen Lewis (The Open University, UK).

2.4 ExoMars 2018 Mission

2.4.1 Mission Architecture

The ExoMars 2018 mission is planned to be launched on a NASA Atlas V 531 rocket in April 2018 and arrive on Mars in January 2019. According to the recent re-configuration, the launch should accommodate a single rover. This mission originally included two rovers, which should have been launched jointly: the ESA *ExoMars Rover* (Fig. 2.7) and the NASA *MAX-C* (*Mars Astrobiology Explorer - Cacher*) rover. Unfortunately, as a result of financial budget, NASA cancelled the MAX-C rover, and ESA and NASA agreed upon a new 2018 mission based on a larger ESA ExoMars rover that will host the ESA Pasteur Payload and the NASA caching system, so merging the scientific objectives of both agencies.

The spacecraft will perform a direct injection onto a Mars T2 transfer trajectory. During the cruise phase, a carrier spacecraft will support the Aeroshell and separate from it shortly before the atmospheric entry. The Aeroshell will decelerate through the initial part of the atmosphere using its heat shield, followed by parachute descent, and finally, by a fully controlled descent and touchdown phase (i.e., the *sky crane* system). The sky crane will lower the rover onto the surface of Mars on a support platform. Once

on the surface, the rover will deploy their appendages, perform check out tests, and egress from the platform. The landing site will be chosen in 2011-2012. The ESA ExoMars TGO 2016 will support data relay communications for the rover.

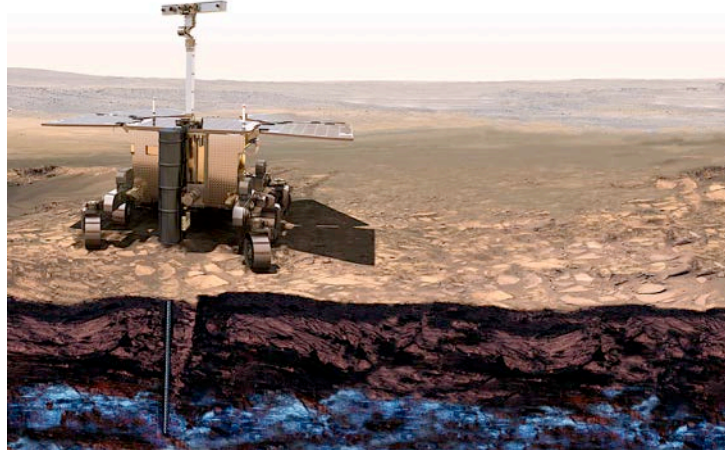


Fig. 2.7: ESA ExoMars Rover concept (ESA, 2010).

The objectives of the ExoMars Rover are:

- To land or reach a location possessing high exobiology interest for past or present life signatures, i.e., access to the appropriate geological environment.
- To collect scientific samples from different sites, using a rover carrying a drill capable to reach into the subsurface and surface rocky outcrops down to 2 m.
- To conduct an integral set of measurements at multiple scales at each site: beginning with a panoramic assessment of the geological environment, progressing to smaller-scale investigations on surface outcrops, and culminating with the collection of well-selected subsurface (or surface) samples to be studied in the rover's analytical laboratory.

The objectives of NASA caching system are:

- To identify, acquire, and cache outstanding samples suitable for collection by a future Mars Sample Return Mission.

According to the first plan, the ESA ExoMars would be controlled by the Rover Operations Control Centre (ROCC), Turin, Italy, via commands transmitted by the TGO, but after descopeing the whole mission into a single rover, this task will be rediscussed by ESA and NASA. Science operations for payload will be managed in

coordination with scientific groups. The original nominal mission of the ExoMars Rover was of 180 sols, but it will probably be revised.

The communication opportunities will be 1 or 2 short sessions per sol. Scientists on Earth will designate target destinations on the basis of compressed stereo images acquired by the cameras mounted on the Rover mast. The Rover must then calculate navigation solutions and safely travel approximately 100 m per sol. To achieve this, it creates digital maps from navigation stereo cameras and computers a suitable trajectory. Close-up collision avoidance cameras are used to ensure safety.

The ExoMars Rover can travel several kilometres. Its subsurface sampling device will then autonomously drill to the required depth (maximum 2 m) while investigating the borehole wall mineralogy, and collect a sample. This sample will be delivered to the analytical laboratory inside the vehicle; it will be crushed into fine powder. By means of a dosing station the powder will then be presented to instruments for performing detailed chemistry, physical, and spectral analyses. The scientific data will be compressed and transmitted back to Earth via a Mars orbiter relay satellite. The transmission between the Rover and the relay orbiter will be in the UHF band. The average data volume transmitted will be ~ 100 Mb/sol.

2.4.2 ExoMars Rover

The work performed in coordination with the Project Scientist of the ExoMars mission was aimed to define the scientific requirements and design the reference surface mission of the payload for the ESA ExoMars Rover. These tasks were accomplished in 2010 at ESA-ESTEC, before the merging of the two rovers (2011). The new mission concept has not been defined yet.

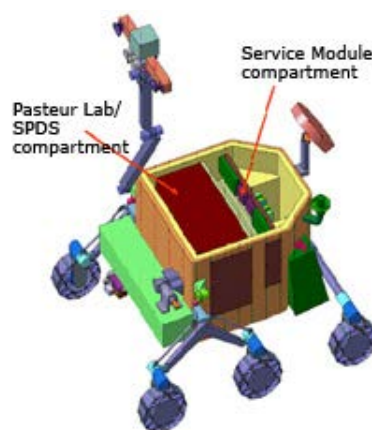


Fig. 2.8: ExoMars Rover PPL and SPDS accommodation (ESA, TAS-I).

The ESA ExoMars Rover has an overall mass of about 300 kg. It will carry a drill and a suite of instruments dedicated to exobiology (*Pasteur Payload*) and geochemistry research (18.7 kg). The ExoMars *Rover Module (RM)* (Fig. 2.8) is composed by: the *Rover Vehicle (RV)*, the *Pasteur Payload (PPL)*, and the *Payload Support Equipment (PSE)*. The RV includes the following subsystems: Structure, Locomotion, Navigation and Localisation, Camera Mast, Thermal Control System, Power Generation System, Communication System, Data Handling System, Harness, Software. The PPL experiments suites are subdivided into *Survey Instruments* (i.e., PanCam, WISDOM, CLUPI, and Ma_Miss) and *Analytical Instruments* (i.e., MicrOmega, RLS, MARS-XRD, MOMA, and LMC). The PSE includes: the *Sample Acquisition System* (i.e., the *Drill*) and the *Sample Preparation and Distribution System (SPDS)*.

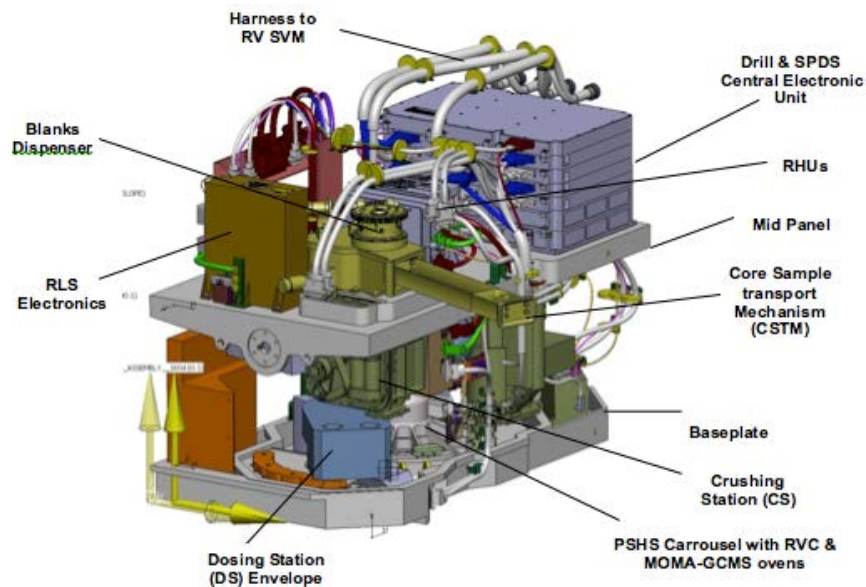


Fig. 2.9: Sample Preparation and Distribution System (SPDS) (ESA, TAS-I).

The SPDS (Fig. 2.9) is an assembly of structures including: the Core Sample Transport Mechanism (CSTM), which receives the samples collected by the drill and transport them into SPDS; the Crushing Station (CS), which is used to produce a powder with the desired particle size distribution; the Blanks Dispenser (BD), which processes organically inert mission samples to demonstrate rover's cleanliness along the entire sample transportation and distribution chain; the Powder Sample Dosing and Distribution System, which includes 2 Dosing Stations for distributing powder to the Refillable Container and to one of several ovens hosted by a carrousel, and a Positioner for fixing the Dosing Station; the Flattening Device (FD), which renders particulate

matter flat for observation by instruments; the Refillable Container (RC), which serves the instruments MicrOmega, RLS, MOMA-LDMS, and MARS-XRD; the Powder Sample Handling System (PSHS), which consists in a carousel equipped with re-usable sample containers and a finite number of ovens for the instrument MOMA-GCMS; and the Tapping Station (TS), which seals the crushed sample material into the used MOMA-GCMS oven. SPDS elements and the scientific instruments will be assembled in the Analytical Laboratory Drawer (ALD) (Fig. 2.10).

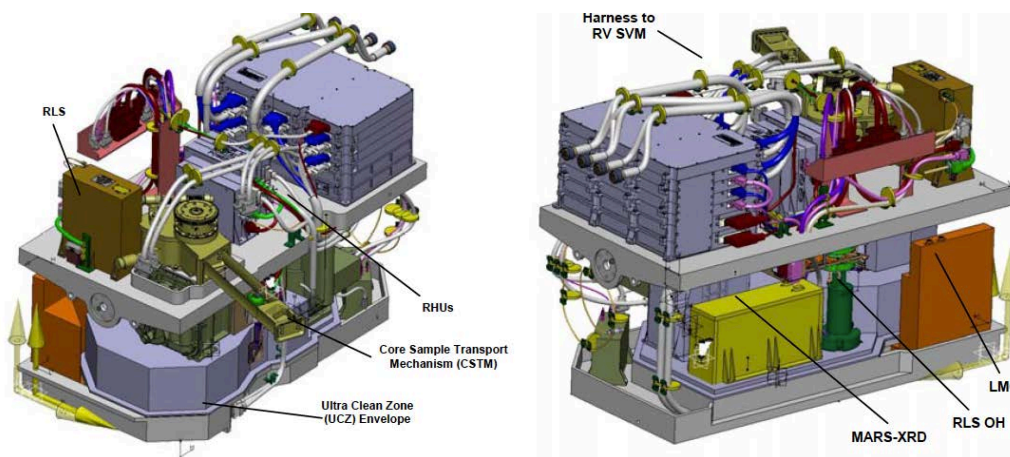


Fig. 2.10: Analytical Laboratory Drawer (ALD) (ESA, TAS-I).

The rover uses solar panels to generate the required electrical power and is designed to survive the cold Martian nights with the help of batteries and heater units. The locomotion of the rover is achieved through six wheels. Each wheel pair is suspended on an independently pivoted bogie (i.e., the articulated assembly holding the wheel drives), and each wheel can be independently steered and driven. Inclinometers and gyroscopes are used to enhance the motion control robustness. Sun sensors are utilised to determine absolute attitude. The camera system (PanCam) images, combined with the data collected by the ground penetrating radar (WISDOM), while travelling, will allow scientists on-ground to define a suitable drilling location.



Fig. 2.11: ExoMars Drill in laboratory (ESA, TAS-I).

The *ExoMars Drill* can penetrate the soil, acquire a core sample (1-cm diameter and 3-cm length) down to a maximum depth of 2 m, extract it, and deliver it to the inlet port of the Rover Payload Module, where the sample will be distributed, processed and analyzed by the ALD.

The Drill Unit consists mainly of the following elements:

- *A Drill Tool*: It is a stainless steel drill, 700 mm long, equipped with the sample acquisition device, inclusive of a shutter, movable piston, position and temperature sensors. It operates in a *Drilling Mode* (i.e., to penetrate the soil) and a *Coring Mode* (i.e., equipped with a central retractable piston to collect core samples). The Ma_Miss TIP (Sect. 2.4.3) is accommodated inside the Drill Tool with its window between two augers.
- *3 Extension Rods*: They are aluminium alloys rods, each one 500 mm long, designed to extend the penetration length to 2 m by combining them. They are provided with electrical contacts and guarantee the transmission of the optical signal to the Ma_Miss spectrometer, located in the upper part of the Drill Unit.
- *A Rotation-Translation Group*: It includes the sliding carriage motors and sensors, the gear mechanisms, the Ma_Miss optical rotary joint.
- *A Drill Box Structure*: It is a carbon fibre case, including the clamping system for the rods (rod magazine group), and the automatic engage-disengage mechanism for the rods. On the drill box structure the Ma_Miss spectrometer and the drill proximity electronics are installed.
- *A back-up Drill Tool*: It is designed for non-nominal situations.

The Drill Unit is supported by a dedicated positioning system, capable of deploying it from its storage position on the front of the Rover chassis to its operational position, orthogonally to the terrain, and to allow the delivery of the acquired soil sample to the SPDS inlet port. The Drill positioning system is equipped with an emergency jettison device, to be used in case the unit would remain blocked in the terrain, endangering the Rover mobility and the continuation of the mission. The Drill Unit materials and Assembly, Integration and Verification (AIV) approach will be compatible with the class IVb planetary protection directives applicable to the ExoMars Mission.

2.4.3 ExoMars Rover Pasteur Payload

A summary of the scientific instruments included in the Pasteur Payload (PPL) for the ESA ExoMars Rover is reported in Tab. 2.1, which is useful to understand the tasks accomplished in Sect. 0 and 0.

Instrument	Description	PI
PanCam	PanCam (Panoramic Camera System) includes two Wide-Angle Cameras (WACs) for multi-spectral stereoscopic panoramic imaging, and a High-Resolution Camera (HRC) for high-resolution colour imaging. The WACs use a 1024 x 1024 pixels CMOS APS with 12 geological filters ruled by a wheel and have a FOV of 34° x 34°; the HRC uses a 1024 x 1024 pixels CMOS APS, has a focal length of 180 mm, a FOV of 5° x 5°, and a resolution up to 1 mm. PanCam can perform digital mapping, geological study of outcrops and atmospheric study, and support the rover and other instruments activities by providing context information about the environments. PanCam is installed on the ExoMars Rover mast.	Andrew Coates, Malin Space Science Laboratory / University College London, UK
WISDOM	WISDOM (Water Ice and Subsurface Deposit Observations on Mars) is a polarimetric Ground-Penetrating Radar (GPR) operating in the UHF frequency range (500 MHz - 3 GHz). It relies on two Vivaldi antennas (i.e., co-planar broadband-antennas, which are made from an on both sides metalized dielectric plate), which are used for transmitting pulses and receiving the reflected signals. Electromagnetic waves penetrating into the ground are reflected where there is a sudden transition in soil electrical parameters (permittivity, conductivity) allowing to characterize subsurface stratigraphy to a depth of 3-5 m with a resolution of 2 cm. WISDOM antennas are installed on the rear of the ExoMars Rover, while its electronics is mounted inside.	Valérie Ciarletti, LATMOS, France
CLUPI	CLUPI (Close-Up Imager) is an optical colour (RGB) microscope. It uses a 2652 x 1768 pixels APS sensor with a resolution of 15 µm/pixel at 20 cm from the target. CLUPI allows to approach selected outcrops for closer and detailed observation of structures in order to study the depositional environment and potential morphological signatures of past biological activity preserved on the texture of surface rocks and drilled cored samples after they are deposited in the sampler drawer. CLUPI will be installed on a side of the Drill Box.	Jean-Luc Josset, Institute for Space Exploration, Neuchâtel, Switzerland
Ma_Miss	Ma_Miss (Mars Multispectral Imager for Subsurface Studies) is a miniaturized wide-range (0.4-2.4 µm) infrared spectrometer integrated to the Drill Tool for mineralogical investigations in the drill borehole. Multispectral images are acquired by means of a sapphire window placed on the lateral wall of the Drill Tool as close as possible to the drill head. The images are gathered by means of an optical fibre system and analysed using the spectrometer. The results that Ma_Miss can give are related to: geology and evolution of the upper crust and regolith (e.g., lithology, composition, physical properties, and structure); distribution and state of subsurface water and other volatiles; possible presence of minerals useful for preservation of biomarkers; possible organic molecules	Angioletta Coradini, INAF, Rome, Italy

	and other potential indicators of past or present life in the subsurface; nature and distribution of oxidants as a function of depth; characterization of some geophysical environment parameters and properties.	
MicrOmega	MicrOmega (Micro Observatoire pour la Minéralogie, l'Eau, les Glaces et l'Activité) is a near-infrared hyperspectral imaging spectrometer. It can sample 5 mm x 5 mm areas with 20- μ m spatial sampling. MicrOmega delivers the IR spectrum (0.85-3.3 μ m) of each 20- μ m pixel in 500 contiguous spectral steps. The objective of MicrOmega is to study samples collected by the Drill to characterise structure and composition at grain-size level, e.g., hydrated minerals, phyllosilicates, sulphates, carbonates, nitrates, Fe-oxides, Fe-bearing mafic silicates (olivine, pyroxene), organic aromatic and/or aliphatic compounds, H_2O and CO_2 ices. MicrOmega can work in coordinated measurements with RLS, MOMA-LDMS, MARS-XRD and CLUPI.	Jean-Bibring, Institut d'Astrophysique Spatiale, Orsay, France
RLS	RLS (Raman Laser Spectrometer) is a Raman spectrometer (i.e., the vibrational transitions undergone by a compound's chemical bonds are analysed after excitation by a monochromatic light source) to provide geological and mineralogical information for igneous, metamorphic, and sedimentary processes. The full potential science of RLS needs to be coordinated with MicrOmega, MOMA, and MARS-XRD. RLS will be accommodated in ALD studying the sample material collected by the Drill.	Fernando Rull, Universidad de Valladolid/CAB, Spain
MARS-XRD	MARS-XRD (MinerAlogy and chemistRy analySer - X-Ray Diffractometr) is a compact X-ray diffractometer for the analysis of powdered rock samples. The target range for data analysis includes all the silicate minerals (e.g., clays or other phyllosilicates characterised by high inter-planar lattice distance), oxides, carbonates, and evaporates (mainly sulphates). The full potential science of MARS-XRD needs to be coordinated with MicrOmega, RLS, and MOMA.	Lucia Marinangeli, IRSPS, Pescara, Italy
MOMA	MOMA (Mars Organic Molecule Analyzer) includes the Gas-Chromatography Mass-Spectrometry (GCMS) to analyze volatile organic molecules, and the Laser Desorption Mass Spectrometry (LDMS) to study large macromolecules and inorganic materials. The task of MOMA is to study the possible origin, evolution, and distribution of life on Mars by detecting organic molecules, identifying possible chirality, and analyzing trace gases in atmospheric samples. The full potential science of MOMA needs to be coordinated with MicrOmega, RLS, and MARS-XRD.	Fred Goesmann, Max-Planck-Institut für Sonnensystemforsche nung, Lidau, Germany
LMC	LMC (Life Marker Chip) consists of the Microfluidic Lab-on-a-Chip and the Sample Processing Unit. The working principle derived from immunodiagnosics by exploiting the highly specific recognition and binding properties of molecular receptors (e.g., antibodies or their fragments) via liquid extraction of molecules from the crushed sample material obtained by the drill. The LMC targets will include biomolecules with a potentially long lifetime ($> 10^6$ years), and control markers (e.g., cometary and meteoritic organic material). LMC shall be accommodated in ALD.	Mark Sims, University of Leicester, UK

Tab. 2.1: The Pasteur Payload (PPL) instruments.

2.4.4 ExoMars Rover Scientific Payload Requirements

The work performed in coordination with the Project Scientist of the ExoMars mission included the checking and updating the *ExoMars Rover Scientific Payload Requirements Document (SPRD)* - EXM-PL-RS-ESA-00001 for the ExoMars Rover 2018. The SPRD defines the top level science, measurement, accommodation, and deployment requirements from all the ExoMars Rover scientific instruments to the Rover design. The previous version of the SPRD was referred to the ExoMars mission concept before 2009. The improvements applied to the SPDR during this work were the following:

- Deletion of all instrument of the Humboldt Payload from the surface operations according to the changes of the ExoMars mission profile approved in 2009.
- Updating of the Pasteur Payload including the Survey Instruments (i.e., PanCam, WISDOM, CLUPI, and Ma_Miss) and the Analytical Instruments (i.e., MicrOmega, RLS, MARS-XRD, MOMA, and LMC).
- Implementation and check of Science, Measurement, and Accommodation Requirements for the instruments as suggested from a scientific point of view and according to the mission profile (2009-2010).
- Check and verification of accordance between the SPDR and the *ExoMars Pasteur Payload Experiment Interface Requirements Document (PPL E-IRD)* - EXM-PL-IRD-ESA-00001, which defines all the technical, managerial and programmatic requirements applicable to each scientific instrument interface with the ExoMars Spacecraft and Mission.

In November 2010, the SPRD has been submitted to the ESA ExoMars Payload and Assembly, Integration and Verification (AIV) team and the teams responsible of each scientific instrument for approval.

2.4.5 ExoMars Rover Reference Surface Mission

The work performed in coordination with the Project Scientist of the ExoMars mission included also the critical revision of the ESA ExoMars Rover Reference Surface Mission. This is the nominal exploration scenario of the rover on the surface of Mars to accomplish the scientific objectives fixed within the ExoMars Programme

(*ExoMars Reference Surface Mission* - EXM-PL-RS-ESA-00002). The work mainly concentrated on:

- Update the sequence of operations to be performed by each scientific instrument on board the rover (Sect. 2.4.3), the rover movement strategy, and the SPDS and drill operations (Sect. 2.4.2), starting from existing guidelines.
- Determine the power and energy consumption and utilisation timelines of the scientific instruments of the Pasteur Payload, the Drill, and the SPDS.

The timelines define how much such elements have to operate per each sol according to the scientific objectives of the mission and based on energy and power consumption and data rate budgets. In this work, the plan was formulated fully respecting the scientific and engineering requirements, and was, then, submitted to the ESA ExoMars Rover System Engineers, ESA ExoMars Payload and AIV team, and to the teams responsible of each instrument for the successive steps in the mission design.

The ESA ExoMars Rover scientific operations should start 12 sols after the landing, following the rover egress and functional commissioning, and should be carried out for 180 sols. Two types of complex scientific sequences will be performed:

- *6 Experiment Cycles (EC)*: an EC involves the acquisition and analysis of a surface and a subsurface sample at an individual site; an EC will be accomplished in 13-19 sols depending on the rover journey.
- *2 Vertical Surveys (VS)*: a VS consists of obtaining and analyzing five subsurface 3-cm long samples, acquired every 50 cm from 0 to 200 cm depth; a VS will be accomplished in 19 sols.

The timeline for the operations of the Pasteur Payload shall respect several scientific and technical requirements, whose most important technical requirements about the payload and the Drill operations are:

- Total energy consumption ≤ 1000 Wh/sol
- Total data volume ≤ 150 Mb/sol

Scientific instruments need calibration before being operative. Generally, this is operationally very costly, and, therefore, calibrations will be performed only when strictly necessary (Tab. 2.2). The scientific schedule of the whole ExoMars Rover mission is summarized in Tab. 2.3.

Instrument	Calibration
PanCam	Occasional images of calibration target to be transmitted as non-critical data.
CLUPI	Occasional images of calibration target to be transmitted as non-critical data.
WISDOM	Included instrument needs to adjust for terrain's electromagnetic parameters.
Ma Miss	Included needed to subtract window contamination signature.
MicrOmega	Occasional hypercube of calibration target to be transmitted as non-critical data.
RLS	Included needed to subtract background.
MARS-XRD	Included but only ½ h calibration of sensor.
MOMA-LDMS	Occasional measurement of calibration target to be transmitted as non-critical data.
LMC	Not required. Calibration is internal to instrument.

Tab. 2.2: Calibration requirements for the ExoMars Rover instruments.

ESA ExoMars Rover Reference Surface Mission		
Sol	Sols	Phase
0	10	Rover egress and functional commissioning
10	2	Rover moves 200 m away from the landing site and rocket plume contamination area Rover ALD set closed WAC takes a 360° colour image of the landing site
12	3	Rover ALD set open ALD analyzes drill blank material ALD perform a full calibration and organic cleanliness verification
15	13	EC #1: Rover traverse ≤ 50 m
28	13	EC #2: Rover traverse ≤ 100 m
41	14	EC #3: Rover traverse ≤ 200 m
55	15	EC #4: Rover traverse ≤ 300 m
70	16	EC #5: Rover traverse ≤ 400 m
86	19	VS #1
105	17	EC #6: Rover traverse ≤ 500 m
122	19	VS #2
141	4	LMC
145	35	Margin of 35 sols
180	0	End of the nominal mission

Tab. 2.3: ESA ExoMars Rover Reference Surface Mission (2010).

An Experiment Cycle comprises all actions necessary to select, approach, study a target location, and transmit the collected data to the Rover Operations Control Centre (ROCC). An EC includes:

- 1) Identify the location where to perform the next Measurement Cycle based on analysis of orbital and Rover data (i.e., PanCam images), and managed by Ground Control.
- 2) Drive the Rover to the new location.
- 3) Perform a full Measurement Cycle.
- 4) Transmit all relevant scientific data, housekeeping, and navigation data to Earth.

It is assumed that the Rover position (d) at the beginning of an EC is approximately 20 m from the intended exploration location. According to Eq. (2.1), in Tab. 2.4, the visual coverage (C) of the WACs (WC) and HRC (HC) are reported (Fig. 2.12).

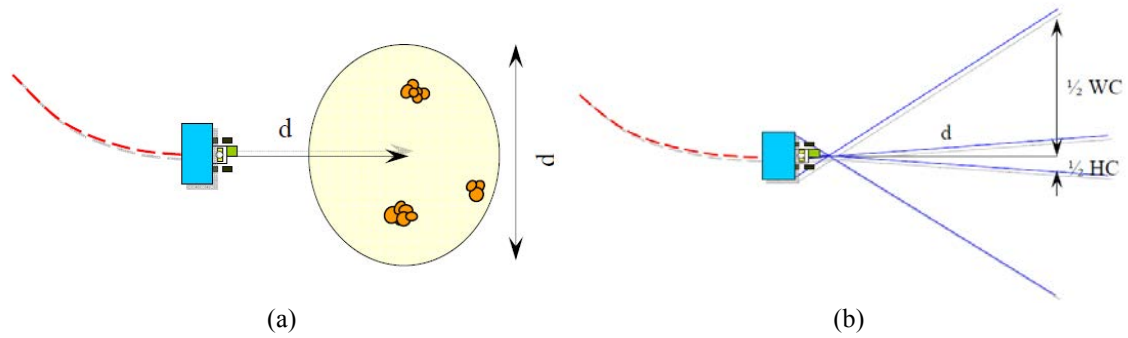


Fig. 2.12: (a) Assumed position at the beginning of the EC. (b) Coverage of the cameras.

$$C = 2d \tan(FOV / 2) = 0.61d \quad (2.1)$$

Camera	Field of View (FOV)	Coverage at a distance (d) of 20 m
WAC	34°	WC = 12 m
HRC	5°	HC = 1.75 m

Tab. 2.4: Coverage of the cameras onboard the ExoMars Rover.

The soil model used to estimate the drill performance was supposed to be characterized by two types of layers, i.e., *loose soil* and *hard soil*, (Tab. 2.5).

Category	Type	Density (kg/m ³)	Compressive Strength (MPa)	Depth (cm)
Loose Soil	Base regolith	1.37·10 ³	60	EC: 0-130 VS: 0-190
Hard Soil	Sedimentary	2.75·10 ³	120	EC: 130-150 VS: 190-200

Tab. 2.5: Main properties of the soil model used to estimate Drill performance.

A *Measurement Cycle* groups all measurements activities required to scientifically characterize a target location. It includes:

- 1) Carry out a panoramic-scale investigation of the chosen site on surface (i.e. with PanCam WACs and HRC, Fig. 2.13) and in subsurface (i.e., with WISDOM).

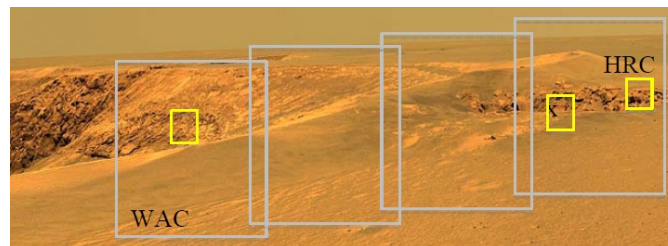


Fig. 2.13: Example of images, which could be taken with the PanCam WACs and HRC (ESA).

- 2) Select an interesting surface target for collecting a sample (i.e., with the Drill) and imaging at close scale (i.e., with CLUPI, Fig. 2.14). Interesting targets could be outcrops, which could reveal valuable knowledge about underlying deposits;

moreover, possible organic molecules could be found below 1.5 m depth, preserved from oxidant and ionising radiation damage. The ground penetrating radar (i.e., WISDOM, Fig. 2.15) can be used to map the underground stratigraphy and identify a suitable location for subsurface drilling.

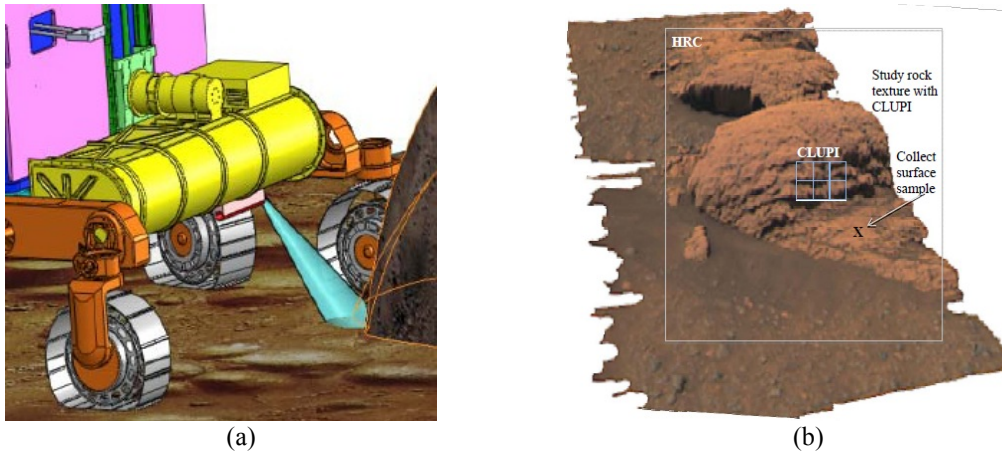


Fig. 2.14: (a) CLUPI position on the ExoMars Rover. (b) Study of rock textures with CLUPI. (ESA).

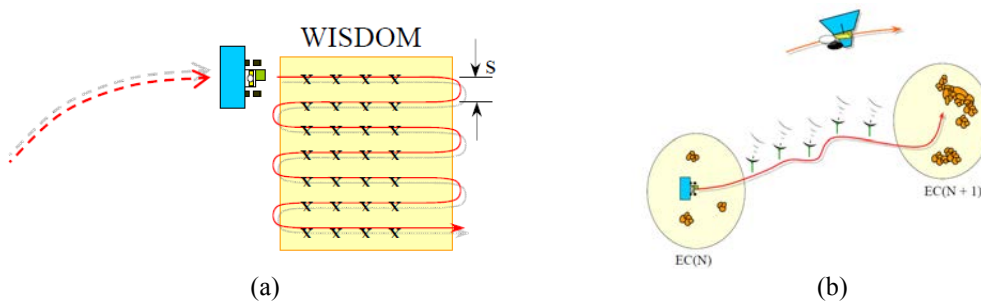


Fig. 2.15: (a) WISDOM soundings ($s = 100$ cm); (b) Rover traverse phase performing WISDOM sounding. (ESA).

3) Approach the surface target, document its texture with sub-mm scale imaging (e.g., with CLUPI), drill (Fig. 2.16), scan (i.e., with Ma_Miss, Fig. 2.17), and collect a surface sample.

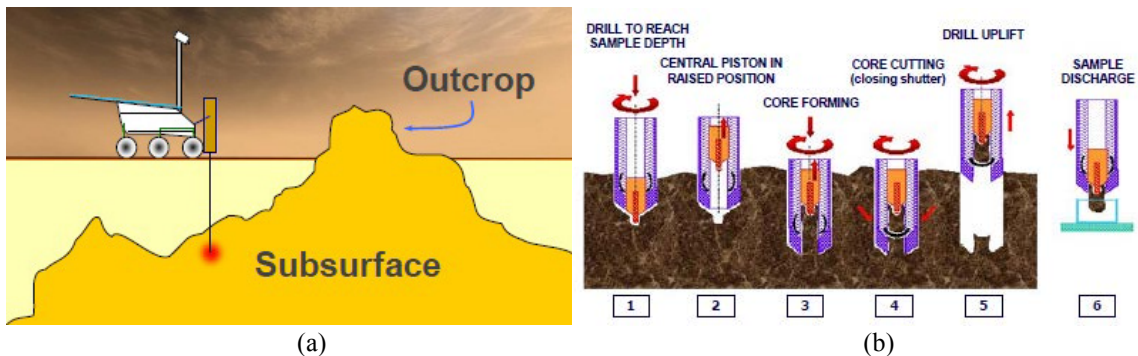


Fig. 2.16: (a) Outcrop approach and drill into subsurface. (b) The Drill operations. (ESA).

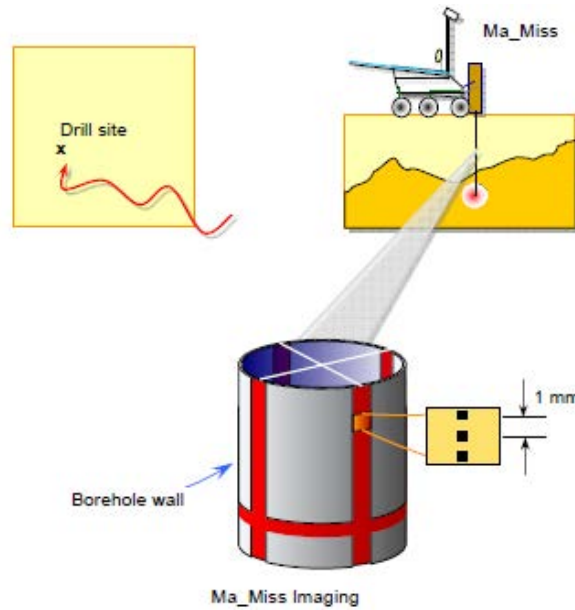


Fig. 2.17: Subsurface drilling phase with Ma_Miss measurements (ESA).

- 4) Perform a series of measurements and analyses on the collected surface sample with the analytical laboratory instruments (i.e., MicrOmega, RLS, MARS-XRD, MOMA-LDMS, LMC).
- 5) Drill to collect a subsurface sample from a given depth on the basis of the information acquired on the surface target, and on data from subsurface radar scans.
- 6) Perform a series of measurements and analyses on the collected subsurface sample with the analytical laboratory instruments (i.e., MicrOmega, RLS, MARS-XRD, MOMA-LDMS, LMC).
- 7) Process all data and prepare them for transmission.
- 8) Collect and analyze other samples, if necessary.
- 9) Dispose the sample material according to Planetary Protection rules.

Sol	Beginning Rover position	Rover journey	Experiment Cycle Scientific Operations
1	20 m from the target	0 m	<ul style="list-style-type: none"> • 10 WAC images to identify surface interesting targets • 10 HRC images of the surface interesting targets • 1 WISDOM simple sounding
2	3 m from the target	20 m to the target	<ul style="list-style-type: none"> • 40 WISDOM simple sounding + 1 WISDOM calibration during the Rover movement • 1 WAC image with 12 geological filters • 8 HRC colour images to conduct image mosaic • 1 WISDOM calibration + 100 WISDOM simple sounding
3	At the target	3m to the target	<ul style="list-style-type: none"> • 1 HRC colour image encompassing the area to be imaged with CLUPI • 6 CLUPI colour images to construct an high resolution mosaic
4	At the target	0 m	<ul style="list-style-type: none"> • 1 CLUPI colour image of location to drill into • Drill 3 cm into an outcrop and collect a sample • 1 CLUPI colour image of drill fines

			<ul style="list-style-type: none"> • 2 CLUPI colour images of sample on CSTM tray • Deliver the sample to ALD • RLS calibration
5	At the target	0 m	<ul style="list-style-type: none"> • Deliver the sample to Crushing Station • Crush the sample • Fill a Dosing Station • Pose Dosing Station over Refillable Container • Deliver the sample to Refillable Container • Prepare the sample with Flattening Device • 2 MicrOmega IR spectral cubes for RLS and MOMA-LDMS measurements • 20 RLS spectra, targeted on the basis of MicrOmega IR information • 2 MOMA-LDMS broad survey run on the basis of MicrOmega IR information
6	At the target	0 m	<ul style="list-style-type: none"> • 1 MARS-XRD measurement • 10 WAC stereo colour images with RRGB filters
7	10 m from WISDOM search area	10 m to WISDOM search area	<ul style="list-style-type: none"> • 306 WISDOM full polarimetric soundings • 8 WAC stereo colour images with RRGB filters in support to WISDOM pattern
8	5 m from the drilling location	5 m to the drilling location	<ul style="list-style-type: none"> • Ma_Miss calibration (2 rings on calibration target + 1 ring with lamp off in borehole) • Drill 10 cm in loose soil + Ma_Miss ring measurement (depth 0-10 cm) • Drill 10 cm in loose soil + Ma_Miss ring measurement (depth 10-20 cm) • Drill 10 cm in loose soil + Ma_Miss ring measurement (depth 20-30 cm) • Drill 10 cm in loose soil + Ma_Miss ring measurement (depth 30-40 cm) • Drill 10 cm in loose soil + Ma_Miss ring measurement (depth 40-50 cm) • Retrieve the drill from 50 to 0 cm depth + 4 Ma_Miss vertical sequences • 2 CLUPI colour images of drill fines
9	Drilling location	0 m	<ul style="list-style-type: none"> • Drill 0 to 50 cm to the previous sol's depth • Retract the mandrel and engage the 2nd rod • Ma_Miss calibration (2 rings on calibration target + 1 ring with lamp off in borehole) • Drill 10 cm in loose soil + Ma_Miss ring measurement (depth 50-60 cm) • Drill 10 cm in loose soil + Ma_Miss ring measurement (depth 60-70 cm) • Drill 10 cm in loose soil + Ma_Miss ring measurement (depth 70-80 cm) • Drill 10 cm in loose soil + Ma_Miss ring measurement (depth 80-90 cm) • Drill 10 cm in loose soil + Ma_Miss ring measurement (depth 90-100 cm) • Retrieve the drill from 100 to 50 cm depth + 4 Ma_Miss vertical sequences • Uncouple and store the 2nd rod • Forward the mandrel and engage the 1st rod • Retrieve the drill from 50 to 0 cm • 2 CLUPI colour images of drill fines
10	Drilling location	0 m	<ul style="list-style-type: none"> • Drill 0 to 50 cm to the previous sol's depth • Retract the mandrel and engage the 2nd rod • Drill 50 to 100 cm to the previous sol's depth • Retract the mandrel and engage the 3rd rod • Ma_Miss calibration (2 rings on calibration target + 1 ring with lamp off in borehole) • Drill 10 cm in loose soil + Ma_Miss ring measurement (depth 100-110 cm) • Drill 10 cm in loose soil + Ma_Miss ring measurement (depth 110-120 cm) • Drill 10 cm in loose soil + Ma_Miss ring measurement (depth 120-130 cm) • Drill 10 cm in hard soil + Ma_Miss ring measurement (depth 130-140 cm) • Drill 10 cm in hard soil + Ma_Miss ring measurement (depth 140-150 cm) • Cut the sample and secure it in the drill • Retrieve the drill from 150 to 100 cm depth + 4 Ma_Miss vertical sequences • Uncouple and store the 3rd rod • Forward the mandrel and engage the 2nd rod • Uncouple and store the 2nd rod • Forward the mandrel and engage the 1st rod • Retrieve the drill from 50 to 0 cm • Pose the drill for delivering sample to rover • Deploy SPDS sample receiving mechanism • Drill the delivering sample • 2 CLUPI colour images of drill fines • 4 HRC colour images • Retract SPDS sample receiving mechanism
11	Drilling location	0 m	<ul style="list-style-type: none"> • Deliver the sample to Crushing Station • Crush the sample • Fill a Dosing Station • Position Dosing Station over Refillable Container

			<ul style="list-style-type: none"> • Deliver the sample to Refillable Container • Prepare the sample with Flattening Device • 2 MicrOmega IR spectral cube • Calculate targets for RLS and MOMA-LDMS based on MicrOmega IR information • 20 RLS measurements • 2 MOMA-LDMS broad survey
12	Drilling location	0 m	<ul style="list-style-type: none"> • 3 MOMA-LDMS broad survey • Rotate carousel to position MOMA oven under Dosing Station • Fill MOMA oven with sample material • Rotate carousel to position MOMA oven under Tapping Station • 1 MOMA-GCMS • Empty Refillable Container, and, if necessary, the Dosing Station
13	Drilling location	0 m	<ul style="list-style-type: none"> • 1 MARS-XRD measurement • 10 WAC colour images with RRGB filter
14	Drilling location	100 m	<ul style="list-style-type: none"> • 10 WISDOM simple sounding (1 every 10 m)
15	TBD	100 m	<ul style="list-style-type: none"> • 10 WISDOM simple sounding (1 every 10 m)
16	TBD	100 m	<ul style="list-style-type: none"> • 10 WISDOM simple sounding (1 every 10 m)
17	TBD	100 m	<ul style="list-style-type: none"> • 10 WISDOM simple sounding (1 every 10 m)
18	TBD	100 m	<ul style="list-style-type: none"> • 10 WISDOM simple sounding (1 every 10 m)
19	TBD	0 m	<ul style="list-style-type: none"> • Deliver sample to LMC • LMC measurements

Tab. 2.6: Experiment Cycle (EC) timeline.

The basic EC operations (Tab. 2.6) are performed from sol 1 to 13. Depending on rover traverse (0-500 m), the ECs can have a duration of 13-17 sols. Sol 18 is considered optional, Sol 19 is related to LMC operations (duration 4 sols) and it has not exactly been scheduled yet. In Fig. 2.18 and Fig. 2.19 the energy consumption and science duration timelines per sol for the Experimental Cycles are shown, respectively.

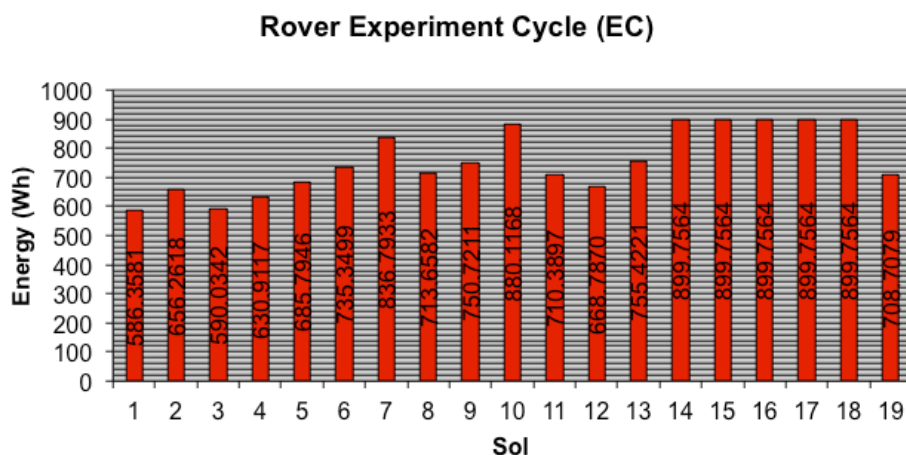


Fig. 2.18: Energy consumption per sol in an Experiment Cycle.

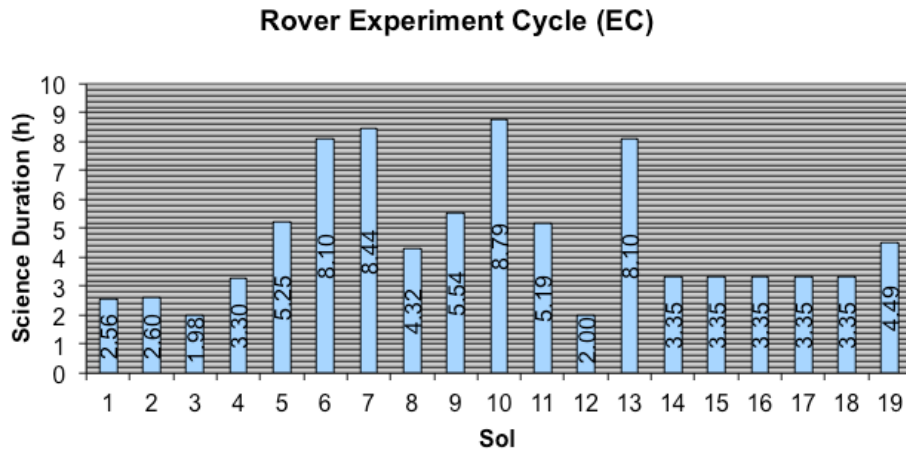


Fig. 2.19: Science duration per sol in an Experiment Cycle.

A Vertical Survey has to fully characterize, at a selected location, the soil's geochemical and organic distribution as a function of depth. It includes:

- 1) At one location, drill, scan (i.e., with Ma_Miss), obtain 3-cm length samples from depths of 0, 50, 100, 150 and 200 cm, and document the samples with sub-mm scale imaging (e.g., with CLUPI).
- 2) Perform a complete series of measurements and analyses on each selected subsurface sample with the analytical laboratory instruments (i.e., MicrOmega, RLS, MARS-XRD, MOMA-LDMS).

In Tab. 2.7 is reported the sequence of operations for the Vertical Survey, while in Fig. 2.20 and Fig. 2.21 the energy consumption and science duration timelines per sol for the Vertical Surveys are shown, respectively.

Sol	Beginning Rover position	Rover journey	Vertical Survey Scientific Operations
1	10 m from the drilling position	10 m to the drilling position	<ul style="list-style-type: none"> • 1 CLUPI colour image • Pose drill in drilling configuration • Drill 3 cm into the outcrop • Cut a sample and secure it in drill • 1 CLUPI colour image of drill fines • Pose drill for delivering sample to Rover • Deploy SPDS sample receiving mechanism • Drill the delivering samples • 2 CLUPI colour images of the drilled samples • 4 HRC colour images • Retract SPDS sample receiving mechanism • 3 RLS measurements
2	Drilling location	0 m	<ul style="list-style-type: none"> • Deliver the sample to Crushing Station • Crushing the sample • Fill a Dosing Station • Pose the Dosing Station over Refillable Container • Deliver sample to Refillable Container • Prepare sample with Flattening Device • 2 MicrOmega IR spectral cubes for RLS and MOMA-LDMS measurements • 20 RLS spectra, targeted on the basis of MicrOmega IR information

			<ul style="list-style-type: none"> • 2 MOMA-LDMS broad survey run on the basis of MicrOmega IR information
3	Drilling location	0 m	<ul style="list-style-type: none"> • 1 MARS-XRD measurement • 10 WAC stereo colour images with RRGB filters
4	Drilling location	0 m	<ul style="list-style-type: none"> • Ma_Miss calibration (2 rings on calibration target + 1 ring with lamp off in borehole) • Drill 10 cm in loose soil + Ma_Miss ring measurement (depth 0-10 cm) • Drill 10 cm in loose soil + Ma_Miss ring measurement (depth 10-20 cm) • Drill 10 cm in loose soil + Ma_Miss ring measurement (depth 20-30 cm) • Drill 10 cm in loose soil + Ma_Miss ring measurement (depth 30-40 cm) • Drill 10 cm in loose soil + Ma_Miss ring measurement (depth 40-50 cm) • Retrieve drill from 50 to 0 cm depth + 4 Ma_Miss vertical sequences • 2 CLUPI colour images of drill fines
5	Drilling location	0 m	<ul style="list-style-type: none"> • Deliver the sample to Crushing Station • Crush the sample • Fill a Dosing Station • Position the Dosing Station over Refillable Container • Deliver the sample to Refillable Container • Prepare the sample with Flattening Device • 2 MicrOmega IR spectral cube • Calculating targets for RLS and MOMA-LDMS based on MicrOmega IR information • 20 RLS measurements • 2 MOMA-LDMS broad survey
6	Drilling location	0 m	<ul style="list-style-type: none"> • 3 MOMA-LDMS broad survey • Rotate carousel to position MOMA oven under the Dosing Station • Fill MOMA oven with the sample material • Rotate carousel to position MOMA oven under Tapping Station • 1 MOMA-GCMS • Empty Refillable Container, and, if necessary, the Dosing Station
7	Drilling location	0 m	<ul style="list-style-type: none"> • 1 MARS-XRD measurement • 10 WAC colour images with RRGB filter
8	Drilling location	0 m	<ul style="list-style-type: none"> • Pose drill bit over borehole • Drill 0 to 50 cm to the previous sol's depth • Retract the mandrel and engage the 2nd rod • Ma_Miss calibration (2 rings on calibration target + 1 ring with lamp off in borehole) • Drill 10 cm in loose soil + Ma_Miss ring measurement (depth 50-60 cm) • Drill 10 cm in loose soil + Ma_Miss ring measurement (depth 60-70 cm) • Drill 10 cm in loose soil + Ma_Miss ring measurement (depth 70-80 cm) • Drill 10 cm in loose soil + Ma_Miss ring measurement (depth 80-90 cm) • Drill 10 cm in loose soil + Ma_Miss ring measurement (depth 90-100 cm) • Cut the sample and secure it in drill • Retrieve drill from 100 to 50 cm depth • 4 Ma_Miss vertical sequences • Uncouple and store 2nd rod • Forward the mandrel and engage the 1st rod • Retrieve drill from 50 to 0 cm depth • 2 CLUPI colour images of drill fines • Retract SPDS sample receiving mechanism
9	Drilling location	0 m	<ul style="list-style-type: none"> • Deliver the sample to Crushing Station • Crush the sample • Fill a Dosing Station • Position the Dosing Station over Refillable Container • Deliver the sample to Refillable Container • Prepare the sample with Flattening Device • 2 MicrOmega IR spectral cube • Calculating targets for RLS and MOMA-LDMS based on MicrOmega IR information • 20 RLS measurements • 2 MOMA-LDMS broad survey
10	Drilling location	0 m	<ul style="list-style-type: none"> • 3 MOMA-LDMS broad survey • Rotate carousel to position MOMA oven under the Dosing Station • Fill MOMA oven with sample material • Rotate carousel to position MOMA oven under Tapping Station • 1 MOMA-GCMS • Empty Refillable Container, and, if necessary, the Dosing Station
11	Drilling location	0 m	<ul style="list-style-type: none"> • 1 MARS-XRD measurement • 10 WAC colour images with RRGB filter

12	Drilling location	0 m	<ul style="list-style-type: none"> • Pose drill bit over borehole • Drill 0 to 50 cm to the previous sol's depth • Retract the mandrel and engage the 2nd rod • Drill 50 to 100 cm to the previous sol's depth • Retract the mandrel and engage the 3rd rod • Ma_Miss calibration (2 rings on calibration target + 1 ring with lamp off in borehole) • Drill 10 cm in loose soil + Ma_Miss ring measurement (depth 100-110 cm) • Drill 10 cm in loose soil + Ma_Miss ring measurement (depth 110-120 cm) • Drill 10 cm in loose soil + Ma_Miss ring measurement (depth 120-130 cm) • Drill 10 cm in loose soil + Ma_Miss ring measurement (depth 130-140 cm) • Drill 10 cm in loose soil + Ma_Miss ring measurement (depth 140-150 cm) • Cut the sample and secure it in drill • Retrieve drill from 150 to 100 cm depth + 4 Ma_Miss vertical sequences • Uncouple and store the 3rd rod • Forward the mandrel and engage the 2nd rod • Retrieve drill from 100 to 50 cm depth • Uncouple and store the 2nd rod • Forward the mandrel and engage the 1st rod • Retrieve drill from 50 to 0 cm depth • 2 CLUPI colour images of drill fines • Retract SPDS sample receiving mechanism
13	Drilling location	0 m	<ul style="list-style-type: none"> • Deliver the sample to Crushing Station • Crush the sample • Fill a Dosing Station • Position the Dosing Station over Refillable Container • Deliver the sample to Refillable Container • Prepare the sample with Flattening Device • 2 MicOmega IR spectral cube • Calculating targets for RLS and MOMA-LDMS based on MicOmega IR information • 20 RLS measurements • 2 MOMA-LDMS broad survey
14	Drilling location	0 m	<ul style="list-style-type: none"> • 3 MOMA-LDMS broad survey • Rotate carousel to position MOMA oven under the Dosing Station • Fill MOMA oven with sample material • Rotate carousel to position MOMA oven under Tapping Station • 1 MOMA-GCMS • Empty Refillable Container, and, if necessary, the Dosing Station
15	Drilling location	0 m	<ul style="list-style-type: none"> • 1 MARS-XRD measurement • 10 WAC colour images with RRGB filter
16	Drilling location	0 m	<ul style="list-style-type: none"> • Pose drill bit over borehole • Drill 0 to 50 cm to the previous sol's depth • Retract the mandrel and engage the 2nd rod • Drill 50 to 100 cm to the previous sol's depth • Retract the mandrel and engage the 3rd rod • Drill 100 to 150 cm to the previous sol's depth • Retract the mandrel and engage the 4th rod • Ma_Miss calibration (2 rings on calibration target + 1 ring with lamp off in borehole) • Drill 10 cm in loose soil + Ma_Miss ring measurement (depth 100-110 cm) • Drill 10 cm in loose soil + Ma_Miss ring measurement (depth 110-120 cm) • Drill 10 cm in loose soil + Ma_Miss ring measurement (depth 120-130 cm) • Drill 10 cm in loose soil + Ma_Miss ring measurement (depth 130-140 cm) • Drill 10 cm in hard soil + Ma_Miss ring measurement (depth 140-150 cm) • Cut the sample and secure it in Drill • Retrieve drill from 150 to 100 cm depth + 4 Ma_Miss vertical sequences • Uncouple and store the 4th rod • Forward the mandrel and engage the 3rd rod • Retrieve drill from 150 to 100 cm depth • Uncouple and store the 3rd rod • Forward the mandrel and engage the 2nd rod • Retrieve drill from 100 to 50 cm depth • Uncouple and store the 2nd rod • Forward the mandrel and engage the 1st rod • Retrieve drill from 50 to 0 cm depth • 2 CLUPI colour images of drill fines • Retract SPDS sample receiving mechanism

17	Drilling location	0 m	<ul style="list-style-type: none"> • Deliver the sample to Crushing Station • Crush the sample • Filling a Dosing Station • Position the Dosing Station over Refillable Container • Deliver the sample to Refillable Container • Prepare sample with Flattening Device • 2 MicOmega IR spectral cube • Calculating targets for RLS and MOMA-LDMS based on MicrOmega IR information • 20 RLS measurements • 2 MOMA-LDMS broad survey
18	Drilling location	0 m	<ul style="list-style-type: none"> • 10 WISDOM simple sounding (1 every 10 m)
19	Drilling location	0 m	<ul style="list-style-type: none"> • 1 MARS-XRD measurement • 10 WAC colour images with RRGB filter

Tab. 2.7: Vertical Survey (VS) timeline.

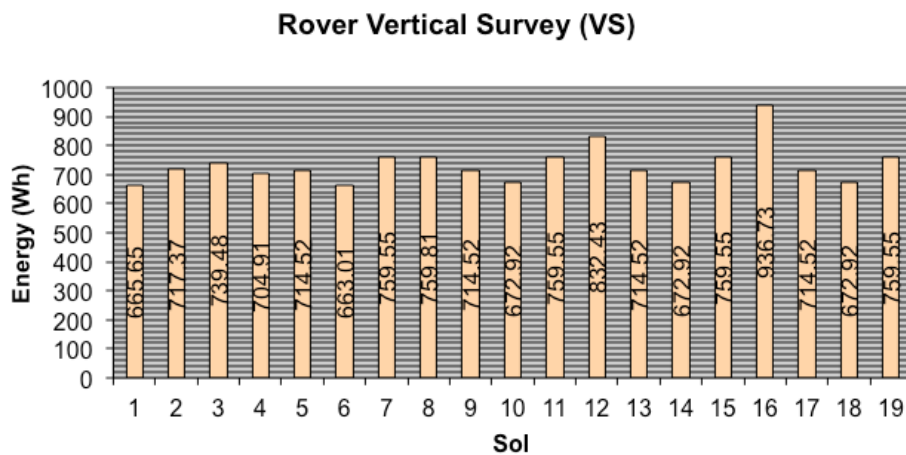


Fig. 2.20: Energy consumption per sol in a Vertical Survey.

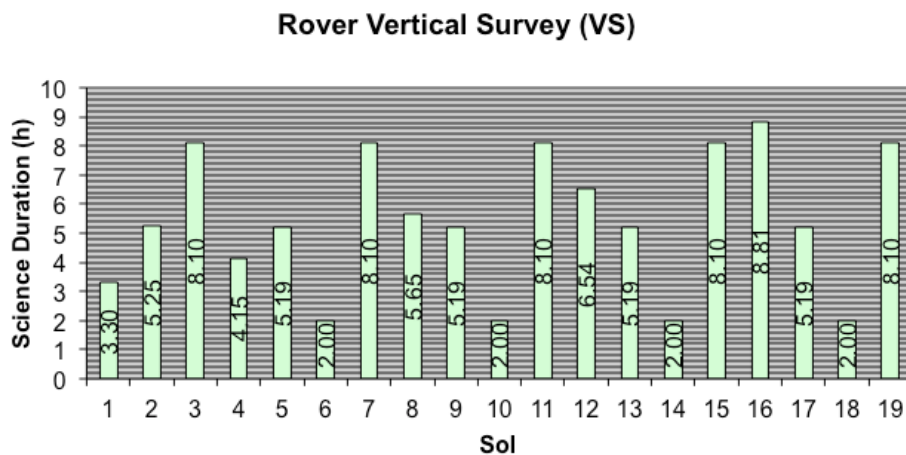


Fig. 2.21: Science duration per sol in a Vertical Survey.

The complete and detailed dataset about each operation, quoted in Tab. 2.6 and Tab. 2.7, and whose results summed up in Fig. 2.18, Fig. 2.19, Fig. 2.20, and Fig. 2.21, are here omitted as confidential data. In addition to the very interesting scientific aspects

widely discussed in Chapter 1 and 2, the following important remarks were done about the rover operations:

- Rover motion, when executed, requires the most energy/sol, i.e., assuming a Rover speed of 0.5 m/min, the energy consumption is about 27.3 Wh/m. The most significant ranges (100 m) occur for an EC on sols 14, 15, 16, 17, and 18.
- Drill operations require a lot of energy and time in comparison to each scientific instrument. In fact, assuming a drill speed of 15 mm/min in loose soil and 3 mm/min in hard soil, the energy consumption for drilling 0.22 Wh/cm in loose soil and 1.56 Wh/cm in hard soil, respectively. Moreover, because the drill is compound with modules, every 50 cm to drill, the drill operation is complicated by retrieving the drill for the previous 50-cm-drilled length, uncoupling and storing the n -extension rod, forwarding the mandrel and engaging the $(n-1)$ -extension rod, which meanly needs about 25.98 Wh. Therefore, when the maximum depth (i.e., 2 m) has to be reached, the energy requirement and duration are very high. That occurs for an EC on sols 9 (depth 0-50 cm) and 10 (50-150 cm), and for a VS on sols 4 (0-50 cm), 8 (50-100 cm), 12 (100-150 cm), and 16 (150-200 cm).
- The estimation of the data volume per sol to define the plan was not reported here as its accordance with the above requirements has been guaranteed by other independent studies led by ESA.

3 AEROSOL ANALYSIS

A general description of the models and techniques about aerosol measurements, with particular regard to the MEDUSA (Chapter 4) and MicroMED (Chapter 5) applications, is reported in this Chapter. The main topics are fluid dynamics concepts to deal with fluid and particles flows, i.e., aerosol flows, and optical concepts to deal with particles detection via light scattering. The work on the MEDUSA and MicroMED instruments aims at analysing coupling between fluid dynamics and optical aspects in order to optimize grain measurements.

From a fluid dynamics point of view, the main feature, which characterizes the flow regime where MEDUSA and MicroMED operate, is that the mean free molecular path of the atmospheric fluid (5 μm on average) has the same order of magnitude of the particle size (range $\sim 0.05\text{-}10 \mu\text{m}$; see Chapter 1). These working conditions have been poorly investigated for applications to planetary research or commercial devices aimed at aerosol particles monitoring. In fact, experience and literature about aerosol applications with micro-sized particles in rarefied environment are very poor.

3.1 Fluid Dynamics Models

Aerosols are assemblies of liquid or solid particles suspended in a gaseous medium long enough to be observed and measured. In this section the general models and equations dealing with the fluid phase and the particle discrete phase are recalled.

3.1.1 Fluid Phase

A gas flow may be mathematically modelled at either macroscopic or microscopic level (Bird, G.A., 1994). The *microscopic* or *molecular model*, i.e., the *Boltzmann equation*, describes the structure of the gas by the position, velocity, and state of each molecule at any time, but non-trivial problems are too complex to be solved. The *macroscopic model*, i.e., the *Navier-Stokes equations*, regards the gas as a continuous medium described by spatial and temporal variations of variables, which can be defined as long as there are a sufficient number of molecules within a small finite volume. The Navier-Stokes equations do not form a determinate set unless the diffusive terms (i.e., mass species fluxes, stresses, and heat fluxes) can be expressed through lower-order

macroscopic quantities. In fact, the transport terms fail when gradients of the macroscopic variables become too steep and their length scale is of the same order of the *mean free molecular path*, i.e., the average distance travelled by a molecule between two successive collisions with other molecules. Flow rarefaction is typically classified by the *Knudsen number* (Kn) (Tab. 3.1), i.e., the ratio between the mean free molecular path (l) and a characteristic dimension (L):

$$Kn = \frac{l}{L} \quad (3.1)$$

Kn	Flow Regime	Numerical Models	Characteristics
0	Inviscid Limit	Continuum Model (Euler equations) or Discrete Molecular Model (Boltzmann equation)	No diffusive effects occur.
0-10 ⁻³	Continuum Flow	Continuum Model (Navier-Stokes equations with no slip boundary conditions) or Discrete Molecular Model (Boltzmann equation)	Gas molecular collisions occur near walls and particles are decelerated.
10 ⁻³ -10 ⁻¹	Slip Flow	Continuum Model (Navier-Stokes equations with slip boundary conditions) or Discrete Molecular Model (Boltzmann equation)	Particles may slip on walls.
10 ⁻¹ -10	Transition Flow	Discrete Molecular Model (Boltzmann equation)	Intermolecular collisions have to be taken into account yet.
10-∞	Collisionless or Free-molecule Flow	Discrete Molecular Model (Boltzmann equation)	Intermolecular collisions are negligible compared with collisions between gas molecules and walls.

Tab. 3.1: A classification of flow regimes with respect to the Knudsen Number (Kn).

A *simple gas* consists of a single or more chemical species, whose molecules, anyway, are assumed to have similar structure and behaviour.

Velocity of molecular particles (\underline{v}) results from the sum of the *mean mass velocity* (\underline{V}) and the *peculiar or diffusion velocity* due to thermal motion (\underline{C}) (Eq. (3.2)). In order to describe the motion of each particle, a velocity probability distribution function (f) is used. Such a function was obtained by the *Chapman-Enskog theory* (Chapman, S., Cowling, T.G., 1952). Maxwellian velocity distribution (Eq. (3.3)) is suitable if molecules are point-like with respect to their motion and move freely without influencing each other because of the lack of intermolecular forces.

$$\underline{v} = \underline{V} + \underline{C} \quad (3.2)$$

$$f = f_0 \left[1 - \frac{4K\beta^2}{5nk_B} (\beta^2 C^2 - 5/2) C \frac{\partial(\ln T)}{\partial \underline{r}} - \frac{4\mu\beta^4}{\rho} (\underline{CC})_0 : \frac{\partial \underline{v}}{\partial \underline{r}} \right] \quad (3.3)$$

$$f_0 = \frac{\beta^3}{\pi^{3/2}} e^{-\beta^2 C^2} \quad (3.4)$$

$$\beta = (2RT)^{-1/2} \quad (3.5)$$

$$K = \frac{15}{4} R\mu \quad (3.6)$$

where f_0 is the *equilibrium or Maxwellian distribution function*, \underline{r} is the molecule position vector, k_B is the Boltzmann constant ($1.380 \cdot 10^{-23}$ J/K), n is the molecule number density, μ is the viscosity coefficient, K is the coefficient of heat conduction (Eq. (3.6)), β is the reciprocal of the most probable molecular velocity in an equilibrium gas, R is the gas constant, $(\underline{CC})_0$ is the traceless tensor of (\underline{CC}) , i.e., the tensor (\underline{CC}) with the sum of the diagonal terms equal to zero.

According to the equal partition principle, the internal energy of a molecule (e_M), which is the sum of the translational kinetic energy (e_{Mti}), the rotational kinetic energy (e_{Mri}), and the vibrational kinetic energy (e_{Mvi}), has a value of $1/2 k_B T$ for each degree of freedom (ξ). Hence, the internal energy of a molecule is:

$$e_M = \frac{\xi}{2} k_B T \quad (3.7)$$

The absolute temperature (T) of a gas is defined as a quantity proportional to the mean translational kinetic energy of the molecules:

$$\left\langle \frac{1}{2} m C^2 \right\rangle = \frac{3}{2} k_B T \quad (3.8)$$

The number of molecules in one mole of gas is the Avogadro's number (N_A), while the Avogadro's law states that the volume occupied by one mole of any gas at a particular temperature and pressure is the same for all gases. The mass of a single molecule (m) and the molecular mass (m_0) are related by:

$$m_0 = N_A m \quad (3.9)$$

Gas	Molar mass	Molecule diameter at $p = 1.013 \cdot 10^5$ Pa and $T = 293$ K
Air	28.97 g/mol	$3.75 \cdot 10^{-9}$ m
CO_2	44.01 g/mol	$4.66 \cdot 10^{-9}$ m
N_2	28.01 g/mol	$3.65 \cdot 10^{-9}$ m
O_2	32.00 g/mol	$2.92 \cdot 10^{-9}$ m
CH_4	16.04 g/mol	$3.82 \cdot 10^{-9}$ m

Tab. 3.2: Molar mass and molecular diameter of some gases (Bird, G.A., 1994).

The average volume available to a molecule is $1/N$, so the mean molecular spacing (δ_M) is:

$$\delta_M = N^{-1/3} \quad (3.10)$$

Supposing that all molecules have the same diameter (d_M), two molecules collide if the distance between their centers decreases to d_M (Tab. 3.2). The force field between molecules could be assumed spherically symmetric.

The proportion of the space occupied by a gas that actually contains a molecule is of the order of $(d_M/\delta_M)^3$. The condition $\delta_M \gg d_M$ define a *dilute gas*: only an extremely small portion of space is occupied by molecules, each molecule will often move outside the range of influence of other molecules, and achieve seldom binary collisions. For such a fluid it is possible to use the Maxwellian velocity distribution that permits to determine the mean molecular velocity ($\langle C \rangle$) and the mean quadratic velocity ($\langle C^2 \rangle$):

$$\langle C \rangle = \sqrt{\frac{8}{\pi} \frac{k_B T}{m}} \quad (3.11)$$

$$\langle C^2 \rangle = \frac{3k_B T}{m} \quad (3.12)$$

Moreover the mean free molecular path (l) can be evaluated as:

$$l = \frac{\pi}{2^{7/2}} z d_M^2 N \quad (3.13)$$

where z is the number of molecules that each molecule can hit simultaneously, and N is the molecules number density. The mathematical passage from the microscopic physics to macroscopic models is possible only if the *evolutive equilibrium condition* is conceivable, i.e., the time to reach microscopic equilibrium is shorter than the characteristic macroscopic time of the motion of the fluid.

Each quantity (Π) used to represent a flow with a macroscopic model is defined statistically through a density distribution function. Considering a position vector \underline{r} moving in a region where there are M particles such that at an instant of time t , the i -th particle has a position \underline{r}_i , a velocity \underline{v}_i , and a generic quantity Π_i , the density of the quantity Π_i (P_Π) is expressed through a statistical average ($\langle \ \rangle$) (Pozzi, A., 2003):

$$P_\Pi(\underline{r}, t) = \left\langle \sum_{i=1}^M \Pi_i \delta(\underline{r} - \underline{r}_i) \right\rangle \quad (3.14)$$

where $\delta(\underline{r}-\underline{r}_i)$ is the Dirac Delta function, which has the dimensions of the inverse of a volume. Differencing Eq. (3.14), the conservation law of the quantity Π is obtained:

$$\frac{\partial P_{\Pi}(\underline{r}, t)}{\partial t} = \left\langle \sum_{i=1}^M \dot{\Pi}_i \delta(\underline{r} - \underline{r}_i) \right\rangle - \nabla \cdot \left\langle \sum_{i=1}^M \Pi_i \underline{v}_i \delta(\underline{r} - \underline{r}_i) \right\rangle \quad (3.15)$$

Applying Eq. (3.14) to mixture mass (Eq. (3.16)), k -th species mass (Eq. (3.17)), momentum (Eq. (3.18)), and energy (Eq. (3.19)), the balance laws for the macroscopic quantities, i.e., the Navier-Stokes equations, are obtained:

$$\frac{\partial \rho}{\partial t} + \nabla \cdot \rho \underline{V} = 0 \quad (3.16)$$

$$\frac{\partial \rho_k}{\partial t} + \nabla \cdot \rho_k \underline{V} = -\nabla \cdot \underline{J}_k + P_k^+ \quad (3.17)$$

$$\rho \frac{\partial \underline{V}}{\partial t} + \rho \underline{V} \cdot \nabla \underline{V} = \nabla \cdot \underline{\tau} + \rho \underline{f}_m \quad (3.18)$$

$$\rho \frac{\partial}{\partial t} \left(e + e_p + \frac{V^2}{2} \right) + \nabla \cdot \rho \underline{V} \left(e + e_p + \frac{V^2}{2} \right) = -\nabla \cdot \underline{J}_t - \nabla \cdot \underline{V} \cdot \underline{\tau} \quad (3.19)$$

where ρ is the fluid density, \underline{V} is the fluid velocity, ρ_k is the k -th species mass density, \underline{J}_k is the k -th mass diffusion flux, P_k^+ is the k -th species mass source, $\underline{\tau}$ is the stress tensor, \underline{f}_m is the mass force per unit of mass, e is the specific internal energy, e_p is the potential energy due to mass conservative forces, \underline{J}_t is the thermal flux. The macroscopic quantities are related to the microscopic quantities: mass density (Eq. (3.20)), mass velocity (Eq. (3.21)), k -th species mass density (Eq. (3.22)), k -th species convective flux (Eq. (3.23)), k -th species mass source (Eq. (3.24)), momentum diffusive flux (Eq. (3.25)), and thermal diffusive flux (Eq. (3.26)).

$$\rho = \left\langle \sum_{i=1}^M m_i \delta(\underline{r} - \underline{r}_i) \right\rangle \quad (3.20)$$

$$\underline{V} = \frac{\left\langle \sum_{i=1}^M m_i \underline{v}_i \delta(\underline{r} - \underline{r}_i) \right\rangle}{\left\langle \sum_{i=1}^M \delta(\underline{r} - \underline{r}_i) \right\rangle} \quad (3.21)$$

$$\rho_k = \left\langle \sum_{i=1}^{M_k} m_{ki} \delta(\underline{r} - \underline{r}_i) \right\rangle \quad (3.22)$$

$$\underline{J}_k = \left\langle \sum_{i=1}^{M_k} m_{ki} \underline{v}_i \delta(\underline{r} - \underline{r}_i) \right\rangle \quad (3.23)$$

$$P_k^+ = \left\langle \sum_{i=1}^{M_k} \dot{m}_{ki} \delta(\underline{r} - \underline{r}_i) \right\rangle \quad (3.24)$$

$$\underline{\tau} = \left\langle \sum_{i=1}^M m_i \underline{C}_i \underline{C}_i \delta(\underline{r} - \underline{r}_i) \right\rangle \quad (3.25)$$

$$\underline{J}_i = \left\langle \sum_{i=1}^M \left(\frac{1}{2} m_i C_i^2 + e_{r_i} + e_{v_i} \right) \underline{C}_i \delta(\underline{r} - \underline{r}_i) \right\rangle \quad (3.26)$$

In general, the diffusive fluxes (\underline{J}_k , $\underline{\tau}$, J_i) can be obtained by resolving the statistical mean values through appropriate distribution functions. The mass diffusion processes are due to molecular exchanges depending on random molecular motions. Diffusion becomes macroscopically evident when mixtures of two or more components are involved. The rate of diffusion is far slower than the main molecular speed ($\langle C \rangle$). The rigorous kinetic theory shows that k -th species mass fluxes (\underline{J}_k) may be caused by non-uniform species concentrations, pressure and temperature gradients:

$$\underline{J}_k = -\rho \left[\sum_{j=1}^{N_k} D_{jk} \nabla \left(\frac{\rho_k}{\rho} \right) + \frac{\rho_j}{\rho} \frac{\rho_k}{\rho} \frac{p_{m,j} - p_{m,k}}{p_m} \nabla \ln p \right] - \alpha_k \nabla \ln T \quad (3.27)$$

D_{jk} is the mass diffusive coefficient between the j -th and k -th species; $p_{m,j}$, $p_{m,k}$, and p_m are the mean pressures for the j -th and k -th species, and the mixture, respectively; α_k is the thermal diffusion coefficient. For a dilute gas the kinetic theory yields the relationship (Chapman, S., Cowling, T.G., 1970):

$$D_{jk} = \frac{0.001858 T^3 \left[\frac{m_{0,j} + m_{0,k}}{m_{0,j} m_{0,k}} \right]^{1/2}}{p \sigma_{jk} \Omega_D} \quad (3.28)$$

where σ_{jk} is the effective collision diameter (in Å) for a mixture of the j -th and k -th species determinable with Eq. (3.29) from the collision diameter of the related mono-species gases σ_j and σ_k , Ω_D is the diffusion collision integral determined experimentally with Eq. (3.30), in which the effective temperature T_{ejk} (Eq. (3.31)) and the temperature ratio T^* (Eq. (3.32)) for the mixture are obtained experimentally from the related terms of the mono-species gases (Tab. 3.3):

$$\sigma_{jk} = \frac{\sigma_j + \sigma_k}{2} \quad (3.29)$$

$$\Omega_D = 1.0(T^*)^{-0.145} + (T^* + 0.5)^{-2.0} \quad (3.30)$$

$$T_{ejk} = (T_{ej} T_{ek})^{1/2} \quad (3.31)$$

$$T^* = \frac{T}{T_{ejk}} \quad (3.32)$$

Gas	σ , Å	T_e , K
H ₂	2.827	59.7
He	2.551	10.22
Ar	3.542	93.3
Air	3.711	78.6
CO ₂	3.941	195.2
CO	3.690	91.7
O ₂	3.467	106.7
N ₂	3.798	71.4
NO	3.492	116.7
N ₂ O	3.828	232.4
Cl ₂	4.217	316.0
CH ₄	3.758	148.6

Source: R.A. Svehla, *NASA Tech. Rep. R-132*, 1962.

Tab. 3.3: Effective collision diameter (σ) and effective temperature (T_e) for mono-species dilute gases (White, F.M., 1991).

When the species in a mixture have similar-sized molecules, the species mass diffusion coefficients are simplified into the *self-diffusion coefficient*. For a dilute gas the dependence is only on temperature; in this case the *Fick's Law* is suitable:

$$\underline{J}_k = -\rho D_k \nabla \left(\frac{\rho_k}{\rho} \right) \quad (3.33)$$

Pressure is defined from the stress tensor ($\underline{\tau}$) as the isotropic and reversible stress or as the stress when fluid is in a quiet flow. For Newtonian fluids with Maxwellian velocity distribution, pressure is related to thermal motion of the particle:

$$p = \frac{1}{3} \rho \langle C^2 \rangle = \frac{\rho k_B T}{m_0} \quad (3.34)$$

This leads to the *equation of state for ideal gases*:

$$p = \rho R T \quad (3.35)$$

where R is the *gas constant*:

$$R = \frac{N_A k_B}{m_0} = \frac{R_0}{m_0} \quad (3.36)$$

At standard temperature (298 K) and pressure ($1.013 \cdot 10^5$ Pa), most real gases are considered as ideal. Deviation from an ideal gas occurs at higher temperature and lower density since the work performed by intermolecular forces becomes less significant

compared with the particles' kinetic energy, and the size of the molecules becomes less significant compared to the empty space between them. The ideal gas model tends also to fail at lower temperature or higher pressure, when intermolecular forces and molecular size become more important. At some point of low temperature and high pressure, real gases undergo a phase transition, such as to a liquid or a solid. However, the model of an ideal gas does not describe or allow phase transitions. These must be modelled by other complex equations of state.

Specific internal energy (i.e., internal energy per unit mass) (e) is given by Eq. (3.37), and the *specific heat at constant volume* (c_v) is defined by Eq. (3.38):

$$e = \frac{\xi}{2} RT = c_v T \quad (3.37)$$

$$c_v = \frac{\xi}{2} R \quad (3.38)$$

The *specific enthalpy* (h), i.e., a thermodynamic potential, can be defined differentially by:

$$dh = c_p dT = de + \frac{1}{\rho} dp \quad (3.39)$$

It can be demonstrate that c_p is the *specific heat at constant pressure*. Moreover, Eqs. (3.40), (3.41) and (3.42) can be derived:

$$R = c_p - c_v \quad (3.40)$$

$$c_p = R + c_v = R + \frac{\xi}{2} R = \left(1 + \frac{\xi}{2}\right) \quad (3.41)$$

$$\gamma = \frac{c_p}{c_v} = \left(1 + \frac{2}{\xi}\right) \quad (3.42)$$

The *speed of sound* (a) is the velocity at which a pressure disturbance propagates in a fluid medium. For a simple gas, the speed of sound is given by Eq. (3.43). The ratio between the fluid mean velocity (U) and the speed of sound is the *Mach number* (M):

$$a = \sqrt{\gamma RT} \quad (3.43)$$

$$M = \frac{U}{a} \quad (3.44)$$

Viscosity is the property that relates the stresses, i.e., the momentum diffusive transport to the resulting strain rate. Newtonian fluids (e.g., most planetary atmospheres) have a linear relationship between stress and strain rates. For Non-Newtonian fluids, instead, the relationship between causes (i.e., the velocity gradient) and effects (i.e., the momentum diffusive transport) is non-linear such that the diffusive coefficients depend on gas composition, pressure, temperature, and also the transported quantity (i.e., the viscosity depends on the stress). The stress tensor for Newtonian fluids is expressed by:

$$\underline{\underline{\tau}} = 2\mu \left[\left(\frac{\nabla \underline{V} + \nabla \underline{V}^T}{2} \right) - \frac{1}{3} \text{Tr} \left(\frac{\nabla \underline{V} + \nabla \underline{V}^T}{2} \right) \underline{I} \right] + \mu_b \text{Tr} \left(\frac{\nabla \underline{V} + \nabla \underline{V}^T}{2} \right) \underline{I} - p \underline{I} \quad (3.45)$$

where μ is the *viscosity coefficient*, and μ_b is the *bulk viscosity coefficient* (negligible for atmospheric gases), $\nabla \underline{V}$ and $\nabla \underline{V}^T$ are the velocity gradient tensor and its transposed tensor, and \underline{I} is the identity tensor. The velocity gradient tensor ($\nabla \underline{V}$) is defined as:

$$\nabla \underline{V} = \begin{bmatrix} \frac{\partial U}{\partial x} & \frac{\partial U}{\partial y} & \frac{\partial U}{\partial z} \\ \frac{\partial V}{\partial x} & \frac{\partial V}{\partial y} & \frac{\partial V}{\partial z} \\ \frac{\partial W}{\partial x} & \frac{\partial W}{\partial y} & \frac{\partial W}{\partial z} \end{bmatrix} \quad (3.46)$$

where U , V and W are the fluid velocity component along the main reference frame axis x , y and z , respectively. For Newtonian fluids, no single functional relation $\mu(p, T)$ describes any large class of fluids, but reasonable accuracy ($\pm 20\%$) can be achieved by non-dimensionalizing the data with respect to the critical point (T_c , p_c) with rough experimental functions of the reduced temperature (T/T_c) and the reduced pressure (p/p_c) (Fig. 3.1). At low pressure and density, the dependence of viscosity on pressure is negligible, and μ could be considered as function of only temperature.

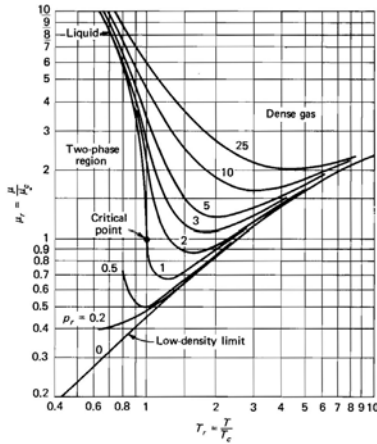
Viscosity is proportional to density ρ , mean free path l , and speed of sound a through the Maxwell equation, or by the Chapman and Cowling expressions (White, F.M., 1991):

$$\mu = 0.67 \rho \lambda a \quad (3.47)$$

$$\mu = \frac{2.68 \cdot 10^4 \sqrt{m_0 T}}{\sigma \Omega_v} \quad (3.48)$$

where σ is the collisional diameter, m_0 is the molecular mass, T is the temperature, μ is the viscosity, and Ω_v is the collisional integral, which is given by Eq. (3.49) and the data in Fig. 3.1:

$$\Omega_v \approx 1.147 \left(\frac{T}{T_\varepsilon} \right)^{-0.145} + \left(\frac{T}{T_\varepsilon} + 0.5 \right)^{-2.0} \quad (3.49)$$



(a)

Substance	Molecular weight	$T_c, ^\circ\text{R}$	p_c, atm	$\mu_c, \mu\text{Pa} \cdot \text{s}$	$k_c, \text{mW} / (\text{m})(\text{K})$
H ₂	2.016	60.0	12.8	3.47	90.0
He	4.003	9.47	2.26	2.54	20.8
Ar	39.944	272	48.0	26.4	29.8
Air	28.97 †	238 †	36.4 †	19.3 †	38.1 †
CO ₂	44.01	548	72.9	34.3	51.1
CO	28.01	239	34.5	19.0	36.2
N ₂	28.02	227	33.5	18.0	36.3
O ₂	32.00	278	49.7	25.0	44.1
NO	30.01	324	64	25.8	49.5
N ₂ O	44.02	557	71.7	33.2	54.9
Cl ₂	70.91	751	76.1	42.0	40.7
CH ₄	16.04	343	45.8	15.9	66.1

† Values for air are pseudocritical properties computed for the average composition of sea-level dry air.

(b)

Fig. 3.1: (a) Reduced viscosity (μ/μ_c) vs. reduced temperature (T/T_c) for different values of reduced pressure (p/p_c). (b) Temperature (T_c), pressure (p_c), viscosity (μ_c), and thermal conductivity (k_c) at the critical point for some gases (White, F.M., 1991).

Common approximations for viscosity of dilute gases are the *power-law* deduced by Maxwell and Rayleigh in Eq.(3.50), or the *Sutherland Law* (1893) in Eq. (3.51), which resulted from the kinetic theory using an idealized intermolecular-force potential:

$$\frac{\mu}{\mu_0} \approx \left(\frac{T}{T_0} \right)^n \quad (3.50)$$

$$\frac{\mu}{\mu_0} \approx \left(\frac{T}{T_0} \right)^{\frac{3}{2}} \frac{T_0 + S}{T + S} \quad (3.51)$$

where μ_0 is the viscosity at a reference temperature T_0 , n is a parameter for the power-law, and S is the *Sutherland constant*, which depend on the gas (Tab. 3.4).

Gas	T_0 , K	μ_0 , N · s / m ²	n	Error, % temperature range, K	S, K	Temperature range for 2% error
Air	273	1.716E - 5	0.666	±4 210-1900	111	170-1900
Argon	273	2.125E - 5	0.72	±3 200-1500	144	120-1500
CO ₂	273	1.370E - 5	0.79	±5 209-1700	222	190-1700
CO	273	1.657E - 5	0.71	±2 230-1500	136	130-1500
N ₂	273	1.663E - 5	0.67	±3 220-1500	107	100-1500
O ₂	273	1.919E - 5	0.69	±2 230-2000	139	190-2000
H ₂	273	8.411E - 6	0.68	±2 80-1100	97	220-1100
Steam	350	1.12E - 5	1.15	±3 280-1500	1064	360-1500

Source: Data from Hilsenrath et al. (1955).

†No data given above maximum temperature listed. Formulas inaccurate below minimum temperature listed.

Tab. 3.4: Parameters for the power law (T_0 , μ_0 , n) and Sutherland law (T_0 , μ_0 , S) for viscosity of some gases (White, F.M., 1991).

In a mixture, the *thermal flux* is characterized by a term due to heat conduction through the *thermal conductive coefficient* (k) according to the Fourier's Law, and a term due to species mass diffusion:

$$\underline{J}_t = -k\nabla T + \sum_{k=1}^{N_k} h_k \underline{J}_k \quad (3.52)$$

Also for the thermal conductivity coefficient, correlations between reduced variables are applicable, and for dilute gas the dependence is mainly on temperature. A power-law (Eq. (3.53)) and a Sutherland law (Eq. (3.54)) for conductivity also exist as for viscosity, in which k_0 is the thermal conductivity at the reference temperature T_0 , n is a parameter for the power-law, and S is the Sutherland constant for conductivity (Tab. 3.5):

$$\frac{k}{k_0} \approx \left(\frac{T}{T_0} \right)^n \quad (3.53)$$

$$\frac{k}{k_0} \approx \left(\frac{T}{T_0} \right)^{\frac{3}{2}} \frac{T_0 + S}{T + S} \quad (3.54)$$

Gas	T_0 , K	k_0 , W / m · K	n	Error, % temperature range, K	S, K	Temperature range for ±2% error, K
Air	273	0.0241	0.81	±3 210-2000	194	160-2000
Argon	273	0.0163	0.73	±4 210-1800	170	150-1800
CO ₂	273	0.0146	1.30	±2 180-700	1800	180-700
CO	273	0.0232	0.82	±2 210-800	180	200-800
N ₂	273	0.0242	0.74	±3 210-1200	150	200-1200
O ₂	273	0.0244	0.84	±2 220-1200	240	200-1200
H ₂	273	0.168	0.72	±2 200-1000	120	200-1000
Steam	300	0.0181	1.35	±2 300-900	2200	300-700

Source: Data from White (1988).

Tab. 3.5: Parameters for the power law (T_0 , k_0 , n) and Sutherland law (T_0 , k_0 , S) for thermal conductivity of some gases (White, F.M., 1991).

In the momentum balance equation (Eq. (3.18)), the term \underline{f}_m should include all the external mass forces acting on the fluid (e.g., gravity, electromagnetic, etc.), which determine the momentum source $\rho \underline{f}_m$. Typically for atmospheric gases only the gravity effect is considered relevant, and, hence $\underline{f}_m = \underline{g}$, where \underline{g} is the gravity acceleration vector. In the energy balance equation (Eq. (3.19)), the term e_p include all the potential energy due to conservative forces. If only gravity is considered relevant, as usually assumed, $e_p = gr$, where r is the distance from the level where the reference potential energy is fixed to zero, i.e., r is the height from the reference surface.

For a gas mixture of n_c components, the molecular mass can be considered as the average of the molecular mass of the components weighed with respect to the mole fractions (x_i):

$$m_0 = \sum_{i=1}^{n_c} x_i m_{0,i} \quad (3.55)$$

For non-polar gas mixtures, whose molar mass and molecules diameter are similar (< 2%), an approximated empirical relationship derived from the Sutherland and Wassiljewa formulation can be used to determine the viscosity (Brokaw, R.S., 1968):

$$\mu = \frac{\sum_{i=1}^{n_c} x_i \sqrt{\mu_i}}{\sum_{j=1}^{n_c} \frac{A_{ij}}{\sqrt{\mu_j}} x_j} \quad (3.56)$$

$$A_{ij} = m_{ij} \left(\frac{m_{0,j}}{m_{0,i}} \right)^{1/2} \left[1 + \frac{\left(\frac{m_{0,i}}{m_{0,j}} \right) - \left(\frac{m_{0,i}}{m_{0,j}} \right)^{0.45}}{2 \left(1 + \frac{m_{0,i}}{m_{0,j}} \right) + \frac{1 + \left(\frac{m_{0,i}}{m_{0,j}} \right)^{0.45}}{1 + m_{ij}}} m_{ij} \right] \quad (3.57)$$

$$m_{ij} = \left[\frac{4m_{0,i}m_{0,j}}{(m_{0,i} + m_{0,j})^2} \right]^{1/4} \quad (3.58)$$

The Navier-Stokes equations are valid only if Kn is globally and locally very small ($Kn < 0.1$). When the Maxwell distribution is suitable, the mean free molecular path can be expressed by the following relationship (Anderson Jr, J.D., 1989):

$$l = \frac{k_B T}{\sqrt{2} \pi d_M^2 p} \quad (3.59)$$

Knowing the mean free molecular path at a reference condition (l_r), i.e., $p = 1.101 \cdot 10^5$ Pa and $T = 293$ K, a relationship can also be used to take into account the effect of pressure and temperature variations (Baron, P.A., Willeke, K., 2001):

$$l = l_r \left(\frac{1.101 \cdot 10^5}{[p]_{Pa}} \right) \left(\frac{[T]_K}{293} \right) \left(\frac{1 + S / 293}{1 + S / [T]_K} \right) \quad (3.60)$$

where S is the Sutherland constant of the gas.

When rarefaction occurs and the non-slip boundary condition is not satisfied (*Knudsen layer*), the regime is a *slip flow*. The gas molecules may undergo several collisions and may escape from a wall after a residence time, during which exchange momentum between the fluid and the wall is accomplished. Therefore, Millikan, R.A., 1923, suggested calculating a slip coefficient by measuring forces and torques acting on bodies in order to evaluate a slip correction factor in the slip ($10^{-3} < Kn < 10^{-1}$) and transition regime ($10^{-1} < Kn < 10$). For $Kn < 0.1$, the Knudsen layer is very thin and can be neglected by extrapolating the bulk gas flow variables towards the walls in order to determine a finite slip velocity value at the wall. Therefore, in a slip flow regime the flow is governed by the Navier-Stokes equations, and rarefaction effects are modelled using Maxwell's slip velocity and temperature jump boundary conditions. First-order slip conditions are suitable for flows with relatively small Knudsen numbers, but second-order slip models become necessary for flows with larger Knudsen numbers; for $Kn > 0.2$, the slip models significantly under-predict the rarefaction effects (Zhang, G., et al., 2006). Guo, X., et al., 2008, analyzed numerical solutions of Navier-Stokes equations with first-order slip velocity for microchannel flows (i.e., ducts with hydraulic diameter below 1 mm). Nobile, U., 1954, showed that at a first-order approximation the slip velocity (u_w) of a gas on a wall is:

$$u_w \cong l \left(\frac{\partial U}{\partial x_n} \right)_{wall} = \frac{l}{\mu} \tau_w \quad (3.61)$$

where l is the mean free path, U is the velocity of the gas, x_n is the spatial coordinate normal to the wall, and τ_w is the tangential stress at the wall (Monti, R., Zuppari, G., 2007).

If we relate the above discussion to the Martian atmosphere at the surface level, we can assert that the Maxwellian hypothesis, simple dilute gas model and Newtonian conditions are fully applicable since the gas mixture is mainly composed by a prevalent species as about 95% by volume and mass is carbon dioxide (CO_2), molecules are quite similar sized, and the mean free molecular path (on average $4.74 \cdot 10^{-6}$ m) is quite larger than the molecules size (about $4.66 \cdot 10^{-9}$ m). Therefore, the equation of state and the expression proposed for the diffusive coefficients are valid. The Knudsen number is of the order of magnitude higher than 10^{-3} only for geometrical bodies with size smaller than 1 mm. This condition does not occur for the geometry of the ducts which are considered in this thesis, but it occurs at the interaction between the fluid and the Martian dust particles when $Kn > 1$. As it will be discussed in Sect. 3.1.2 in such cases the Navier-Stokes equations are valid and *ad hoc* parameters are introduced to prevent the failure of the model when considering the dynamics of micrometer-sized particles dispersed in the flow regime. Instead, the no slip flow condition should be considered not significant with respect to the interaction of the fluid with the walls of the working geometry. Finally, the approximation of considering the Martian atmospheric fluid as composed only of CO_2 , neglecting the other less abundant components, introduces an error of less than 2%, which is acceptable for the fluid dynamics studies that were developed to characterize the particles' dynamics inside the MEDUSA and MicroMED instruments.

3.1.2 Particles Dynamics

The dynamics of particles through a fluid is calculated by integrating the forces balance (\underline{F}) on each particle in a Lagrangian reference frame:

$$m_p \frac{d\underline{V}_p}{dt} = \underline{F} \quad (3.62)$$

where m_p is the mass of the particles, \underline{V}_p the velocity of the particles, and \underline{F} the resulting force acting on the particle. The most common forces that can act on a particle are summarized in Tab. 3.6. Among the forces quoted in Tab. 3.6, the most relevant forces in determining the dynamics of the particles in the cases considered in this thesis are the drag force and the gravity force. Secondary effects are introduced by the Saffman lift force when steep gradients of the fluid velocity occur normally to the direction of the particles' motion and random effects are introduced by the Brownian force. The

buoyancy force, virtual mass force, and pressure gradient force do not influence significantly the particles dynamics as $\rho/\rho_p \sim 10^{-5}$. Electrostatic and thermophoretic forces will occur only in specific environments, i.e., in presence of electric fields and fluid temperature gradients, respectively. Adhesion forces on particles impacted or deposited on walls occur even if a not well-know quantification has been made.

Force	Equation	Characteristics and validity	
Aerodynamic Drag	$\underline{F} = \frac{1}{2} \rho (\underline{V} - \underline{V}_p)^2 \frac{\pi d_p^2}{4} C_D$	<ul style="list-style-type: none"> ▪ Aerodynamic force 	(3.63)
Gravity	$\underline{F} = m_p \underline{g}$	<ul style="list-style-type: none"> ▪ Gravity effect 	(3.64)
Virtual mass	$\underline{F} = \frac{1}{2} m_p \frac{\rho}{\rho_p} \frac{d}{dt} (\underline{V} - \underline{V}_p)$	<ul style="list-style-type: none"> ▪ Required to accelerate the fluid surrounding the particle ▪ Negligible for $\rho_p \gg \rho$ 	(3.65)
Buoyancy	$\underline{F} = -m_p \underline{g} \frac{\rho}{\rho_p}$	<ul style="list-style-type: none"> ▪ Negligible for $\rho_p \gg \rho$ 	(3.66)
Pressure gradient	$\underline{F} = m_p \frac{\rho}{\rho_p} \underline{V}_p \cdot \nabla \underline{V}$	<ul style="list-style-type: none"> ▪ Due to the pressure gradient in the fluid 	(3.67)
Saffman lift	$\underline{F} = 1.614 d_p^2 \sqrt{\mu \rho} \frac{(\underline{V} - \underline{V}_p) \times \nabla \times (\underline{V} - \underline{V}_p)}{\sqrt{ \nabla \times (\underline{V} - \underline{V}_p) }}$	<ul style="list-style-type: none"> ▪ Particle rotation and lifting due to velocity gradient of fluid (shear flows) ▪ $Re \ll 1$ ▪ $Re < \sqrt{\frac{d_p^2}{\mu} \frac{dU}{\rho dy}}$ 	(3.68)
Brownian	$\underline{F} = m_p \underline{\xi} \sqrt{\frac{\pi S_0}{\Delta t}}$	<ul style="list-style-type: none"> ▪ Modeled as a Gaussian white noise ▪ Only for non-turbulent models 	(3.69)
Electrostatic	$\underline{F} = n_e e^- \underline{E}$	<ul style="list-style-type: none"> ▪ Significant when gravity effects are negligible (i.e., submicrometer-sized particles and/or microgravity conditions) 	(3.70)
Thermophoretic	$\underline{F} = -\underline{D}_{T,p} \frac{\nabla T}{T}$	<ul style="list-style-type: none"> ▪ Acting on small particles suspended in a gas as effect of temperature gradients. ▪ Spherical particles ▪ Ideal gas 	(3.71)

Tab. 3.6: Forces acting on particles.

The *aerodynamic drag* (Eq. (3.63)) is a resistive force that opposes to the relative motion $(\underline{V} - \underline{V}_p)$ of a particle through a fluid. It depends on the dynamic pressure $1/2\rho(\underline{V} - \underline{V}_p)^2$, the particle shape (through the drag coefficient C_D) and cross section size $(\pi d_p^2/2)$.

Typically, C_D (Tab. 3.7) depends on the flow regime through the Reynolds number, which is defined as:

$$\text{Re}_p = \frac{\rho d_p |\underline{V} - \underline{V}_p|}{\mu} \quad (3.72)$$

Drag coefficient	Validity	Reference	
$C_D = \frac{24}{\text{Re}_p}$	<ul style="list-style-type: none"> ▪ $\text{Re}_p \ll 1$ ▪ Smooth spherical particles 	Stokes drag force coefficient	(3.73)
$C_D = a_1 + \frac{a_2}{\text{Re}_p} + \frac{a_3}{\text{Re}_p^2}$ $0 < \text{Re}_p < 10^{-1}: a_1 = 0, a_2 = 24, a_3 = 0$ $10^{-1} < \text{Re}_p < 1: a_1 = 3.690, a_2 = 22.73, a_3 = 0.0903$ $1 < \text{Re}_p < 10: a_1 = 1.222, a_2 = 29.1667, a_3 = -3.889$ $10 < \text{Re}_p < 10^2: a_1 = 0.6167, a_2 = 46.50, a_3 = -116.67$ $10^2 < \text{Re}_p < 10^3: a_1 = 0.3644, a_2 = 98.33, a_3 = -2778$ $10^3 < \text{Re}_p < 5 \cdot 10^3: a_1 = 0.357, a_2 = 148.62, a_3 = -47500$ $5 \cdot 10^3 < \text{Re}_p < 10^4: a_1 = 0.46, a_2 = -490.546, a_3 = 578700$ $\text{Re}_p > 10^4: a_1 = 0.5191, a_2 = -1662.5, a_3 = 5416700$	<ul style="list-style-type: none"> ▪ Smooth spherical particles 	Morsi, S.A., Alexander, A.J., 1972	(3.74)
$C_D = \frac{24}{\text{Re}_p} \left(1 + b_1 \text{Re}_p^{b_2} \right) + \frac{b_3 \text{Re}_p}{b_4 + \text{Re}_p}$ $b_1 = e^{2.3288 - 6.4581\delta_s + 2.4486\delta_s^2}$ $b_2 = 0.0964 + 0.5565\delta_s$ $b_3 = e^{4.905 - 13.8944\delta_s + 18.4222\delta_s^2 - 10.2599\delta_s^3}$ $b_4 = e^{1.4681 + 12.2584\delta_s - 20.7322\delta_s^2 + 15.8855\delta_s^3}$	<ul style="list-style-type: none"> ▪ Re computed with the diameter of a sphere having the same volume 	Haider, A., Levenspiel, O., 1989	(3.75)

Tab. 3.7: Drag coefficient evaluation.

The shape factor of a particle (δ_s) is defined as the ratio between the surface area of a sphere having the same volume as the particle, and the actual surface area of the particle.

The mean free molecular path is given by Eq. (3.59) or (3.60) and the *Knudsen number* (Kn) is defined as the ratio between the mean free molecular path (l) and the particle radius Eq. (3.76).

$$Kn_p = \frac{l}{d_p/2} \quad (3.76)$$

In order to calculate the drag force in rarefied flows (i.e., $Kn > 1$), the drag force coefficient from Tab. 3.7 has to be reduced by the *Cunningham Correction factor* (C_c):

$$C_D = \frac{[C_D]_{Kn=0}}{C_c} \quad (3.77)$$

C_c was obtained by experimental tests for $Kn_p < 500$ and several gases (e.g., air, O_2 , CO_2 , Ar , He , etc.):

$$C_c(Kn_p) = 1 + \alpha_c Kn_p \quad \begin{array}{l} \text{Cunningham, E., 1910} \\ \text{Sorensen, C.M., Wang, G.M., 2000} \end{array} \quad (3.78)$$

$$C_c(Kn_p) = 1 + Kn_p \left(\alpha_c + \beta_c e^{-\left(\frac{\gamma_c}{Kn_p}\right)} \right) \quad \text{Allen, M.D., Raabe, O.G., 1985} \quad (3.79)$$

where α_c , β_c , and γ_c are experimental parameters which have been demonstrated to be approximately independent on the gas within 2% (Schmid, O., et al., 2002). Some evaluations are reported in Tab. 3.8.

Parameters	Experimental Conditions	Reference
$\alpha_c = 1.142$ $\beta_c = 0.558$ $\gamma_c = 0.999$	Not-spherical particles made of Polystyrene Latex-divinylbenzene (PSL) in air for $0.01 \leq Kn_p \leq 10$	Allen, M.D., Raabe, O.G., 1985
$\alpha_c = 1.2310$ $\beta_c = 0.4695$ $\gamma_c = 1.1783$	Spherical particles made of Polystyrene Latex-divinylbenzene (PSL) in air for $0.06 \leq Kn_p \leq 500$	Hutchins, D.K., et al., 1995
$\alpha_c = 1.165$ $\beta_c = 0.483$ $\gamma_c = 0.997$	Spherical particles made of Polystyrene Latex-divinylbenzene (PSL) for $8.27 \text{ kPa} \leq p \leq 28.58 \text{ kPa}$ and $0.5 \leq Kn \leq 83$	Kim, J.H., et al., 2005

Tab. 3.8: Parameters for the Cunningham slip correction factor.

The *gravitational force* is proportional to particle mass (m_p) and gravitational acceleration (g) (Eq. (3.64)). The difference between the density of the particle and the density of the surrounding medium causes the *buoyancy force* (Eq. (3.66)). As a particle begins to move in a gravitational field, the gas surrounding the particle exerts an opposing drag force, which after a short period of acceleration, equals the gravitational force, and the particle reaches its *terminal settling velocity* (V_{ts}). By equating the drag force (i.e., the Stokes drag force corrected with the Cunningham factor) to the gravitational force, the terminal velocity is obtained:

$$V_{ts} = \frac{(\rho_p - \rho)d_p^2 g C_c}{18\mu} \quad (3.80)$$

The *particle relaxation time* (t_r) is the time a particle takes to reach $(1-1/e)V_{ts}$:

$$t_r = \frac{\rho_p d_p^2 C_c}{18\mu} \equiv \frac{V_{ts}}{g} \quad (3.81)$$

When a particle is injected into a fluid with initial velocity V_0 , the product of the relaxation time and the initial particle velocity is referred as *stopping distance* (s_d):

$$s_d = V_0 t_r \quad (3.82)$$

When gas flow conditions change suddenly (e.g., at the particle collection surface of an impactor), the ratio of the stopping distance to a characteristic dimension (L), defined as the *Stokes number* (Stk), is commonly referred to classify the dynamics:

$$Stk = \frac{s_d}{L} \quad (3.83)$$

If $Stk \ll 1$, the particles follow the fluid streamlines as they have a relatively low inertia; if $Stk \gg 1$, the particles go on with their momentum and do not follow strictly the fluid flow when flow deviations occur. An approximated relationship between the fluid velocity and the particle velocity is given by:

$$\psi = \frac{V}{V_p} = \frac{1}{1 + Stk} \quad (3.84)$$

When the gas differs in composition from one location to another, diffusion of the gas occurs. As a result of the gas diffusion suspended particles acquire a net velocity as a function of the gas diffusion (*diffusiophoresis*), i.e., the particles are pushed in the direction of the larger molecule flow. The force is a function of the molecular weight and diffusion coefficients of the diffusing gases and is largely independent of the particle size. *Diffusion* is also the ensemble motion of the particles due to their concentration gradient. The diffusive flux (\underline{J}_p) of particles is:

$$\underline{J}_p = -D\nabla N_p \quad (3.85)$$

where D is the *diffusion coefficient* or *diffusivity*. Diffusive effects are relevant for small particles, while inertial effects are relevant for large particles. A complex Eulerian approach should be used in order to determine the particles concentration field (N_p),

while a simpler Lagrangian approach is typically used to study the particle inertial effects. The balance equation of the particle concentration is:

$$\frac{\partial N_p}{\partial t} + \nabla \cdot N_p \underline{V} = \nabla \cdot D \nabla N_p - \nabla \cdot N_p \underline{C}_p \quad (3.86)$$

where N_p is the particles density number, \underline{V} is the fluid velocity and \underline{C}_p is the particle settling velocity. The diffusion coefficient can be computed as:

$$D = \frac{k_B T C_c}{3\pi\mu d_p} = k_B T B \quad (3.87)$$

where B is the mechanical mobility.

Brownian motion is the random movement of a particle suspended in a fluid due to collision with fluid molecules. The components of the Brownian force (Eq. (3.69)) can be modelled as a Gaussian white noise with spectral intensity $S_{n,ij}$ (Li, A., Ahmadi, G., 1992):

$$S_{n,ij} = S_0 \delta_{ij} \quad (3.88)$$

$$S_0 = \frac{216\nu k_B T}{\pi^2 \rho d_p^5 \left(\frac{\rho_p}{\rho}\right)^2 C_c} \quad (3.89)$$

In Eq. (3.69), ζ are zero-mean, unit variance-independent Gaussian random numbers. The amplitudes of the Brownian force components are evaluated at each time step (Δt). The root mean square distance (s_{rms}) that a particle can travel in the time step Δt due to Brownian motion is:

$$s_{rms} = \sqrt{2D\Delta t} \quad (3.90)$$

Application of electrostatic forces is particularly effective for submicrometer-sized particles for which gravity forces are weak. For a particle with a total charge of n_e times the elementary unit of charge (e^-), under the electric field \underline{E} , the electrostatic force is given by Eq. (3.70). Many processes can contribute to charge aerosol particles: *static electrification* (i.e., transfer of charge to a particle as it is separated from bulk material, e.g., due to electrochemical potential differences with a contacting surface, particle separation from a surface under an electric field, disruption of liquid surfaces, and/or separation of highly dielectric liquids from solid surfaces), *triboelectric effect* (i.e., due to friction between particles), *photoemission* (i.e., electrons emission due to incident

photons), *thermoionic emission* (i.e., electrons emission due to heat transfer), charging by small gas ions (i.e., loss of α and β particles), and *self-charging of radioactive aerosols* (i.e., injection of valence electrons or release of charged fragments during α , β , and γ radiations). A dielectric particle in a uniform electric field E can induce distortion of the electric field causing ions migration along the field lines and deflection toward the particle, resulting in increasing the particle charge q with time t as:

$$q = q_s \frac{e^- Z N_p t}{e^- Z N_p t + 4 \epsilon_0} \quad (3.91)$$

$$q_s = \left(\frac{3 \epsilon_r}{\epsilon_r + 2} \right) \pi \epsilon_0 E d_p^2 \quad (3.92)$$

$$Z_p = \frac{n_c e^- C_c}{3 \pi \mu d_p} \quad (3.93)$$

where q_s is the saturation charge level, Z_p is the particle electrical mobility, N_p is the concentration number. The induced charge of a particle in a uniform electric field as it is separated from contact with a conductive surface was estimated by Shelton, H., et al., 1960, Cho, A.W.H., 1964, and Colver, G.M., 1976:

$$q_s = \frac{\pi^2}{6} \pi \epsilon_0 d_p E = 1.65 \pi \epsilon_0 d_p^2 E \quad (3.94)$$

Moreover, the charge that a single particle can acquire when residing on an infinite conductive plane was valued by Novick, V.J., et al., 1989 as:

$$q_s = 1.37 \pi \epsilon_0 d_p^2 E \quad (3.95)$$

When a particle is in contact with a surface, a *force of adhesion* holds the particle in a static equilibrium. When the particle is being removed from the surface by an increasing force, it continues to remain attached to the surface until it snaps off the surface. The adhesion force when snap-off occurs, which is different from the force of adhesion, is termed *pull-off force* (F_{po}). An expression for determining the pull-off force was given by Szarek, T.R., Dunn, P.F., 2007:

$$F_{po} = C_1 \pi \gamma_s d_p (1 + C_2 RH) C_3 \quad (3.96)$$

where γ_s is the surface energy of adhesion, RH is the relative humidity, C_1 is the dimensionless Tabor's parameter (i.e., the ratio of the elastic displacement of the particle surface at the point of separation from the substrate surface to the equilibrium

atomic spacing), which is determined theoretically and typically equal to 0.75-1.0 (Maugis, D., 1991), C_2 is the coefficient for the effect of relative humidity, which is determined experimentally ($C_2 = 0.009$ according to Corn, M., 1961), and C_3 is the pull-off force reduction factor for the effect of the asperity roughness height (σ), which was studied by Cheng, W., Dunn, P.F., Brach, R.M., 1993 (Fig. 3.2).

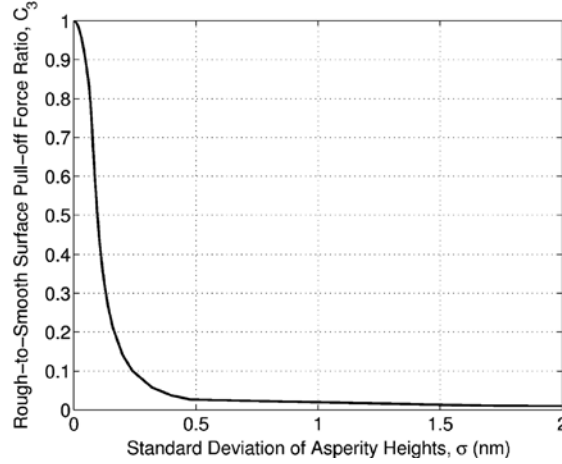


Fig. 3.2: Reduction factor of particle pull-off force C_3 with increasing surface roughness as characterized by the standard deviation of surface asperity heights σ (Cheng, W., Dunn, P.F., Brach, R.M., 2002).

Particles in a thermal gradient are bombarded more strongly by gas molecules on the hotter side and, are, therefore, forced away from a heat source. Thus, heated surfaces tend to remain clean, while relatively cold surfaces tend to collect particles (*thermophoresis effect*). The thermophoretic force can be evaluated by Eq. (3.71), with an expression of the thermophoretic coefficient matrix ($\underline{D}_{T,p}$) given by Talbot, L., et al. 1980:

$$\underline{D}_{T,p} = \frac{6\pi d_p \mu^2 C_s (K + C_t Kn_p)}{\rho (1 + 3C_m Kn_p) (1 + 2K + 2C_t Kn_p)} \underline{I} \quad (3.97)$$

where Kn is the Knudsen number, $K = k/k_p$, k is the fluid thermal conductivity based on translational energy only ($15/4 \mu R$), k_p is the particle thermal conductivity, $C_s = 1.17$, $C_t = 1.09$, $C_m = 0.57$.

Electromagnetic radiation or *photophoresis* can have a direct effect on particle motion by transferring momentum to the particle. Light impinging on a particle can be reflected, refracted, or absorbed. The fraction of momentum transfer from the light beam to the particle depends on the geometric cross section of the particle as well as the average direction of the scattered light.

As a particle moves along its trajectory, heat and mass transfer between it and the continuous phase should be computed via the heat and mass transfer laws. The trajectory equations, and any auxiliary equations describing heat or mass transfer to/from the particle, should be solved by stepwise integration over discrete time steps. The particle temperature (T_p) can be determined by solving the heat exchange equation between a particle and the fluid:

$$m_p c_{pp} \frac{dT_p}{dt} = h_c A_p (T - T_p) + \varepsilon_p A_p \sigma (\theta_R^4 - T_p^4) \quad (3.98)$$

where c_{pp} is the particle heat capacity, A_p is the particle surface area, h_c is the convective heat transfer coefficient, ε_p is the particle emissivity, θ_R is the radiation temperature, and σ is the Stefan-Boltzmann constant. Eq. (3.98) assumes that the particle internal resistance to heat transfer is negligible (i.e., no temperature gradients through the particle). The convective heat transfer coefficient comes from the *Nusselt number* (Nu):

$$Nu = \frac{h_c d_p}{k} = 2.0 + 0.6 Re_p^{1/2} Pr^{1/3} \quad (3.99)$$

The radiation temperature comes from the integral of the radiation intensity (I) over the solid angle (Ω):

$$\theta_R = \frac{G}{4\sigma} = \frac{1}{4\sigma} \int_{4\pi} I d\Omega \quad (3.100)$$

The particle boundary at walls can be expressed through the normal (e_n) and tangential (e_t) coefficient of restitution, which define the amount of momentum in the relative direction with respect to the wall that is retained by the particle after the collision with the boundary (i.e., the ratio between the particle momentum after the impact and the particle momentum before the impact). If $e_n = 1$ and $e_t = 1$ the impact is an elastic reflection; if $e_n = 0$ and $e_t = 0$ the particle escape from the fluid.

Some typical values of the parameters which characterize the particles' interaction with a fluid and dynamics in a typical Martian environment are reported in Fig. 3.3. The Knudsen number (Kn_p) related to the size of the particles was evaluated with Eq. (3.76), in which the free molecular path for a gas mixture prevalently made of CO_2 was evaluated with Eq. (3.59) at the standard conditions ($T = 293$ K, $p = 1.1013 \cdot 10^5$ Pa, $d_M = 4.66 \cdot 10^{-9}$ m) obtaining the reference value $l_r = 4.14 \cdot 10^{-10}$ m, and reported to typical average Martian temperature and pressure conditions ($T = 215$ K,

$p = 6.10 \cdot 10^2$ Pa) with Eq. (3.60), in which the Sutherland constant S is equal to 222 K obtaining a free molecular path l equal to $4.74 \cdot 10^{-6}$ m. The Cunningham slip correction factor (C_c) was evaluated with Eq. (3.79), in which the coefficients $\alpha_c = 1.142$, $\beta_c = 0.558$, and $\gamma_c = 0.999$ are considered according to Allen, M.D., Raabe, O.G., 1985 (Tab. 3.8); they are average estimates for non-spherical particles similar to those expected on Mars. The terminal velocity of the particles (V_{ts}) was evaluated with Eq. (3.80), considering that the Martian gravity is on average 3.73 m/s^2 , the particle density is on average $2.73 \cdot 10^3 \text{ kg/m}^3$, and the fluid viscosity obtained by the Sutherland formula (Eq. (3.51)) is $1.029 \cdot 10^{-5} \text{ Pa}\cdot\text{s}$. The thermophoretic coefficient ($D_{T,p}$) was evaluated with Eq. (3.97), in which the particles' thermal conductivity k_p is equal to 100 W/m/K and the fluid thermal conductivity is equal to $9.70 \cdot 10^{-3} \text{ W/m/K}$.

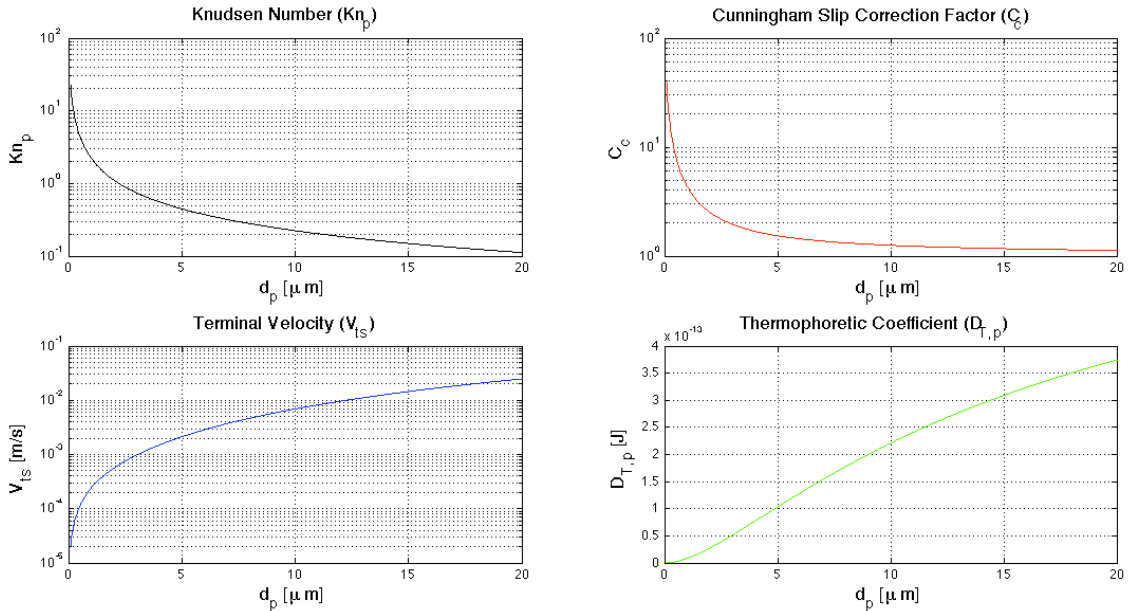


Fig. 3.3: Knudsen number (Kn_p), Cunningham slip correction factor (C_c), terminal velocity (V_{ts}), and thermophoretic coefficient ($D_{T,p}$) for dust particles in Martian atmosphere at surface ($\rho_p = 2.73 \cdot 10^3 \text{ kg/m}^3$, $g = 3.73 \text{ m/s}^2$, $p = 610 \text{ Pa}$, $T = 215 \text{ K}$) with respect their diameter.

3.1.3 Numerical Methods for Aerosol Dynamics

Typically, the equations for the particles, which represent a discrete phase, are Ordinary Differential Equations (ODE), while the equations for the continuous phase (i.e., the Navier-Stokes equations) are Partial Differential Equations (PDE).

When the flow is globally considered not rarefied, the fluid phases can be treated as a continuum by solving the time averaged Navier-Stokes equations (Euler approach). Computational Fluid Dynamics (CFD) methods are generally based on solving systems

of coupled partial differential equations, which represent conservation laws of physical quantities for the continuous phases. The integral form of the conservation equation of an arbitrary quantity φ is:

$$\underbrace{\int_V \frac{\partial \rho \varphi}{\partial t} dV}_{\text{Unsteady Term}} + \underbrace{\int_{\partial V} \rho \varphi \underline{V} \cdot \underline{n} dS}_{\text{Convective Flux}} = \underbrace{\int_{\partial V} \Gamma_\varphi \nabla \varphi \cdot \underline{n} dS}_{\text{Diffusive Flux}} + \underbrace{\int_V S_\varphi dV}_{\text{Source Term}} \quad (3.101)$$

where V is the finite volume, ∂V is the boundary of V , \underline{n} is the normal to the surface, Γ_φ is the diffusion coefficient, S_φ is the source of φ per unit volume.

The most common CFD tools solve the system by discretizing the equations through the *Control Volume (CV)* method. The Control Volume method converts scalar transport equations to algebraic equations. In order to analyze fluid flows, flow domains are split into smaller subdomains (cells or elements), which are made up of geometric primitives like quadrilaterals and triangles (2D domains), and hexahedra and tetrahedra (3D domains). The collection of cells constitutes the mesh or grid. The Navier-Stokes equations are discretized as:

$$\underbrace{\frac{\partial \rho \varphi}{\partial t} V}_{\text{Unsteady Term}} + \underbrace{\sum_f^{N_{\text{faces}}} \rho_f V_f \varphi_f \cdot \underline{n}_f S_f}_{\text{Convective Flux}} = \underbrace{\sum_f^{N_{\text{faces}}} \Gamma_\varphi \nabla \varphi_f \cdot \underline{n}_f S_f}_{\text{Diffusive Flux}} + \underbrace{S_\varphi V}_{\text{Source Term}} \quad (3.102)$$

where N_{faces} is the number of faces enclosing cell, φ_f is the value of φ connected through face f , and solved inside each of subdomain. The discretized scalar transport equations contain unknown scalar variables at the cell center and in surrounding neighbour cells. These equations could be non-linear with respect to these variables, but can be linearized.

Dispersed phases can be considered as discrete phases solved by tracking particles with the force balance acting on each particle (Eq. (3.62)) computed in a lagrangian frame at time steps. This hypothesis is suitable if the dispersed phases occupy a small volume fraction (10-12%), even through high mass loading ($\dot{m}_{\text{particles}} \geq \dot{m}_{\text{fluid}}$) is acceptable. Particles are introduced in the fluid flow by defining initial position, velocity, size and temperature. The trajectory and heat/mass transfer calculations are based on integrating numerically the balance of forces on the particles and on the convective/radiative heat and mass transfer from the particle, using the local continuous phase conditions as the particle moves through the flow considering a one-way or two-

way coupling. In the uncoupling or one-way coupling, the fluid phase influences the particulate phase via drag and turbulence, but the particulate phase has no influence on the gas phase; in the two-way coupling, the fluid phase influences the particulate phase and the particulate phase influences the fluid phase via source terms of mass, momentum and energy. Boundary conditions for the particles also consider wall interactions (e.g., escape, reflection, trapping).

A mesh for the numerical solution can be: structured, i.e., characterized by regular connectivity that can be expressed as a two or three dimensional array, the elements are quadrilaterals (2D domains) or hexahedra (3D domains), and the regularity of the connectivity allows to conserve space since neighborhood relationships are defined by the storage arrangement; unstructured, i.e., characterized by irregular connectivity, and the storage requirements can be substantially larger since the neighborhood connectivity must be explicitly stored; hybrid, i.e., contains structured and unstructured portions.

The advantages of using the Control Volume Method are: the spatial discretization is carried out directly in the physical space (i.e., there are no problems with any transformation between coordinate systems); the method is very flexible and convenient for complex geometries (i.e., it can be easily implemented on structured as well on unstructured grids).

Fluxes (i.e. surface integrals) and source terms (i.e., volume integrals) are evaluated through interpolation functions depending on variables valued at some locations on the cell faces. The cell face values are approximated through the values at the Control Volume centroids. The interpolation functions can be modelled to have specified order of accuracy.

The requirements for the mesh are: the mesh must have appropriate resolution (i.e., cells must be denser where gradients are higher); the mesh must have good quality (i.e., cells must not be skewed, and changes in cells size must be spatially regular and gradual). The most common parameters to classify cells quality are: aspect ratio (i.e. the difference between the cell's shape and the shape of an equilateral cell of equivalent volume) and skewness (i.e., the measure of the stretching of the cell).

Even though the balance and the conservation equations of fluid dynamics are valid in all flow regimes, the solution of the Navier-Stokes equations becomes lacking with increasing the flow rarefaction. In fact, the numerical integration of the Navier-Stokes

equations relies also on the computation of shear stress, heat flux and diffusion of chemical species. In low-density regimes, the phenomenological equations of Newton, Fourier and Fick, computing these parameters, are no longer valid. Moreover, as the density decreases, the intermolecular collisions in the gas get too few to maintain the isotropy of the pressure tensor. The conventional no-slip condition fails, and the knowledge of slip velocity and temperature jump is necessary for fixing the boundary conditions on the body surface.

The *Direct Simulation Monte Carlo (DSMC)* method, developed by Bird since 1963 (Bird G.A., 1994), is a method solving the whole transitional regime. The DSMC deals with the gas as made up of a number of discrete molecules with translational, rotational and vibrational energies due to excitation of several degrees of freedom as a result of high temperature and chemical reactions. The gas is made of hundred thousands or million of simulated molecules, each one representing a number of real molecules. The evolution of each molecule (Direct Simulation), which exchanges momentum and energy, is produced by collisions with other molecules and the body with which they interact in a simulated physical space. The method is statistic and stochastic as its procedure relies on sampling probability functions by means of random numbers (Monte Carlo). In DSMC, the simulated volume, including the body, is discretized in cells and sub-cells. Position, velocity, and internal state of each molecule in the cells are computed concurrently. DSMC uses the cells only for sampling the macroscopic properties and for selecting the colliding molecules. Use of sub-cells allows an effective selection of collision pairs by the logic of the “nearest neighbour”. Movement of each molecule from a cell to another one is the product of the velocity and a prefixed time step (Δt). In order to uncouple molecular motion and collisions, the time step has to be shorter than the mean collision time or the time interval between two successive collisions (Δt_c). As a result, the typical dimension of the cells should be smaller than the local mean free path, and, so, it should be also small compared with the distance over which there is a significant change of flow properties. Macroscopic thermo-fluid-dynamics quantities of the flow as density, temperature, pressure, etc., are computed by an average over the molecules in each cell. The DSMC does not involve numerical instabilities as it is just a computer method and not a numerical method, and parameters such as the Mach number, the Reynolds number, etc., have no sense.

The DSMC method, which is typically used to simulate blunt bodies in hypersonic regime, could be suitable for simulating rarefied flow regimes and the interaction of gas molecules with micrometer-sized particle, which should be approximated as part of a non-chemically active species made of larger molecules. Nevertheless, DMSC for aerosol measurements was considered too complex and expensive to be applied in the cases studied in this thesis. Therefore, it was preferred to use numerical methods based on the finite volume solving the Navier-Stokes equations with the Cunningham correction (Sect. 3.1.1 and 3.1.2).

3.2 Particles Measurement

This section is focused on how to physically collect, select and identify dust particles by suitable sensors with particular regard to planetary research applications.

3.2.1 Aerosol Measurements in Planetary Research

Measurement of aerosol and dust properties in planetary atmospheres can be based on two different approaches: *remote sensing* and *in situ monitoring*.

Remote sensing approach is performed from orbiters or ground-based systems depending on technique. Several instruments on Mars' orbiters and landers performed optical analysis of dust with spectroscopic measurements (e.g., TES, Thermal Emission Spectrometer, on board Mars Global Surveyor) or LIDAR measurements (e.g., LIDAR on board Phoenix lander) giving some information about the vertical dust distribution and number concentration (Sect. 1.2.3).

Spectroscopic measurements are based on analysing spectra of the atmosphere in order to infer composition and/or optical and geometrical properties of suspended dust particles. Depending on the spectral range of measurements, spectra can include emission and/or absorption and scattering features. Since materials emit and absorb at characteristic wavelengths, by observing these wavelengths, their composition can be determined. Comparison of the spectral contrast of observed features with synthetic spectra, computed using the radiative transfer equation, give information about the abundance and size distribution of dust. LIDAR (Light Detection and Ranging) techniques can measure some properties, such as concentration and distance of targets by illuminating them with light waves (usually a pulsed laser), and analysing the backscattered waves. Aerosol soundings are also performed by observing the

occultation of sources, as stars or the Sun, or scattering of solar light at limb by dust suspended in the atmosphere (e.g., MCS, Mars Climate Sounder, on board Mars Reconnaissance Orbiter) to evaluate its physical properties at different heights above the planetary surface. The vertical resolution obtained with these observations is about 10 km, so they give limited information in the Planetary Boundary Layer.

Typically, remote sensing measurements need *ad hoc* assumptions in order to infer data about the sample. In order to determine particle size distribution, assumptions about the particles' morphology and composition are required, which are not always possible to make *a priori* to validate the collected data. The dust concentration obtained by optical remote measurements depends on a set of parameters such as chemical composition, size distribution and shape of the grains, whose effects overlap each other and make difficult their deconvolution. Dust size distribution has been often represented with gamma function distributions to fit available optical data, but this assumption can be questionable and not easily verifiable. In fact, light diffusion significantly depends on morphology and composition of particles and it is difficult to determine all parameters involved by scattering measurements, especially by remote sensing. Remote sensing of volatiles is usually based on spectroscopy. Abundances of species in the atmosphere can be derived from shape and intensity of absorption lines. Nevertheless, these measurements can be affected by overlapping of spectral features from surface materials with those from atmospheric volatiles. Therefore, remote sensing measurements are sometimes not exhaustive.

In situ approach is performed closer to the target with direct monitoring, which permits to overcome several drawbacks affecting the remote sensing approach. In Earth science, two approaches are usually considered: *in situ* data collection and analysis or laboratory analysis after sample acquisition. The latter solution usually requires sophisticated sample handling techniques and the application of destructive procedures, which, generally, are not suitable for planetary research. The only attempt to perform direct atmospheric dust monitoring on Mars surface was aimed at measuring dust settling with time onto a horizontal surface by MAE (Material Adherence Experiment) on board Mars Pathfinder. The MAE experiment had two sensors: a) a movable collecting window exposed to dust settling partly covering a GaAs solar cell, whose current generated by solar light was monitored with and without the collecting window;

b) a quartz crystal oscillator. An efficiency reduction of 0.29% per day was registered as a result of dust deposition on the collecting window. The quartz crystal oscillator gave no results.

In situ measurements include techniques based on: *optical detection*, which can determine shape, size distribution, concentration, refractive index, composition and/or velocity depending on technique and available complementary information; *settling detection*, which can determine mass flux; and *impact detection*, which can determine mass, velocity, momentum, and/or mass flux.

The optical detection techniques are generally considered suitable for grain monitoring and analysis. They are based on the detection of light scattered by particles, which are lighted with a high radiative source like a focused laser beam. The mathematical formulation of scattering problems will be dealt in Sect. 3.2.2. Optical detection instruments can be divided in *extractive* instruments and *non-extractive* instruments, if they do or do not extract the aerosol sample from the environment to focus it in a sensing region, respectively, and in *Single Particle Counters (SPCs)* and *Multiple Particle Counters (MPCs)*, if they perform single or ensemble particles detections, respectively.

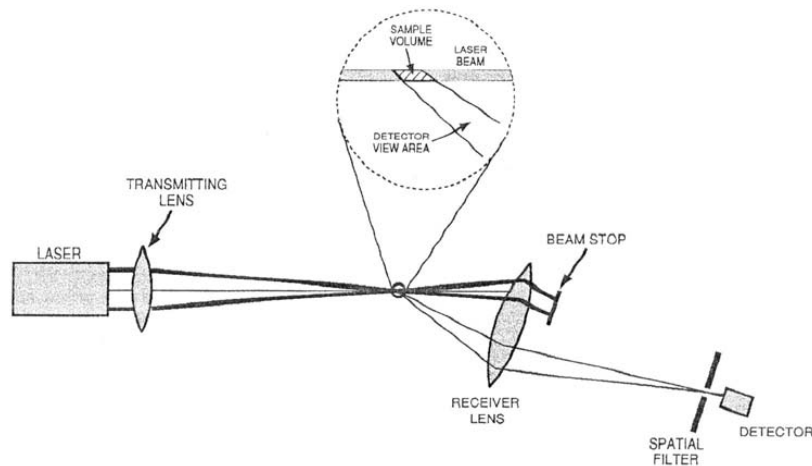


Fig. 3.4: Single Particle Counter (SPC) working principle (Rader, D.J., O'Hern, T.J., 2001).

In extractive instruments, an aerosol sample is withdrawn from its environment and transported through sample lines to a sensing region inside the instrument where the particle measurement is made. The sampling efficiency (Sect. 3.2.3) depends on the configuration of the device (e.g., orientation of the probe, size and shape of the inlet, velocity of the sample flow) and aerosol characteristics (e.g., velocity and direction of

the gas, particle size). Extractive techniques are widely used to determine size distribution, chemical composition, hygroscopicity and/or refractive index of particles. The non-extractive instruments permits to have real-time and direct measurements.

Single Particle Counters (SPCs) illuminate a particle crossing a sensing region with a well-focused light and collect scattered light with detectors (Fig. 3.4). SPCs derive the size of the particles (*optical equivalent diameter*) from the pulse height corresponding to the scattered light, while the size distribution of grains is derived by directing the pulse to a proper size channel, where the total count for each size range is made. In non-extractive SPCs, it is also possible to correlate data about scattered light and particles' properties such as to also have the particles velocity with a spatial resolution. SPCs are often based on the assumption that the scattered signal is monotonic with respect to the particle size, which, unfortunately, is not always true according to the Mie theory (Sect. 3.2.2). SPCs can suffer of coincidence errors since multiple measurements induce systematic errors on counting efficiency and resolution in case of high concentration, but become less efficient at too low concentrations. Moreover, since the single particle size is usually inferred from the amount of scattered light and scattering properties depend on particle shape (to assume spherical particles simplifies the problem, but this assumption is not rigorously correct), ambiguity can arise in assigning a size to each detected particle. Another problem derives from the laser beam non-uniformity in the sensing region, which causes a dependence of the scattered light on the crossing point of the particles.

An example of commercial non-extractive SPCs is the *Phase Doppler Anemometer (PDA)*. PDAs are able to perform simultaneous real-time and *in situ* measurements of velocity and size, mass flux, and/or concentration of spherical particles ($d_p \sim 0.5 \mu\text{m} - 10 \text{mm}$). In these devices, a particle scatters light from two incident laser beams; both scattered waves interfere in space and create a beat signal with a frequency (i.e., Doppler frequency), which is proportional to the velocity of the particle. Two detectors receive this signal with different phases, whose phase shift is proportional to the diameter of the particle. This implies that no calibration is required, e.g., the dependence on the velocity is linear if the detector is positioned such as one light scattering mode dominates, while simultaneous detection of different scattering modes of comparable intensity leads to non-linearity (Fig. 3.5). Nevertheless, PDAs need that particles are

spherical, morphologically and chemically homogeneous with known refractive index moving in a known continuum medium, and the phase shift is calculated in the range $(0, 2\pi)$, which defines and limits the distinguishable particle size range.

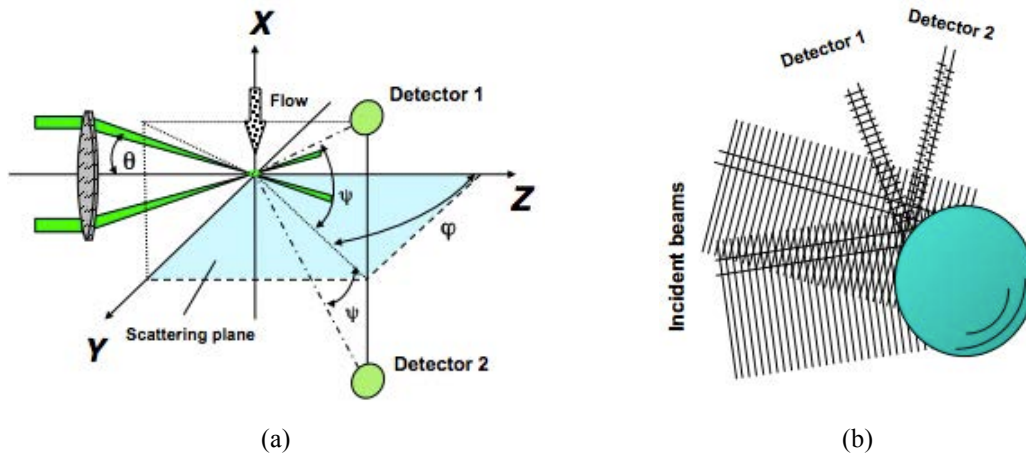


Fig. 3.5: Phase Doppler Anemometer (PDA) working principle (Dantec Dynamics). (a) θ is the beam intersection angle, φ is the scattering angle and ψ is the elevation angle. (b) A particle scatters light from two incident laser beams, which interfere and are received by two detectors.

Multiple Particle Counters (MPCs) are based on ensemble techniques and operate by illuminating a large number of particles. MPCs work by taking snapshots of the illuminated sampling volume and measuring the collected scattered light (number/volume). The main drawback of multiple particle instruments is the difficulty to obtain real-time read-out of the results. Typically, SPCs give particle concentration (number/volume), while MPCs give particle flux (mass/area/time). Ensemble techniques are quite suitable for high concentrations, but they are likely to fail for too low concentrations (Baron, P.A., Willeke, K., 2001).

Other particle detection techniques are based on impact on *sensing diaphragms*, which are connected to piezoelectric elements (Colangeli, L., Mazzotta Epifani, E., Palumbo, P., 2004; Nogami, K., et al., 2010). Particles momentum is measured by acoustic waves produced when the particle impacts on the diaphragms. The impacts are detected with piezoelectric sensors giving a voltage signal proportional to the deformation of the diaphragm. The signal is a function of the particle momentum and tensile and flexural elasticity of the system.

Other dust monitoring systems are based on the collection of dust on proper sensing surfaces and are able to measure particles mass flux. Deposited mass is usually measured by means of oscillating piezoelectric devices as *Quartz Microbalances*

(*QCM*) or *Tapered Element Oscillating Microbalance (TEOM)*. A QCM gives a frequency signal proportional to the dust mass deposited on the sensing surface. This technique requires calibration as the sensor response is sensitive to particle volume and mass. Moreover, as the sensor measures accumulated mass, saturation is reached (usually several orders of magnitude over the sensitivity) giving no response to further deposition (Landis, G.A., et al., 1996; Palomba, E., et al., 2002). In TEOMs the sensing element used is like a spring, whose oscillating frequency depends on the mass deposited on one end (Rupprecht, E., Meyer, M., Pataschnick, H., 1992). The active element is a tapered oscillating hollow tube made of elastic material; at the narrow end a filter is used to collect the material whose mass has to be determined. Frequency is measured by means of phototransistors observing a LED light source, which is chopped by TEOM's oscillations. The signal gives also the electrical feedback needed to maintain the tapered element in oscillation. As the oscillation frequency is about several hundreds of Hz, TEOMs usually do not have adherence problems with the collected sample; particles flaking-off from the collector filter usually occurs after the filter itself is clogged. Nevertheless, TEOMs can have more problems in space applications than QCMs due to thermal instability, need of a filter collector, saturation and difficulty in miniaturization.

Other techniques use particle charging, by discharge or photoelectric effect, to perform detection or selection in mass and/or dimension based on differential mobility or electrostatic precipitation.

MEDUSA and MicroMED that will be dealt in Chapter 4 and 5 respectively, are *in situ* instruments based on the optical detection principle. MEDUSA was conceived as a miniaturization and arrangement to the Martian boundary conditions of the GIADA instrument (Colangeli, L., et al., 2007). *GIADA (Grain Impact Analyzer and Dust Accumulator)* on board the Rosetta probe is an instrument to measure number, mass, momentum and velocity distribution of grains expelled from the nucleus of the 67P/Churyumov-Gerasimenko. GIADA is equipped with the module Grain Detection System (GDS) to perform *in situ* optical detection of the incoming dust grains without modifying their dynamical properties, measurement of their speed in the normal direction with respect to the sensing plane, and measurement of the particle scattering cross section, which contains information on dimension, optical properties and shape.

GDS looks for particles with size more than 10 μm , while smaller particles are detected by a cumulative mass deposition system based on quartz microbalances. Each grain entering the instrument crosses a light curtain generated by an illumination-collimator system, and is detected by two series of receivers (i.e., 4 photodetectors, each one equipped with a Winston cone to concentrate the radiation), which measure the time of flight across the curtain to derive grains velocity. Since the detected signals are related to the geometric cross-section and the scattering efficiency of the grains, data about particle size, composition and aggregation status can be retrieved by calibration. The optical detection guarantees that the dynamical properties of the grains will not be altered during detection.

3.2.2 Optical Detection Principle

In this section hints on the scattering theory on which the optical detection principle is based, are given. Scattering is the physical process where radiation is forced to deviate from a straight trajectory by one or more localized non-uniformities in the medium through which it passes. Light scattering by particles (i.e., size of 50 nm – 1 mm) are used to obtain information on concentration, size distribution and composition of the particles in several fields of Earth science (e.g., environment control, industrial processing, clean-room monitoring, cloud and fog formation, biological science) and can be applied for planetary exploration as seen in Sect. 3.2.1.

Light is an electromagnetic radiation involving synchronous oscillations of both electric and magnetic waves orthogonally each other propagating at a speed, which in vacuum is equal to $3 \cdot 10^8$ m/s. Light is fully described by wavelength, intensity, polarization and phase. The *wavelength* is the spatial distance over which the electric and magnetic waves repeat their oscillations. The *intensity* is the measure of the energy flux over the period of the electromagnetic wave, i.e., *irradiance*, which is the optical power per unit area. The *polarization* is defined as the orientation of the oscillation of the electric field orthogonally to the direction of propagation of the electromagnetic wave. The *phase* is the fraction of the electric and magnetic field that has elapsed relatively to an arbitrary point.

A light beam, which propagates through a medium where particles are dispersed, interacts with them. The incident radiation on a particle is partly diffracted, reflected,

refracted, and/or absorbed, which generate a characteristic pattern of irradiation depending on particle geometric and optical properties and incident light properties (Fig. 3.6). *Diffraction* is the bending of the waves direction around a relatively small obstacles and/or spreading out of the waves past relatively small openings, where “relatively small” means with respect to the light wavelength. *Reflection* is a change in direction of a wave at an interface between two different media so that wave returns diffusively towards the medium from which it originated. *Refraction* is the change in direction of a wave due to a change in its speed when passing from a medium to another. The *scattering angle* (θ) is the angular coordinate to describe the light scattered field by a single particle measured from the incident light beam direction: *forward scattering* is the scattering for $\theta \approx 0^\circ$; *backward scattering* is the scattering for $\theta \approx 180^\circ$.

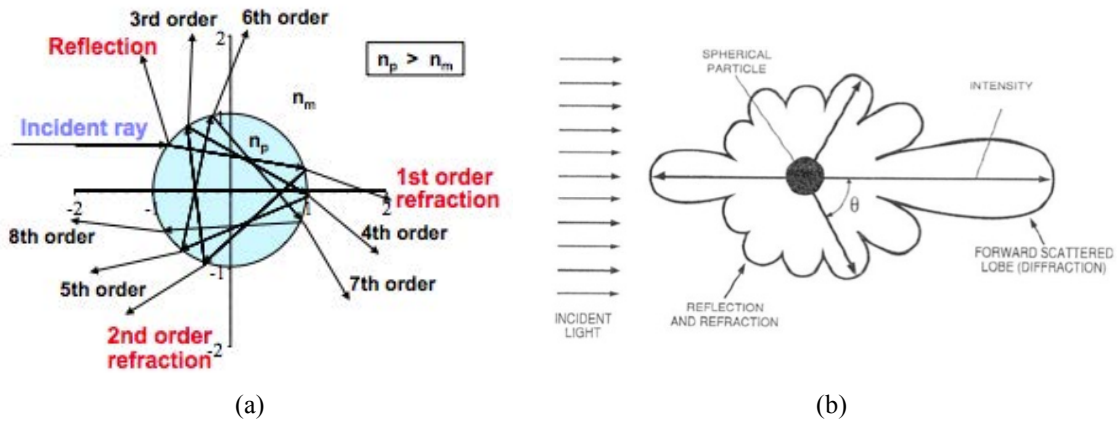


Fig. 3.6: (a) Light scattering by a particle. (b) Irradiation pattern (Rader, D.J., O’Hern, T.J., 2001).

The light scattered field by a particle depends on: particle size (d_p), particle shape, particle orientation, particle complex refractive index (n), and wavelength (λ), intensity (I_0), polarization and phase of the incident light. The *size parameter* is commonly used to model the scattering behaviour of a particle:

$$\alpha = \pi \frac{d_p}{\lambda} \quad (3.103)$$

The *complex refractive index* ($n = n_r - in_i$) is a measure of electromagnetic propagation in a material, whose real part (n_r) indicates the phase speed and is the ratio of the speed of light in vacuum to that in the material, and the imaginary part (n_i) is the amount of the absorption due to the material crossing.

The probability of light to be scattered by a particle is expressed with the *differential cross section* ($d\sigma/d\Omega$), i.e., the hypothetical scattering area per unit solid angle:

$$\frac{d\sigma}{d\Omega} = \frac{\frac{\Phi_s}{\Phi_i} \Delta S}{\Delta\Omega} \quad (3.104)$$

where Φ_s and Φ_i are the scattered and incident flux, respectively, ΔS is the elementary surface, $\Delta\Omega$ is the elementary solid angle. The *integral cross section* (σ) is, then, defined as:

$$\sigma = \int \frac{d\sigma}{d\Omega} d\Omega \quad (3.105)$$

The *Mie theory* (also called *Lorenz-Mie theory* or *Lorenz-Mie-Debye theory, 1908*) is a rigorous analytical solution of the Maxwell's equations for the scattering of electromagnetic radiation from a spherical, homogeneous, isotropic and non-magnetic particle of any diameter in a non-absorbing medium (Barber, P.W., Hill, S.C., 1990; Bohren, C.F., Huffman, D.R., 1998). Due to the symmetry, the problem of the scattering by spherical particles was solved in spherical coordinates and the solution was expressed as the superposition of spherical waves with boundary conditions defined on the surface of the spherical scattering particles to obtain the coefficients of the analytical solution. According to the Mie theory, the scattered irradiance (I_s) of a polarized beam of incident irradiance I_0 on a spherical particle in the perpendicular (I_{s1}) and parallel planes (I_{s2}) are, respectively:

$$I_{s1} = I_0 \frac{\lambda^2}{4\pi^2 r^2} i_1 = I_0 \frac{\lambda^2}{4\pi^2 r^2} \left| \sum_{k=1}^{\infty} \frac{2k+1}{k(k+1)} [a_k \pi_k \cos\theta + b_k \tau_k \cos\theta] \right|^2 \quad (3.106)$$

$$I_{s2} = I_0 \frac{\lambda^2}{4\pi^2 r^2} i_2 = I_0 \frac{\lambda^2}{4\pi^2 r^2} \left| \sum_{k=1}^{\infty} \frac{2k+1}{k(k+1)} [b_k \pi_k \cos\theta + a_k \tau_k \cos\theta] \right|^2 \quad (3.107)$$

where r is the distance from the scatterer, π_k and τ_k are parameters defined by the Legendre polynomials $P_k^l(\cos\theta)$:

$$\pi_k = \frac{1}{\sin\theta} P_k^l(\cos\theta) \quad (3.108)$$

$$\tau_k = \frac{d}{d\theta} P_k^l(\cos\theta) \quad (3.109)$$

$$P_k^l(\cos\theta) = (-1)^{k+l} \frac{(k+l)!}{(k-l)!} \frac{(1-\cos^2\theta)^{-l/2}}{2^k k!} \frac{d^{k-l}}{d\cos^{k-l}\theta} (1-\cos^2\theta)^k \quad (3.110)$$

a_k and b_k are the electric and magnetic multipole coefficients of the scattered light calculated through the Riccati-Bessel functions ψ and ξ (Abramowitz, M., Stegun, I.A., 1972):

$$a_k = \frac{n\psi'_k(n\alpha)\psi'_k(\alpha) - \psi_k(\alpha)\psi'_k(n\alpha)}{n\psi_k(n\alpha)\xi'_k(\alpha) - \xi_k(\alpha)\psi'_k(n\alpha)} \quad (3.111)$$

$$b_k = \frac{\psi'_k(n\alpha)\psi'_k(\alpha) - n\psi_k(\alpha)\psi'_k(n\alpha)}{\psi_k(n\alpha)\xi'_k(\alpha) - n\xi_k(\alpha)\psi'_k(n\alpha)} \quad (3.112)$$

The Riccati-Bessel functions are the following:

$$\psi_k(x) = \sqrt{\frac{\pi x}{2}} J_{k+1/2}(x) \quad (3.113)$$

$$\xi_k(x) = -\sqrt{\frac{\pi x}{2}} Y_{k+1/2}(x) \quad (3.114)$$

where J_k and Y_k are the spherical Bessel functions of the first and second kind, respectively:

$$J_k(x) = \frac{1}{2\pi i} \oint e^{(x/2)(t-1/t)} x^{-k-1} dt \quad (3.115)$$

$$Y_k(x) = \frac{J_k(x)\cos(k\pi) - J_{-k}(x)}{\sin(k\pi)} \quad (3.116)$$

For unpolarized beam, the scattered irradiance is given by:

$$I_s = I_0 \frac{\lambda^2}{4\pi^2 r^2} \frac{i_1 + i_2}{2} \quad (3.117)$$

The dimensionless response function ($F(\alpha, n, \theta)$) represent the effective scattering cross section normalized by λ^2 and is obtained by integrating the Eq. (3.106), (3.107), and/or (3.117) over the solid angle Ω :

$$F(\alpha, n, \theta) = \int_{\Omega} \left(\frac{i_1 + i_2}{2} \right) d\Omega \quad (3.118)$$

A complete solution of the light-grain interaction problem goes beyond this treatment. Scattering problems are usually solved to determine the scattered irradiance pattern ($I_s(\theta)$) with suitable models depending on the size parameter (α):

- $\alpha \ll 1$: *Rayleigh Scattering* \rightarrow $I_s \propto d_p^6$
- $\alpha \approx 1$: *Mie Scattering* \rightarrow $I_s = f(d_p)$

- $\alpha \gg 1$: *Geometric Optics Approximation (GOA)* $\rightarrow I_s \propto d_p^2$

When $\alpha \ll 1$, light scattering is described in relatively simple terms by the Rayleigh theory that implies the scattered light is proportional to the 6th power of the particle size, which make severe requirements on the dynamics of the photodetectors used in instruments to measure relatively wide ranges of particles size. The amount of Rayleigh scattering is given by:

$$I = I_0 \frac{1 + \cos^2(\theta)}{2r^2} \left(\frac{2\pi}{\lambda} \right)^4 \left(\frac{n^2 - 1}{n^2 + 2} \right) \left(\frac{d_p}{2} \right)^6 \quad (3.119)$$

where I_0 is the incident light, r is the distance between the light source and the particle, θ is the scattering angle, and n is the particle refractive index.

When $\alpha \gg 1$, light scattering can be analysed by the Geometric Optics Approximation (GOA), which traces diffracted, reflected and refracted rays of light through the particle, which implies the scattered light is proportional to the 2nd power of the particle size. According to GOA, the incident plane wave can be represented as a collection of independent parallel rays (*Snell law* and *Fresnel's equations*). The scattered light (I_s) from a monochromatic incident beam on a spherical particle is simplified as the linear superposition of three terms: diffraction ($I_0(\theta, \alpha)$), reflection ($I_1(\theta, n)$) and refraction ($I_2(\theta, n)$).

$$I_s(\theta, \alpha, n) = I_0(\theta, \alpha) + I_1(\theta, n) + I_2(\theta, n) \quad (3.120)$$

Therefore, the variables of the problem are θ , α , and n . The influence of these terms depends on the scattering angle θ as inferred by the width of the scattering lobes:

$$\text{Diffraction } I_0(\theta, \alpha) \quad \theta < \theta_{\min} = \sin^{-1} \left(\frac{5\pi}{4\alpha} \right) \quad (3.121)$$

$$\text{Reflection } I_1(\theta, n) \quad 0^\circ < \theta_{\min} < 180^\circ \quad (3.122)$$

$$\text{Refraction } I_2(\theta, n) \quad \theta < \theta_{\max} = 2 \cos^{-1} \left(\frac{1}{n} \right) \quad (3.123)$$

Eq. (3.121) shows that diffraction is mainly relevant in the forward direction. Moreover, in the forward direction light scattered depends more on α than on n , while, conversely, scattered light in the backward direction depends more on n than on α . This is due to the fact that diffraction, dependent on α , irradiates the most energy in the forward direction,

and reflection and slightly refraction, dependent on n , irradiate the most energy in the backward direction.

Between the extreme cases of the Rayleigh scattering and GOA ($\alpha \approx 1$), i.e., when particle size and wavelength are of the same order of magnitude, the light scattering falls in the Mie scattering regime, where there is a strong interaction between the particle and incident beam, which makes a complex relationship between the scattered light and the particle size. For example, a typical phenomenon that affect Mie scattering is the non-monotonic trend of the scattered irradiance with respect to particle size (Sect. 4.5.2). Both Mie and Rayleigh theories consider elastic scattering processes, in which the energy and wavelength of the light is not substantially changed. However, electromagnetic radiation scattered by moving particles undergo a Doppler shift, which can be detected and used to measure the velocity of the scattering centers as performed by LIDAR and radar techniques.

The instruments for aerosol measurements based on the optical detection principle typically work in the GOA regime ($\alpha \gg 1$), for which light scattering dependency on size of the particles is quite easy. They collect the scattered light usually with photodiodes or Charge-Coupled Devices (CCD) along one or more directions with certain angular amplitudes ($\theta, \theta + \Delta\theta$) depending on technique, complexity of the device, objectives of the measurement, and measurement accuracy. For example, as mentioned above, the forward direction is preferable to infer the particle size, and the backward direction is preferable to infer the refractive index. Finally, light scattered captured normally, at $\theta = 90^\circ$, is also largely used as affected by less background noise as generally minima scattered light occur at $\theta = 90^\circ - 130^\circ$.

Unfortunately, the Mie theory can solve analytically only the ideal case of spherical particles, and, with some modifications, can be applied to spheroidal and ellipsoidal particles, but dust grains can have shapes significantly different than spheres, so making the scattering analysis very hard. The light scattering behaviour of non-spherical particles can be either computed theoretically or measured experimentally. Theoretical models, i.e., analytical methods, surface-based methods, and volume-based methods, can be used to study scattering characteristics, but, often, accurate determinations for realistic irregular particles are computationally very expensive. Experimental measurements using visible or infrared light can deal with those particles, but often the

experimental apparatus is complicate and not all the scattering properties can be easily measured. However, scattering by non-spherical particles is similar to scattering by area-equivalent spherical particles near the forward direction, but differences between them occur increasing the scattering angle; in particular, scattering patterns by non-spherical particles are azimuthally dependent as they tend to be flatter than those of spherical particles at angles greater than about 90°.

Light scattering is typically performed using a laser as light source. Commonly, laser beams have a TEM₀₀ (Transverse ElectroMagnetic oscillation, radial mode 0, angular mode 0) Gaussian profile, which is expressed by:

$$I(r, z) = \frac{2P}{\pi w^2} e^{\left[-2\left(\frac{r}{w}\right)^2\right]} \quad (3.124)$$

$$w(z) = w_0 \left[1 + \left(\lambda z / \pi w_0^2 \right)^2 \right]^{1/2} \quad (3.125)$$

$$w_0 = \frac{\lambda}{\pi \theta_b} \quad (3.126)$$

where P is the beam power, r is the radial coordinate, z is the axial coordinate, $w(z)$ is the beam radius at $1/e^2$ intensity, w_0 is the beam radius at waist ($z = 0$), and θ_b is the far field half-angle of convergence. This implies that in order to have a uniformly illuminated sensing region avoiding dependence on particle trajectories, a laser beam need to be collimated from the source to the sensing region with optical lenses.

The physical properties of the particles dispersed in a fluid depend on many factors. Distribution functions based on particle properties are typically introduced to describe the particles' behaviour. If $\Delta N_p(r_p, \beta_i)$ is the number of particles per unit volume with size in the range $(r_p, r_p + \Delta r_p)$, and eventual other properties in the range $(\beta_i, \beta_i + \Delta \beta_i)$, a distribution function $f(r_p, \beta_i)$ is defined as:

$$f(r_p, \beta_i) = \lim_{\substack{\Delta r_p \rightarrow 0 \\ \Delta \beta_i \rightarrow 0}} \frac{\Delta N_p}{\Delta r_p \Delta \beta_i} \quad (3.127)$$

Since, typically, data about dust particle distribution are obtained by scattering measurements, the size distribution function are expressed through optical parameters.

$$\text{Particle number density} \quad N_p = \int_0^{\infty} f(r_p) dr_p \quad (3.128)$$

$$\text{Mean radius for scattering} \quad r_s = \frac{\int_0^{\infty} r_p \pi r_p^2 Q_s f(r_p) dr_p}{\int_0^{\infty} \pi r_p^2 Q_s f(r_p) dr_p} \quad (3.129)$$

$$\text{Effective radius} \quad r_{eff} = \frac{\int_0^{\infty} r_p \pi r_p^2 f(r_p) dr_p}{\int_0^{\infty} \pi r_p^2 f(r_p) dr_p} = \frac{1}{G} \int_0^{\infty} \pi r_p^3 f(r_p) dr_p \quad (3.130)$$

$$\text{Effective variance} \quad v_{eff} = \frac{1}{Gr_{eff}^2} \int_0^{\infty} (r_p - r_{eff})^2 \pi r_p^2 f(r_p) dr_p \quad (3.131)$$

$$\text{Effective skewness} \quad s_{eff} = \frac{1}{Gr_{eff}^3 v_{eff}^{2/3}} \int_0^{\infty} (r_p - r_{eff})^3 \pi r_p^2 f(r_p) dr_p \quad (3.132)$$

The *mean radius for scattering* (r_s) is defined through the cross-section $\sigma_s = \pi r_p^2 Q_s$, where Q_s is the scattering efficiency (Eq. (3.129)). If $r_s \gg \lambda$, $Q_s \approx 1$ and Eq. (3.129) can be simplified into Eq. (3.130), which gives the *effective radius* (r_{eff}), where G is the geometric cross-sectional area of particles per unit volume. Eq. (3.131) gives the *effective variance* (v_{eff}), which is largely used to fit data in the gamma and gamma-modified functions, while Eq. (3.132) gives the 3rd order moment of the distribution function $f(r_p)$, i.e., the *effective skewness* (s_{eff}).

The most used distribution functions are: Junge; log-normal; gamma; gamma-modified. In particular, the gamma and gamma-modified have been largely used to model and fit data about dust size distribution on Mars (Sect. 1.2.3).

The *Junge distribution* is given by:

$$f(r_p) = A(2r_p)^c \quad (3.133)$$

where A is a constant and c is a parameter typically equal to 4.

The *log-normal distribution* is given by:

$$f(r_p) = \frac{N_p}{(2\pi)^{1/2} \sigma_g r_p} e^{-\left(\frac{\ln r_p - \ln r_g}{2\sigma_g^2}\right)^2} \quad (3.134)$$

$$\ln r_g = \int_0^{\infty} \ln r_p f(r_p) dr_p \quad (3.135)$$

$$\sigma_g^2 = \int_0^{\infty} (\ln r_p - \ln r_g)^2 f(r_p) dr_p \quad (3.136)$$

where r_g is the *mean geometric radius*, which in the log-normal distribution is also equal to the *median radius*, i.e., the radius that equally divides the sample distribution, and σ_g is the standard deviation.

The *gamma distribution* is given by:

$$f(r_p) = \frac{N_p (r_{eff} v_{eff})^{(2v_{eff}-1)/v_{eff}}}{\Gamma[(1-2v_{eff})/v_{eff}]} r_p^{(1-3v_{eff})/v_{eff}} e^{-r_p/(r_{eff} v_{eff})} \quad (3.137)$$

$$\Gamma(x) = \int_0^{\infty} z^{x-1} e^{-z} dz \quad (3.138)$$

$$r_m = r_{eff} (1 - 2v_{eff}) \quad (3.139)$$

$$\sigma = r_{eff}^2 v_{eff} (1 - 2v_{eff}) \quad (3.140)$$

where $f(r_p)$ is based on the gamma function $\Gamma(x)$, being known the relationship between the mean radius (r_m) and standard deviation (σ) with r_{eff} and v_{eff} .

The *gamma-modified distribution* is given by:

$$f(r_p) = N_p c_2 \left(\frac{c_1}{c_2}\right)^{c_2} \Gamma^{-1}\left(\frac{c_1+1}{c_2}\right) r_{md}^{-(c_1+1)} r_p^{c_1} e^{\frac{c_1}{c_2} \left(\frac{r}{r_{md}}\right)^{c_2}} \quad (3.141)$$

$$r_m = r_{md} \left(\frac{c_2}{c_1}\right)^{\frac{1}{c_2}} \frac{\Gamma\left(\frac{c_1+2}{c_2}\right)}{\Gamma\left(\frac{c_1+1}{c_2}\right)} \quad (3.142)$$

$$\sigma^2 = r_{md}^2 \left(\frac{c_2}{c_1}\right)^{\frac{2}{c_2}} \frac{\Gamma\left(\frac{c_1+3}{c_2}\right) \Gamma\left(\frac{c_1+1}{c_2}\right) - \Gamma\left(\frac{c_1+2}{c_2}\right)^2}{\left(\Gamma\left(\frac{c_1+1}{c_2}\right)\right)^2} \quad (3.143)$$

$$r_{eff} = r_{md} \left(\frac{c_2}{c_1} \right)^{\frac{1}{c_2}} \frac{\Gamma\left(\frac{c_1+4}{c_2}\right)}{\Gamma\left(\frac{c_1+3}{c_2}\right)} \quad (3.144)$$

$$v_{eff} = \frac{\Gamma\left(\frac{c_1+5}{c_2}\right) \Gamma\left(\frac{c_1+3}{c_2}\right)}{\left(\Gamma\left(\frac{c_1+4}{c_2}\right)\right)^2} - 1 \quad (3.145)$$

that is obtained from the gamma distribution with some modifications introduced by the coefficients c_1 and c_2 , calculated from r_{eff} , v_{eff} and the *modal particle radius* (r_{md}), which is the radius corresponding to the maximum of the sample distribution.

3.2.3 Aerosol Sampling and Transport

An aerosol sampling system generally consists of:

- A *sample inlet*, i.e., a nozzle to extract aerosol sample from the external environment;
- A *sample transport system*, i.e., a pipeline system to convey the aerosol sample to a sensing region or to a storage chamber;
- A *sample storage volume*, i.e., a collection container, optionally present, depending on measurement requirements.

The design of an inlet implies to define and/or know: velocity and direction of the gas flow; orientation of the aerosol sampling probe; velocity of the sample flow; particle size range. The design of both the inlet and the transport system has to minimize the loss of the sample particles keeping them intact to the region, where they should be examined. The capacity of the instrument to perform aerosol sampling is usually evaluated through efficiency parameters for each phase of the sampling process.

The *aspiration efficiency* (η_{asp}) is defined as the concentration of the particles for a given size in the gas entering the inlet divided by their concentration in the ambient environment from which the sample is taken. The *transmission efficiency* (η_{trans}) is defined as the fraction of aspirated particles for a given size that are transmitted through the inlet to the rest of the sampling system. It is the product of the gravitational settling efficiency ($\eta_{trans, grav}$) and the inertial losses efficiency ($\eta_{trans, inert}$).

$$\eta_{trans} = \eta_{trans, grav} \eta_{trans, inert} \quad (3.146)$$

The *inlet efficiency* (η_{inlet}) is defined as the fraction of aerosol particles for a given size in the environment that are aspirated through the inlet plane and transmitted through the inlet into the sampling line. It is the product of the aspiration and transmission efficiency:

$$\eta_{inlet} = \eta_{asp} \eta_{trans} \quad (3.147)$$

The *transport efficiency* ($\eta_{flow\ element, mechanism}$) is defined as the fraction of particles for a given size entering a flow element that are not lost by a deposition mechanism during the transit through the flow element. The *total transport efficiency* ($\eta_{transport}$) is defined as the product of the transport efficiencies for each mechanism in each flow element of the sample transport system for a given particles size:

$$\eta_{transport} = \prod_{\substack{Flow \\ Elements}} \prod_{Mechanism} \eta_{flow\ element, mechanism} \quad (3.148)$$

Finally, the sampling efficiency (η_{sample}) is the product of the inlet and total transport efficiencies:

$$\eta_{sample} = \eta_{inlet} \eta_{transport} \quad (3.149)$$

Several empirical estimations of the aspiration (η_{asp}), transmission (η_{trans}), and transport efficiencies ($\eta_{transport}$), deduced for specific cases about terrestrial optical particle counters, are reported in Baron, A., Willeke, K., 2001.

The sampling processes can be classified with respect to velocity direction as: *isoaxial*, i.e., the direction of the sample flow is aligned with the gas flow; *anisoaxial*, i.e., the sample flow and gas flow directions are slanted by an angle (Fig. 3.7).

The sampling processes can be classified with respect to mean velocity module as: *isokinetic*, i.e., the sampling is isoaxial and the mean sample flow velocity through the face of the inlet is equal to the gas flow velocity; *super-isokinetic*, i.e., the sampling velocity is higher than the gas velocity; *sub-isokinetic*, i.e., the sampling velocity is lower than the gas velocity. The most efficient and representative aspiration processes occurs for isokinetic and isoaxial sampling.

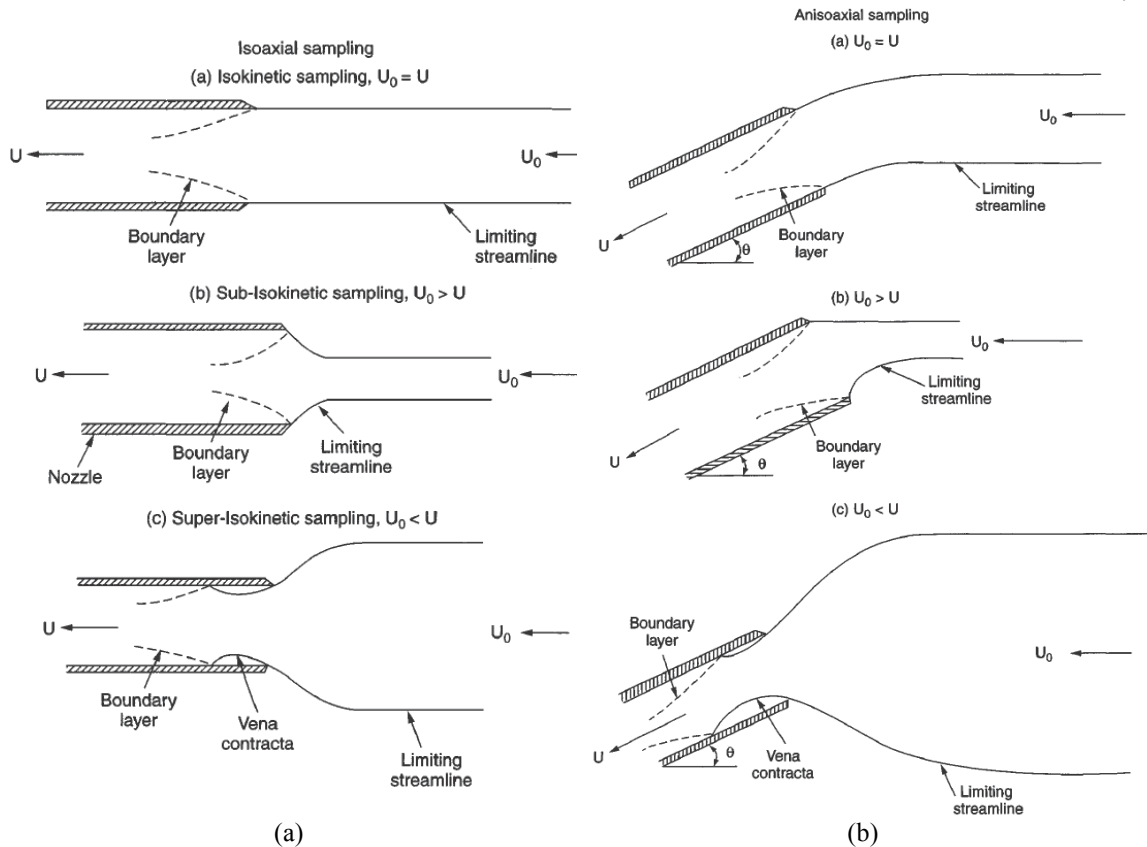


Fig. 3.7: Scheme of a thin walled nozzle: (a) Isoaxial sampling. (b) Anisoaxial sampling. (Baron, P.A., Willeke K., 2001).

Fig. 3.7 shows aspiration processes by a cylindrical nozzle for a subsonic flow. Due to the mass conservation of the fluid, which flows from the upstream environment to the nozzle of section A , i.e., the mass flow rate ($\dot{m} = \rho UA$) is constant, if the free stream velocity (U_0) is larger than the sampling velocity (U), the streamlines should diverge from up-stream to the nozzle entrance. Supposing ρ approximately constant for incompressible flows, the decrease of the velocity from U_0 to U implies that the asymptotic up-stream capture section is smaller than the nozzle section. In such case, the particles with sufficient inertia that lie outside the limiting streamline can cross the limiting streamline and are aspirated by the nozzle making an aspiration efficiency higher than 1. Conversely, if $U_0 < U$ the streamlines should converge from up-stream to the nozzle entrance, so the asymptotic up-stream capture section is larger than the nozzle section. In such case, particles with sufficient inertia that lie within the limiting streamline can cross the limiting streamline and are not aspirated by the nozzle making an aspiration efficiency lower than 1. The flow inside the nozzle also makes a boundary layer. *Boundary layer* is a zone in a fluid near walls where diffusive and convective

effects become of the same order of magnitude and is characterized by significant variations of the fluid dynamics variables; in a *laminar flow* the fluid flows in parallel layers without disruptions between them; in a *turbulent flow* the fluid is characterized by chaotic and stochastic fluctuations of the fluid dynamics variables. Moreover, in the case $U_0 < U$, fluid should accelerate outside the nozzle and rapidly decelerate when boundary layer begins, giving rise to local separations and recirculation (*vena contracta*, i.e., the region where the diameter of the stream is the least due to a flow constriction), which cause particles loss due to turbulent deposition.

Among the factors that can cause errors in particles sampling, we can quote: low aspiration and deposition in the sample inlet during extraction; deposition during transport through a sampling line or storage; high or low, and inhomogeneous ambient concentrations; agglomeration of particles during transport through the sampling line; evaporation and/or condensation of aerosol material during transport through the sampling line; re-entrainment of deposited aerosol material back into the sample flow; high local deposition causing flow restriction or plugging; inhomogeneous particle distributions in inlets and transport tubes.

The most important causes, which can determine particles losses are: gravitational settling; inertial impact on the inner walls of the nozzle; inertial deposition (e.g., impact of particles on the inside lip of the nozzle facing the free-stream velocity for anisoaxial sampling or deposition at bends and flow constrictions); free-stream turbulence; turbulent deposition (e.g., for super-isokinetic sampling in *vena contracta*); diffusional deposition; electrostatic deposition; thermophoretic deposition; diffusiophoretic deposition (Sect. 3.1.2).

Commonly, larger particles are more subjected to gravitational and inertial effects, while smaller particles are more subjected to diffusive effects. Therefore, the sampling gas velocity must be low enough so that sampled particles can accommodate themselves to the sampling gas flow within a distance comparable to the inlet diameter (*inertial condition*), and must be high enough so that sampled particles do not settle appreciably in the time that sampling occurs (*gravitational settling condition*). Davies, C.N., 1968 found an experimental rule for sampling in calm air ($U_0 \approx 0$) with a small tube according to the inertial and gravitational settling conditions (Eq. (3.150), (3.151)) (Davies, C.N., 1968); Agarwal, J.K., Liu, B.Y.H., 1980, found a rule valid for

$V_{ts}/U_s > 10^{-3}$ and $Stk_s > 1$ (Eq. (3.152)), with a sampling efficiency of 90%, by correlating theoretical predictions based on Navier-Stokes solutions for the field around an upward-facing inlet and mathematical and experimental determination of the particles trajectories:

Inertial condition

$$(Davies, C.N., 1968) \quad Stk_s = \frac{t_r U_s}{D} \leq 0.016 \quad (3.150)$$

Gravitational settling condition

$$(Davies, C.N., 1968) \quad \frac{V_{ts}}{U_s} \leq 0.04 \quad (3.151)$$

Inertial and gravitational settling condition

$$(Agarwal, J.K., Liu, B.Y.H., 1980) \quad Stk_s \frac{V_{ts}}{U_s} \leq 0.5 \quad (3.152)$$

where Stk is the Stokes number (Eq. (3.83)), U_0 is the free-stream velocity, U_s is the sampling velocity, V_{ts} is the terminal velocity (Eq. (3.80)), t_r is the relaxation time (Eq. (3.81)), and D is the duct diameter.

Typically devices for aerosol monitoring work at flow regime with low Mach number, so the flow can be considered *incompressible*, i.e., fluid density is approximately uniform in all the regions of the instrument and depends only on atmospheric gas, pressure and temperature, but not on kinematics quantities as the flow rate of the pump and fluid velocity, which implies that a constant mass flow rate across a section also results in a constant volumetric flow rate. Supposing a device, which aspires aerosol portions at a constant volumetric flow rate Q , and analyzes scattering from particles with mean velocity U crossing a laser spot or beam with size Δs in a time interval Δt , the particle number density N_p can be valued with Eq. (3.153):

$$N_p = \frac{n_p}{\Delta V} = \frac{n_p}{\frac{\Delta V}{\Delta t} \Delta t} = \frac{n_p}{Q \Delta t} = \frac{n_p U}{Q \Delta s} \quad (3.153)$$

If N_p is valued for each size, the size distribution function can also be obtained.

The concepts discussed in this section will be taken into account to make evaluations of the performance of MEDUSA (Chapter 4) and define the design of MicroMED (Chapter 5) from a fluid dynamics point of view.

4 MEDUSA FOR THE EXOMARS LANDER

4.1 MEDUSA Concept

MEDUSA is the acronym for *Martian Environment Dust Systematic Analyzer*, which is an instrument for *in situ* measurement of dust grain size, size distribution, concentration, deposition, electrification and velocity, and water vapour abundance in the Martian atmosphere at ground level.

The MEDUSA instrument was designed by the *Laboratory of Cosmic Physics and Planetology* at *INAF - Astronomical Observatory of Capodimonte*, Naples, Italy, and its development funded by *European Space Agency (ESA)* and *Agenzia Spaziale Italiana (ASI)* in different project phases. MEDUSA also implied contributions by international partners: the *Dust Deposition and Electrification Stage (DDES)* subsystem by *Innoware* and *Aarhus University*, Denmark, and the *Main Electronics (ME)*, by *Instituto de Astrofísica de Andalucía*, Granada, Spain. MEDUSA inherited the knowhow and experience acquired during the development of the *GIADA* instrument (Sect. 3.2.1).

The MEDUSA concept was developed within the *ESA ExoMars Programme*. It was initially conceived to be accommodated in the *Pasteur Payload (PPL)* on the *ExoMars Rover*, and, then, relocated in the *Humboldt Payload (HPL)* on the *ExoMars lander*, which were scheduled for launch in 2016. In 2009, the MEDUSA instrument successfully passed the *ESA Preliminary Design Review (PDR)* with *Technology Readiness Level (TRL) 5.3*.

4.2 MEDUSA Scientific Objectives and Measurements

The scientific objectives of MEDUSA are part of the more general goals of the *ExoMars Programme* (Sect. 2). In fact, the information that can be obtained by MEDUSA over different time spans (days, seasons, years) is important for more general scientific objectives:

- Exobiology on Mars:
 - by determining the present climatic conditions at Mars surface;
 - by searching for water;
 - by determining the physical parameters impacting on presence of life on Mars;

- by deriving information about past history of Mars climate;
- by providing ground-truth for validation of data coming from orbiter observations.
- Operations on Mars:
 - by evaluating hazardous conditions due to the Martian environment;
 - by placing constraints on operative conditions at Mars;
 - by supporting the definition of future human exploration of Mars.

MEDUSA contributes to these general objectives by performing *in situ* measurements to determine dust grains size and dust size distribution, abundance and electrification properties, which are mainly interesting to refine the dust cycle and climatic models, to detect possible traces of water, and to evaluate local wind speed. The scientific objectives are accomplished with different kinds of measurements performed by the subsystems of the MEDUSA suite. The physical quantities measured by the MEDUSA subsystems are:

- *Atmospheric dust grains size and dust size distribution*

The dust particle size is the equivalent radius or diameter (Sect. 3.2) measured in the range of $d_p = 0.2\text{-}20\ \mu\text{m}$ via light scattering analysis, and in the range of $d_p = 0.05\text{-}0.4\ \mu\text{m}$ via accumulation on a microbalance. The dust size distribution is the fractional occurrence of the particles with respect to their size and is obtained by counting the grains analysed in different size bins.

- *Atmospheric dust particle number density*

The atmospheric dust particle number density is the number of particles per unit of fluid volume. It is derived from the previous measurement since the volume sampled by the system is known.

- *Atmospheric water vapour abundance*

The atmospheric water vapour abundance is the mass or volume fraction of water in the atmospheric fluid. MEDUSA is able to measure the water vapour partial pressure by the detection of water condensation on the surface of a thermally controlled device, i.e., a microbalance (Sect. 4.3). The relative humidity can be also estimated using the values of the atmospheric pressure and temperature, which are measured by other sensors, e.g.,

AEP (Advanced Environmental Package) in HPL. The measurement has sensitivity better than 10 ppm.

- *Dust deposition/removal rate*

The dust deposition/removal rate is the dust accumulation/removal with respect to time. It is measured by the detection of scattered light from dust accumulating on a transparent surface. It has a sensitivity better than 0.1%/sol.

- *Electrification of suspended dust particles*

The electrification of suspended dust particles is the amount of the net electrical charge stored in the particles. It is measurable in the range $\pm 10^3$ - 10^6 electrons/grain by applying electric fields to a dust accumulation surface.

- *Dust velocity (horizontal component and direction)*

By measuring light scattered by suspended grains, velocity and, therefore, wind speed/direction can be quantified. Dust velocity is measured in a horizontal plane with a sensitivity of less than 20%.

4.3 MEDUSA System

The MEDUSA system is a suite of sensors. It consists in a dust collector (Main Body, Fig. 4.1) and two separate stages for water vapour monitoring (MBwv, Fig. 4.5) and for dust deposition and electrification measurements (DDES, Fig. 4.6).

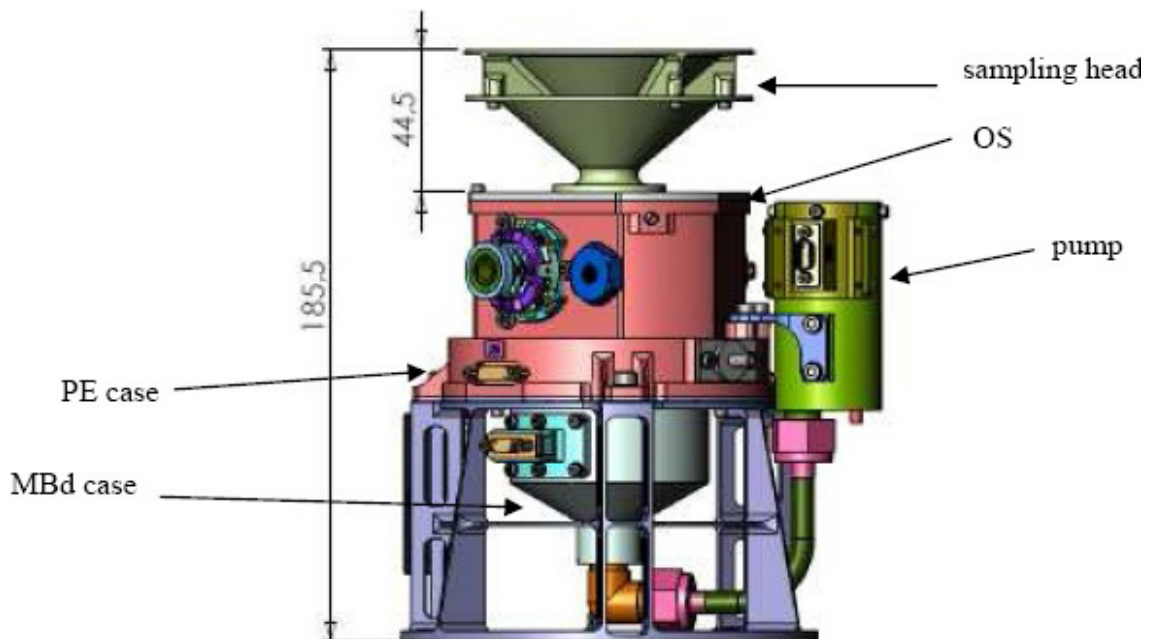


Fig. 4.1: MEDUSA Main Body concept (2009).

The configuration of MEDUSA is the result of a development in order to make the device compliant with the requirements of the ESA ExoMars HPL, i.e., mass, accommodation, power, thermal and mechanical interfaces requirements, which depend on the host lander resources and on the Martian boundary conditions. Two breadboards were designed and manufactured (Phase B).

The first MEDUSA breadboard was designed, manufactured and tested in 2006-2007 in order to verify the operating principle of the instrument. The second MEDUSA breadboard (Fig. 4.2) was designed, manufactured and analyzed in 2008-2010. This breadboard implemented the last configuration of the ExoMars HPL, before the mission was redesigned in 2009. This thesis is exclusively focused on the second MEDUSA breadboard.

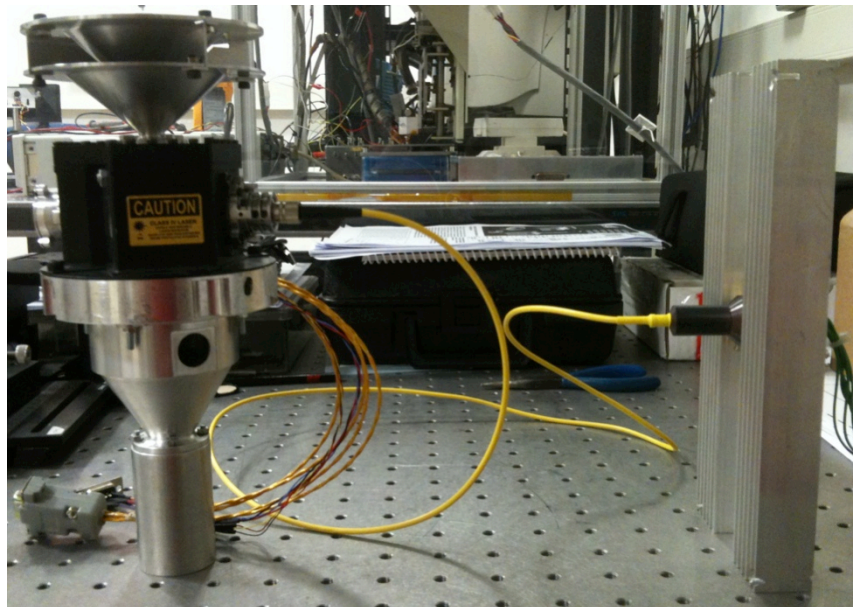


Fig. 4.2: The MEDUSA breadboard on a test bench.

The MEDUSA *Main Body* (Fig. 4.1) includes the following components:

- *Sampling Head*
- *Optical Stage (OS):*
 - *Inlet duct and outlet duct*
 - *Sampling Volume (SV)*
 - *Anamorphic objectives and baffles*
 - *Forward (FW) and backward (BW) collecting mirrors*

- *Forward (FW) and backward (BW) detectors*
- *Light trap*
- *Proximity Electronics (PE)*
- *Pump*
- *Microbalance for dust (MBd)*

The *Sampling Head* (Fig. 4.3) is an Al 6082-T6 inlet, shaped as a subsonic nozzle through which atmospheric aerosol flows to the Optical Stage, and then to the Microbalance for dust collection. The inlet has a cylindrical symmetry and is mechanically mounted on the upper part of the OS. Moreover, the upper surface of the inlet is a radiative sink to the sky temperature and a thermal flux interface.

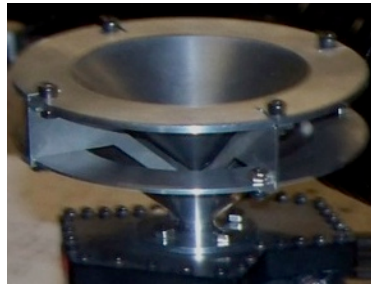


Fig. 4.3: MEDUSA Sampling Head.

The *Optical Stage (OS)* is a box including optical and electronic elements to perform scattering analysis. The gas, coming from the Sampling Head, flows through the OS via an *inlet duct*, and, then, reaches a sensing region (*Sampling Volume*). A laser beam, generated by a laser diode accommodated outside the OS in the *Laser Diode Assembly (LDA)*, is conveyed to the Sampling Volume via an optical fiber and collimated with anamorphic objectives. The laser beam lights dust particles dispersed in the aerosol, which flows through the Sampling Volume. Two *photodetectors* pick up forward and backward dust scattering signals, properly concentrated by collecting mirrors. The acquired signals are conditioned by the *Proximity Electronics (PE)*. The detection process is optimized with small and thin baffles to reduce stray light in the OS. Particles geometry and optical properties are obtained by coupling the forward and backward scattering signals according to the Mie theory (Sect. 3.2.2). The particles, after crossing the Sampling Volume, exit from the OS through an *outlet duct*, then reach the microbalance sensor for dust collection and measurement.

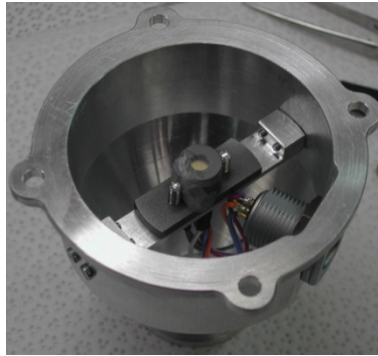


Fig. 4.4: The Microbalance for dust (MBd) MK21 QCM in the dust collection stage case.

The *Microbalance for dust (MBd)* is a Quartz Crystal Microbalance (QCM), model MK21 supplied by QCM Research (Sect. 3.2.1). For the breadboard, a commercial device with identical characteristics, has been used, supplied by Novaetech S.r.l.. It is accommodated in the dust collection stage placed under the OS (Fig. 4.1 and Fig. 4.4). The MBd measures the amount of deposited dust mass versus time. The measurement is performed by comparing the shift of the crystal oscillation frequency of the MBd, due to the accumulation of dust over its sensitive surface with respect to a reference crystal that is subjected to the same temperature and pressure conditions, but not exposed to dust fluxes. The MBd has a nominal oscillation frequency of 1-2 kHz. The MBd sensitivity is $5.09 \cdot 10^8$ Hz/g/cm², which allows to measure the mass accumulation up to a maximum of $1.84 \cdot 10^8$ particles with size of 1 μ m and density of $3 \cdot 10^3$ kg/m³.

The *pump* is placed at the end of the acquisition chain (OS+MBd), through a suitable pipeline, to guarantee gas and dust flux through the system contrasting particles dispersion, adhesion and gravitational settling (Fig. 4.1). The design pump volumetric flow rate is 6 l/min. This value was chosen in order to have more than 10^4 particles, dispersed in a typical Martian dusty scenario (Sect. 1.2.3), crossing the Sampling Volume with negligible coincidence events, supposing that MEDUSA works for 100 s in each operative run (Sect. 4.3.2.4). The volume of the aerosol sampled as a result of the pump aspiration is proportional to the time during which the pump is turned on, as the volumetric flow rate is quite stable and constant after a short initial unsteady phase, which is less than 10 s.

The *Microbalance for water vapour (MBwv)* is a small device, conceptually similar to the MBd (QCM MK20), integrated with a Peltier element. The Peltier element is able to thermally control the sensor oscillator, while a heat sink dissipates the heat flux

generated during the sensor cooling. The crystal sensor is cooled under the frost point (i.e., the temperature at which atmospheric water vapour condenses into ice at constant atmospheric pressure) by the Peltier element and the deposition curve is monitored in order to derive the condensation behaviour in the Mars atmosphere. The temperature at which the MBwv detects the frosting signal associated to the phase change allows the determination of the value of the atmospheric water vapour partial pressure and, hence, the relative humidity. The MBwv works independently by the Main Body and MBd. It is protected with a case to avoid dust contamination and direct solar irradiation (Fig. 4.5). The configuration of the aperture allows free access to the environmental water vapour, but is placed so that gravity deposition of dust is not permitted.

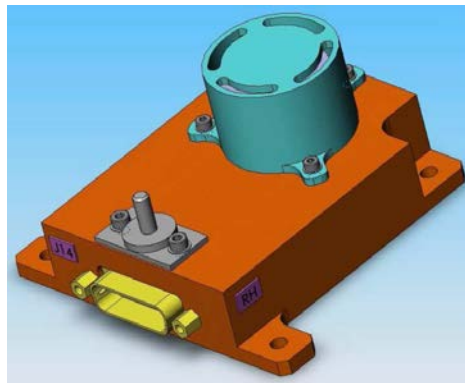


Fig. 4.5: The Microbalance for water vapour (MBwv) subsystem 3D model.

The *Dust Deposition and Electrification Stage (DDES)* was designed at the Mars Simulation Laboratory of the University of Aarhus, Denmark (Fig. 4.6). It works independently from the Main Body, MBd, and MBwv. DDES is an optoelectronic sensor, which uses laser scattering in order to determine the deposition of dust upon its sensitive surface and measure the velocity of individual dust grains suspended in the atmosphere. The wind speed measurement (2-20 m/s) is performed by calculating the time of flight of the flowing dust grains passing through a laser pattern with three lines. Light scattered by the grains is collected onto a detector using a Fresnel lens. The detected light signal reproduces the light pattern (i.e., three peaks, the time separation of which quantifies the wind speed in a particular direction). By using several laser patterns with differing orientation, the wind speed and direction can be extracted. The dust grain detection rate can be used as a quantification of the suspended dust concentration. In addition all the six laser beams passing through the surface of the instrument allow light scattered by deposited dust to be collected on a set of six

photodiodes giving a collective signal, which quantifies the amount of dust accumulated on different surface locations. The technique used for studying dust electrification consists in applying an electric field to some of these surfaces to collect electrified dust and, therefore, give a measurement of the degree and amount of electrification. Hence, dust grain electrification (i.e., the average charge per grain) can be quantified.

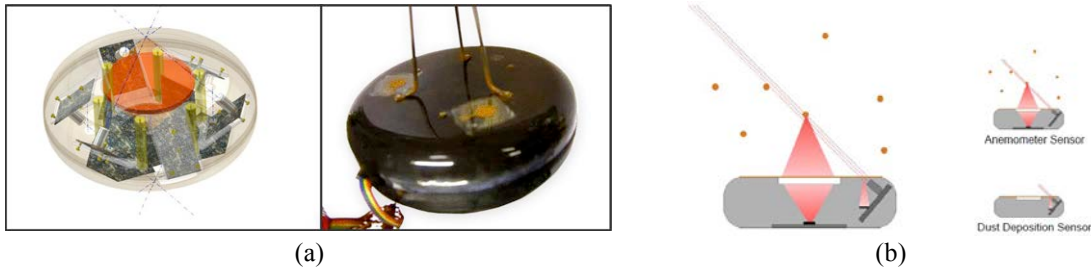


Fig. 4.6: (a) Dust Deposition and Electrification Stage (DDES) (120 mm diameter x 45 mm height). (b) DDES functioning scheme.

The *Main Electronics (ME)* is used to manage the power supply and data control process (Fig. 4.7). It was developed by IAA, Spain. The ME manages telemetry (TM) and telecommands (TM) between MEDUSA and the Descent Module (DM), and the communication protocol, TCs processing, operational timelines associated with TCs, power conditioning of all the sensing subsystems (PE, LDA, Peltier and pump), control signals generation for PEs, data reading from PEs, analog-to-digital (ADC) conversion, data processing to extract information and limit the data volume to be transmitted to ground, data organization in packets for transmission, data delivery to system, management of contingencies and appropriate reactions. The Main Body, MBwv and DDES are connected to the ME via harness and the optical fiber. The ME is placed in the Common Electronics Box in the lander. The ME consists of two boards, one for the Power Supply Unit (PSU) and another for Data Acquisition and Process Unit (DAPU). The boards are Eurocard (size 160 mm x 100 mm).

The work for this thesis on the MEDUSA system has been mainly concentrated on the analysis of the dynamic behavior of the particles sampled in the instrument, and of the functionality and performance of the optical detection system. Hence, only the subsystems relevant for these tasks (OS, LDA, and pump) will be discussed in more detail in the following sub-sections.

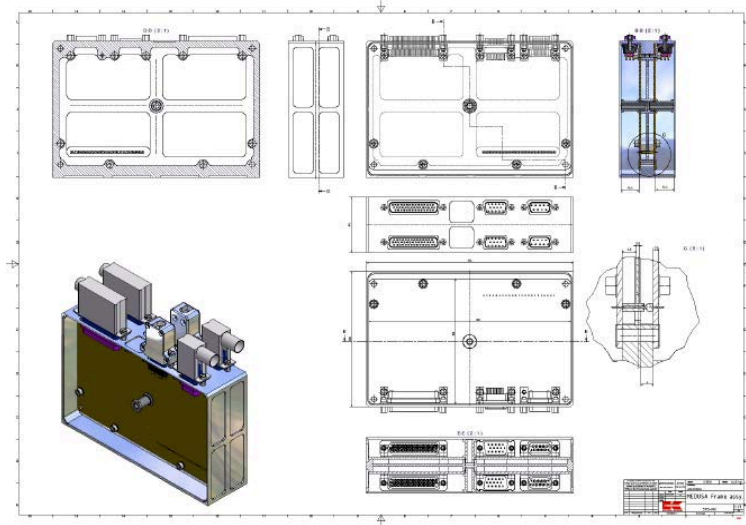


Fig. 4.7: MEDUSA Main Electronics (ME).

4.3.1 Laser Diode Assembly (LDA)

The *laser diode* is the source of a coherent light beam used to light the dust particles, which cross the MEDUSA OS. The selected baseline laser diode is the item FMLD-1M-808B-TO3-FC-2008 from Frankfurt Laser Company (Fig. 4.8) with monitor photodiode to stabilize the output power and a thermoelectric cooler (TEC) for temperature stabilization. The laser emission is coupled through a gradient anti-reflective coated lens to a multi-mode bare-end fiber.

Laser Diode	
Supplier	FLC - Frankfurt Laser Company
Model	FMLD-1M-808B-TO3-FC-2008
Optical Output Power	1000 mW
Wavelength	808 nm (805-811 nm)
Threshold Current	350 mA (350-400 mA)
Forward Current	1800 mA (1600-2000 mA)
Forward Voltage	2.0 V (1.9-2.4 V)
Spectral Width (FWHM)	5 nm (5-8 nm)
Fiber	100/125 μm , NA<0.22, 1 m, FC/PC conn.
Mode Structure	MM
Differential Efficiency	0.7 mW/mA (0.5-0.8 mW/mA)
Monitor Photocurrent	0.2-7.0 mA
Monitor Diode Voltage	5.0 \pm 0.5 V
TEC Forward Current	3.6 A
TEC Forward Voltage	3.7 V
Thermistor Resistance at 20 $^{\circ}\text{C}$	10 k Ω
External Quantum Efficiency	> 30%
Wavelength Temperature Drift	< 0.3 nm/ $^{\circ}\text{C}$
Operating Temperature	-40 $^{\circ}\text{C}$ \div +50 $^{\circ}\text{C}$
Thermal Electric Control (TEC)	20 $^{\circ}\text{C}$
Threshold Current Drift	< 1.0%/ $^{\circ}\text{C}$
Thermal Resistance	< 10 $^{\circ}\text{C}/\text{W}$

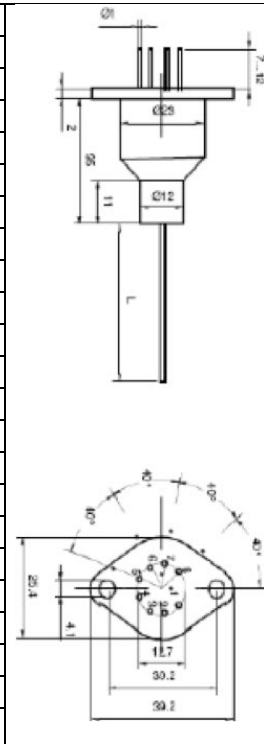


Fig. 4.8: Laser diode FLC FMLD-1M-808B-TO3-FC-2008 datasheet.

The laser diode was chosen during the design phase according to the following scientific and technical criteria:

- The laser wavelength is the result of studies about energetic efficiency and the possibility to optically detect particles with a minimum radius of 0.2 μm (EXM-ME-GA-RP-001, Issue 1, Rev. 1). An acceptable wavelength value is 808 nm.
- The laser nominal optical power guarantees a minimum power density in the Sampling Volume able to perform scattering analysis of particles with size of 0.2-20 μm .
- The laser diode temperature range (Fig. 4.8) is compliant with the mission scenario and accommodation requirements (Tab. 4.9).

The laser beam generated by the laser diode is directed to the MEDUSA OS via an optical fiber. The beam is filtered with an objective system (Sect. 4.3.2.2) and conveyed to the Sampling Volume, which is the zone nearby the middle of the OS where particles cross and from which they scatter light. The size of the Sampling Volume (Sect. 4.3.2.4) results from coupling the laser diode and the objective system (Sect. 4.3.2.2).

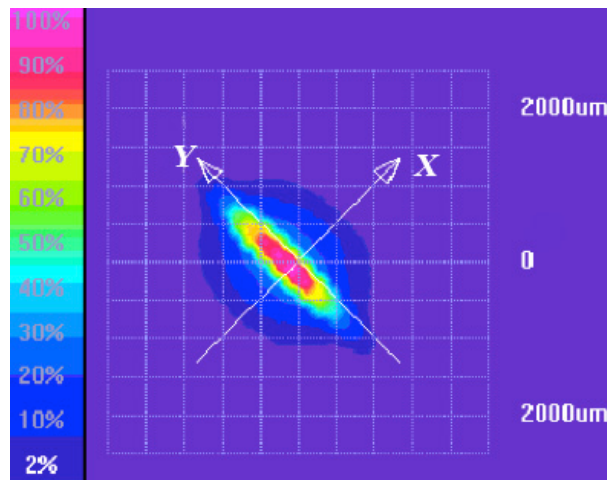


Fig. 4.9: Laser beam intensity distribution over the XY plane at the Sampling Volume centroid.

Fig. 4.9 and Fig. 4.10 show the laser beam intensity distribution in the MEDUSA Sampling Volume, orthogonal to the laser beam direction. The reference frame for the optical design of the laser beam used in Fig. 4.9 is:

- X Particles mainstream direction
- Y Orthogonal direction to X and Z (left-handed triad)
- Z Laser beam direction

Tests performed by Selex Galileo found that the laser beam intensity was approximately uniform within the Sampling Volume. In Fig. 4.9 the intensity profile on a plane orthogonal to the laser beam direction (XY) is shown, and the 85% of the optical energy was collected within the Sampling Volume (size 0.32 mm along X and 3 mm along Y). As also clarified in Fig. 4.10a and Fig. 4.10b, where the beam profile along the main directions (X and Y) are represented respectively, the light energy in the Sampling Volume can be considered uniform within a margin of 15% of the maximum optical power. Instead, where the profile is not completely uniform, the output signals by particles scattering will depend on the Y coordinate at which the particles intersect the lighted region. This possible dependence can introduce mistakes in distinguishing particles with different sizes, e.g., larger particles crossing far from the Sampling Volume centroid can show similar scattering levels of smaller particles crossing closer to the Sampling Volume centroid. Finally, the laser spot is approximately uniform along the Z direction for a length of 1.2 mm centred at the Sampling Volume centroid within a margin of 15% of the maximum optical power. The optical power of the laser beam depends on the laser diode source and on the optical path through the elements of the MEDUSA breadboard. As designed, the optical power is 1,000 mW at the laser diode source, but it decreases reaching the Sampling Volume as reported in Sect. 4.5.2.

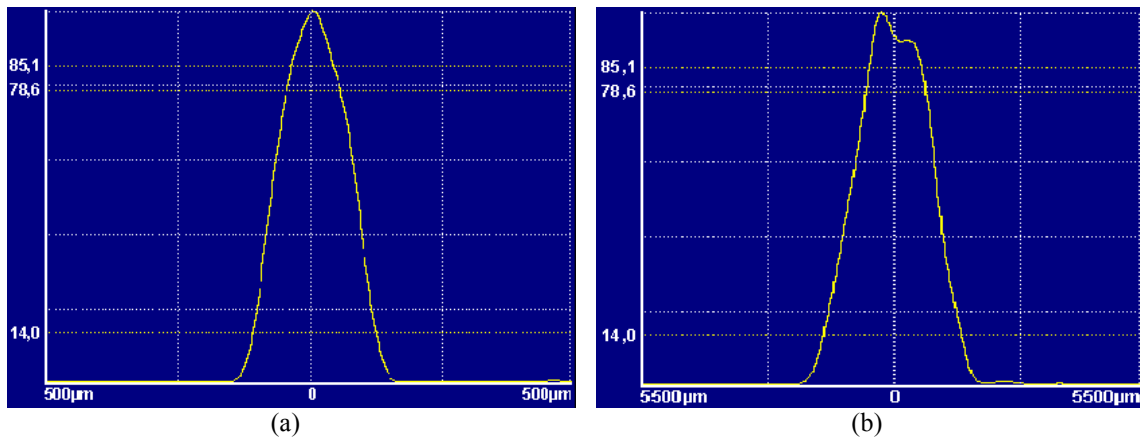


Fig. 4.10: (a) Laser beam intensity profile along the X direction. (b) Laser beam intensity profile along the Y direction.

The laser diode cannot be accommodated inside the MEDUSA case since it can work only in a limited temperature range (233-323 K) and the MEDUSA case will be exposed to the lower Martian temperature (~ 215 K). Therefore, it is accommodated in the *Laser Diode Assembly (LDA)*, mounted in a specified heated location inside the ExoMars HPL *Basic Experiment Drawer (BED)*. Hence, the LDA is mechanically and

thermally interfaced to the BED, electrically and electronically connected to the ME, and optically connected to MEDUSA via an optical fiber.

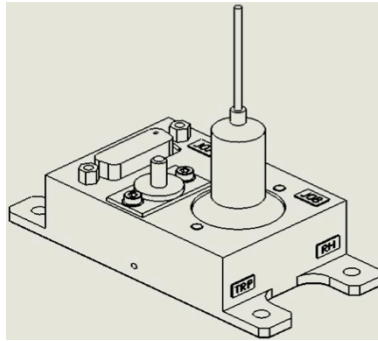


Fig. 4.11: The laser diode in the LDA to be accommodated in HPL BED.

4.3.2 Optical Stage (OS)

The *Optical Stage (OS)* is a box, which includes: a cylindrical duct; anamorphic objectives; two collecting mirrors; the Sampling Volume (SV); a light trap; two detectors; the Proximity Electronics (PE). The OS case is made of the Aluminium alloy Al RSA-905. It has a size of 130 mm (diameter) x 52 mm (height).

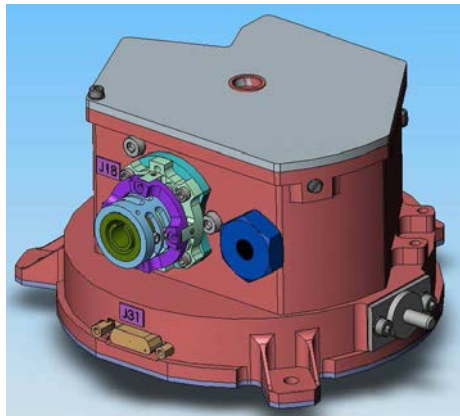


Fig. 4.12: MEDUSA Optical Stage case design.

The OS is based on the *Optical Particle Counter (OPC)* method for detecting and measuring scattered light from small particles. According to the Optical Detection Principle (Sect. 3.2.2), the scattering pattern generated by a particle depends on particle properties as the size parameter (α), shape, orientation, complex refractive index (n), wavelength of the incident beam (λ), and polarization of incident beam. Coupling forward and backward scattering signals gives information on particle optical properties since forward scattering intensity depends mainly on particle size parameter (α) than on complex refractive index (n), and backward scattering intensity depends mainly on particle material (e.g., n) than on particle geometry (e.g., α). A forward and backward

detection channel, both with high and low gain in order to cover a wide range of particle size, were implemented.

In the OS (Fig. 4.13), a laser beam is generated by a laser diode and directed to the Sampling Volume via an optical fiber and anamorphic objectives. The laser beam lights dust particles dispersed in the atmospheric aerosol, which flows through the Sampling Volume. The OS has two photodetectors, which pick up forward and backward light scattered by the particles and reflected by the two mirrors, respectively. The OS is designed to be able to measure dust particles, which have a diameter of 0.4-20 μm .

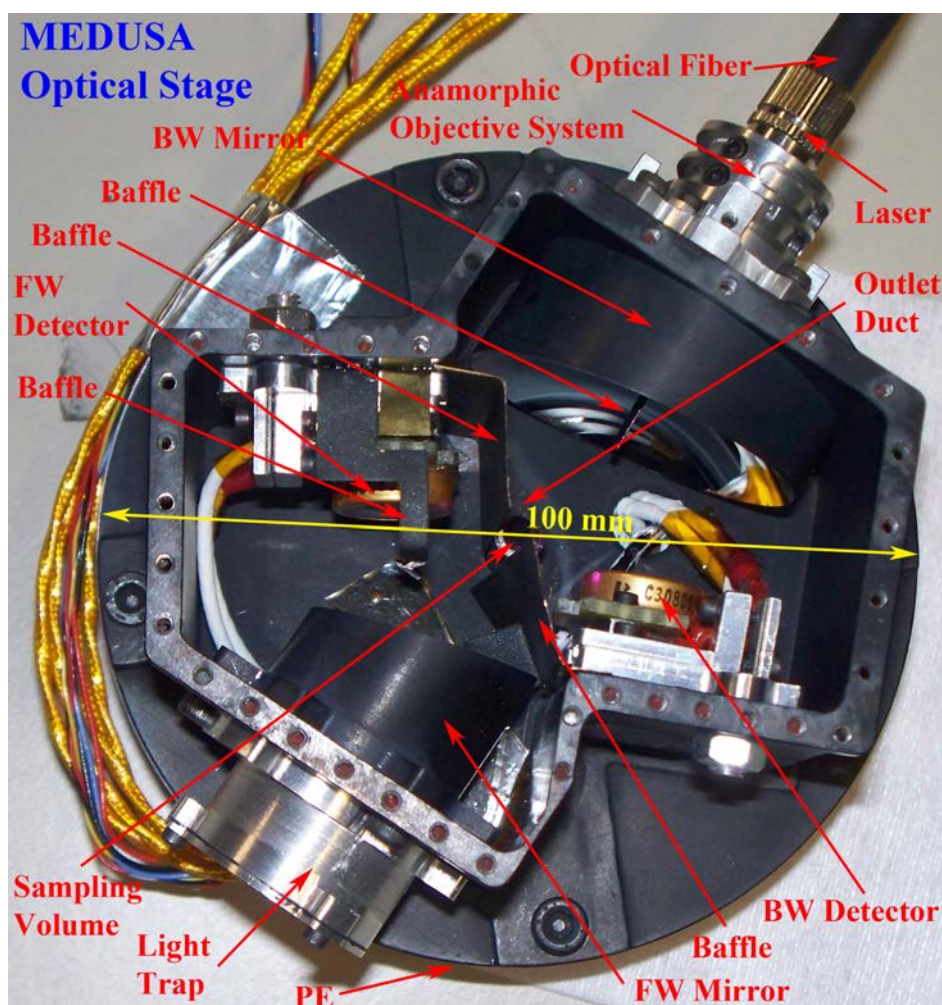


Fig. 4.13: The interior of the MEDUSA Optical Stage (OS).

The internal surfaces of the OS are painted with Aeroglaze, which is a coating to reduce reflectance. Small baffles are also implemented in the OS in order to avoid laser dispersion and reflections. In particular, a small rectangular (4 mm x 12 mm) baffle, painted with Inverama RAL 9005, is placed on the backscattering mirror to reduce the amount of stray light registered with the first MEDUSA breadboard.

4.3.2.1 Inlet Duct and Outlet Duct

In the first MEDUSA breadboard, the Sampling Head converged to a cylindrical duct, which extended from the upper to the lower cover of the OS box, and, then, continued to the pipeline towards the MBd. At the Sampling Volume region, where the laser beam illuminates the crossing particles, a hole in the cylindrical duct is made (Fig. 4.14). The cylindrical duct is made of the Aluminium alloy Al 6082-T6.

In the second breadboard the optical design is refined and the cylindrical duct reduced in diameter from 8 mm to 4 mm in order to minimize particle dispersion and flow turbulence. This implies that the duct is cut at the Sampling Volume region in order to allow the mirrors to collect the light scattered by the particles in the same angular range of the previous breadboard. Hence, the original integral duct is divided into two parts: the *inlet duct*, extended from the upper cover towards the Sampling Volume, and the *outlet duct*, extended from nearby the Sampling Volume towards the following pipeline. Both the inlet and outlet ducts are long approximately half the length of the original duct.

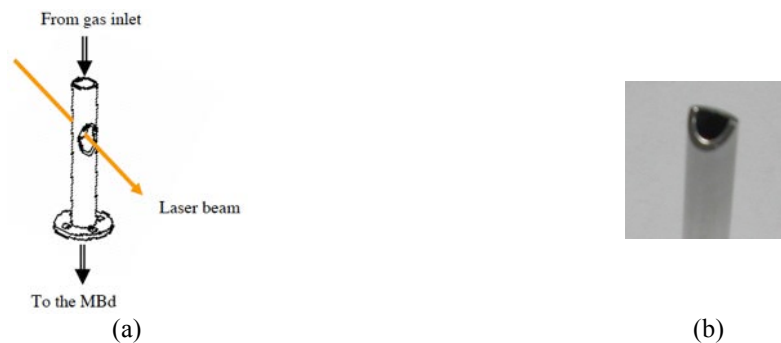


Fig. 4.14: (a) Cylindrical duct scheme in the first MEDUSA breadboard. (b) Cylindrical duct (upper side) in the second MEDUSA breadboard.

The tips of the inlet duct and outlet duct are specular and shaped as a natural extension of the original hole (Fig. 4.14). This choice is more critical from a fluid dynamics point of view as the sharp edges and a non-optimal ratio between the inlet duct diameter and the distance from the outlet section of the inlet duct and the centroid of the Sampling Volume could generate undesired vortex and turbulence inside the OS as it will be shown in Sect. 4.5.1.

4.3.2.2 Objective System

The anamorphic *Objective System* is composed by an aspherical collimating lens and a cylindrical lens to provide the required laser beam shape in the Sampling Volume

region (Fig. 4.15). In fact, the anamorphic lenses optically distort images and correct the natural laser beam divergence as a result of their curvature, and focus the laser beam into a spot as a result of a suitable f-number (i.e., the ratio between the focal length and the effective aperture diameter of a lens).

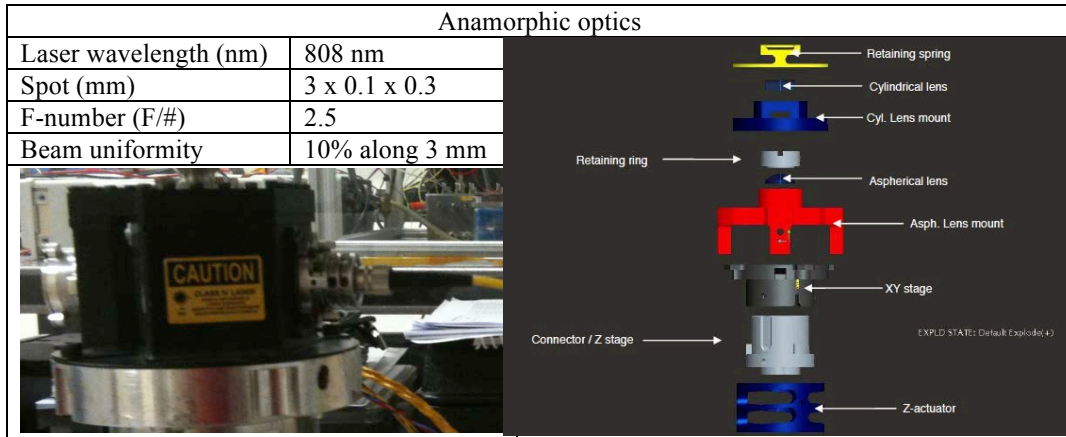


Fig. 4.15: Anamorphic objective system.

The anamorphic system design includes the following subsystems: optical subsystem, fiber optics patch cord, and mechanical subsystem. The anamorphic objective design is closely related to the OS, as the volume constraints limit the range of available solutions.

The mechanical mount of the anamorphic objective includes: a cylindrical lens mounted in a cell with a retaining spring; an aspherical lens mounted in a cell with a stop ring; an XY stage; an FC connector; a Z-actuator. The anamorphic mount is made of RSA 905, which is an Aluminium alloy with a low coefficient of thermal expansion ($18 \cdot 10^{-6}$ mm/mm/K) that guarantees a large operative temperature range and a surface roughness down to 20 Å. The cylindrical lens and aspherical lens are made of fused silica. The selection of the optical fiber depends upon the environmental requirements. The fiber patch cord is terminated with FC connectors on both sides.

4.3.2.3 Forward (FW) and Backward (BW) Collecting Mirrors

The *collecting mirrors* are used to collect the laser beam to the forward (FW) and backward (BW) photodetectors (Tab. 4.1). Both mirrors are spherical and have a central hole to allow the accommodation of the anamorphic objectives and the transit of the light beam in one case, and the transit of the exiting direct light beam and the accommodation of the light trap in the other case.

The collecting mirrors can introduce light losses due to relative position with respect to the detectors, mirror surface reflectance efficiency and mirror scattering phenomena.

Collecting mirrors	Forward scattering	Back Scattering
Collecting angle	$\pm 33^\circ$	$\pm 47^\circ$
Diameter	26 mm	40 mm
Radius of curvature	22 mm	6.6 mm
Aperture offset	7.4 mm	3 mm
Surface roughness	50 Å	50 Å
Reflectance	0.95	0.95
Efficiency	0.88	0.88
Energy on detector	> 95%	> 95%
Detector housing size	4 mm x 4 mm	4 mm x 4 mm

Tab. 4.1: Collecting mirrors datasheet.

4.3.2.4 Sampling Volume (SV)

The *Sampling Volume (SV)* is the ideal sensitive region defined by the optical design (Fig. 4.16). Only the particles crossing this region can be detected by the MEDUSA detection system. Assuming isokinetic sampling, i.e., complete coupling between gas and dust, the particle density inside and outside the instrument are the same. So, the Sampling Volume is sized according to the expected particle density range, to achieve meaningful sampling of Mars atmosphere in terms of counting individual particles.

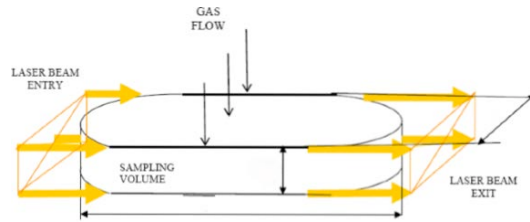


Fig. 4.16: Sampling Volume scheme.

The number of particles crossing the Sampling Volume (n_c) in a sampling time (T_s) is approximately estimated with Eq. (4.1), which does not consider the dispersion of particles in the OS that do not cross the Sampling Volume:

$$n_c = N_p Q T_s \quad (4.1)$$

where N_p is the particle number density and Q is the volumetric flow rate. The particle velocity value is taken as the average value on the duct section (S_d) (Eq. (4.2)), which is overestimated as it does not consider losses in the pipeline. Moreover, the hypothesis that particles velocity is approximated to the flow velocity is acceptable at this design phase as the particles are completely settled in the fluid for this regime. An accurate

estimation of particle velocity (V_p) with respect to size, mass and boundary conditions will be done in Sect. 4.5.1.

$$V_p = \frac{Q}{S_d} \quad (4.2)$$

The *fraction of coincidence events* (F), i.e., the ratio between the probability to detect 2 or more particles (detection probability, P_2) and the probability to detect 1 or more particles (coincidence events probability, P_1), in the Sampling Volume (V_s) is a parameter to take into account as it practically reduces the effective number of sampled particles (Eq. (4.3), Fig. 4.17).

$$F = \frac{P_2}{P_1} = \frac{1 - e^{-N_p V_s} - N_p V_s e^{-N_p V_s}}{1 - e^{-N_p V_s}} \quad (4.3)$$

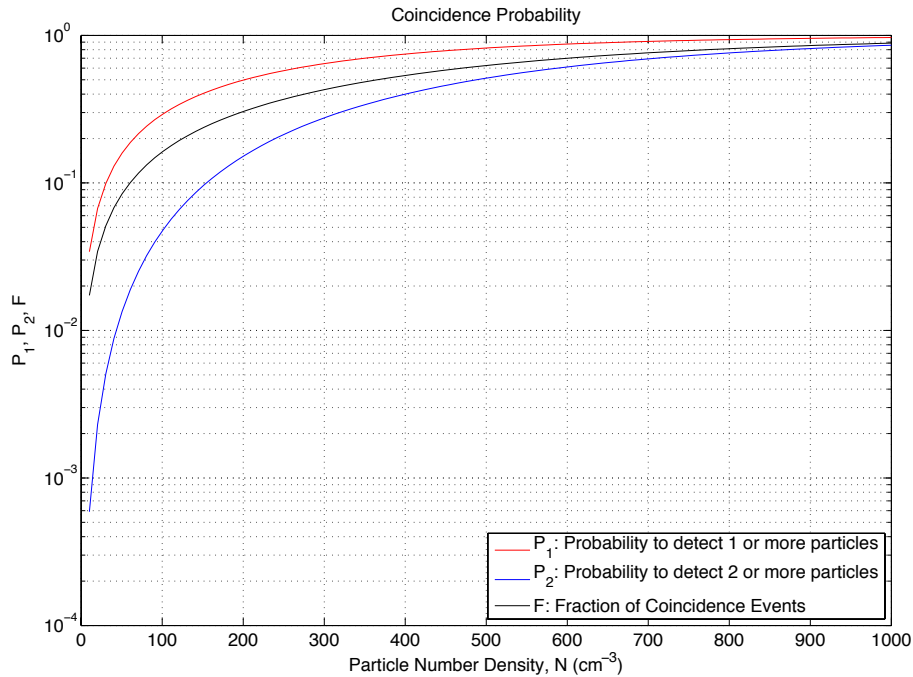


Fig. 4.17: Coincidence probability for sampling particles with MEDUSA.

The Sampling Volume (Tab. 4.2) was designed according to the following requirements:

- Effective shape of the laser beam;
- Sufficient number of particles detected in a short observation time;
- Small fraction of coincidence ($F < 0.05$) to have a single particle counter;
- Capability for a large range of dust grain number density.

In a typical Martian constant haze scenario about $3 \cdot 10^4$ dust particles, with a very small probability of coincidence events ($F = 5.15 \cdot 10^{-3}$) should cross the Sampling Volume during a MEDUSA run of 100 s as reported in Tab. 4.2. The duration of a run is chosen as a result of a compromise between collecting a meaningful amount of scientific data and limiting the power consumption.

Sampling Volume	
Sampling Volume (SV) length in the mainstream direction (X-direction)	$3.20 \cdot 10^{-4}$ m
Sampling Volume (SV) length in the Y-direction	$3.00 \cdot 10^{-3}$ m
Sampling Volume (SV) length in the laser beam direction (Z-direction)	$1.20 \cdot 10^{-3}$ m
Sampling Volume (SV) size (V_s)	$3.44 \cdot 10^{-9}$ m ³
Inlet duct diameter (D_{id})	$4.00 \cdot 10^{-3}$ m
Inlet duct section (S_D)	$1.25 \cdot 10^{-5}$ m ²
Pump Volumetric Flow Rate (Q)	$1.00 \cdot 10^{-4}$ m ³ /s = 6 l/min
Sampling time (T_{Vs})	100 s
Dust particles number density (N_{ap})	$3 \cdot 10^6$ m ⁻³ (constant haze)
Dust particles velocity (V_{IP})	7.95 m/s
Particles residence time in the Sampling Volume ($t_{sp.}$)	$4.02 \cdot 10^{-5}$ s
Number of particles crossing the SV in T_{Vs} (N_C)	$3 \cdot 10^4$
Fraction of coincidence events (F)	$5.15 \cdot 10^{-3}$

Tab. 4.2: Sampling Volume (SV) properties and approximated performance estimations.

4.3.2.5 Light Trap

A *light trap* is necessary to absorb the direct laser light that leaves the SV in order to avoid undesired light reflections. The laser beam after crossing the Sampling Volume is directed to the light trap via a hole at the center of the forward mirror. The MEDUSA light trap, which is made of Al RSA905 and has a roughed and anodized surface of diameter 5 mm, collects the light power and dissipates heat by conduction to the OS mechanical box. The light trap can collect up to 1 W of optical power.

However, a very small quantity of light power is reflected by the OS elements generating the so-called *stray light* (Tab. 4.3). The stray light depends on the laser diode emission and generates a constant photocurrent in the detectors. The factors that affect the stray light are light diffusion from anamorphic objective, and accidental light incidence over the mirrors and/or the inlet.

Stray light	
Stray light (optical power) on the forward scattering detector	40 ± 1 μ W
Stray light (optical power) on the backward scattering detector	5 ± 1 μ W

Tab. 4.3: Stray light estimation in the MEDUSA OS.

4.3.2.6 Detectors

The two detectors to collect forward and backward scattered light are silicon PIN photodiodes (Fig. 4.18, Tab. 4.4). A photodiode is based on a semiconductor diode and is capable of converting absorbed light into current or voltage. The MEDUSA photodetectors exhibit good responsivity in the IR spectral range selected for the laser source.



Fig. 4.18: The PerkinElmer C30809EH photodiode.

As the MEDUSA Main Body is exposed to the Mars atmosphere, and taking into account that no thermal control is offered by HPL for such element, the photodetectors have to face very low temperatures (minimum temperature 153 K), and a specific space qualification is required.

Detectors	
Supplier	PerkinElmer Optoelectronics
Model	C30809EH
Type	Silicon PIN photodiode
Configuration	TO8 Package
Wavelength (λ)	400-1100 nm
Sensing area	50 mm ²
Sensing area diameter	8 mm
Field of View	74°
DC Reverse Operating Voltage (V_R)	< 100 V
Photocurrent Density at 22°C (J_p)	5 mA/mm ² (average) - 20 mA/mm ² (peak)
Forward Current (I_F)	10 mA (average) - 20 mA (peak)
Breakdown voltage (V_{BR})	100 V
Responsivity	0.5 A/W at $\lambda = 808$ nm 0.6 A/W at $\lambda = 900$ nm
Quantum efficiency	83% at $\lambda = 900$ nm
Dark current (I_d)	2.5 · 10 ⁻⁸ A at 10 V 7.0 · 10 ⁻⁸ A at 45 V
Noise current (I_n)	1.5 · 10 ⁻¹³ A/Hz ^{1/2}
Noise Equivalent Power (NEP)	2.0 · 10 ⁻¹³ W/Hz ^{1/2}
Capacitance (C_d)	35 pF
Rise time (t_r)	10 ns at $R_L = 50 \Omega$, $\lambda = 900$ nm
Fall time	15 ns at $R_L = 50 \Omega$, $\lambda = 900$ nm
Storage temperature	-60°C ÷ +100°C
Operating temperature	-40°C ÷ +80°C

Tab. 4.4: Detectors datasheet.

4.3.2.7 Proximity Electronics (PE)

The *Proximity Electronics (PE)* is a Printed Circuit Board (PCB), basically constituted by amplifiers, for the conditioning of the output voltage signals from the photodetectors.

Taking into account the expected range for the dust grain size, the photodetectors provide output currents with a lower bound of few nA. Since the signal amplitude varies widely depending on the size of the dust particles, two differential outputs with different gains are used for both the forward and backward detector: $2 \cdot 10^4$ for low gain output and $2 \cdot 10^7$ for high gain output. Therefore, MEDUSA has 4 acquisition channels: forward high gain (FWH), forward low gain (FWL), backward high gain (BWH), and backward low gain (BWL). The relationship between the output voltage ΔV from each PE channel and the related optical power P due to light scattering is given by:

$$\Delta V = Pfg \quad (4.4)$$

where f is the transfer function of the PE/detectors ($f = 0.52 \text{ A}^{-1}$), and g is the gain of the channel ($g = 10^7$ for FWH and BWH channels; $g = 10^4$ for FWL and BWL channels).

The PE circuitry is placed in the Main Body, close to the photodetectors in a suitable case under the OS box (Fig. 4.1). Hence, it cannot benefit of the benign thermal environment offered by HPL electronics box and its minimum storage temperature is about 150 K, which is quite lower than the tolerable value of the commercially available components (220 K). In fact, Martian night thermal environment requires a larger temperature range than space qualified components can offer. Therefore, MEDUSA off-phases at Martian night (when temperature is at minimum values) require thermal control by heaters. The main concern is related to mechanical stress at temperature lower than 220 K due to different thermal expansion coefficients of the adjacent materials that could rupture inside the components and the interface between the component and the PCB, or fatigue at bonding level. A possible solution has been envisaged in the System on Package (SoP) technology, which allows to connect all the components inside a single package, and, using particular substrates and resins, allows this package to sustain temperatures lower than 220 K. During the MEDUSA operations, which occur with warmer temperatures during day, no significant thermal problems are foreseen.

4.3.3 Pump

MEDUSA is equipped with one rotary vane pump (Fig. 4.19), which is placed at the end of the acquisition chain. The original position was axially with respect to the Optical Stage. Nevertheless, in order to cope with maximum height requirements on HPL, although introducing additional mass (~ 260 g), the pump should be positioned on a side of the OS implying a pipe elbow (Fig. 4.1).

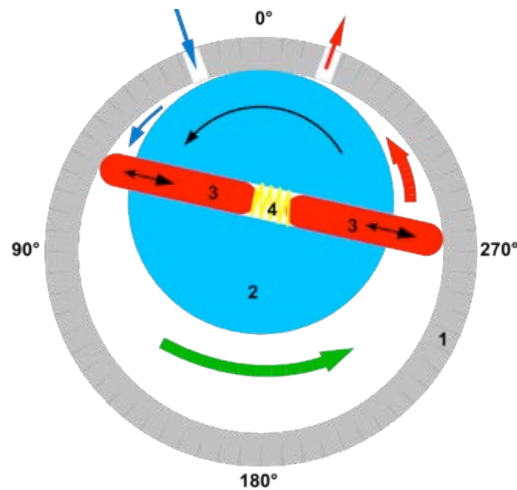


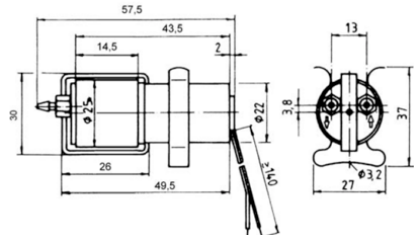
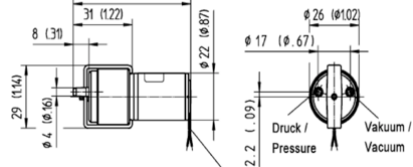


Fig. 4.19: The rotary vane pump scheme.

The pumping head is composed by a rotor fixed on the motor axis and containing the vanes, and by an eccentric external case. The vanes simply slide on the slot of the rotor and drag on the case pushed out just by the centrifugal force. The vanes are made with an auto-lubricating material in carbon.

Two models of commercial pumps were used for the MEDUSA second breadboard: Fürgut Model DC06/21FK and Gardner Denver Thomas Model G 12/04 EB (Tab. 4.5). They are chosen for the following reasons:

- Flow rate stability: MEDUSA needs a stable flow rate guaranteed by the simultaneity of the aspiration and compression phases, which avoids alternative closing of the inlet and the outlet port.
- Reliability: The pumps are constructively quite simple. The vanes are auto-lubricating without any fluid lubricants, valves or gasket on the ports, avoiding deterioration during the life in vacuum ambient, even if problems could arise at very low temperature due to different thermal dilatation between the case and the rotor.
- Miniaturization: The pumps have moderate dimensions, mass and power consumption.

Supplier	Fürgut	Gardner Denver Thomas
Model	DC06/21FK	G 12/04 EB
		
Maximum Flow Rate	5.5 l/min	6.2 l/min
Maximum vacuum	-125 mbar	-150 mbar
Maximum pressure	125 mbar	150 mbar
Voltage	6 V DC	12 V DC
Current consumption	0.29-0.50 A	0.18-0.47 A
Operating temperature	-30°C ÷ +40°C	-120°C ÷ +50°C
Weight	101 g	100 g
Draft		

Tab. 4.5: Pumps for the MEDUSA breadboard.

The pumps have similar fluid dynamics performance at standard temperature (Tab. 4.6). Nevertheless, only the Gardner Denver Thomas G 12/04 EB pump is suitable for the MEDUSA operative breadboard. In fact, the Fürgut Model DC06/21FK is incompatible at very low temperature due to coupling between motor and rotor, made with lubricated ball bearings. The Gardner Denver Thomas G 12/04 EB pump, instead, showed malfunctions, as the power consumptions increased and the flow rate decreased after 3 h of continuous working in lower temperature (-80°C ÷ -120°C). The blockage of the pump is caused by mechanical stress due to thermal factors: high temperature gradients between the rotating parts (blades, rotor) and the external frame of the pump.

Chamber pressure [mbar]	Power supply [V]		Switch-on current peak [A]		Current at steady flow rate [A]		Flow rate [l/min]	
	Fürgut	Thomas	Fürgut	Thomas	Fürgut	Thomas	Fürgut	Thomas
3	4.5	11	0.48	0.37	0.08	0.11	4.99	8.26
3	5	12	0.49	0.40	0.09	0.14	5.29	8.53
3	6	15	0.53	0.43	0.13	0.19	6.27	9.7
6	4.5	11	0.47	0.38	0.08	0.11	4.68	7.26
6	5	12	0.5	0.39	0.09	0.13	5.19	7.69
6	6	15	0.52	0.45	0.13	0.19	5.75	8.84
10	4.5	11	0.48	0.37	0.08	0.12	4.46	6.89
10	5	12	0.5	0.38	0.1	0.13	4.91	6.95
10	6	15	0.53	0.43	0.13	0.19	5.53	7.93

Tab. 4.6: Fürgut DC06/21FK and Gardner Denver Thomas G 12/04 EB pump performance.

The Gardner Denver Thomas pump is able to generate volumetric flow rates, which are approximately constant with temperature and slightly depend on pressure. Moreover, the volumetric flow rate is adjustable by setting the voltage/current supply (Tab. 4.6). Therefore, the pump volumetric flow rate is suitably controlled, which is very useful to determine how many particles could be sampled, as the number of sampled particles is strictly connected to the volumetric flow rate and environmental concentration. In a typical MEDUSA run, the pump should work with a volumetric flow rate of 6 l/min as explained in Sect. 4.3.2.4.

Finally, the inlet of the pump should be protected with an HEPA filter in order to avoid that dust grains could block the pump mechanism, even if no significant problems should occur with particles of size less than 100 μm .

4.4 MEDUSA for the ExoMars Humboldt Payload (HPL)

4.4.1 MEDUSA Requirements

The science, measurements and accommodation requirements of the MEDUSA experiment on board the ExoMars Humboldt Payload are officially defined in EXM-PL-ICD-ESA-00006 Issue 1, Rev. 2, and are here briefly reported in Tab. 4.7, Tab. 4.8, and Tab. 4.9, respectively.

The science requirements (Tab. 4.7) define the purpose of the MEDUSA instrument as described in Sect. 4.2. We anticipate that these scientific requirements will be partly reconsidered for the successive design of MicroMED (Chapter 5).

MEDUSA Science Requirements
<ul style="list-style-type: none"> • MEDUSA shall allow studying the physical properties of atmospheric dust at the landing site. • MEDUSA shall allow studying dust devils, dust storms, and steady wind patterns at the landing site. • MEDUSA shall contribute to characterize the effect of atmospheric dust on spacecraft equipment and operations. • MEDUSA shall allow to determine the atmospheric dust size distribution. • MEDUSA shall allow to measure the number density vs. size of suspended dust particles. • MEDUSA shall allow to measure electrification (positive and negative) of suspended dust particles. • MEDUSA shall allow to determine the atmospheric dust deposition/removal rate. • MEDUSA shall allow to determine the absolute water vapour abundance in the local atmosphere. • MEDUSA shall allow to estimate the wind velocity from the traces of moving dust particles. • MEDUSA shall allow to monitor diurnal short-term and long-term evolution of all above parameters. • MEDUSA shall allow to measure variations in the atmospheric humidity during the nighttime.

Tab. 4.7: MEDUSA Science Requirements (EXM-PL-ICD-ESA-00006 Issue 1, Rev. 2).

The requirements in Tab. 4.8 define quantitatively the MEDUSA measurements. In particular, MEDUSA shall perform *in situ*, not-invasive measurements, which will not

alter and/or contaminate the environment. A minimum of 4 runs per sol is considered sufficient to have a statistically satisfactory sample of measurements. Dust will be monitored also both during the day and at night to find correlations between dust and water vapour content and give detailed data for the study of the dust cycle as suggested in Chapter 1. Dust measurements should also be performed during special dusty events as dust devils and dust storms, if they occur in order to give further quantitative data about dust load. In fact, MEDUSA is designed to survive and operate even in very dusty conditions.

MEDUSA Measurement Requirements
<ul style="list-style-type: none"> • The MEDUSA implementation shall support Humboldt Payload science operations: 1) by measuring physical properties of atmospheric dust particles; 2) by determining the water vapour abundance in the atmosphere; 3) by allowing to study the effects of atmospheric dust on spacecraft equipment and operations. • The MEDUSA implementation shall allow to sample the local atmosphere without significantly modifying its dust particle content or properties. • The MEDUSA implementation shall allow to measure the atmospheric dust size distribution for particles in the size range of 0.05-10 μm. • MEDUSA's accuracy for measuring atmospheric dust concentration shall be $\leq 20\%$ for dust particles sizes $\geq 2 \mu\text{m}$. • The MEDUSA implementation shall allow to determine the suspended dust particle number density vs. size under different environment conditions. • MEDUSA's sensibility for measuring the dust deposition/removal rate shall be $\leq 0.1\%/sol$. • MEDUSA shall be capable to measure dust particle electrification in the range $\pm 10^3-10^6 e/\text{grain}$. • MEDUSA's sensibility for measuring the atmospheric water vapour content shall be $\leq 10 \text{ ppm}$. • MEDUSA's accuracy for determining the wind velocity (speed and direction) shall be $\leq 20\%$. • MEDUSA shall perform a minimum of 4 full runs/sol; typically during early morning, midday, afternoon, and evening; plus 6 DDES dust measurements/sol. • A MEDUSA DDES dust accumulation electrification measurement (8 h run) shall be performed at least once during the mission and, possibly, once per week. • MEDUSA shall perform (occasionally) dust and water vapour measurements during the nighttime. • During special events (i.e., dust devils), the MEDUSA implementation shall allow to perform up to 20 runs within a short period (no longer than 1 sol). • During special events, MEDUSA shall execute its measurements using appropriate parameter settings, tailored to the event's nature. • MEDUSA special events shall not constitute a design driver for lander resources. • The lander's data processing function shall be able to tag MEDUSA "special event" data for high priority transmission to ground. • The lander's data processing function shall be able to run MEDUSA compression and/or data processing algorithms on the collected data. • The instrument team shall provide all MEDUSA data processing and compression algorithms to be implemented by the lander. • The lander's data processing function shall require 25 MB of memory space for processing a typical set of MEDUSA products.

Tab. 4.8: MEDUSA Measurement Requirements (EXM-PL-ICD-ESA-00006 Issue 1, Rev. 2).

The accommodation requirements (Tab. 4.9) should be respected in order to have suitable MEDUSA operations. According to the Planetary Protection Requirements, MEDUSA was classified in the instruments Group I, which implies the bioburden of the

instrument hardware should be less than 100 bacterial spores and the bioburden density should be less than 300 bacterial spores/m².

MEDUSA Accommodation Requirements
<ul style="list-style-type: none"> • MEDUSA shall be accommodated on the ExoMars Lander. • MEDUSA sensors shall be protected from dust prior to and during landing. • The MEDUSA atmospheric sampling head shall be in a vertical position prior to commencing its science operations. • The MEDUSA accommodation shall guarantee sufficient free space around the atmospheric sampling head to avoid biasing the instrument's measurement: a circular (azimuthal) area with radius ≥ 1 m centered on the atmospheric sampling head. • The MEDUSA accommodation shall guarantee sufficient distance from any heat sources that may bias (directly or indirectly) the instrument's measurements. • The MEDUSA accommodation shall guarantee that no spacecraft-induced particulate material can bias the instrument's measurements. • The MEDUSA accommodation shall guarantee that the output of its atmospheric sampling pump can be evacuated to free space. • The MEDUSA Laser Diode Assembly (LDA) shall be accommodated in a benign thermal environment compatible with the laser requirements. • The MEDUSA water vapour sensor assembly shall be accommodated with its sensitive surface facing downwards. • The thermal interface of MEDUSA water vapour sensor assembly with Humboldt shall allow the dissipation of the heat generated by the sensor during its operation (6.38 W for 10 min once every 4 h); the temperature at thermal interface shall not be greater than 0°C during MBwv operation, i.e., while dissipating 6.38 W. • The MEDUSA DDES accommodation shall guarantee undisturbed wind flow above and around the sensor head.

Tab. 4.9: MEDUSA Accommodation Requirements (EXM-PL-ICD-ESA-00006 Issue 1, Rev. 2).

4.4.2 MEDUSA Engineering Budgets

In this section the engineering budgets of the MEDUSA instruments are reported, as accepted by ESA for accommodation on the ExoMars HPL. Nevertheless, as a result of the choice to have a very small payload in the EDM, the mass and power consumption should be drastically reduced, as described for MicroMED in Chapter 5.

The mass of the MEDUSA instrument is reported in Tab. 4.10, while the power consumption profile depends on the instrument Operation Modes as sum of contribution from the different subsystems (Tab. 4.11). The electrical primary power supplied to MEDUSA is dissipated as heat in the different units of the instrument, depending on the operation mode (Tab. 4.12).

The heat dissipation in the Main Body derives from OS light trap, OS PE, MBd and pump. The MBwv shall be thermally connected to a heat sink; this shall be thermally designed in order to maintain its temperature as close as possible to the external atmospheric temperature and shall not be exposed to the Sun.

The data volume generated by MEDUSA depends on the operating mode (Tab. 4.13). During dust measurements, the data volume depends on the number of events and/or grains detected by the OS. This budget does not take into account packet headers and checksum (4 bytes), housekeeping data (20 bytes/s), and asynchronous telemetry and TC acknowledge (0.4 bytes/s).

MEDUSA Subsystems	MEDUSA Components	Mass [g]
Sampling Head	Inlet structure	49
Laser Diode Assembly (LDA)	Laser diode Laser diode box Connector Bonding stud	117
Optical sensor	OS box Inlet duct Outlet duct Objective system Collecting mirrors (2) Light trap Detectors (2) HEPA filter Connectors Bonding stud	294
Proximity Electronics (PE)	PE board PE box	110
Microbalance for dust (Mbd)	MBd MBd box Connector	105
Pump	Pump Support Pipeline KT accommodation	236
Microbalance for water vapour (Mbwv)	MBwv MBwv box Connector Bonding stud	168
Dust Deposition and Electrification Stage (DDES)	DDES sensor DDES box Electronics	118
Main Electronics (ME)	Eurocard DC/DC converter Components Connectors Frame Screws	871.6
Other mass	Main Body screws LDA accommodation KT accommodation	632
TOTAL		2700.6

Tab. 4.10: MEDUSA mass budget (EXM-ME-GA-RP-001, Issue 1, Rev. 1; EXM-PL-OCD-ESA-000006, Issue 1, Rev. 2).

Subsystem	Power [W]
Proximity Electronics (PE)	2
Microbalance for Dust (MBd)	0.13
Pump	3
Microbalance for Water Vapour (MBwv)	6.38 (High Power) 5.1 (Medium Power) 2.55 (Low Power)
Dust Deposition and Electrification Stage (DDES)	0.98 (Wind Mode) 0.33 (Dust Mode)
Main Electronics	4.1
Laser Diode	4.85
TOTAL (MAXIMUM)	21.44

Tab. 4.11: MEDUSA subsystems power consumption (EXM-ME-GA-RP-001, Issue 1, Rev. 1).

Operation	Subsystems	Total ME Secondary [mW]	DC/DC Losses [mW]	LDA [mW]	Main Body [mW]	MBwv [mW]	DDES [mW]
Standby + ME Inizialization and Check	ME	2500	1071	0	0	0	0
Dust Suite Self-Check and Calibration	ME+OS +MBd+LDA	3700	4577	3850	3130	0	0
Water Vapour Self-Check and Calibration	ME+MBwv	2500	1127	0	0	130	0
DDES Self-Check and Calibration	ME+DDES	2500	1491	0	0	0	980
Dust Sampling	ME+OS +MBd+Pump +LDA	3700	5863	3850	6130	0	0
Water Vapour Measurement	ME+MBwv	4100	4491	0	0	6380	0
Dust and Electrification Measurement	ME+DDES	2500	1491	0	0	0	980
Electrification Dust Accumulation	DDES	2500	1213	0	0	0	330

Tab. 4.12: Heat dissipation of MEDUSA items (EXM-ME-GA-RP-001, Issue 1, Rev. 1).

Operation	Subsystems	Data Rate [b/s]	Time per Run [s]	Data Volume [b/run]	Operation frequency [Runs/sol]	Data Volume [Mb/sol]
Standby + ME Inizialization and Check	ME	160	10	1600	4	0.00610
Dust Suite Self-Check and Calibration	ME+OS +MBd+LDA	160	10	1600	4	0.00610
Water Vapour Self-Check and Calibration	ME+MBwv	160	10	1600	4	0.00610
DDES Self-Check and Calibration	ME+DDES	160	10	1600	4	0.00610
Dust Sampling	ME+OS +MBd+Pump +LDA	1360	100	1360000	4	0.519
Water Vapour Measurement	ME+MBwv	8	600	15328	4	0.0585
Dust and Electrification Measurement	ME+DDES	216	60	12960	10	0.124
Electrification Dust Accumulation	DDES	3	28800	83936	0.14	0.0112
TOTAL			29600			0.736

Tab. 4.13: MEDUSA data volume for Operation Modes (EXM-ME-GA-RP-001, Issue 1, Rev. 1).

4.4.3 MEDUSA Operations and Maintenance

MEDUSA nominal operations consist in a series of runs for dust measurements (OS+MBd and DDES) and for water vapour measurements (MBwv) to be accomplished according to a pre-planned sol-based sequence and activated by telecommands in case of environment sampling/characterization during special events. The MEDUSA Operation Modes are: *Safe Mode*, *Dust Sampling Mode*, *DDES Mode*, and *MBwv Mode* (Tab. 4.14).

The MEDUSA measurements will be performed exclusively when the lander is stationary on the Martian surface. A reference value of 4 runs plus other 6 DDES dust sessions per sol were suggested as a good compromise between scientific and engineering requirements. Electrical dust accumulation by DDES had to be performed at least once during the mission (duration 8 h).

Operation Mode	Description	Accepted Telecommands	Data Generated
Safe Mode (Stand-by, Self-Check and Calibration)	Not operative: all critical systems turned off to allow instrument checking and setting by uploading (e.g., new software versions, memory patches and setting files)	Accepted context; Load script; Run script; Time update; Ping; Mode Transitions	Housekeeping; Acceptance reports and events linked to Safe Mode; Pong related to Connection Test
Dust Sampling Mode	OS+MBd operations	Laser; OS; MBd; Pump switching; OS setting; Transition to Safe Mode	Housekeeping; Science TM; Laser TM; MBd TM; Pump TM
DDES Mode	DDES operations	DDES	Housekeeping; Science TM; Acceptance reports and events linked to DDES Mode
MBwv Mode	Water vapour measurements.	MBwv switching; Transition to Safe Mode	Housekeeping; MBwv TM; Acceptance reports and events linked to Water Vapour MB Mode

Tab. 4.14: MEDUSA Operation Modes (EXM-ME-GA-RP-001, Issue 1, Rev. 1).

4.5 Analysis of the MEDUSA Breadboard

The analysis of the MEDUSA breadboard developed during the work of this thesis was based on the verification and improvement of the detection system for dust particles via light scattering. These tasks implied both fluid dynamics and optical analysis as the quality of the detection process is obtained by coupling the dynamics behaviour of the particles inside MEDUSA and the capacity of the optical suite, i.e., the LDA and OS elements, to properly execute the functions for those they are installed.

The particle dynamics was valued mainly with numerical simulations (Sect. 4.5.1), while the functionality of the scattering analysis was verified with experimental tests (Sect. 4.5.5). Some specific tests on components were also necessary, as checking the laser beam alignment and the optical power density inside the Sampling Volume (Sect. 4.5.2), and valuating the stray light inside the OS (4.5.3).

4.5.1 Computational Fluid Dynamics Analysis

The working conditions of the MEDUSA OS in the Martian environment were simulated numerically with Computational Fluid Dynamics (CFD) methods to analyze the behaviour of the particle dynamics. The CFD simulations are based on the theoretical discussion described in Sect. 3.1.

The general properties of the Martian atmospheric fluid considered for the CFD simulations are reported in Tab. 4.15. The Martian atmosphere is mainly made of carbon dioxide (CO_2), which is considered an ideal gas. As CO_2 content is about 95%

by volume, even if with limited seasonally and daily variability (Sect. 1.2.1), no significant errors will be done by considering CO_2 as the prevalent component in determining the properties of the atmospheric fluid. For an ideal gas the equation of state (Eq. (3.35)) is applicable. Moreover, the mean free molecular path for maxwellian kinematics (Eqs. (3.59) and (3.60)), and the Sutherland Law for viscosity (Eq. (3.51)) are also applicable.

Fluid		CO_2
Boltzmann Constant (k_B)	J/K	$1.38 \cdot 10^{-23}$
Universal Gas Constant (R_0)	J/K/mol	8.314
Molar Mass (m_0)	g/mole	43.49
Gas Constant (R)	J/K/kg	191.17
Molecular Degrees of Freedom		6
Ratio between Specific Heat Capacities (γ)		1.33
Molecular Diameter (d_M) at $T = 293.15$ K	m	$4.66 \cdot 10^{-10}$
Gravity Acceleration (g)	m^2/s	3.73
Reference Viscosity at $T = 293.15$ K (μ_r)	Pa·s	$1.47 \cdot 10^{-5}$
Reference Speed of Sound at $T = 293.15$ K (a_r)	m/s	273
Reference Thermal Conductivity at $T = 293.15$ K (k_r)	W/m/K	$1.46 \cdot 10^{-2}$
Sutherland Constant for Viscosity at $T = 293.15$ K (S)	K	222
Sutherland Constant for Thermal Conductivity at $T = 293.15$ K (S_k)	K	1800
Mean Molecular Path at $T = 293.15$ K	m	$4.14 \cdot 10^{-8}$

Tab. 4.15: Martian atmospheric fluid properties.

In the Martian conditions, the Knudsen number related to fluid-particles interaction (Kn_p) is typically larger than 1, which, strictly, prevents using the Navier-Stokes equations (Eqs. (3.16), (3.17), (3.18), and (3.19)) to solve the fluid dynamics scalar and vectorial quantities fields. Nevertheless, as explained in Sect. 3.1, since the global Knudsen number, which is referred to the MEDUSA geometry, is smaller than 1, the problem can be afforded by solving the fluid dynamics field with the Navier-Stokes equations and corrective parameters for rarefied effects. Finally, the Navier-Stokes equations are solved numerically using the finite volume method (Eq. (3.102)) implemented in CFD tools.

The particle dynamics was described by considering the aerodynamic drag (Eq. (3.63)), the gravity force (Eq. (3.64)), the virtual mass force (Eq. (3.65)), the buoyancy force (Eq. (3.66)), the pressure gradient force (Eq. (3.67)), the Saffman lift force (Eq. (3.68)), and the Brownian force (Eq. (3.69)). In these cases, the thermophoretic force (Eq. (3.71)) has no effects, as no temperature gradients have been introduced, and the electrostatic force (Eq. (3.70)) was not taken into account as electrically uncharged particles have been considered. Anyway, drag and gravity are the most relevant forces

to influence the particle trajectories. As said above, the interaction between the fluid and the particles is characterized by $Kn_p > 1$, and to take into account the rarefied effects, the aerodynamic drag coefficient (Eq. (3.75)) was corrected with the Cunningham correction factor expressed with Eq. (3.79), where it was assumed that $\alpha_c = 1.142$, $\beta_c = 0.558$, $\gamma_c = 0.999$, which are reasonable values for non-spherical particles (Allen, M.D., Raabe, O.G., 1985). It was chosen to use the data referred to non-spherical variety of particles since on Mars particles with irregular and random surfaces should result from aeolian processes.

The conditions assumed for the simulations were the following:

- Mass flow rate defined at the inflow of the domain
- Atmospheric conditions defined at the inflow of the domain
- Particle injected at the inflow of the domain
- Incompressible flow
- Laminar flow
- Steady flow
- Martian gravity effect
- Isothermal condition between fluid, particles and walls
- No-slip fluid-wall condition and trap particle-wall condition

The mass flow rate (\dot{m}) is determined by the pump volumetric flow rate (Q) and the atmospheric density (ρ) by:

$$\dot{m} = \frac{dm}{dt} = \rho VA = \rho Q \quad (4.5)$$

where V is the average fluid velocity on the section A .

As the MEDUSA pump volumetric flow rate is quite stable with pressure and temperature and is adjustable by tuning the electrical power supply, the volumetric flow rate was considered as an input parameter. Therefore, the mass flow rate, pressure and temperature were defined as boundary conditions at the inflow, while conditions with zero diffusion flux for all flow variables and overall mass balance correction were defined at the outflow. The zero diffusion flux condition applied at outflow cells means that the conditions at the outflow plane are extrapolated from the interior of the domain

and have no impact on the upstream flow. The extrapolation procedure updates the outflow velocity and pressure so that it is consistent with a fully-developed flow assumption. This outflow condition was considered the only way to solve the unknown pressure field, even at the outflow section, where the pump is connected via a pipeline, while the property of the pump was used to guarantee a well-known volumetric flow rate. The pump flow rate was fixed at the design value of 6 l/min.

In general, Martian atmospheric pressure and temperature depend on season, time and location. In this case, pressure of 600 Pa and 700 Pa, typical of Martian regions at 0 MSL, were considered, with a temperature excursion between 150 K and 300 K. By matching the pressure and temperature levels considered, the atmospheric density varies from a more rarefied case ($\rho = 1.05 \cdot 10^{-2} \text{ kg/m}^3$ at $p = 600 \text{ Pa}$ and $T = 300 \text{ K}$) to a more dense case ($\rho = 2.44 \cdot 10^{-2} \text{ kg/m}^3$ at $p = 700 \text{ Pa}$ and $T = 150 \text{ K}$). The environmental conditions considered for the CFD simulations are reported in Tab. 4.16.

Temperature (T)	K	150	300	150	300
Pressure (p)	Pa	600	600	700	700
Density (ρ)	kg/m ³	$2.09 \cdot 10^{-2}$	$1.05 \cdot 10^{-2}$	$2.44 \cdot 10^{-2}$	$1.22 \cdot 10^{-2}$
Viscosity (μ)	Pa·s	$7.43 \cdot 10^{-6}$	$1.50 \cdot 10^{-5}$	$7.43 \cdot 10^{-6}$	$1.50 \cdot 10^{-5}$
Thermal Conductivity (k)	W/m/K	$5.74 \cdot 10^{-3}$	$1.51 \cdot 10^{-2}$	$5.74 \cdot 10^{-3}$	$1.51 \cdot 10^{-2}$
Speed of Sound	m/s	$1.96 \cdot 10^2$	$2.77 \cdot 10^2$	$1.96 \cdot 10^2$	$2.77 \cdot 10^2$
Mean Free Molecular Path (l)	m	$2.76 \cdot 10^{-6}$	$7.86 \cdot 10^{-6}$	$2.36 \cdot 10^{-6}$	$6.74 \cdot 10^{-6}$
Volumetric flow rate (Q)	m ³ /s	$1.00 \cdot 10^{-4}$	$1.00 \cdot 10^{-4}$	$1.00 \cdot 10^{-4}$	$1.00 \cdot 10^{-4}$
Mass flow rate (\dot{m})	kg/s	$2.09 \cdot 10^{-6}$	$1.05 \cdot 10^{-6}$	$2.44 \cdot 10^{-6}$	$1.22 \cdot 10^{-6}$

Tab. 4.16: Environmental conditions.

Fluxes of particles with different diameters ($d_p = 0.2 \text{ }\mu\text{m}$, $1 \text{ }\mu\text{m}$, $5 \text{ }\mu\text{m}$, $10 \text{ }\mu\text{m}$ and $20 \text{ }\mu\text{m}$) and with a constant density of $2.73 \cdot 10^3 \text{ kg/m}^3$, typical for Martian dust (Tab. 4.17), were dispersed and uniformly distributed at the inflow, in order to foresee a sufficient variety of trajectories.

Uncompressible flow hypothesis is suitable as the Mach number (M) is globally and locally smaller than 0.15 in the simulated conditions, so density is approximately constant and depends only on boundary pressure and temperature.

Laminar flow hypothesis is suitable as the Reynolds number (Re) is globally and locally smaller than 100 for the internal flow. Nevertheless, turbulence models should be applied to better describe the phenomena; they would need a detailed match with the initial turbulent boundary conditions, to be evaluated experimentally. At this stage, turbulent models are not implemented.

d_p [μm]	ρ_p [kg/m^3]	m_p [kg]	p [Pa]	T [K]	Kn_p	V_{ts} [m/s]	C_c
0.20	$2.73 \cdot 10^3$	$1.14 \cdot 10^{-17}$	600	150	6.98	$4.81 \cdot 10^{-8}$	12.2
			600	300	19.7	$5.09 \cdot 10^{-8}$	33.9
			700	150	5.91	$4.16 \cdot 10^{-8}$	10.5
			700	150	16.8	$4.37 \cdot 10^{-8}$	29.1
1.0	$2.73 \cdot 10^3$	$1.43 \cdot 10^{-15}$	600	150	1.38	$2.91 \cdot 10^{-7}$	2.95
			600	300	3.93	$2.70 \cdot 10^{-7}$	7.19
			700	150	1.18	$2.60 \cdot 10^{-7}$	2.63
			700	150	3.37	$2.35 \cdot 10^{-7}$	6.25
5.0	$2.73 \cdot 10^3$	$1.79 \cdot 10^{-13}$	600	150	0.28	$3.25 \cdot 10^{-6}$	1.32
			600	300	0.79	$1.90 \cdot 10^{-6}$	2.02
			700	150	0.24	$3.14 \cdot 10^{-6}$	1.27
			700	150	0.67	$1.74 \cdot 10^{-6}$	1.85
10.0	$2.73 \cdot 10^3$	$1.43 \cdot 10^{-12}$	600	150	0.14	$1.14 \cdot 10^{-5}$	1.16
			600	300	0.39	$5.51 \cdot 10^{-5}$	1.47
			700	150	0.12	$1.12 \cdot 10^{-5}$	1.13
			700	150	0.34	$5.24 \cdot 10^{-5}$	1.39
20.0	$2.73 \cdot 10^3$	$1.14 \cdot 10^{-11}$	600	150	0.069	$4.25 \cdot 10^{-5}$	1.08
			600	300	0.20	$1.84 \cdot 10^{-5}$	1.23
			700	150	0.052	$4.21 \cdot 10^{-5}$	1.07
			700	150	0.17	$1.79 \cdot 10^{-5}$	1.19

Tab. 4.17: Properties of particles in Martian conditions.

Steady flow is considered, as MEDUSA works at a stable pump flow rate. During the unsteady phase of the pump (typically less than 10 s) no MEDUSA measurements will be discarded.

In this simulation, it was supposed that the gravity works in the same direction of the mainstream, although this assumption should be confirmed by further accommodation requirements. Anyway, gravity effects are substantially less than aerodynamic effects to determine the particle trajectories. In fact, in these applications for particles with $d_p = 0.2 \mu\text{m}$ the ratio of the gravity and aerodynamic force is of the order of 10^{-6} , while for $d_p = 20 \mu\text{m}$ is of the order of 10^{-3} .

The fluid, particles and walls were considered at the same temperature, supposing that the sensor is exposed to the external environment. This is a realistic assumption as the sensitive elements (as electronics components, laser diode and detectors) will be duly controlled thermally, but decoupled from the instrument body. So, heat exchanges were not considered here.

The flow regime is rarefied with respect to the interaction of the fluid with the particles, but it is considered as a continuum with respect to the interaction of the fluid with the walls; hence, the no-slip fluid-wall condition is suitable.

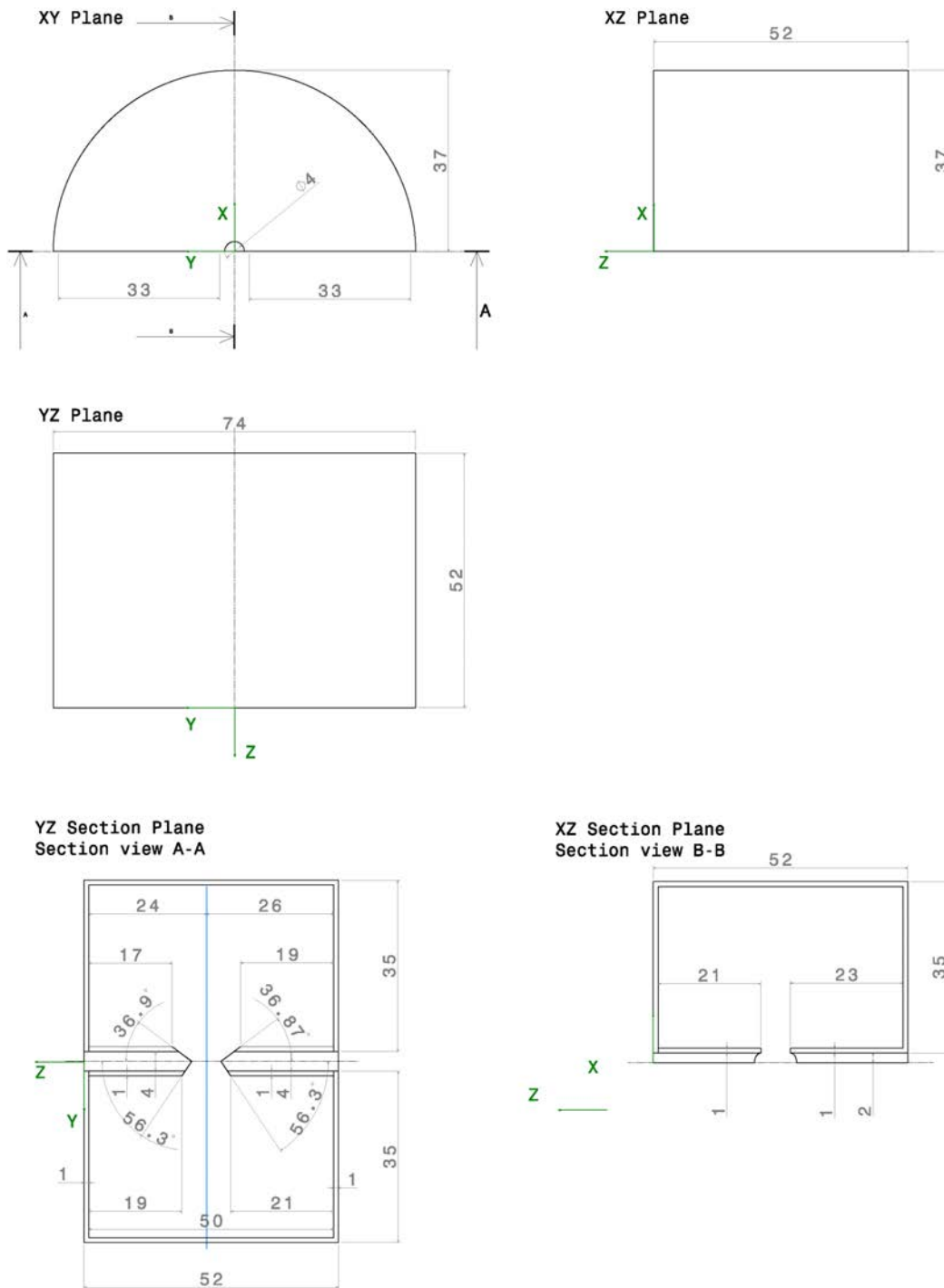


Fig. 4.20: Draft of the MEDUSA OS for the CFD analysis (dimensions in mm).

The behaviour of the particles on wall is, instead, rather complex to model deterministically. It is assumed that particles do not rebound after impacting on walls, i.e., the coefficient of restitution defined as the ratio between the particle momentum after and before the impact is very close to zero as it was observed experimentally on the breadboard model. However, recirculation of particles deposited on walls is induced

by the aspiration of the MEDUSA pump up to cross the Sampling Volume (Sect. 4.5.5). It is reasonable to assume that a particle on a wall can be recirculated by the fluid stresses if the wall tangential stresses and pressure gradients normal to the wall surface are sufficiently high to overcome the adhesion force. These conditions, anyway, are not frequent in internal steady boundary layers as in the inlet and outlet ducts. In the CFD model, the internal walls of the inlet and outlet ducts are the only ones for which it makes sense to consider the interaction with the particles, as the other walls should not basically interact with the particles mainstream, unless particles go away from the Sampling Volume. Practically, detachments of particles from walls should be considered as phenomena, which can affect randomly the MEDUSA performance. Therefore, a conservative criterion suitable for the purpose of this simulation is to assume that a particle is lost after impacting on a wall.

The reference frame chosen for the geometry of the MEDUSA Optical Stage is the following:

- X Orthogonal to Y and Z (left-handed triad)
- Y Light Trap/BW Mirror - Laser Diode/FW Mirror direction
- Z Mainstream anti-direction and gravity anti-direction

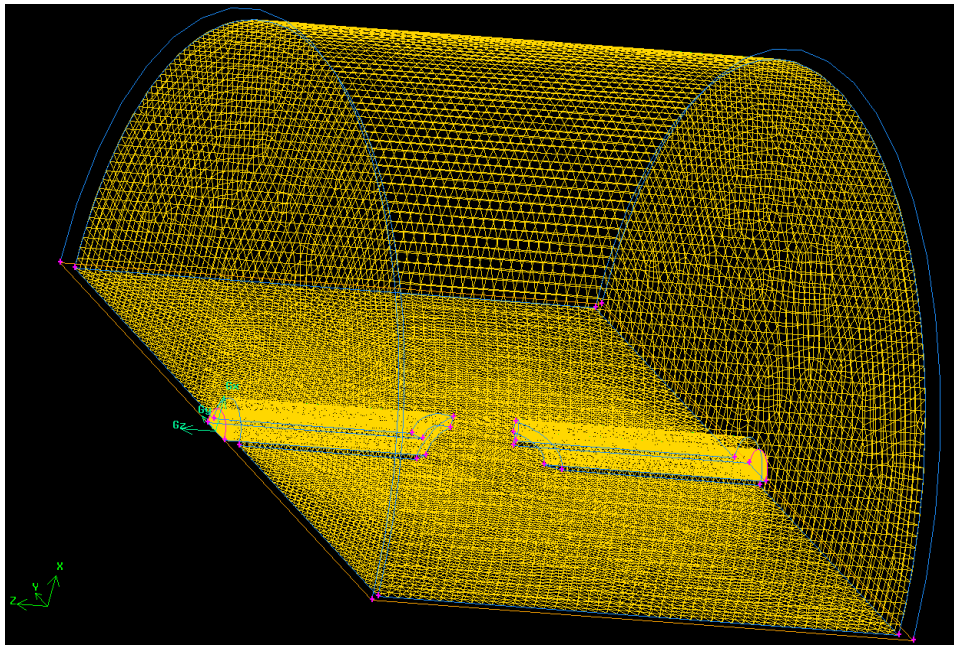


Fig. 4.21: The Finite Volume grid for the MEDUSA OS.

The geometry of the MEDUSA Optical Stage (Fig. 4.20) was modelled as a tridimensional cylinder containing the inlet duct and the outlet duct. The geometry is symmetric with respect to a plane (YZ plane). The optical components as laser diode exit, detectors, mirrors and baffles, were not included in this model as these elements are quite far to be relevant from a fluid dynamics point of view and the analysis is focused on inspecting the Sampling Volume region. For the same reason, the Sampling Head was not included in such analysis. In the draft (Fig. 4.20), the laser beam direction is shown with a blue line. The mesh applied in the domain for the CFD analysis is hybrid and made of tetrahedra with size of 0.1-0.5 mm, which is a suitable compromise between local small regions, particle dynamics resolution, scale of the gradient of the fluid dynamics quantities and computational cost (Fig. 4.21).

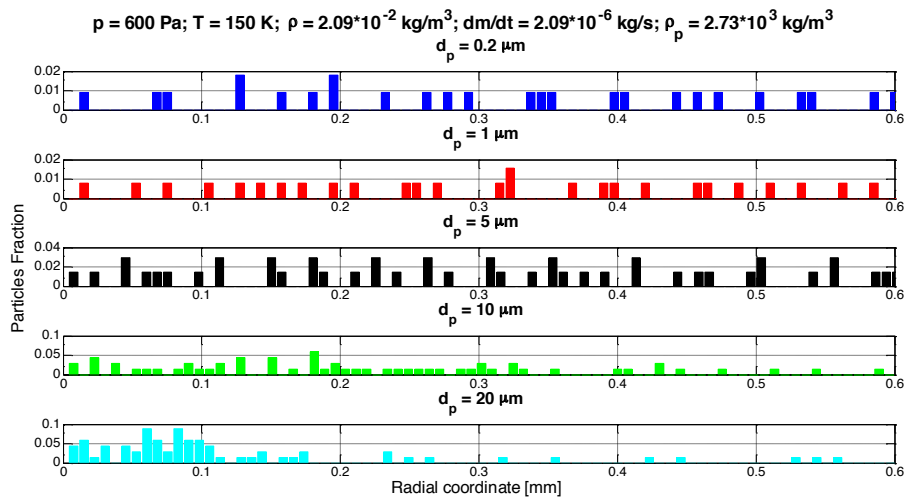


Fig. 4.22: Particle distributions in the middle plane of the Sampling Volume orthogonal to the mainstream ($p = 600 \text{ Pa}$, $T = 150 \text{ K}$, $\rho = 2.09 \cdot 10^{-2}$, $\dot{m} = 2.09 \cdot 10^{-6} \text{ kg/s}$, $\rho_p = 2.73 \cdot 10^3 \text{ kg/m}^3$).

The capability of the MEDUSA OS to sample particles was evaluated by analysing the distributions of the particles across the Sampling Volume, and the related profiles of the axial velocity component (parallel to the mainstream) and of the radial velocity component (orthogonal to the mainstream). The Sampling Volume cross section (orthogonal to the mainstream) was supposed to have an average radius of 0.6 mm as within this region the optical power of the laser spot is above 85% of the peak value. The results at the Sampling Volume middle plane normal to the mainstream, which corresponds to the station where the laser beam has the highest energy, are shown: in Fig. 4.22, Fig. 4.24, Fig. 4.26, and Fig. 4.28 the particle distributions and in Fig. 4.23, Fig. 4.25, Fig. 4.27 and Fig. 4.29 the axial and radial velocity components of the

particles are reported for the discussed boundary conditions. The sampling efficiency (η_{sample}) is estimated as the ratio between the number of particles, which were able to cross the Sampling Volume within a distance of 0.60 mm from the centroid, and the total number of particles injected upstream at the MEDUSA inflow duct. The particle distributions are estimated as the ratio between the number of particles at in a specific range distance from the centroid of the Sampling Volume and the total number of particles crossing the middle plane of the MEDUSA OS, which does not include particles eventually loss upstream.

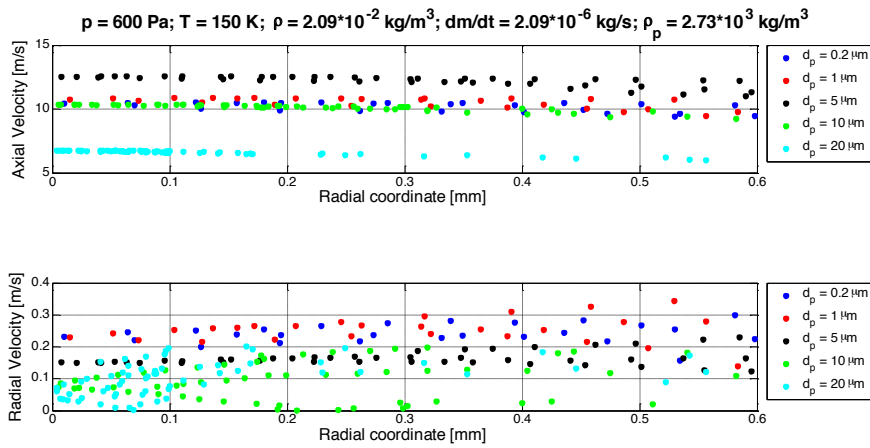


Fig. 4.23: Particle axial and radial velocity components in the middle plane of the Sampling Volume orthogonal to the mainstream ($p = 600$ Pa, $T = 150$ K, $\rho = 2.09 \cdot 10^{-2}$ kg/m³, $\dot{m} = 2.09 \cdot 10^{-6}$ kg/s, $\rho_p = 2.73 \cdot 10^3$ kg/m³).

For each case, the particles that cross the Sampling Volume show a sufficiently uniform velocity profile with a relative standard deviation less than 4% (Tab. 4.18), although it may change abruptly outside the Sampling Volume (Fig. 4.31).

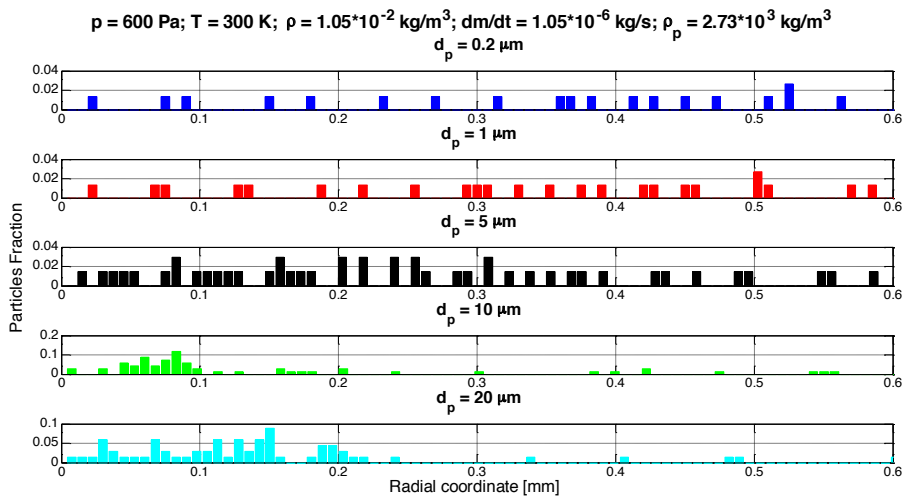


Fig. 4.24: Particle distributions in the middle plane of the Sampling Volume orthogonal to the mainstream ($p = 600$ Pa, $T = 300$ K, $\rho = 1.05 \cdot 10^{-2}$ kg/m³, $\dot{m} = 1.05 \cdot 10^{-6}$ kg/s, $\rho_p = 2.73 \cdot 10^3$ kg/m³).

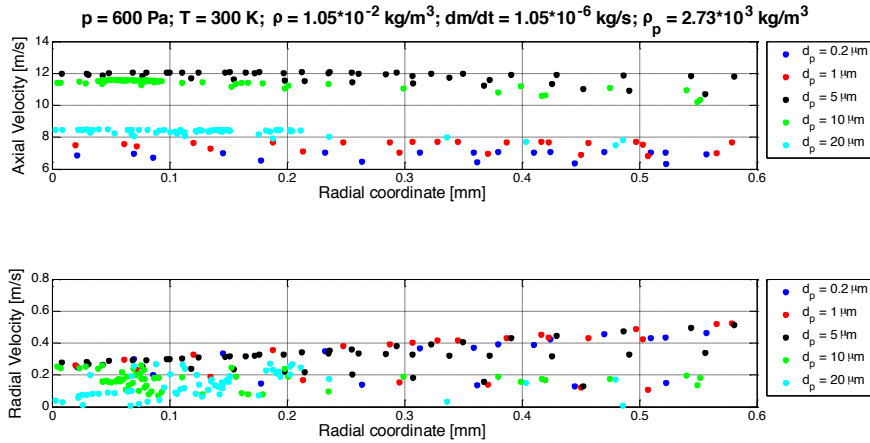


Fig. 4.25: Particle axial and radial velocity components in the middle plane of the Sampling Volume orthogonal to the mainstream ($p = 600 \text{ Pa}$, $T = 300 \text{ K}$, $\rho = 1.05 \cdot 10^{-2} \text{ kg/m}^3$, $\dot{m} = 1.05 \cdot 10^{-6} \text{ kg/s}$, $\rho_p = 2.73 \cdot 10^3 \text{ kg/m}^3$).

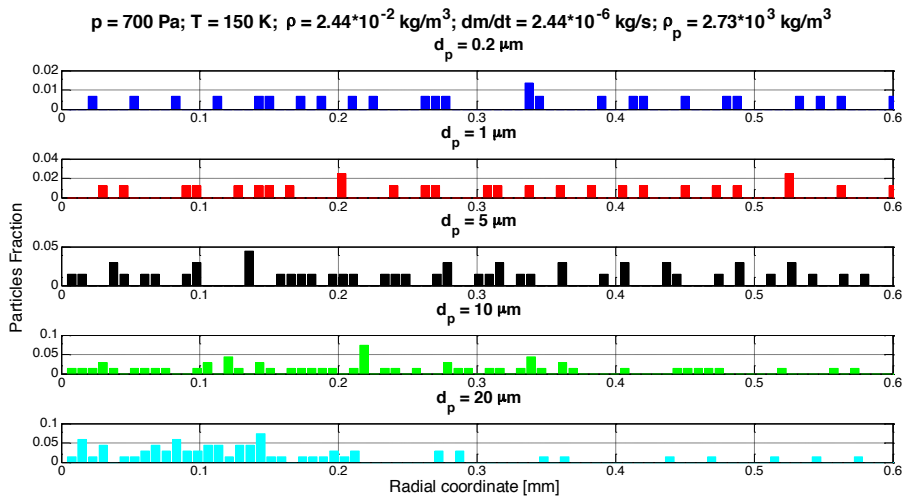


Fig. 4.26: Particle distributions in the middle plane of the Sampling Volume orthogonal to the mainstream ($p = 700 \text{ Pa}$, $T = 150 \text{ K}$, $\rho = 2.44 \cdot 10^{-2} \text{ kg/m}^3$, $\dot{m} = 2.44 \cdot 10^{-6} \text{ kg/s}$, $\rho_p = 2.73 \cdot 10^3 \text{ kg/m}^3$).

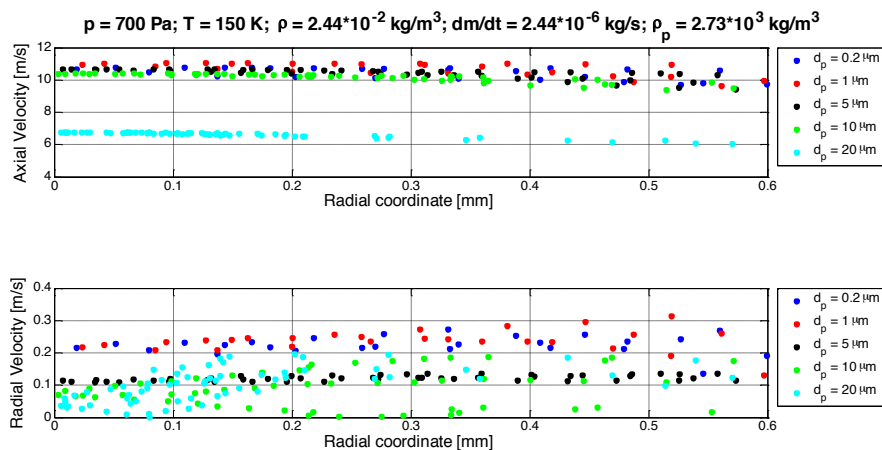


Fig. 4.27: Particle axial and radial velocity components in the middle plane of the Sampling Volume orthogonal to the mainstream ($p = 700 \text{ Pa}$, $T = 150 \text{ K}$, $\rho = 2.44 \cdot 10^{-2} \text{ kg/m}^3$, $\dot{m} = 2.44 \cdot 10^{-6} \text{ kg/s}$, $\rho_p = 2.73 \cdot 10^3 \text{ kg/m}^3$).

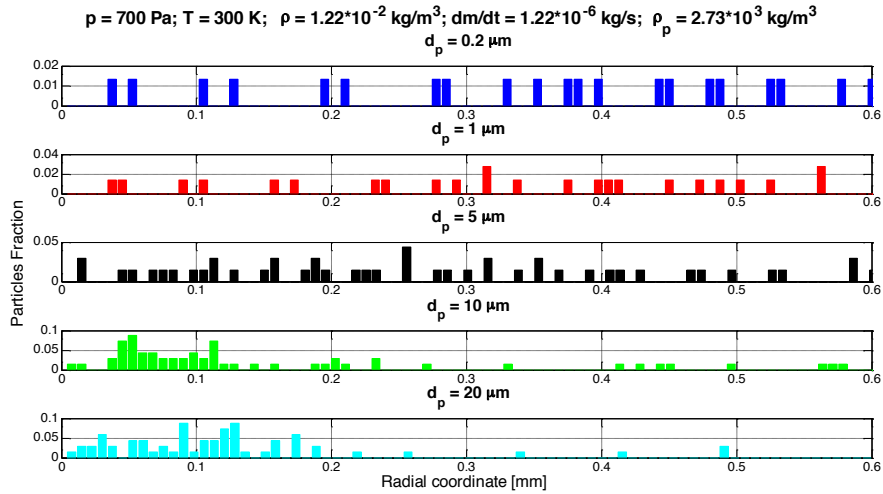


Fig. 4.28: Particle distributions in the middle plane of the Sampling Volume orthogonal to the mainstream ($p = 700 \text{ Pa}$, $T = 300 \text{ K}$, $\rho = 1.22 \cdot 10^{-2} \text{ kg/m}^3$, $\dot{m} = 1.22 \cdot 10^{-6} \text{ kg/s}$, $\rho_p = 2.73 \cdot 10^3 \text{ kg/m}^3$).

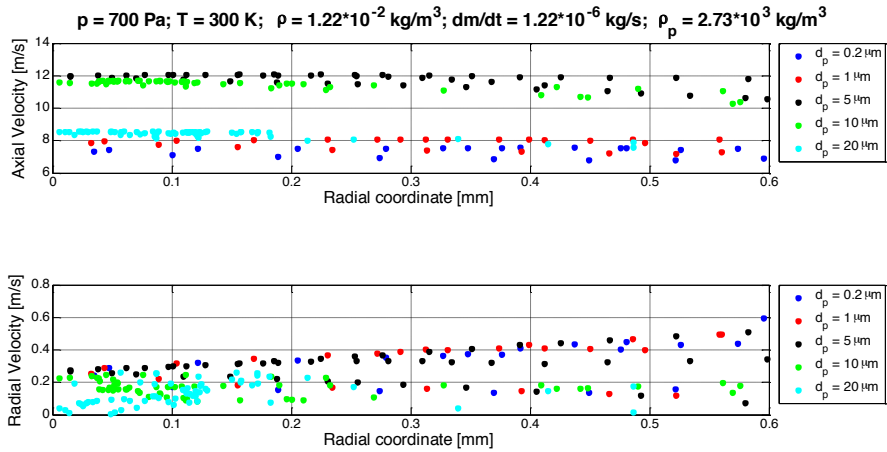


Fig. 4.29: Particle axial and radial velocity components in the middle plane of the Sampling Volume orthogonal to the mainstream ($p = 700 \text{ Pa}$, $T = 300 \text{ K}$, $\rho = 1.22 \cdot 10^{-2} \text{ kg/m}^3$, $\dot{m} = 1.22 \cdot 10^{-6} \text{ kg/s}$, $\rho_p = 2.73 \cdot 10^3 \text{ kg/m}^3$).

The velocity in the Sampling Volume clearly depends on the particle size and inertia and on the boundary conditions. The trend of the axial velocity of the particles in the Sampling Volume region is not clearly monotonic with respect to the particle size (d_p). This behaviour is a result of inertial effects and aerodynamic effects. Inertial effects, which are proportional to the particle mass, imply that particles should conserve mostly their kinematic state when fluid velocity locally accelerates/decelerates. The aerodynamic effects, which are proportional to the frontal area of the particles, imply that the larger particles are mostly subjected to the aerodynamic drag. Hence, the smaller particles, i.e., with low Stokes number (Eq. (3.83)), are subjected to smaller aerodynamic force, but show more acceleration than the larger ones when constrictions or enlargement occur in the domain. Therefore, the larger particles ($d_p > 10 \mu\text{m}$) are

mostly pushed by the drag force at the inlet, but with slower acceleration, so their velocity can be lower than that of the smaller particles in the Sampling Volume. In particular, very large particles ($d_p = 20 \mu\text{m}$) reach more slowly the Sampling Volume as they are not sufficiently accelerated at the inlet. Instead, moderate sized particles ($d_p = 5 \mu\text{m}$) can be both faster than the smaller ones and larger ones in the Sampling Volume region.

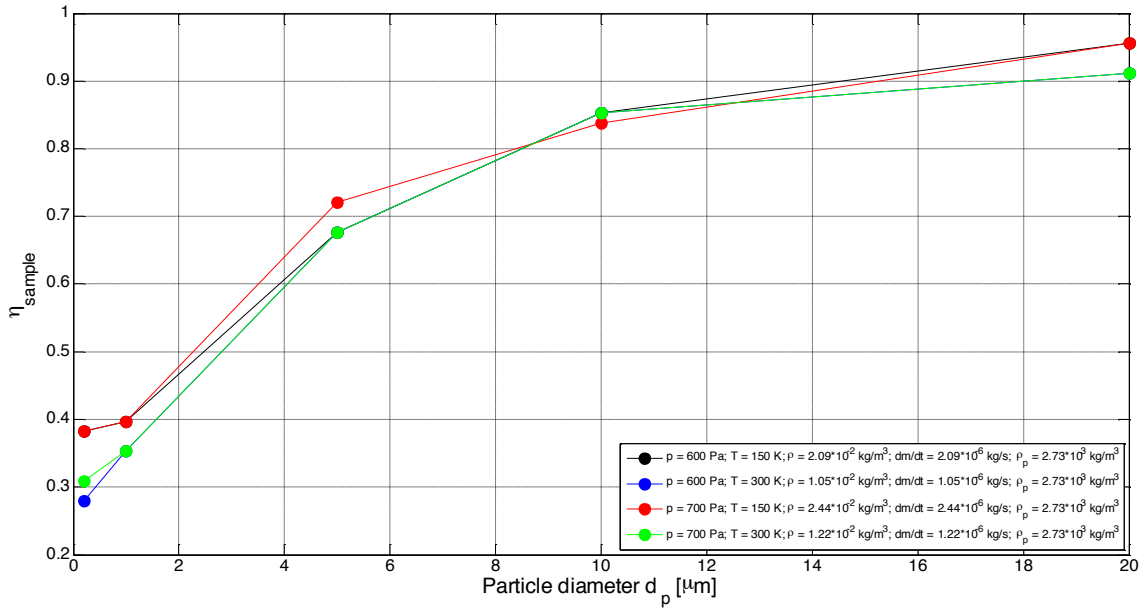


Fig. 4.30: MEDUSA OS sampling efficiency (η_{sample}) with respect to particle diameter (d_p) for different boundary conditions.

The same reasoning can be applied considering the radial velocity components of the particles. In this case, the aerodynamic force is quite lower as the fluid radial component is less than the axial component with a factor of 10^{-1} , so that the aerodynamic drag effects are less relevant. The particles are subjected to lower lateral forces, which cause more lateral deviations in the trajectories of the smaller particles ($d_p < 1 \mu\text{m}$) than of the larger ones, even if the trend is not monotonic as said above. The less radially deviated particles are those with $d_p = 10 \mu\text{m}$. In the worst case, the smallest particles ($d_p = 0.2 \mu\text{m}$) show a value up to about 13%, which is not negligible. Moreover, the smallest particles are disturbed along a larger distance from the centroid of the Sampling Volume (Fig. 4.31 vs. Fig. 4.32). As a result, the smallest particles ($d_p < 1 \mu\text{m}$) show sampling efficiencies $\eta_{\text{sample}} \approx 0.3$, while the largest particles ($d_p > 10 \mu\text{m}$) show $\eta_{\text{sample}} \approx 0.9$.

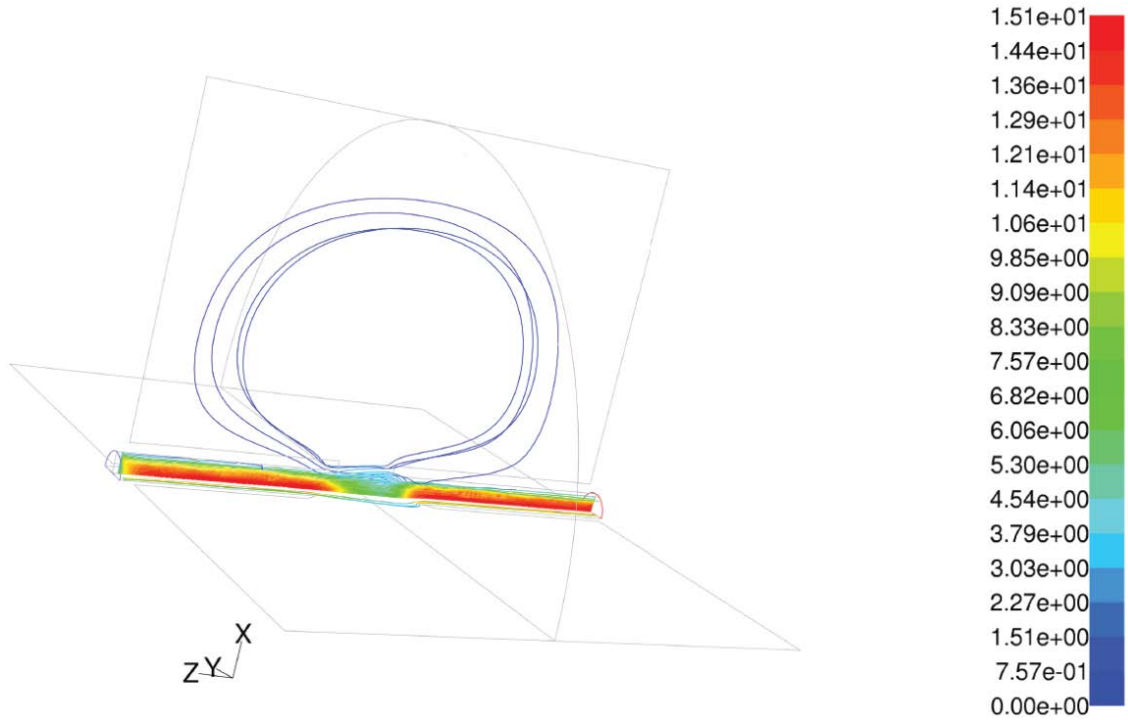


Fig. 4.31: Particle trajectories ($d_p = 0.2 \mu\text{m}$, $\rho_p = 2.73 \cdot 10^3 \text{ kg/m}^3$) coloured with velocity magnitude (m/s) in the MEDUSA OS at $p = 600 \text{ Pa}$, $T = 300 \text{ K}$, $\rho = 1.05 \cdot 10^{-2} \text{ kg/m}^3$, $\dot{m} = 1.05 \cdot 10^{-6} \text{ kg/s}$. The figure represents the geometry projected on 3 main planes and the full 3D trajectories.

The worst case, which implies less sampled particles through the Sampling Volume, occurs when the atmospheric density is low. The most rarefied case was considered for $p = 600 \text{ Pa}$, $T = 300 \text{ K}$ and $\rho = 1.05 \cdot 10^{-2} \text{ kg/m}^3$ (Fig. 4.24 and Fig. 4.25). In these conditions, pressure gradients mostly affect the particle direction in the Sampling Volume. At the Sampling Volume, fluid and particles inevitably spread abruptly in a region wider than the inlet duct, from which they come. Hence, in this region, fluid streamlines and particles trajectories are radially deviated from their main direction: these deviations are more evident when fluid is more rarefied as the weight of the pressure gradients is larger (Fig. 4.31). The sampling efficiency (η_{sample}) is reported in Fig. 4.30 for the discussed boundary conditions. The largest particles show little losses and most of them can be detected by MEDUSA. Several smaller particles spread in the OS and do not intersect the sensing region within a distance of 0.6 mm from the centroid, as confirmed by the sampling efficiency estimation.

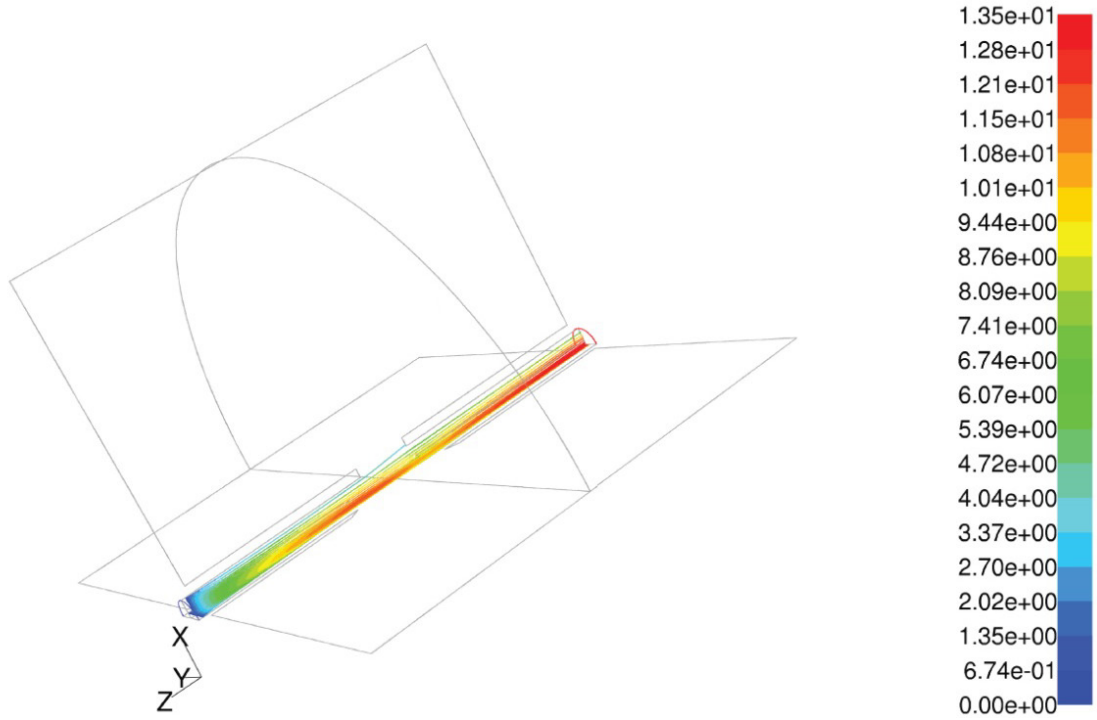


Fig. 4.32: Particle trajectories ($d_p = 10 \mu\text{m}$, $\rho_p = 2.73 \cdot 10^3 \text{ kg/m}^3$) coloured with velocity magnitude (m/s) in the MEDUSA OS at $p = 600 \text{ Pa}$, $T = 300 \text{ K}$, $\rho = 1.05 \cdot 10^{-2} \text{ kg/m}^3$, $\dot{m} = 1.05 \cdot 10^{-6} \text{ kg/s}$. The figure represents the geometry projected on 3 main planes and the full 3D trajectories.

A further aspect that was not considered in the CFD simulations, but that should be taken into account, is the possible occurrence of collisions between particles in the Sampling Volume region and/or in the inlet duct, above all in case of a high environmental concentration of large particles. Unfortunately, the CFD model cannot foresee these collisions and the related effects on the particle dynamics. Fortunately, the particles concentration on Mars should not imply frequent collisions in the operative conditions (Sect. 1.2.3). An approximated way to have idea of the frequency of particle collisions in the Sampling Volume is by calculating the ratio between the average distance between the particles in the Sampling Volume (D_p) and their diameter (d_p), as particle collisions occur when the distance between the centroid of the particles is equal to their diameter. If $\Delta n_p / \Delta V / \Delta t$ is the number of particles Δn_p distributed per unit volume ΔV and time Δt , the number of particles (n_{ps}) simultaneously present in the Sampling Volume (V_s) in the time interval that a particle takes to cross the Sampling Volume (Δt_c) can be valued with the following expression:

$$n_{ps} = \frac{\Delta n_p}{\Delta V \Delta t} V_s \Delta t_c \quad (4.6)$$

Hence, the particle number density in the Sampling Volume (N_{ps}) becomes:

$$N_{ps} = \frac{n_{ps}}{V_s} = \frac{n_p}{\Delta V} \frac{V_s}{\Delta t} \frac{\Delta t_c}{V_s} \approx \frac{N_p Q \Delta t_c}{V_s} \quad (4.7)$$

where N_p is the atmospheric particle number density and Q is volumetric flow rate. Δt_c can be estimated as the time interval that a particle with a velocity magnitude V_p takes to cross the Sampling Volume along the mainstream (Δs) (Eq. (4.15)).

$$V_p = \frac{\Delta s}{\Delta t_c} \Rightarrow \Delta t_c = \frac{\Delta s}{V_p} \quad (4.8)$$

D_p can be approximately valued as the cubic root of the reciprocal of the number of particles per unit volume found in the Sampling Volume:

$$D_p \approx \left(\frac{1}{N_{ps}} \right)^{1/3} = \left(\frac{V_s}{N_p Q \Delta t_c} \right)^{1/3} = \left(\frac{V_s V_p}{N_p Q \Delta s} \right)^{1/3} \quad (4.9)$$

For instance, considering a conservative case with a high Martian dust particle number concentration $N_p = 10^7$ particles/m³ for particles of size $d_p = 10 \mu\text{m}$ at a velocity $V_p = V_{p,a,m} = 11.47$ m/s (Tab. 4.18), and knowing that $V_s = 3.44 \cdot 10^{-9}$ m³, the sampling volume size is $\Delta s = 3.2 \cdot 10^{-4}$ m (Sect. 4.3.2.4), and $Q = 10^{-4}$ m³/s, the ratio D_p/d_p is equal to $\sim 500 \gg 1$, so the particle collision should not be frequent in the operative conditions of MEDUSA.

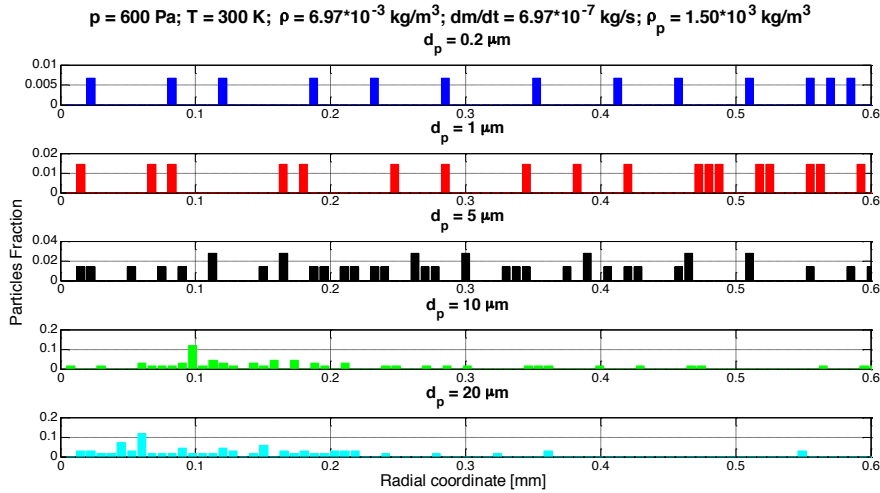


Fig. 4.33: Particle distributions in the middle plane of the Sampling Volume orthogonal to the mainstream ($p = 600$ Pa, $T = 300$ K, $\rho = 6.97 \cdot 10^{-2}$ kg/m³, $\dot{m} = 6.97 \cdot 10^{-7}$ kg/s, $\rho_p = 1.50 \cdot 10^3$ kg/m³) (Sect. 4.5.5, Test Case I).

CFD simulations were also performed in air (not CO_2) at $p = 600$ Pa, $T = 300$ K, $\rho = 6.97 \cdot 10^{-3}$ kg/m³, $Q = 10^{-4}$ m³/s, $\dot{m} = 6.97 \cdot 10^{-7}$ kg/s with sample particles of density $\rho_p = 1.50 \cdot 10^3$ kg/m³, which is a condition reproduced in laboratory to test the optical

detection system of MEDUSA (Sect. 4.5.5, Test Case I). The results related to these simulations are reported in Fig. 4.33, Fig. 4.34, and Fig. 4.35.

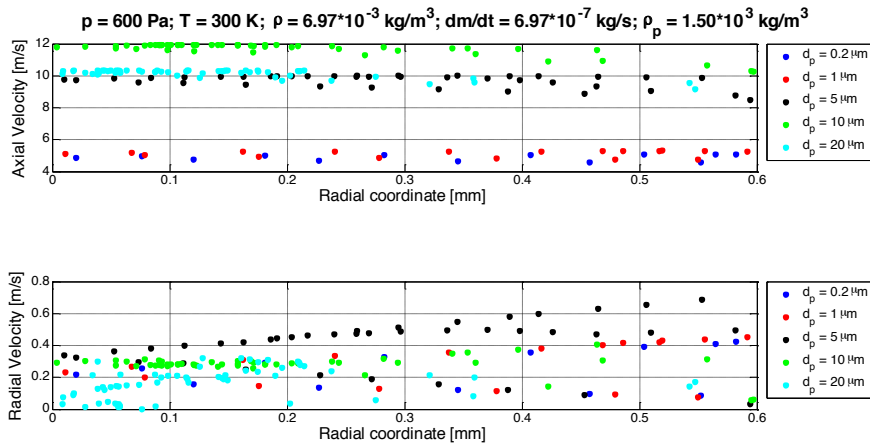


Fig. 4.34: Particle axial and radial velocity components in the middle plane of the Sampling Volume orthogonal to the mainstream ($p = 600 \text{ Pa}$, $T = 300 \text{ K}$, $\rho = 6.97 \cdot 10^{-2} \text{ kg/m}^3$, $\dot{m} = 6.97 \cdot 10^{-7} \text{ kg/s}$, $\rho_p = 1.50 \cdot 10^3 \text{ kg/m}^3$) (Sect. 4.5.5, Test Case I).

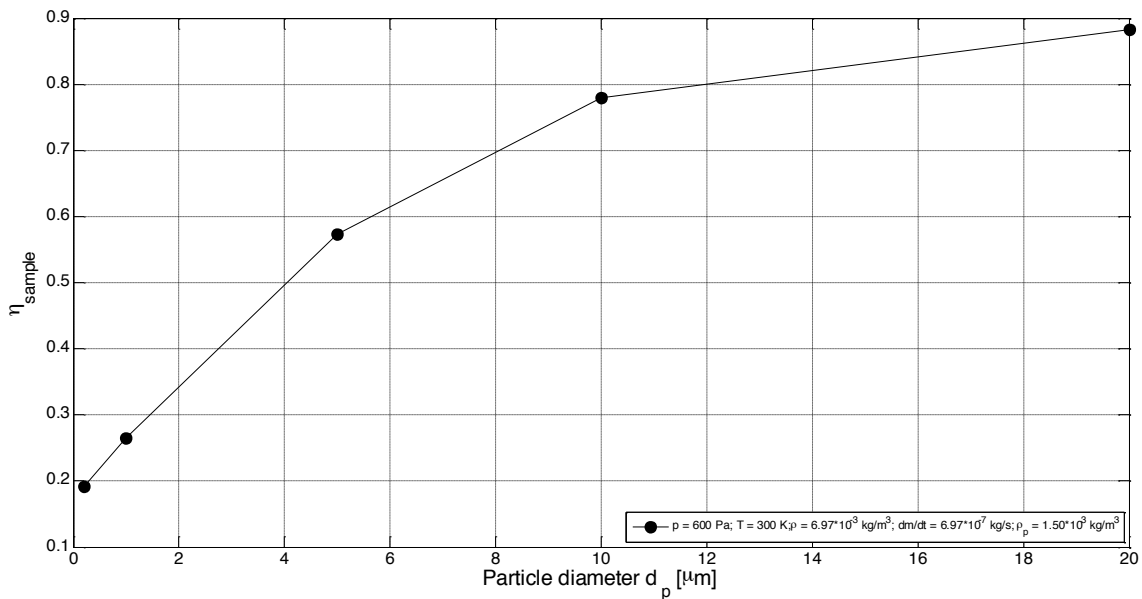


Fig. 4.35: MEDUSA OS sampling efficiency (η_{sample}) with respect to particle diameter (d_p) in air (Sect. 4.5.5, Test Case I).

In this case since the molecular mass of air is smaller than carbon dioxide, at same pressure (600 Pa) and temperature (300 K), air has a lower density than carbon dioxide. The sample particles used in this case are less dense. This is a more difficult condition for the MEDUSA operations. In fact, the sampling efficiency is worse (Fig. 4.35 vs. Fig. 4.30) due to more rarefaction effects involving higher flow divergence in the Sampling Volume region and swirling streamlines in the OS box, which even affect significantly the dynamics of larger particles as for $d_p = 5 \mu\text{m}$ (Fig. 4.36).

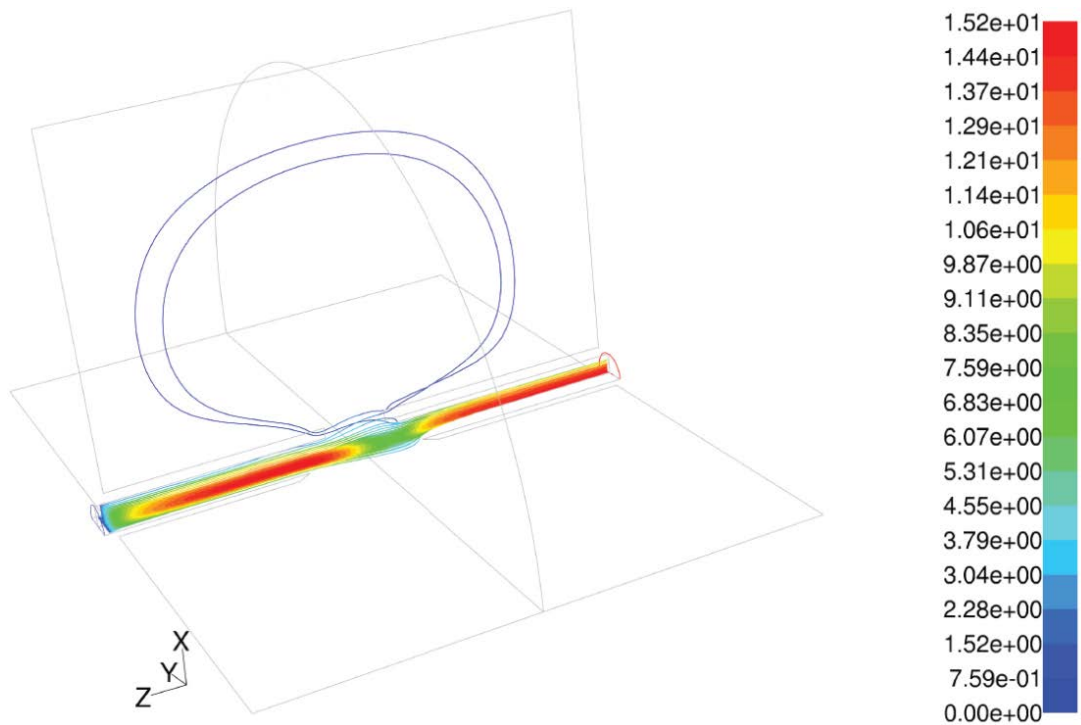


Fig. 4.36: Particle trajectories ($d_p = 5 \mu\text{m}$, $\rho_p = 1.50 \cdot 10^3 \text{ kg/m}^3$) coloured with velocity magnitude (m/s) in the MEDUSA OS at $p = 600 \text{ Pa}$, $T = 300 \text{ K}$, $\rho = 6.97 \cdot 10^{-3} \text{ kg/m}^3$, $\dot{m} = 6.97 \cdot 10^{-7} \text{ kg/s}$ (Sect. 4.5.5, Test Case I). The figure represents the geometry projected on 3 main planes and the full 3D trajectories.

In Tab. 4.18 the mean value and standard deviation of the profiles of the particle axial and radial velocity in the Sampling Volume are reported for all the simulations.

d_p (μm)	p (Pa)	T (K)	ρ (kg/m^3)	\dot{m} (kg/s)	$V_{p,a,m}$ (m/s)	$\sigma_{V_{p,a}}$ (m/s)	$V_{p,r,m}$ (m/s)	$\sigma_{V_{p,r}}$ (m/s)
0.2	600	150	$2.09 \cdot 10^{-2}$	$2.09 \cdot 10^{-6}$	10.18	0.370	0.242	0.030
1					10.51	0.412	0.254	0.041
5					10.22	0.412	0.164	0.022
10					10.13	0.263	0.093	0.058
20					6.62	0.175	0.101	0.053
0.2	600	300	$1.05 \cdot 10^{-2}$	$1.05 \cdot 10^{-6}$	6.86	0.274	0.309	0.123
1					7.47	0.307	0.307	0.132
5					11.82	0.334	0.316	0.080
10					11.38	0.312	0.171	0.052
20					8.36	0.201	0.137	0.076
0.2	700	150	$2.44 \cdot 10^{-2}$	$2.44 \cdot 10^{-6}$	10.43	0.368	0.225	0.027
1					10.69	0.417	0.238	0.034
5					10.41	0.307	0.122	0.008
10					10.18	0.256	0.089	0.056
20					6.62	0.173	0.099	0.053
0.2	700	300	$1.22 \cdot 10^{-2}$	$1.22 \cdot 10^{-6}$	7.31	0.299	0.320	0.129
1					7.82	0.322	0.324	0.121
5					11.75	0.412	0.305	0.089
10					11.47	0.327	0.168	0.045
20					8.43	0.202	0.133	0.074
0.2	600	300	$6.97 \cdot 10^{-3}$	$6.97 \cdot 10^{-7}$	4.89	0.200	0.253	0.124
1					5.13	0.206	0.290	0.134
5					9.69	0.401	0.414	0.154
10					11.72	0.402	0.283	0.056
20					10.17	0.251	0.168	0.094

Tab. 4.18: Particle mean axial velocity ($V_{p,a,m}$) and standard deviation ($\sigma_{V_{p,a}}$) and particle mean radial velocity ($V_{p,r,m}$) and standard deviation ($\sigma_{V_{p,r}}$) in the middle plane of the Sampling Volume orthogonal to the mainstream within a radius of 0.60 mm from the Sampling Volume centroid.

4.5.2 Test and Verification of the Laser Diode

The optical power emitted by the laser diode of MEDUSA was experimentally determined to verify if the breadboard model was compliant to the measurements specifications (Tab. 4.7). Two types of measurements were performed in laboratory:

- The integral optical power of the laser diode coupled with the optical fiber without the MEDUSA OS;
- The integral optical power of the laser diode coupled with the optical fiber and optically connected to the MEDUSA OS.

The Laser Diode Assembly and the MEDUSA OS were mounted on an optical bench in order to direct properly the laser beam to a laser power meter. In the first case the laser beam was measured directly from the Laser Diode Assembly; in the second case it crossed the MEDUSA OS and the beam was received by the detector through the window for the light trap. The laser diode was supplied with a driver control (Fig. 4.37) with which it was set the laser diode to work at its nominal optical power of 1 W.

Power Supply for the Laser Diode	
Supplier	Newport Laser Diode Controller
Model	6000
Current	Typical: 1303.3 mA
Temperature control	20 °C




Fig. 4.37: The Newport Laser Diode Controller.

The integral power of the laser beam collected by the power meter in the two measurements is reported in Tab. 4.19.

Laser diode current	1300 mA
Laser power (laser diode + optical fiber)	0.790±0.005 W
Laser power (laser diode + optical fiber + MEDUSA OS without light trap)	0.665±0.005 W

Tab. 4.19: Laser power measurements.

The measurements confirmed that only a little loss of the optical power of the laser (15.8%) occurred through the MEDUSA OS. The average optical power density in the Sampling Volume region is on average 7,470 mW/mm². Moreover, it was understood that the alignment of the laser beam through the MEDUSA OS is very critical as small misalignments can generate significant reduction of the optical power and stray light increases.

4.5.3 Stray Light Analysis

The stray light, i.e., the baseline electrical response of the MEDUSA OS, was measured to find possible causes of undesired reflection and propagation of the laser light in the OS box, and, then, to identify the background level of the optical power and PE channels signals above which scattering measurements are possible.

In the test, the Laser Diode Assembly was turned on and the light intensity was measured by the photodiodes in order to quantify the MEDUSA OS signal output without particles (i.e., the unwanted light not-absorbed by the light trap or walls). The photodiodes and the PE were fed by a power supply device. The response signals, which came from the photodiodes/PE, were transmitted to an external differential amplifier and, then, to a digital multimeter to be evaluated. The stray light output was quantified as the Voltage response of the PE channels. The measurements were performed individually for the forward and backward channel. The stray light measurements are reported in Tab. 4.20. They are taken into account as the offset signals of the channels (Sect. 4.5.5). Finally a significant influence of the position of the baffles over the stray light was recorded.

Laser diode supply current	1300 mA
Proximity Electronics supply voltage	12 V
Forward Low Gain output from the PE due to the stray light	0.280±0.005 V
Backward Low Gain output from the PE due to the stray light	0.520±0.005 V

Tab. 4.20: Stray light measurements.

4.5.4 Theoretical Scattering Analysis

Theoretical predictions based on the mathematical solution of the Mie theory (Sect. 3.2.2) were used to foresee the performance of MEDUSA to detect particles by scattering analysis. The calculation, made with the support of dedicated routines written in IDL, is based on the following input parameters:

- Laser power density and wavelength in the sensing region;
- Particles complex refractive index and size;
- Angular collection of the light;
- Responsivity of the detector.

Considering a spherical particle with diameter d_p , real refractive index n_r , imaginary refractive index n_i , which is in the Sampling Volume, the total scattered power (P_s) by the particle is:

$$P_s = \Delta Q_s(\lambda, n, d_p) \pi \frac{d_p^2}{4} \quad (4.10)$$

where Δ is the power density, and Q_s is the scattering efficiency derived by the Mie theory (Bohren, C.F., Huffman, D.R., 1998). The power collected by a detector between the angles of scattering of θ and $\theta+\Delta\theta$ is given by ($P_{s,\theta, \theta+\Delta\theta}$):

$$P_{s,\theta,\theta+\Delta\theta} = 2\pi^2 \frac{d_p^2}{4} \Delta Q_s \int_{\theta}^{\theta+\Delta\theta} L(\theta) \sin(\theta) d\theta \quad (4.11)$$

$L(\theta)$ is the scalar phase function so that:

$$2\pi \int_0^{\pi} L(\theta) \sin(\theta) d\theta = 1 \quad (4.12)$$

The detectors receive the optical power and convert it into a current. The output current is related to the optical power through the detectors responsivity $R(\lambda)$:

$$I_s = R(\lambda) P_{s,\theta,\theta+\Delta\theta} \quad (4.13)$$

Moreover, the detector sensibility defines the threshold level above which it is possible to identify the received optical power as a signal from a particle. As seen previously, the laser beam reaches the MEDUSA Sampling Volume with an optical power of 0.665 W at a wavelength of 808 nm (Sect. 4.5.2) and the Sampling Volume is 0.32 mm x 3.0 mm orthogonal to the laser beam and 1.20 mm along the laser beam direction (Sect. 4.5.4). Therefore, the input optical power density in the particle crossing region is $6.927 \cdot 10^5 \text{ W/m}^2$. Typically the complex refractive index of the Martian dust is $n_r = 1.5$. The scattered light is captured within a collecting angle of $\pm 33^\circ$ by the forward mirror and $\pm 47^\circ$ by the backward mirror (Sect. 4.3.2.3). The responsivity of the detector is 0.5 A/W and the dark current is 25 nA (Sect. 4.3.2.6).

The solution shows that the minimum detectable particle diameter is $d_p < 0.4 \mu\text{m}$ with forward scattering and $d_p < 0.6 \mu\text{m}$ with backward scattering. The results are reported in Fig. 4.38 and Fig. 4.39 for the optical power scattered by particles and the related current intensity by the photodetectors, respectively. The minimum sizes detectable by the forward and backward scattering are the intersection between the theoretical Mie's curves and the detectors current threshold (Fig. 4.39, Fig. 4.41).

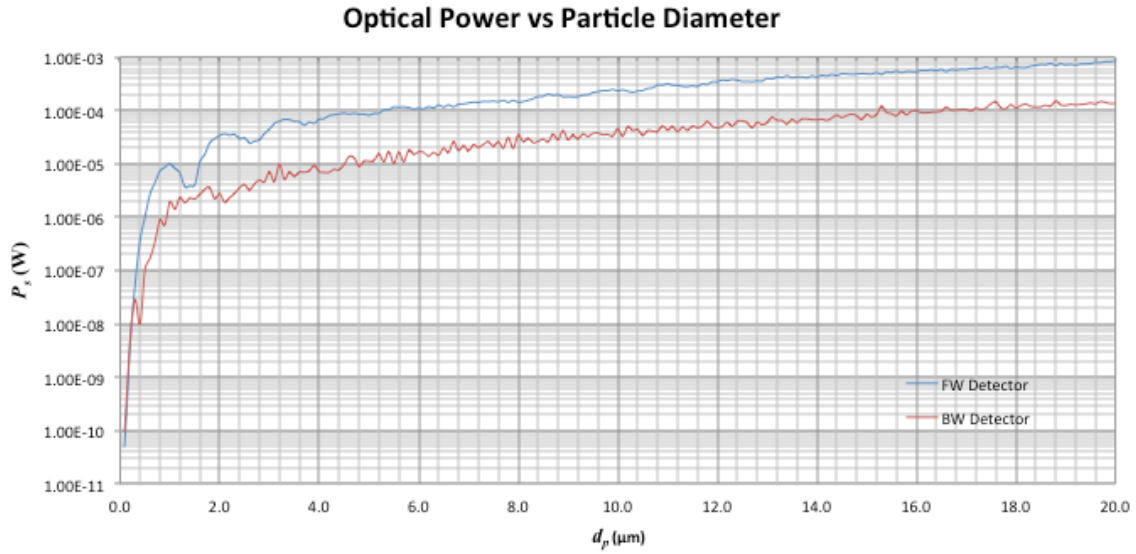


Fig. 4.38: Optical power (P_s) vs. particle diameter (d_p) detectable by the MEDUSA forward and backward detectors as foreseen by the Mie theory.

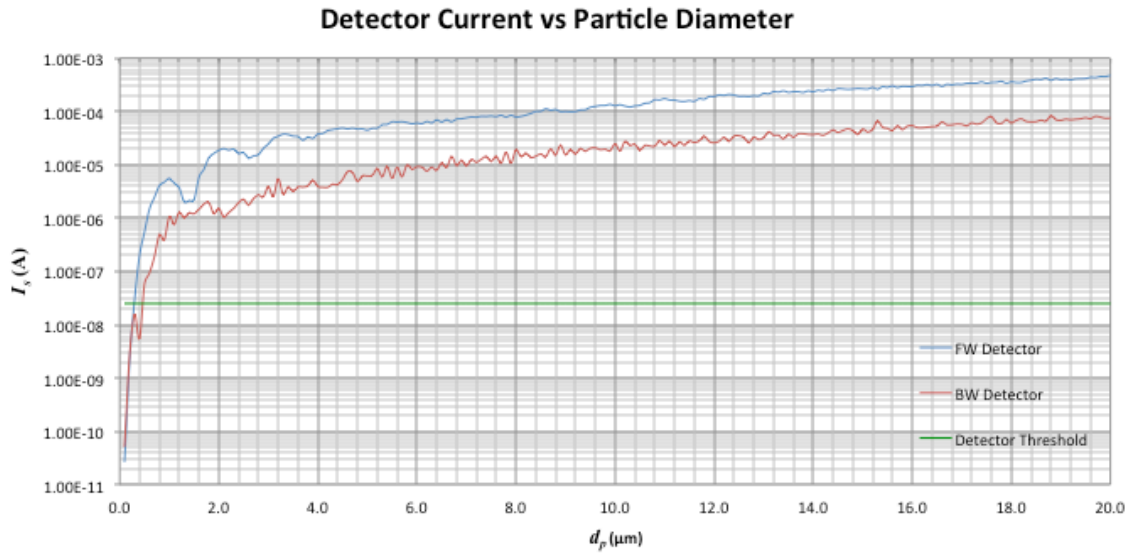


Fig. 4.39: Current intensity (I_s) vs. particle diameter (d_p) detectable by the MEDUSA forward and backward detectors as foreseen by the Mie theory.

The results for the smaller particles (Fig. 4.40, Fig. 4.41) show that the light scattered over a small solid angle shows a polytonic response. The polytonic response is foreseen by the Mie theory and is due to resonance effects, which occur particularly in the diameter range 1-3 μm , mainly for the forward direction, and depend on the refractive index and the scattering angle width. The polytonic behaviour of the scattering response could be a problem for the MEDUSA application since it may generate uncertainty on the particle size determination from the detector current reading. The polytonic behaviour is smoother if the particles are highly absorptive, the scattering direction is

far from 0° (forward direction), and the collecting angle is wide (e.g., 130°). By superimposing the optical power scattered within two solid angular ranges a monotonically increasing response versus particle size can be obtained.

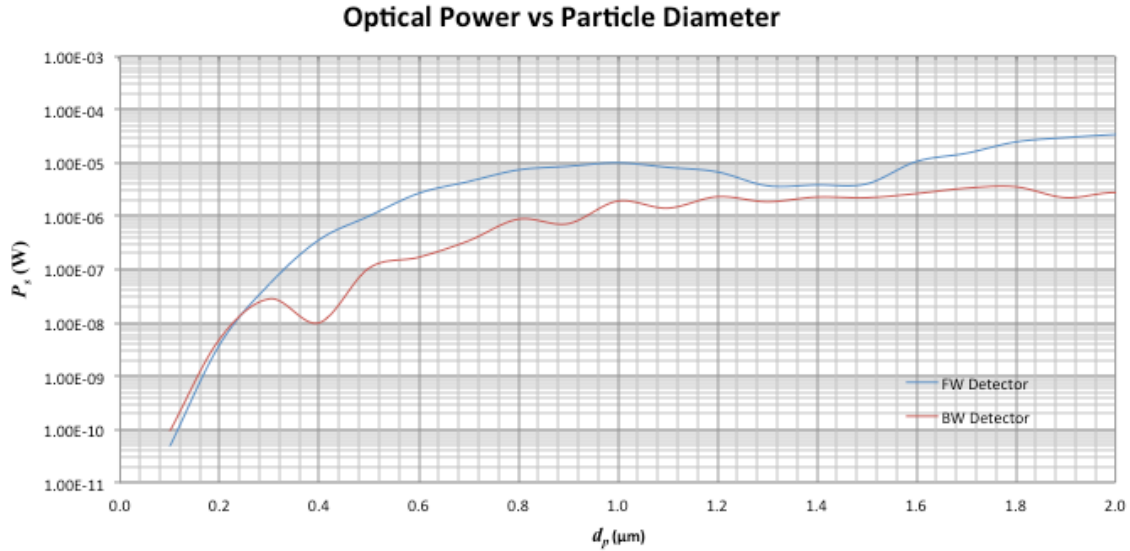


Fig. 4.40: Optical power (P_s) vs. particle diameter (d_p) detectable by the MEDUSA forward and backward detectors as foreseen by the Mie theory (detail in the range $d_p = 0.1\text{-}2 \mu\text{m}$).

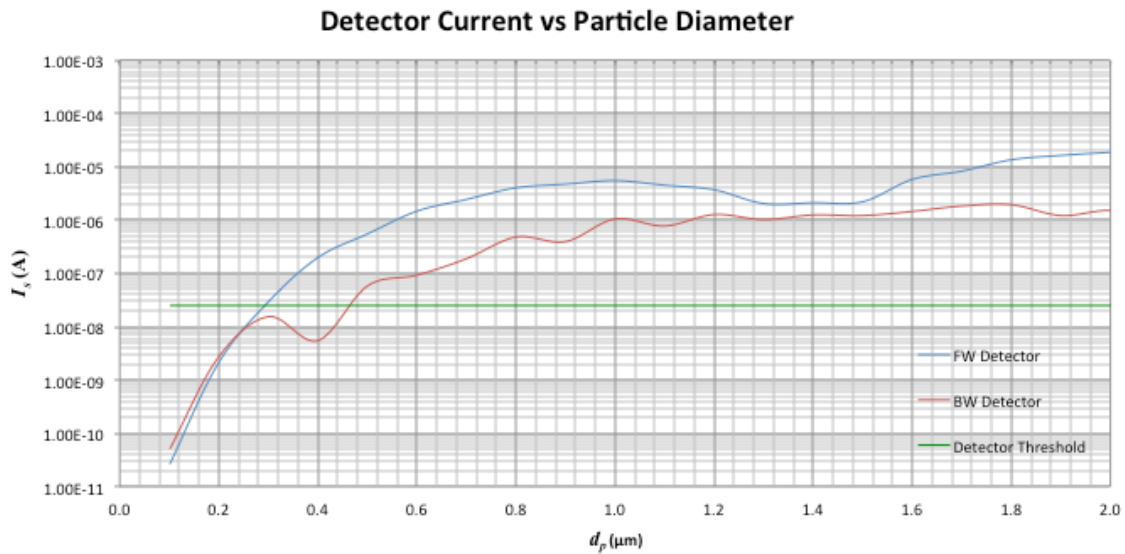


Fig. 4.41: Current intensity (I_s) vs. particle diameter (d_p) detectable by the MEDUSA forward and backward detectors as foreseen by the Mie theory (detail in the range $d_p = 0.1\text{-}2 \mu\text{m}$).

4.5.5 Experimental Tests on the Detection System

The MEDUSA OS breadboard was tested for characterizing the capability to recognize and detect sample particles across the Sampling Volume in order to accomplish the requirements declared in Tab. 4.8. These experimental tests are complementary to the CFD predictions (Sect. 4.5.1), the experimental optical

verifications of the OS elements (Sect. 4.5.2, 4.5.3), and the optical predictions based on the Mie theory (4.5.4). The tests on the MEDUSA detection system were performed in an environment, which partly reproduced the conditions in the Martian atmosphere at surface level (Fig. 4.42).

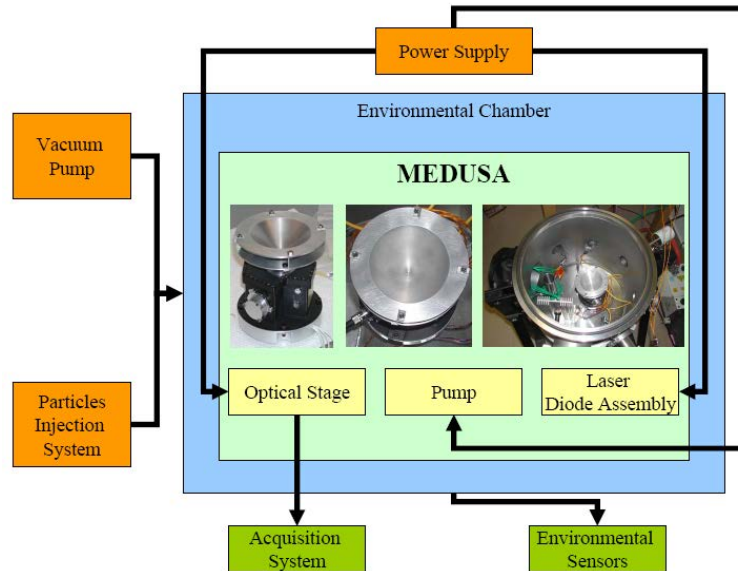


Fig. 4.42: Experimental setup scheme for tests on the MEDUSA OS breadboard.

The MEDUSA breadboard was accommodated in an environmental test chamber. The chamber is a cylinder (internal dimensions 0.32 m x 0.32 m x 0.30 m) made of stainless steel with an internal volume of $25 \cdot 10^{-3} \text{ m}^3$ (25 l). The chamber was sealed and isolated from the external environment and equipped with pipelines to inject sample dust particles. The test chamber was used to reproduce the typical Martian pressure conditions.

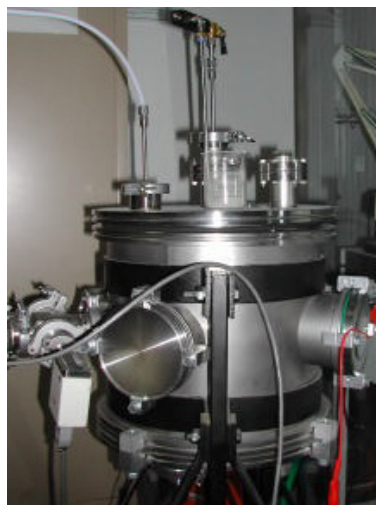


Fig. 4.43: The environmental test chamber.

In these tests, the atmospheric fluid was air. No specific thermal control was applied. Hence, the tests conditions were focused on the most critical parameter, which is the environmental pressure. In fact, as said in Sect. 4.5.1, at specific pressure and temperature conditions, air is less dense than the Martian atmospheric fluid (mainly CO_2). Pressure and temperature in the chamber were monitored with suitable gauges.

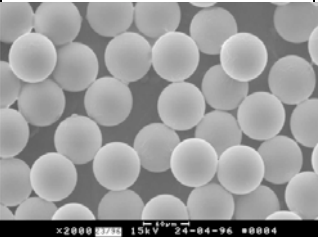
Particles		
Supplier	MicroParticles GmbH, Germany	
Type	MF-R-S1141	
Material	Monodisperse melamine-formaldehyde resin	
Chemical composition	$(C_3H_8N_6O)_n, H_2O$	
Physical state	Dispersed solid sphere	
Appearance	White aqueous dispersion	
Density at 20°C	$1.51 \cdot 10^3 \text{ kg/m}^3$	
Refractive index	1.68	
Solubility	Insoluble in water and in organics	
Melting point	> 300°C	
Diameter	9.78±0.17 μm; 4.83±0.12 μm; 1.14±0.05 μm	

Fig. 4.44: The sample particles datasheet.

Monodisperse sample particles were injected in the chamber in order to cross dynamically the MEDUSA Sampling Volume. The particles (MicroParticles GmbH MF-R-S1141, Fig. 4.44) used for the tests were melamine-formaldehyde resin with diameter of 1 μm, 5 μm, and 10 μm, respectively. Each monodisperse sample carried 1 mg of total mass of particles, which correspond to $1.26 \cdot 10^9$ particles of 1 μm in size, $1.01 \cdot 10^7$ particles of 5 μm in size, and $1.26 \cdot 10^6$ particles of 10 μm in size, respectively. The experimental analysis involved three test cases, whose settings are reported in Tab. 4.21.

	Case I	Case II	Case III
Gas composition	Air	Air	Air
Gas constant (J/kg/K)	287	287	287
Pressure (Pa)	300-600	$1.013 \cdot 10^5$	$1.013 \cdot 10^5$
Temperature (K)	293	293	293
Fluid Density (kg/m^3)	$7.14 \cdot 10^{-3}$	1.225	1.225
Experiment time duration (s)	300	300	300
Sampling particles diameter (μm)	1, 5, 10	1, 5, 10	None
MEDUSA Pump On/Off	On	Off	Off
MEDUSA Pump Voltage (V)	5	-	-
MEDUSA Pump Volumetric Flow Rate (m^3/s)	$1 \cdot 10^{-4}$	-	-
MEDUSA Pump Mass flow rate (kg/s)	$1.18 \cdot 10^{-4}$	-	-

Tab. 4.21: Test cases for the MEDUSA breadboard.

In the test case I, the pressure in the test chamber was set at 600 Pa, which is a typical pressure level of the atmosphere on the surface of Mars, by using a rotary

vacuum pump. The pump was connected to the chamber via an on/off valve to set the desired pressure level. Pressure gauge measured the pressure in the chamber. The chamber was also equipped with a pipeline to introduce the sample particles. In this case the sample particles were introduced separately for each size (1 μm , 5 μm , and 10 μm). As soon the pressure level in the chamber was stabilized at 600 Pa, the particles were injected through the pipeline and spread in the chamber. As the settling velocity of the particles is less than 10^{-2} m/s (Fig. 3.3) and the chamber height is 0.30 m, particles move in the chamber for at least 30 s before gravitational deposition occurs. During this time, the MEDUSA pump was turned on, as in an operative run, in order to aspire the particles dispersed in the chamber. After each run the chamber and the pipelines were carefully cleaned to avoid contamination between the samples. The pressure was also set down to 300 Pa to verify stability of the response at very lower pressure levels.

In the test case II, the sample particles were directly shoot in the MEDUSA OS, pushed by a compressed air flow, which made a jet under the action of a pressure difference of 700 kPa from the laboratory reservoir to the exhaust region in the test chamber. MEDUSA was at a pressure of $1.013 \cdot 10^5$ Pa in the test chamber and the MEDUSA pump was turned off and was not used. These tests were quite different from the operative conditions on Mars. Nevertheless, they were used to inject the particles in the MEDUSA OS and evaluate the PE/detector response to the particles crossings. Also in this case the monodispersed samples (size 1 μm , 5 μm , and 10 μm) were used in separated runs.

In the test case III, the procedure was quite similar to the test case II, but without injecting artificially sample particles. Hence, theoretically MEDUSA was crossed by clean air flows. Again, the MEDUSA pump was turned off. Therefore, in this case all matter that crossed the MEDUSA Sampling Volume was due to previous deposition in the MEDUSA breadboard.

During the tests cases the MEDUSA PE and detectors were electrically supplied and the laser diode was controlled by a suitable driver (Fig. 4.37) to work at its nominal optical power. The LDA was accommodated inside the chamber as no low temperature was reached and low pressure was not critical for the laser. The PE/detectors give 4 output channels (FWH, FWL, BWH, and BWL), as explained in Sect. 4.3.2.7. Their

output signals were acquired with laboratory hardware and software by National Instrument (LabView).

Some stubs with smooth surfaces were placed both in the test chamber and inside MEDUSA for particle deposition. The use of the stubs was necessary to verify the size and accumulation of the injected particles for each test. After each test, the related stubs were observed under a *Scanning Electron Microscope (SEM)*.

The signals acquired by the photodiodes correspond to the optical power of the scattered light by the particles plus a baseline due to stray light and electronics noise. Each signal is converted by the respective MEDUSA forward or backward photodiode into a current, and, then, further converted into a voltage signal by the MEDUSA PE (Sect. 4.3.2.7). The electrical dynamic range of each channel extends in the range ± 10 V.

The signals coming from each of the four channels in absence of particles show a proper temporal oscillation mode at high frequency and under a threshold level, which correspond to the total noise of the channel. When a particle crosses the Sampling Volume, the signal shows a peak. The amplitude of the peak should depend mainly on the size of the particles for the forward channels (FWH and FWL), and on the size and refractive index of the particles for the backward channels (BWH and BWL), according to the Mie theory. The duration of the peak should, instead, depend mainly on the velocity of the particles, which also depends on the boundary conditions, particles inertia (mass, density and size), and their trajectory across the Sampling Volume, as the laser beam intensity is not completely uniform in all points of the Sampling Volume. Numerical simulations in Sect. 4.5.1 show that for the tests case I, the particles should have a velocity of 5-12 m/s, so, if they cross straight the Sampling Volume, which has a size of $3.2 \cdot 10^{-4}$ m, the transit should last $2.67 \cdot 10^{-5}$ - $6.40 \cdot 10^{-5}$ s on average.

These tests have the main goal to demonstrate the functionality of the system in detecting grains with different sizes. At this stage of the project they are not yet intended to establish correspondence functional relationship between the size of the particles and scattering signals acquired by the 4 channels. Some examples of detected signal are shown in the following. In the reported plots, which are extracted from longer temporal acquisitions, the response signals of each series were scaled to an arbitrary

reference starting time 0 s, and the offset of each channel, due to stray light (Tab. 4.20) and noise, was reset at 0 V to facilitate the comparison between the channels.

Signal acquired in the test case I for the high and low gain channels and for the monodispersed sample are reported in Fig. 4.45, Fig. 4.46, Fig. 4.47, Fig. 4.48, Fig. 4.49, and Fig. 4.50, respectively.

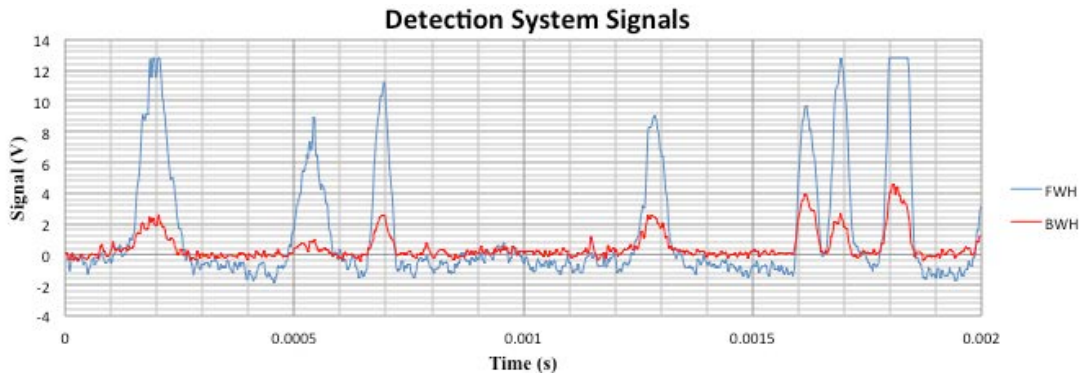


Fig. 4.45: FWH and BWH signals from the Test Case I for $d_p = 1 \mu\text{m}$.

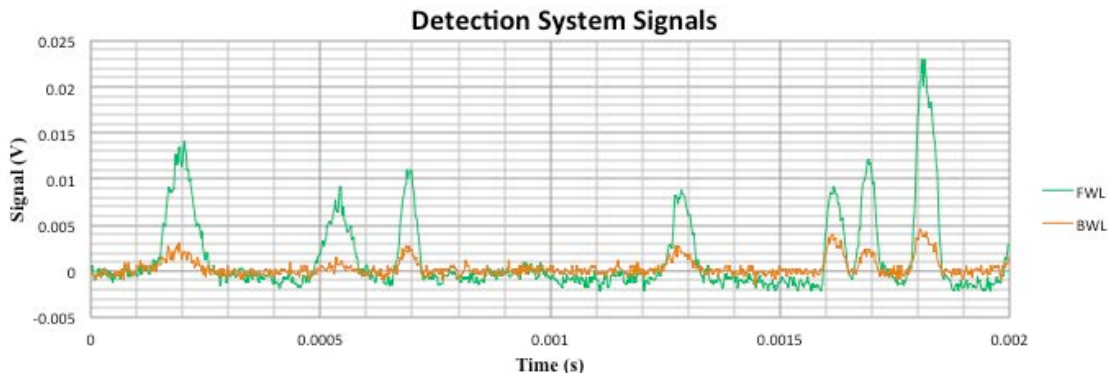


Fig. 4.46: FWL and BWL signals from the Test Case I for $d_p = 1 \mu\text{m}$.

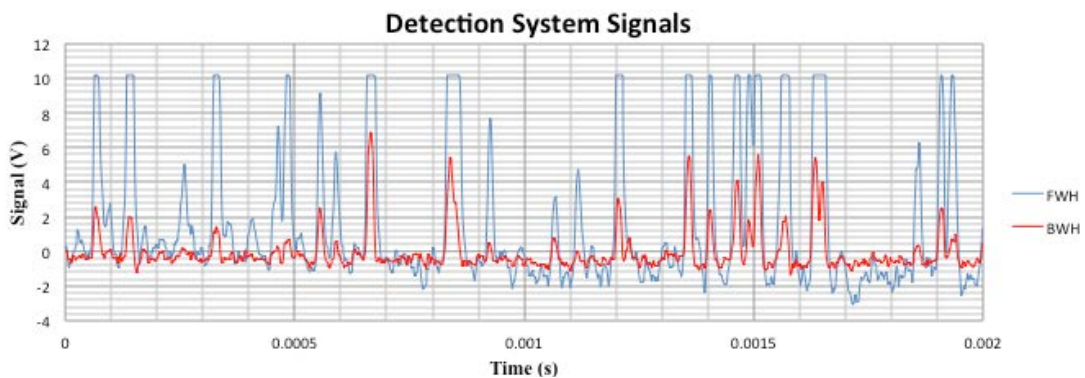


Fig. 4.47: FWH and BWH signals from the Test Case I for $d_p = 5 \mu\text{m}$.

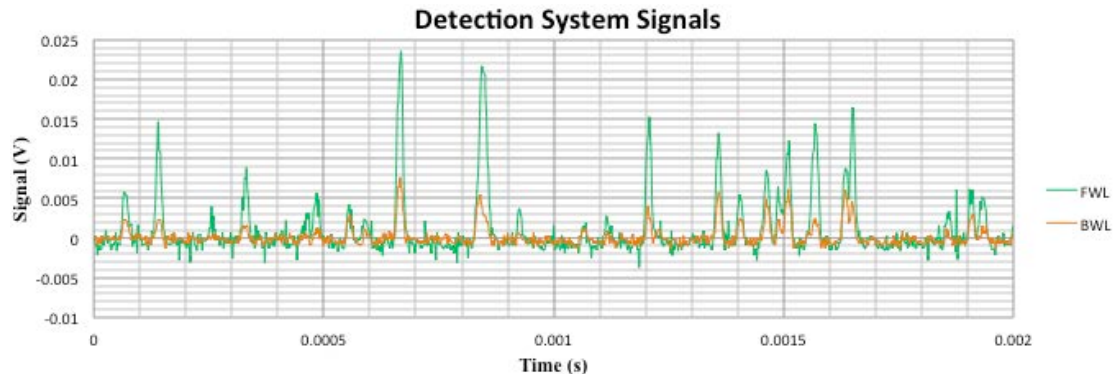


Fig. 4.48: FWL and BWL signals from the Test Case I for $d_p = 5 \mu\text{m}$.

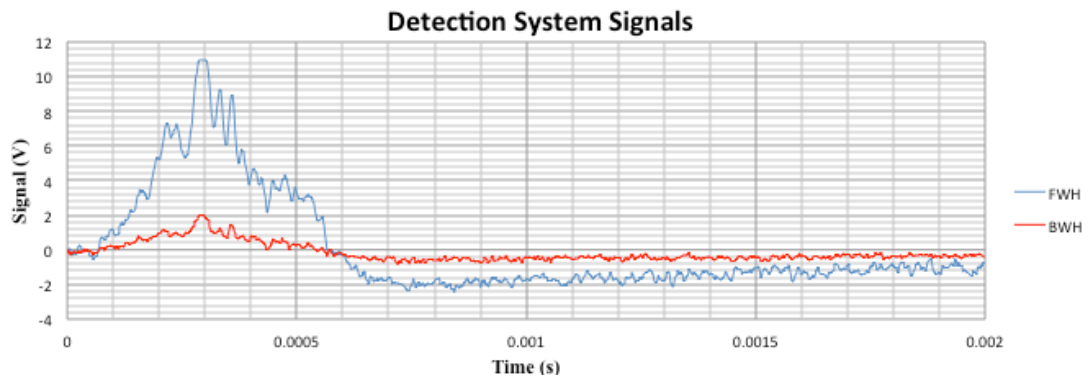


Fig. 4.49: FWH and BWH signals from the Test Case I for $d_p = 10 \mu\text{m}$.

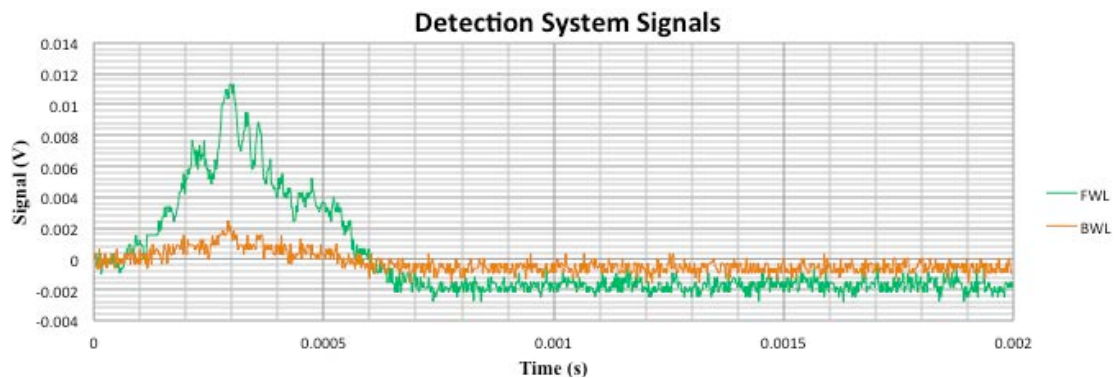


Fig. 4.50: FWL and BWL signals from the Test Case I for $d_p = 10 \mu\text{m}$.

The results of test case I show that the system is sensitive to the passage of particles with different sizes across the Sampling Volume even at very low-pressure levels (300-600 Pa). Each event was registered simultaneously by the 4 channels, but with different amplitude due to scattering direction (forward/backward) and electronics amplification level (high/low gain). The MEDUSA pump was able to work in rarefied conditions and to aspirate particles of different sizes making them to cross the Sampling Volume region.

A wide variety of events is recorded. Several events producing saturation of the high gain channels also occurred for small particles ($d_p = 1 \mu\text{m}$), while saturation should be expected only for large particles ($d_p = 5\text{-}10 \mu\text{m}$). Several events show a duration of about 10^{-4} s, while the expected duration is about 10^{-5} s (Sect. 4.5.1). Saturation of the high gain channels for the smaller particles could be due to a simultaneous crossing of more than one particle seen by the system as a single event. This behaviour is clearly shown when the high gain channels have a large and long peak, while the corresponding low gain channels show several peaks.

Signals acquired from the test case II for the high and low gain channels and for the monodispersed sample are reported in Fig. 4.51, Fig. 4.52, Fig. 4.53, Fig. 4.54, Fig. 4.55, and Fig. 4.56, respectively.

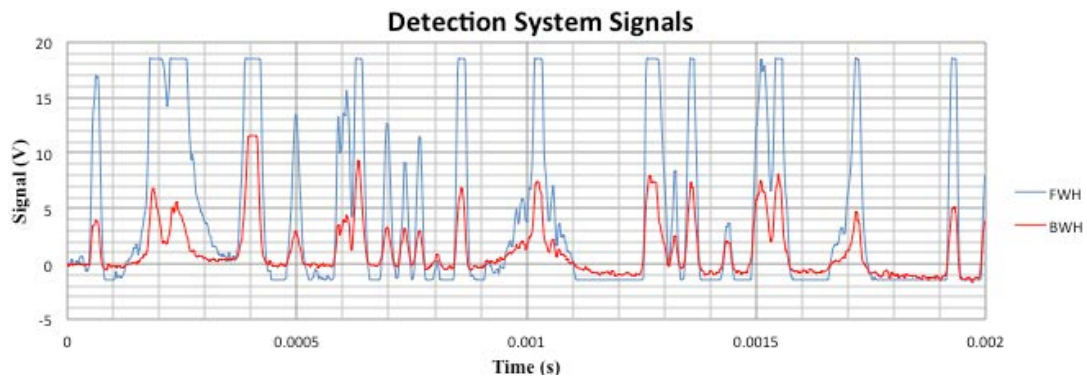


Fig. 4.51: FWH and BWH signals from the Test Case II for $d_p = 1 \mu\text{m}$.

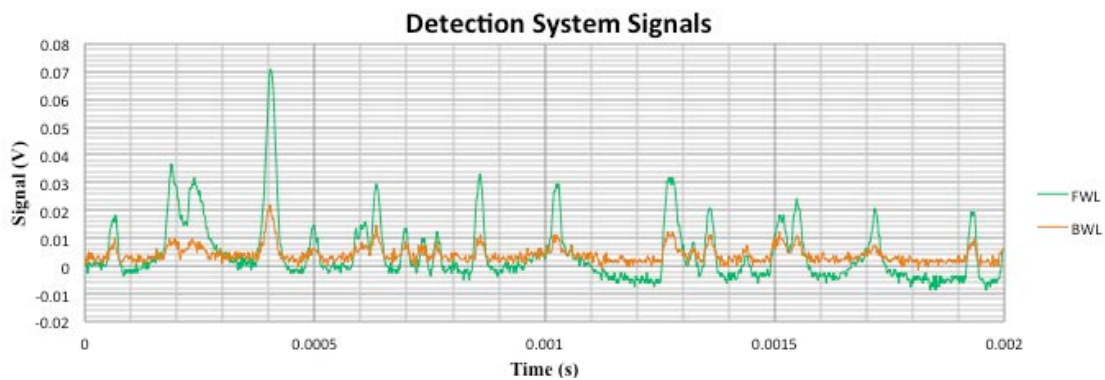


Fig. 4.52: FWL and BWL signals from the Test Case II for $d_p = 1 \mu\text{m}$.

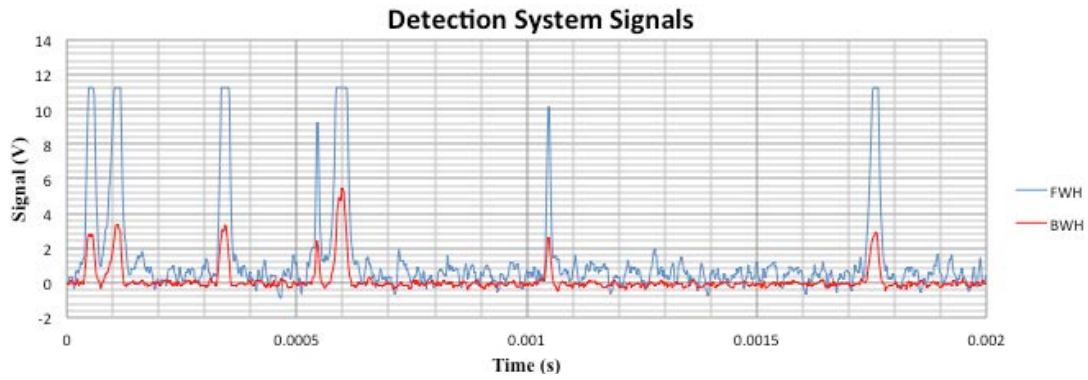


Fig. 4.53: FWH and BWH signals from the Test Case II for $d_p = 5 \mu\text{m}$.

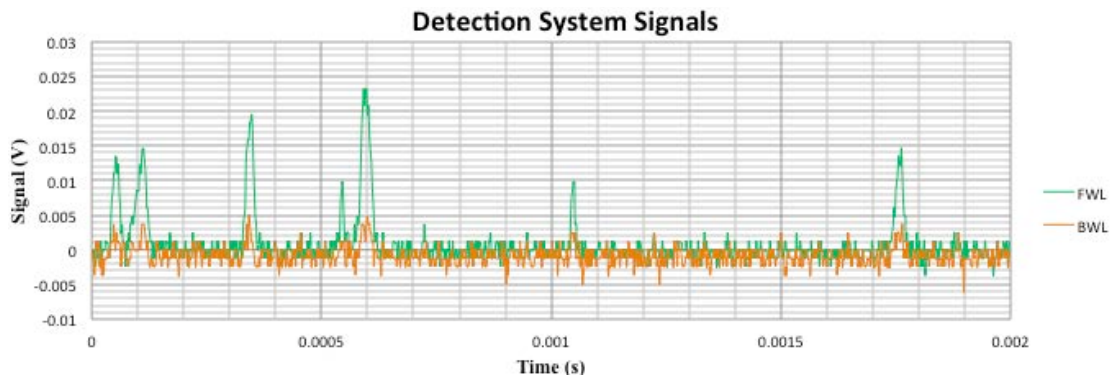


Fig. 4.54: FWL and BWL signals from the Test Case II for $d_p = 5 \mu\text{m}$.

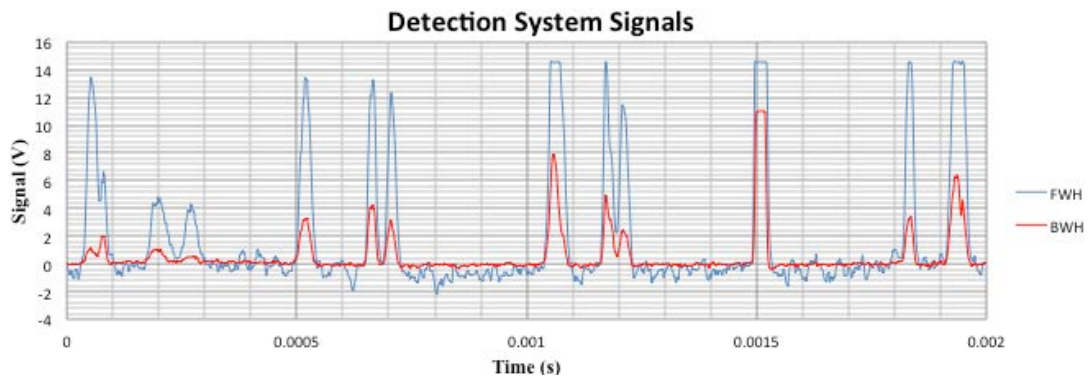


Fig. 4.55: FWH and BWH signals from the Test Case II for $d_p = 10 \mu\text{m}$.

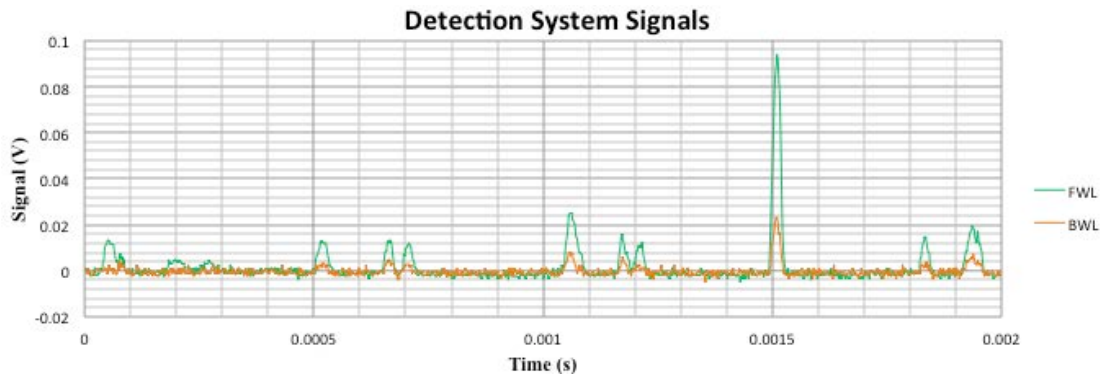


Fig. 4.56: FWL and BWL signals from the Test Case II for $d_p = 10 \mu\text{m}$.

Also in the test case II, there was a significant variety of detected signals, interpreted as both single and multiple events. In this case the experimental setup was based on a different principle to inject the particles (i.e., shooting vs. aspiration) and long events did not occur. It is possible that particles crossed the Sampling Volume faster, but also sometimes closer each other. Indeed, in the test case II the results showed signals shorter in duration and larger in amplitude than in the test case I. This also means that the system is sensitive to the method used to inject the particles. This is encouraging in view of possible different Martian environmental conditions as a calm atmosphere or a more perturbed atmosphere as during dust storms and dust devils.

A more detailed classification of the signals coming from the test case I and II should take into account that the response depends on the trajectory of the particles, which implies both a dependence on the velocity profile of the particles and on the laser spot intensity profile.

Finally, detected signals acquired from the test case II for the high and low gain channels are reported in Fig. 4.57 and Fig. 4.58, respectively.

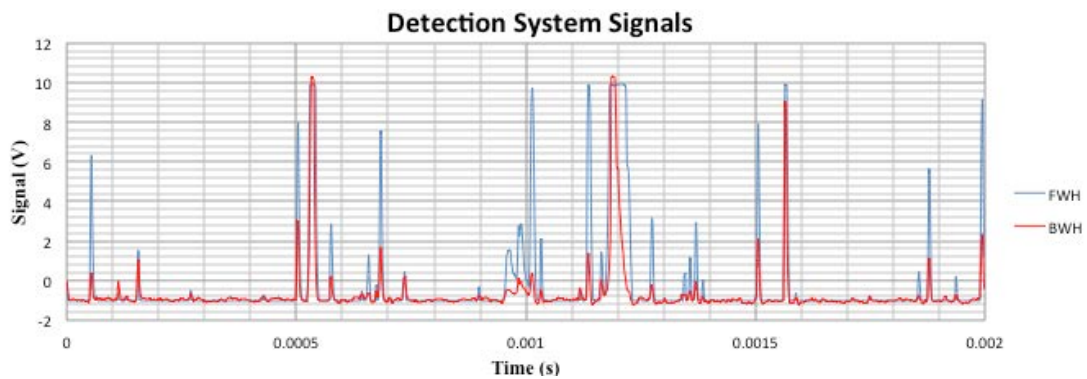


Fig. 4.57: FWH and BWH signals from the Test Case III.

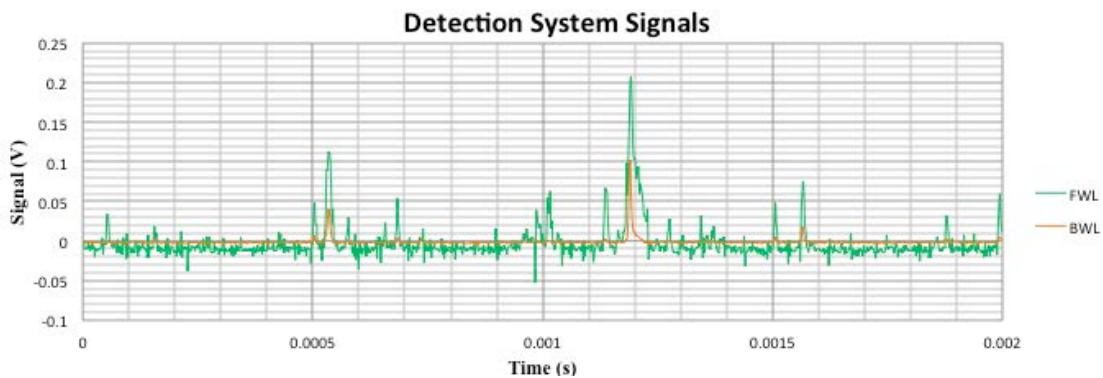


Fig. 4.58: FWL and BWL signals from the Test Case III.

The test case III was performed just only with the aim to check if after several MEDUSA runs, the particles deposited inside the instrument could be recirculated in the successive runs. In fact, signals similar to those seen in the test case II were observed.

These tests showed that the functional validity of the MEDUSA working principle, as particles reach and cross the Sampling Volume and the detection is possible by comparing the response of the 4 channels. A quantitative analysis to associate the response signal levels to the particle geometrical and optical properties was not the aim of this test.

The variety of the response signals obtained for each monodisperse sample demonstrates that some design elements can affect the detection process, among them an element of concern is the wide geometry related to the Sampling Volume region, e.g., the diameter of the inlet and outlet duct in the Sampling Volume and their distance from the centroid of the Sampling Volume as underlined in Sect. 4.5.1.

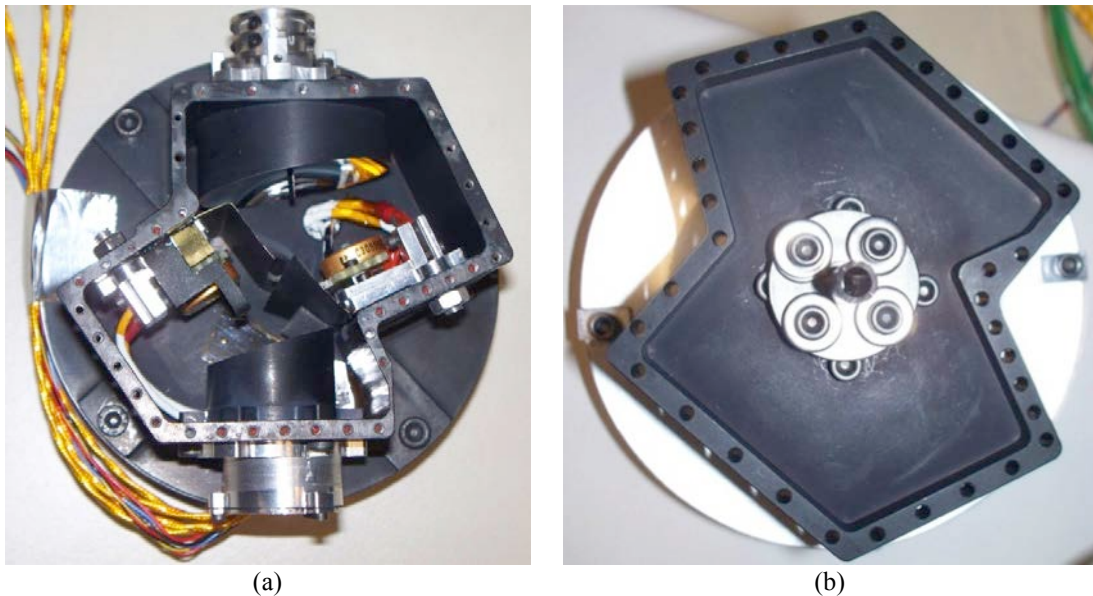


Fig. 4.59: (a) Interior of the MEDUSA Optical Stage (from top to bottom). (b) Cover and inlet duct of the MEDUSA Optical Stage (from bottom to top).

Inspections of the interior of the MEDUSA OS were done after the tests in order to check the cleanness status of the device. The MEDUSA OS was opened and inspected with a microscope where possible. Thin and uniform layers of particles, which were clearly identified as the sample particles injected during the tests, were found on the internal surfaces of the OS as on mirrors, detectors, baffles, etc. (Fig. 4.59). Less relevant deposits of particles were found on the surfaces of the cover; the cover is

oriented in the opposite direction with respect to the main flow in a zone where recirculations are weaker. No relevant deposition was found in the internal walls of the inlet and outlet ducts.

4.5.6 Procedure for the Optical System Calibration of MEDUSA

Experimental setups for calibrating aerosol instruments typically include:

- An aerosol generator
- Aerosol conditioning devices (e.g., diffusion dryer, charge neutralizer, aerosol classifier, aerosol concentrator, dilution air supply)
- A test chamber
- Air monitoring equipment (e.g., pressure and temperature gauges, etc.)
- Calibration standards

A way of calibrating an instrument is to introduce it into a *test chamber*, in which aerosol is uniformly distributed and pressure, temperature and density are monitored, and that contains test standards. This chamber usually has a large test section to provide a quiescent atmosphere in which the entire instrument can be exposed to the aerosol as in the real sampling environment. The test aerosol is introduced at the top of the chamber and uniformly distributed in the section where the instrument is set. The flow rate and turbulence intensity in the chamber should be low, simulating still-air sampling conditions. The air is, then, exhausted from the chamber. A test chamber with static air is not recommended because it is very difficult to avoid convection currents that can affect the measurements (Maynard, A.D., Kenny, L.C., 1995; Aitken, R.J., et al., 1999; Kenny, L.C., et al., 1999).

The aerosol test chamber is used when the instrument to be calibrated operates in a low or zero ambient wind velocity. To evaluate a sampler that will be operated in moving air, a *wind tunnel facility* would be ideal to use (Prandtl, L., 1952). The instrument is located inside the tunnel and should not occupy more than 10-15% of the cross-sectional area of the tunnel's test section to avoid blockage effects. The wind velocity, flow uniformity, and turbulence are monitored using flow-monitoring devices. During the calibration of the instrument, an isokinetic sampler is generally used to collect reference samples. Two types of wind tunnels can be used: an open circuit tunnel (Vincent, J.H., Mark, D., 1982) and a closed circuit tunnel (Ranabe, M.B., et al., 1990).

The open circuit tunnel operates by drawing filtered ambient air into the system and exhausting the air into the ambient downstream of the test section; the closed circuit tunnel circulates the air in a continuous path.

Calibration in Martian environmental simulated conditions would require commercial reference devices that can work at low-pressure level; unfortunately such standard reference devices are not available. This limits the chance to measure particle concentration in a chamber in order to evaluate accurately the performance of the instruments for Martian applications. Therefore, alternative custom ways should be developed to determine the particles concentration in the chamber.

If Martian atmospheric composition (mainly CO_2) and temperature cannot be set for the environmental chamber, the calibration could be alternatively performed by setting only the pressure according to equivalent criteria. The pressure should be ruled so as to have the same Martian atmospheric density. In fact, Martian atmosphere has a molar mass (43.39 g/mole) higher than the terrestrial air (28.97 g/mole), which is mainly made of N_2 and O_2 . As both the atmospheric gases are ideal gases, the equation of state for ideal gases is applicable (Eq. (3.35)). Therefore, in order to have the same density, the following condition should be respected:

$$\rho = \frac{P_{Mars}}{R_{Mars} T_{Mars}} = \frac{P_{Earth}}{R_{Earth} T_{Earth}} \quad (4.14)$$

Therefore, the pressure should be fixed according to:

$$P_{Earth} = \frac{R_{Earth}}{R_{Mars}} \frac{T_{Earth}}{T_{Mars}} P_{Mars} \quad (4.15)$$

An example is reported in Tab. 4.22.

Case	Quantity	Mars	Laboratory
Most Rarefied Case	Pressure (Pa)	600	881
	Temperature (K)	300	293
	Density (kg/m ³)	$1.05 \cdot 10^{-2}$	$1.05 \cdot 10^{-2}$
Most Dense Case	Pressure (Pa)	700	2055
	Temperature (K)	150	293
	Density (kg/m ³)	$2.44 \cdot 10^{-2}$	$2.44 \cdot 10^{-2}$

Tab. 4.22: Laboratory conditions equivalent to Martian surface atmospheric density.

As the pressure regime reproduced in laboratory needs pressure levels higher than on Mars, the pump, which works properly at lower pressure levels, will exhibit a less volumetric flow rate than in the design conditions. In the case of the pump for

MEDUSA, experimental tests showed no significant influence on the volumetric flow rate resulted from temperature variations.

In order to perform the calibration of the optical detection system a procedure is reported. Recalling Eq. (3.124) and considering a particle moving along the y-direction and illuminated by a laser beam along the z-direction, the measurement volume function (J), which is the distribution of intensity of illumination in the Sampling Volume, depends on the scattering intensity (I) scaled with a transfer function (H) to take into account the optical elements of the system:

$$J(x, z, \alpha) = I(x, z)H(x, z, \alpha) \quad (4.16)$$

The detected signal peak amplitude (A) delivered to the pulse-height analyser can be written as:

$$A = G \left(\frac{\lambda^2}{4\pi} \right) J(x, z, \alpha) F(\alpha) \quad (4.17)$$

where G is a constant depending on the detector sensitivity and electric gain, and $F(\alpha)$ is the response function for particles of size parameter α illuminated by a uniform wave. The quantities J and F can be properly normalized with respect to known values J_m and F_m , respectively, obtaining the related dimensionless function:

$$J_n = J / J_m \quad 0 \leq J_n \leq 1 \quad (4.18)$$

$$F_n = F / F_m \quad 0 \leq F_n \leq 1 \quad (4.19)$$

$$A_n = A / A_m \quad 0 \leq A_n \leq 1 \quad (4.20)$$

Therefore, the following normalized relationship is obtained:

$$A_n = J_n F_n \quad (4.21)$$

A statistical procedure can be used to calibrate the MEDUSA optical system (see e.g., by Holve, D., Self, S.A., 1979). Finally, the procedure to calibrate the MEDUSA optical system should includes the following steps:

- 1) Prepare an environmental chamber in which the Martian conditions are simulated and pressure and temperature are monitored.
- 2) Define the aerosol mean velocity at the Sampling Volume (U) by setting the environmental conditions and pump flow rate. Velocity should be preliminary estimated experimentally or with CFD.

- 3) Prepare a monodisperse dust sample k with known diameter d_{pk} and concentration $N(d_{pk})$.
- 4) Inject the monodisperse sample k in the environmental chamber in order to flow across the Sampling Volume.
- 5) Acquire the normalized amplitude (A_{ni}) of the detector signal generated by the particle scattering for a specified time to yield the count rate distribution $C_i = C(A_{ni})$.
- 6) The amplitude interval ($A_{ni}, A_{ni} + \Delta A_{ni}$) is defined according to discretization and resolution criteria and it represents the main interval for the particle class size i .
- 7) Determine $C(A_{ni})$, which is equal to $U \Delta S_{ik} N(d_j)$, where ΔS_{ik} is the cross-sectional area of the Sampling Volume normalized to the flow direction, which yields normalized peak amplitudes in the range ($A_{ni}, A_{ni} + \Delta A_{ni}$) for particles having normalized response function in the range ($F_{nk}, F_{nk} + \Delta F_{nk}$).
- 8) Repeat the procedure for different size classes to yield the other columns of the $\underline{\Delta S}$ matrix.
- 9) The above steps take to the matricial equation $\underline{C} = U \underline{\Delta S} N$, which after the calibration process, can be used to recognize particle concentration as a function of the diameter for polydisperse samples (i.e., $N(d_p)$).

This procedure could also be applied to correct the not-uniform velocity profiles of the particles at the Sampling Volume.

4.6 Conclusions about MEDUSA

The work done on the MEDUSA breadboard was useful to enhance experience about the critical aspects of performing scattering analysis with micrometer-sized particles in very rarefied environment, which is a kind of application poorly investigated by the scientific community and industry so far. MEDUSA is capable to detect particles in the range of 0.4-20 μm , in low-pressure conditions typical of the Martian atmosphere (~ 600 Pa).

In the meanwhile of the work on MEDUSA, the requirements of the next space missions have pushed further in the direction of miniaturized sensors for Mars landing

platforms. Therefore, according to the new guidelines, the MEDUSA concept has been considered too demanding in terms of mass (~ 3 kg) and power consumption (~ 20 W).

The guidelines for the next generation sensors for the Mars exploration have required, then, an effort to drastically reduce the weight at least down to ~ 250 - 300 g and power consumption at least down to ~ 1 W. Therefore, the MEDUSA project has been subjected to a significant redesign and restyling. The work and experience about the MEDUSA breadboard is converted and re-adapted for a more challenging miniaturized MEDUSA design, named MicroMED, which will be the subject of Chapter 5.

5 MICROMED AND DREAMS FOR THE EXOMARS EDM 2016

The concept of *MicroMED* was developed when ESA established to replan the ExoMars lander mission into the Entry, Descent and Landing Demonstrator Module (EDM) 2016 mission (Sect. 2.3). MicroMED was conceived with the aim to exploit the experience gained with the MEDUSA development and to preserve the basic scientific objectives to study the Martian dust. *MicroMED* was studied, accounting for stringent limitations in terms of mass, accommodation and power consumption, as part of the scientific package called *DREAMS* (Sect. 5.1), proposed in response to the ESA Announcement of Opportunity for the EDM science payload. The DREAMS package has been selected by ESA-NASA for the ExoMars EDM 2016 in June 2011, in a descoped configuration not including MicroMED. Nevertheless, the MicroMED study has been carried on for next Mars exploration opportunities. In this chapter the activities performed for MicroMED will be described. The following guidelines have been considered for the MicroMED design:

- To implement the lesson learned during the MEDUSA breadboard development (Chapter 4) with respect to the dynamics and optical detection of particles.
- To comply with the requirements for the accommodation on the EDM 2016 (EXM-DM-IPA-ESA-00001, Issue 1, Rev. 0, 2010 and AO documents) as part of the DREAMS proposal.
- To design and demonstrate test operations in Martian-like environment.

5.1 DREAMS

5.1.1 DREAMS Proposal

DREAMS, acronym for *Dust characterization, Risk assessment and Environment Analyser on the Martian Surface*, is an integrated package of 11 scientific sensors for characterizing fundamental aspects of the Martian climate, geology and boundary layer dynamics at ground level (*DREAMS Proposal - ExoMars Entry Descent and Landing Demonstrator Module (EDM), DREAMS Proposal Team, 01/03/2011*). The DREAMS package was proposed in February 2011 in response to the Announcement of

Opportunity for the *Surface Payload (SPL)* of the *ESA-NASA ExoMars EDM 2016* mission (Sect. 2.3.2). The DREAMS proposal is the result of a strong collaborative effort of a broad international scientific community led by the Principal Investigator (PI) Francesca Esposito (INAF-OAC, Italy) and the Co-PI Franck Montmessin (LATMOS, France).

Despite the limited duration of the EDM mission (2-4 sols), DREAMS will be able to address major scientific Mars exploration goals and to characterize the landing site environment in a dust storm season. The DREAMS package is fully autonomous, providing both power and data handling resources through a Common Electronics Unit (CEU) and a battery. The proposed payload is structured in a modular form to fit the EDM main requirements.

5.1.2 DREAMS Scientific Investigation

The DREAMS proposal included the following sensors:

- *MARIE* (MARs Imager Experiment), a camera system (Lead Co-I Jean-Luc Josset Institute for Space Exploration, Switzerland);
- *MarsTem* (Mars Temperature), a thermometer (Lead Co-I Stefano Debei, CISAS, Italy);
- *MetBaro* (Meteorological Barometer), a capacitive atmospheric pressure sensor (Lead Co-I Ari-Matti Harri, FMI, Finland);
- *MetHumi* (Meteorological Humidity), a capacitive atmospheric humidity sensor (Lead Co-I Ari-Matti Harri, FMI, Finland);
- *MetWind* (Meteorological Wind), a hot film anemometer to measure horizontal wind speed and direction (Lead Co-I Colin Wilson, University of Oxford, UK);
- *MicroARES* (Micro Atmospheric Relaxation and Electric Field Sensor), a sensor for the measurement of atmospheric electrical field and conductivity (Lead Co-I Franck Montmessin, LATMOS, France);
- *MicroMED* (Micro Martian Environment Dust Systematic Analyzer), a sensor for dust size distribution and concentration (Lead Co-I Francesca Esposito, INAF-OAC, Italy);

- *MicroMetSIS* (Micro Meteorological Solar Irradiance Sensor), an UV and NIR solar irradiance sensor (Lead Co-I Ignacio Arruego Rodríguez, INTA, Spain);
- *MicroMIMA* (Micro Martian Infrared Mapper), a Fourier Transform spectrometer to monitor trace gases and organics (Lead Co-I Giancarlo Bellucci, IFSI, Italy);
- *Microphone*, a sensor for sounds detection (Lead Co-I David Mimoum, Institut Supérieur de l’Aeronautique et de l’Espace, France);
- *VISTA* (Volatile In Situ Thermogravimetric Analyzer), a sensor for dust and ice settling, aerosol content, and water vapour abundance (Lead Co-I Ernesto Palomba, IFSI, Italy).

The Traceability Matrix (TM) reported in Tab. 5.1 shows the flow down from main goals and objectives flow down to the science requirements and to the DREAMS design. The DREAMS scientific aims are related for the Martian exploration objectives (Sect. 1.3.2), fixed by the ExoMars Programme (Chapter 2):

- 1) Airborne dust knowledge improvement
- 2) Meteorology characterization
- 3) Geological and Mineralogical characterization
- 4) Trace Gases research
- 5) Risk assessment
- 6) Education and Public Outreach

The EDM mission offers a unique opportunity to study processes that are not accessible from the orbit. Mars’ near surface hosts some of the key processes that control current weather and climate. Major hurdles in modelling the climate actually relate to a lack of constraints on these near surface processes. The dust lifting process is one example of the key mechanisms still suffering from the absence of relevant *in situ* data. DREAMS will study dust grains flux and granulometry (MicroMED and MicroMetSIS) and quantify the role of the electric field on dust lifting mechanism (MicroARES) that has never been directly assessed so far. Constraining the dust size distribution over a range of 0.2-30 μm with a resolution of 0.1-0.2 μm was considered theoretically sufficient to characterize the relevant dust grain sizes that are potentially lifted from the surface. Simultaneous wind velocity measurements by MetWind with a

precision of 10%, assisted by temperature measurements by MarsTem and pressure measurements by MetBaro, will provide the relevant information to infer dust horizontal fluxes, from which vertical fluxes can be estimated. Monitoring daily variations (6 sequences during day time and 1 at night) shall allow us to identify lifting events and to constrain the associated threshold friction velocity that can be deduced from the atmospheric roughness height (Sect. 1.2.2), even if only measurements from a single height location are provided in the DREAMS baseline configuration. VISTA will monitor variations in the dust mass deposited on its microbalance allowing the inference of dust particles settling rates, and, therefore, will characterize the dust deposition processes. The dust effective bulk density shall be estimated by combining measurements of the particle number density by MicroMED with cumulative mass by VISTA. At the same time, MicroARES electrode, at height of 25 cm from the EDM, will provide information on DC electric fields and establish their correlations with dust concentration and flux variations, giving insights in the role of electric forces on dust lifting processes. Dust column abundance above the landing site can be derived and studied by NIR irradiation measurements with MicroMetSIS, providing additional information on its impact on radiative balance. In addition, VISTA will also be able to extract the abundance of water absorbed in dust particles through heating cycles performed on the collected samples. At night, VISTA will probably monitor possible water ice settling and will give information about the water vapour abundance.

DREAMS will assess meteorology by performing pressure (MetBaro), temperature (MarsTem), humidity (MetHumi), wind speed (MetWind), and dust opacity (MicroMetSIS) measurements. MetBaro can also be used as a detector for the occurrence of dust storms and dust devils since pressure variations are systematically associated with these phenomena, and, so, it can be used to trigger switch-on of other sensors for depth characterization in such conditions.

The geomorphological characterization of the landing site by the MARIE camera will allow us to characterize the landing site, from which the surface roughness can be estimated. Inferences on mineralogy can be deduced from spectral information in the Red, Green, and Blue (RGB) filters. For instance, Red/Blue ratios can be used to determine the oxidation state of rock dust coating and soil: if dust cover is minimal,

rock colour in the 3 bands can be diagnostic of mineralogy. Estimations of the porosity and cohesion of the soil particles will also be possible by studying landing alterations.

Science Goal	Objectives	Measurement Requirements	Sensor Requirements	DREAMS Sensors	DREAMS Sensors Performance
I. Mars' Near Surface Environment Characterization	Airborne dust knowledge improvement	Airborne Dust horizontal flux (ρV) _{dust}	Near surface wind (10%) and dust number density (50%)	MicroMED* MetWind	Dust concentration: 20%
		Dust size properties	Size distribution ($d_p = 0.5-10 \mu\text{m}$)	MicroMED*	Sensitivity: 0.2-20 μm
		Existence of electric forces (relevant for lifting) and discharges	Quasi-DC electric field (< 100 kV/m) + AC field (~kHz)	MicroARES*	Q-DC: < 10 kV/m
		Dust physical properties	Dust composition and hygroscopy	VISTA*	Adsorbed water
	Meteorological characterization	1) Measure Pressure (p), Temperature (T), wind (V), humidity (QH_2O) and opacity (τ) 2) Characterize daily variations	1) p (res. < 1 Pa), T , V , QH_2O and τ (prec. 1-20%) 2) Make > 2 meas./day	MetBaro MarsTem MetWind MetHumi VISTA MicroMetSIS	1) p : res. 0.5 Pa T : res. 0.04 K V : prec. 10% QH_2O : prec. < 30% τ : prec. < 20%) 2) 6 meas. at daytime + 1 meas. at night
	Geological and Mineralogical characterization	Landing area images	Camera with panoramic capability	MARIE**	FOV: 80 x 55° Res.: 0.3 mm
	Risk assessment	Solid matter contamination	Dust concentration, size distribution and settling rate	MicroMED* VISTA*	Dust size distribution: 0.2-30 μm . Dust settling rate
		EM noise and vehicle electrostatic charging	EM waves (VLF range)	MicroARES*	AC Fields: 2-2 kHz
UV radiation at surface		EUV fluxes (200-400 nm)	MicroMetSIS**	UV radiation: 200-300 nm	
II. Trace Gases Characterization in support to ExoMars TGO Science	Trace gases research	High sensitivity detection of CH_4 and other TGO listed species (e.g., hydrocarbons, sulfur compounds)	IR spectroscopy at high resolution ($\lambda/\Delta\lambda > 1000$) and high SNR (> 1000): CH_4 detection limit < 5ppb	MicroMIMA**	Full column CH_4 (<1 ppb), H_2O , HO_2 , SO_2 , C_2H_2
	Trace gases research	H_2O , O_3 , electric fields and discharges	IR and UV spectroscopy at high SNR (> 100), quasi-DC (> 100 V/m) and AC fields	MicroMIMA** MicroARES* MicroMetSIS**	HO_2 , O_3 (full column) + AD/DC fields
III. Education and Public Outreach	Education and Public Outreach	Color images / Sound	RGB images + sound recording	MARIE** Microphone*	RGB images + sound recording

*First-time measurements at Mars; **Also foreseen in some missions in preparation.

Tab. 5.1: Science Traceability Matrix of DREAMS.

The characterization of dust lifting mechanisms can be achieved both in dusty and in moderate haze conditions. The very short duration of the mission might prevent it from capturing any particular dust event, yet DREAMS measurements will provide reference data points in areas not covered by previous missions that could be used in climate models.

The monitoring of methane and other trace gases (which is also a main goal of the ExoMars TGO) performed by DREAMS together with the study of electric fields and dust dynamics, shall provide major advances in our knowledge of organics chemistry on

Mars. MicroMIMA will add the chance to monitor trace gases and study organic chemistry as this Fourier Transform spectrometer was designed to encompass the 3.3 μm spectral region where CH_4 and other hydrocarbons have an intense absorption band, covering a wavelength range of 1.7-3.5 μm with a spectral resolution $\lambda/\Delta\lambda > 1,000$. Oxidants production in presence of large electric fields, if they exist, will be deduced by monitoring abundance changes in CO , OH , O_3 and H_2O_2 by MicroMetSIS, in relation to changes in electric fields measured by MicroARES.

The DREAMS sensors can also provide comprehensive datasets to help quantifying hazards for equipment and future human crew: dust abundance and size (MicroMED), dust settling (VISTA), velocity of windblown dust grains (MetWind), electrostatic charging of dust grains, existence of discharging events, electromagnetic noise potentially affecting communications (MicroARES) and UV radiations (MicroMetSIS).

Finally, DREAMS will contribute to public outreach with the Microphone to perform the first acoustic recording at the Martian surface and to be possibly able to capture particular processes in the vicinity of the lander (vortex, dust devils) as well as electrical phenomena, and with the MARIE camera to offer a nearly “human” experience of the Martian surface by returning true colour images of Martian landscapes, i.e., the first “interview” to Mars.

Conf.	Objectives	MARIE	Mars Tem	Met Baro	Met Humi	Met Wind	Micro ARES	Micro MED	Micro MetSIS	Micro MIMA	Micro-phone	VISTA
#1	1	S	R			R	R	R	S			R
#2	1-2-(5)	S	R	R	R	R	R	R	R			R
#3	1-2-3-(5)	R	R	R	R	R	R	R	R			R
#4	1-2-3-4-5	R	R	R	R	R	R	R	R	R		R
#5	1-2-3-4-5-6	R	R	R	R	R	R	R	R	R	R	R

Tab. 5.2: DREAMS measurement strategies. R = Required, S = Support.

The plan of the measurements that the DREAMS team proposed to ESA-NASA was subdivided in 5 alternative strategies in order to optimize the scientific objectives according to the mass and power budget available for the EDM (Tab. 5.2).

5.1.3 DREAMS System Architecture

The total mass, power and data volume budget of the DREAMS payload proposal is reported in Tab. 5.3. DREAMS is designed to be compliant to the E-PIP requirements (Sect. 2.3.2). The DREAMS Assembly consists in the following units:

- *Primary Battery*

- *Central Electronics Unit (CEU)*
- *Scientific Sensors (Sect. 5.1.2)*

Total Mass (kg)	3.835
Energy Consumption for 4 sols (Wh)	200
Data Volume for 4 sols (Mb)	50

Tab. 5.3: DREAMS engineering budgets.

The Primary Battery should provide the necessary energy to supply the scientific instruments for the whole mission. It requires to be thermally controlled to work at temperature above 250 K to have sufficient efficiency. In the proposal, it was dimensioned for the maximum mission duration, i.e., 4 sols, even if this constraint could be rediscussed. The battery includes heaters, thermostats and a thermometer for thermal control. The total energy consumption for the whole mission is 200 Wh, considering an operational profile of the scientific sensors over 7 measurement slots per sol for a duration of 3.5 h/sol. The CEU should provide electronics management for all the instruments. Taking into account the sensor and the lander requirements, two possible accommodations were hypothesized for the components of the DREAMS package within the EDM Warm Compartment (Fig. 5.1 and Fig. 5.2).

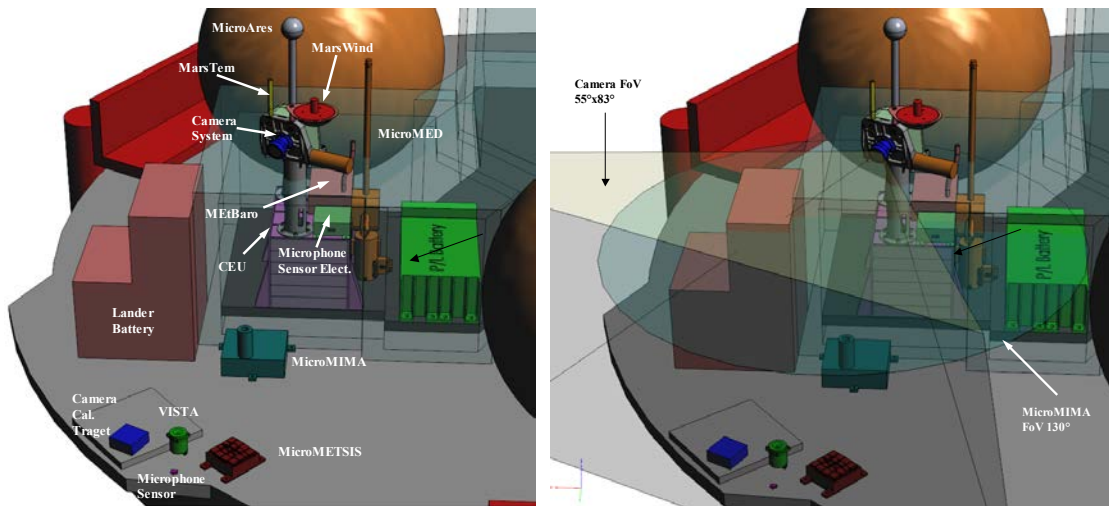


Fig. 5.1: DREAMS accommodation #1 (CEU and Primary Battery in place of the CTPU position specified in the E-PIP, Fig. 2.5).

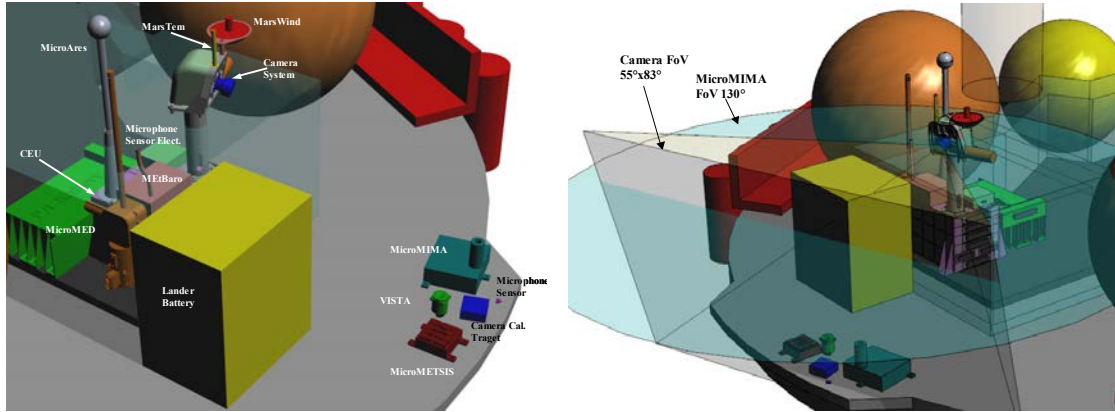


Fig. 5.2: DREAMS accommodation #2 (CEU and Primary Battery in place of UHF Electronics position specified in the E-PIP, Fig. 2.5).

5.1.4 DREAMS Operations

The DREAMS observing profile has been designed to fulfil requirements of the proposed investigations while fitting DREAMS battery resources. Characterization of dust properties and related processes, as well as of meteorological state at the landing site, demand several measurements every day in order to properly constrain daily variation of the measured quantities.

Atmospheric Pressure	650-690 Pa
Atmospheric Temperature	210-260 K
Atmospheric Density	$1.30 \cdot 10^{-2}$ - $1.80 \cdot 10^{-2}$ kg/m ³
Gravity Acceleration	3.73 m/s ²
Wind Speed	5-10 m/s
Average Dust Particles Number Density	1-100 cm ⁻³
Average Dust Particles Density	$2.73 \cdot 10^3$ kg/m ³
Average Dust Particles Diameter	3.2 μm
Dust Particles Refractive Index	1.2-1.7
Water vapour column density	10-25 pr-μm

Tab. 5.4: Reference atmospheric conditions for the DREAMS mission.

The most probable landing site should be in a Martian equatorial region, nearby the *Meridiani Planum* (Sect. 2.3.1) at $L_S = 240^\circ$ - 260° (northern autumn), which is a season when dust storms occurrence is frequent. The main environmental conditions foreseen for such a scenario are reported in Tab. 5.4.

DREAMS power resources allow for a total of ~ 12 h of continuous operations. The following constraints guided the design of DREAMS observing profile:

- 1) Return data every day of the mission;
- 2) Target daily periods of expected maximum science interest (function of each sensor);
- 3) Provide sufficient sampling to characterize daily evolution;

4) Use power resources optimally.

The DREAMS operational scenario foresees the following sequences:

- Switch-on and Check-out
- Sensors Operations
- Switch-off

For each science operation session Switch-on, Check-out and Switch-off will be repeated, while the Sensors Operations may change depending on the time of measurement. DREAMS will start acquiring scientific data after EDM touchdown and switch-on of its battery. Based on the above constraints, the following daily observation profile has been elaborated: 6 sequences of ~ 30 min during daytime plus 1 sequence of 15 min during night-time. As shown in Fig. 5.3, the 6 sampling periods have been selected to consistently sample daytime variations. Sampling periods are spaced by about 2-3 h except near noon, when major convective activity is expected, where sampling frequency is increased (1/h). With such a strategy, it is expected to monitor some essential components of the Mars PBL, both in view of capturing discrete dusty events and of fulfilling requirements of a basic meteorological state characterization of the landing site (Sect. 5.1.2).

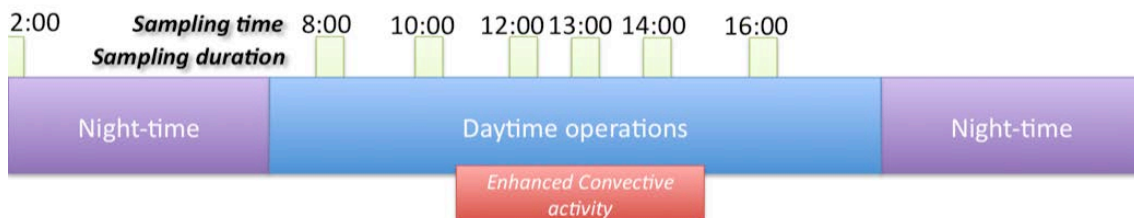


Fig. 5.3: DREAMS daily operations profile.

Acquired data will be stored in the CEU non-volatile memory. The data will be transferred to Earth via the ExoMars TGO or other ESA or NASA Relay Orbiters. A strategy was designed based on a communication scenario via the TGO, as quoted by the AO. Before the first TGO passage (landing + 4 sols), acquired data will be transferred to the EDM system, and, this shall conclude the nominal SPL mission. In case the EDM data uplink to the TGO is not sufficient during the first TGO passage, the EDM shall be able to re-transmit all the data to the TGO during the second passage (landing + 8 sols). If resources availability allows the nominal SPL mission to be extended, this shall be detected autonomously by the CEU that will resume data

acquisition and storage. The payload shall autonomously switch itself off, while leaving enough energy to be switched on again by the EDM for final data transfer to the EDM system before the second TGO passage (landing + 8 sols). If all or part of the data is successfully uplinked during the first passage, the EDM may allow further science data to be acquired and received from the payload. During the second passage, EDM shall first re-transmit the remaining data of the first session and then allow the new science data to be uplinked, provided EDM resources and capabilities allow it. EDM shall be able to connect the SPL CEU at a planned time, which shall be able to receive an updated timeline prior to EDM separation from the Orbiter Module.

5.1.5 DREAMS Final Arrangement

In June 2011, ESA-NASA approved the DREAMS project, but, due to the very tight EDM engineering requirements and temporal constraints for the mission preparation, a subset of the DREAMS sensors was chosen for the EDM payload. The choice was made with the aim to contain the total mass (max 3 kg) and data volume (max 50 Mb) within the EDM requirements. In fact, the original DREAMS proposal, even if it was considered very rich and complete from a scientific point of view, exceeds the mass available for the mission (3.835 kg) requiring a review of the system and power consumption. The descoped DREAMS package includes only 5 sensors, to which also the French *ODS (Optical Depth Sensor)* has been added. Therefore, as also reported in Sect. 2.3.2, the DREAMS package for the EDM 2016 mission will include: *MetWind*, *MetHumi*, *MetBaro*, *MarsTem*, *ODS (Optical Depth Sensor)*, and *MicroARES*.

5.2 MicroMED for the DREAMS Proposal

5.2.1 The MicroMED Scientific Objectives and Measurements

The MicroMED basic scientific objectives are the same of MEDUSA (Sect. 4.2), for what concerns *in situ* classification of dust grain size and size distribution and concentration, while water vapour and DDES measurements were dropped. A comparison between the physical quantities measured by MEDUSA and MicroMED is reported in Tab. 5.5.

Quantity	MEDUSA	MicroMED
Forward (0°) Scattering	OS (Angle = ±33°)	-
Normal (90°) Scattering	-	OS (Angle = ±65°)
Backward (180°) Scattering	OS (Angle = ±47°)	-
Particle Time of Flight	OS	OS
Dust Particle Number Density	OS (1-500 cm ⁻³)	OS (1-500 cm ⁻³)
Dust Grain Size and Shape	OS (Grain size = 0.2-20 μm)	OS (Grain size = 0.2-20 μm)
Dust Size Distribution	OS	OS
Dust Mass Accumulation	MBd (Total mass = 2·10 ⁻¹³ -2·10 ⁻⁹ kg)	-
Water Vapour Abundance	MBwv (Abundance > 1 ppb)	-
Dust Deposition	DDES (1-100%)	-
Dust Electrification	DDES (Electrical charge = 10 ³ -10 ⁶ e ⁻)	-
Wind Speed	DDES (Speed = 2-20 m/s)	-

Tab. 5.5: Physical quantities measurable by MEDUSA (Sect. 4.3) and MicroMED subsystems (Sect. 5.2.2).

5.2.2 The MicroMED System

The MicroMED instrument concept, as shown in Fig. 5.4, is equipped with the following components:

- *Sampling Head*
- *Optical Stage (OS):*
 - *Inlet duct and outlet duct*
 - *Laser diode*
 - *Collimating lenses*
 - *Collecting mirror*
 - *Sampling Volume (SV)*
 - *Light trap*
 - *Detector*
 - *Proximity Electronics (PE)*
- *Pump*
- *Main Electronics (ME)*

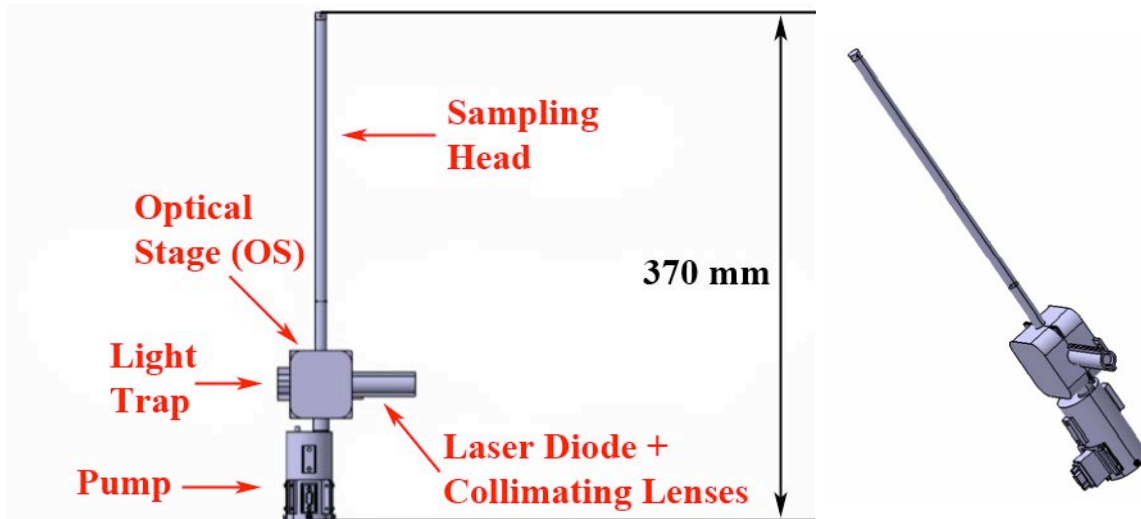


Fig. 5.4: MicroMED Concept.

MicroMED is an Optical Particle Counter (OPC) (Sect. 3.2.1), which uses a pump to drag aerosol from Martian atmosphere via a Sampling Head. The particles are pulled towards the Optical Stage (OS) under the action of a pressure difference generated by the pump. In the OS, the particles cross a collimated IR laser beam emitted by a laser diode. The light scattered by the particles is collected by a mirror, which reflects light towards a photodiode. The electrical signal is processed by the Proximity Electronics (PE).

The *Sampling Head* is a simple inlet to capture atmospheric aerosol. It has been conceived as a tube in Aluminium alloy with the upper end, which is exposed to the external environment, covered and 4 holes equally distributed on the lateral surface of the tube nearby the cover, while the other end, which is open, is directed towards the sensing region. The geometry of the Sampling Head will be discussed in more detail in Sect. 5.3, with specific concern to the fluid dynamics design.

The *Optical Stage (OS)* design is the result of a compromise between mass limitations, particles dynamics behaviour (Sect. 5.3) and optical detection requirements (Sect. 5.4).

The *Proximity Electronics (PE)* is an amplifier based on a commercial off-the-shelf component, the AD8304 by Analog Devices, that is a monolithic logarithmic amplifier, also thermally stabilized, which provides a large dynamic range of 160 dB, from 100 pA to 10 mA. The power consumption at +5 V DC is 32 mW, which gives a strong contribution to reduce the MicroMED power consumption with respect to MEDUSA.

The bandwidth at 10 nA peak input current is 24 kHz. The PE should be accommodated in the OS box, behind the photodetector in order to minimize cables length.

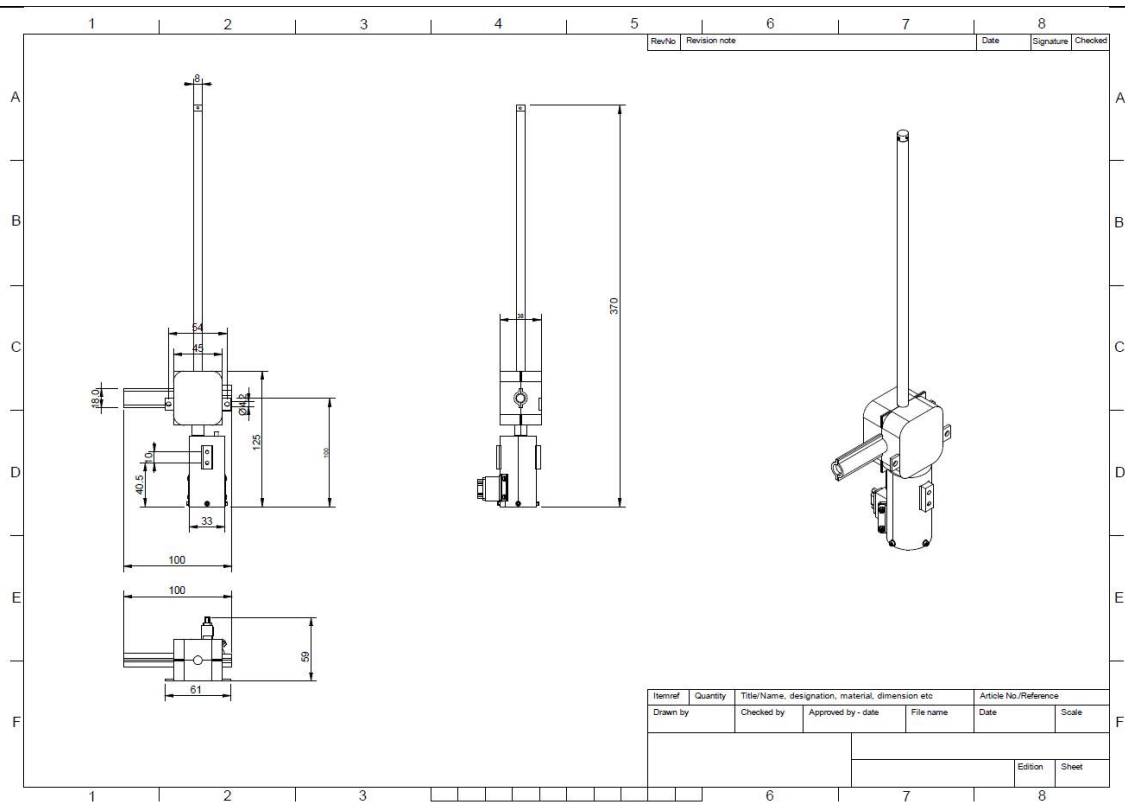


Fig. 5.5: MicroMED overall dimensions (mm).

The MicroMED pump is quite similar to the MEDUSA pump, but it will work at lower volumetric flow rate, and, therefore, should need less power. The pump will be connected via a primary pipeline to the OS box and a secondary pipeline will exhaust the flow outside (Fig. 5.4). The volumetric flow rate should be 1-3 l/min.

As MicroMED was supposed to be part of the DREAMS package, the *Main Electronics (ME)* is shared between all the sensors of the system, so it is not a specific element of MicroMED and will not be discussed further.

The overall dimensions of MicroMED (Fig. 5.5) were defined both in order to minimize the MicroMED envelope and mass for the EDM platform and as a result of a preliminary mechanical and structural analysis based on the Finite Element Method (FEM) performed by Ser.Tec. S.r.l..

5.2.3 MicroMED Requirements

The accommodation of MicroMED should guarantee that MicroMED shall be protected from dust prior to and during landing, the Sampling Head shall be in a vertical position during operations with a tolerance of $\pm 20^\circ$ and with a free space of more than 20 cm in radius around it to avoid biasing the instrument measurements, no spacecraft induced particulate material should bias the instrument measurements, the output of the MicroMED pump should be evacuated to free space, and a temperature range of $-60^\circ\text{C} \div +60^\circ\text{C}$ shall be guaranteed for the laser diode.

	MEDUSA	MicroMED
Total Mass (g)	2,243	< 300
Envelope (mm x mm x mm)	186 x 153 x 153	370 x 100 x 59
Power Consumption per run (W)	21.44	1-1.5
Data Volume per run (Mb)	0.184	0.176
Sampling Head	Conical Nozzle	Minimized tube
Laser diode power (mW)	1,000	100
Laser diode wavelength (nm)	808	850
Sampling Volume Size (mm)	1.2 x 0.32 x 3	0.3 x 0.3 x 0.3
Detectors	2	1
Mirrors	2	1
Volumetric flow rate (l/min)	5-6	1-3

Tab. 5.6: MEDUSA and MicroMED main differences in terms of budget requirements.

The most relevant differences between MEDUSA and MicroMED in terms of budget requirements are reported in Tab. 5.6.

The accommodation hypothesized for MicroMED on board the EDM consisted in putting MicroMED inside the EDM Warm Compartment to satisfy operational temperature constraints of both pump electronics and laser (Fig. 2.5, Fig. 5.1, Fig. 5.2), while the Sampling Head had to protrude from the Warm Compartment in order to be outside of the fluid dynamics boundary layer made by the EDM platform interaction with the Martian atmosphere.

5.2.4 MicroMED Engineering Budgets

An assessment of the mass budget is reported in Tab. 5.7, with the target to contain the total mass within 300 g.

An estimation of the power/energy budgets for a mission duration of 4 sols and 6 runs per sol is shown in Tab. 5.8.

MicroMED Components	Mass [g]
Case	150
Laser Diode	12
Proximity Electronics (PE)	20
Pump	100
Other mass (mirror, detector, etc.)	?
TOTAL TARGET	< 300

Tab. 5.7: MicroMED mass target budget.

Op. Mode	Subsystem	Op. Time per Sol (s)	Op. per Sol	Op. Sols	Power Supply (W)	Voltage Supply (V)	Current Supply (mA)	Energy per Run (Wh)	Energy per Sol (Wh)	Energy per Mission (Wh)
Science	PE	160	6	4	$3.2 \cdot 10^{-2}$	5 DC	5.5	$1.422 \cdot 10^{-3}$	$8.533 \cdot 10^{-3}$	$3.413 \cdot 10^{-2}$
	Laser Diode	130	6	4	$5.0 \cdot 10^{-1}$	3.3 DC	200	$1.806 \cdot 10^{-2}$	$1.083 \cdot 10^{-1}$	$4.333 \cdot 10^{-1}$
	Pump	130	6	4	$5.0 \cdot 10^{-1}$	5 DC	100	$1.806 \cdot 10^{-2}$	$1.083 \cdot 10^{-1}$	$4.333 \cdot 10^{-1}$
	Total MicroMED	160	6	4				$3.753 \cdot 10^{-2}$	$2.252 \cdot 10^{-1}$	$9.008 \cdot 10^{-1}$

Tab. 5.8: MicroMED power and energy target budgets.

5.2.5 MicroMED Operations

The nominal operation is performed by a series of runs, with duration of 160 s each: 20 s for switching on and initialization, 130 s for the acquisition of scientific and housekeeping data, ~ 10 s for the switching off. Results of a single run include counting of the dust particles, which have crossed the sensing region, and determination of the dust size distribution and number density. Results from different runs give the time trend vs. time of the parameters over Martian sols.

A suitable schedule for the MicroMED activity in the DREAMS package on the EDM 2016 is based on 6 runs per sol for a mission duration of 4 sols: 2 runs in the morning (08:00 LT, 12:00 LT), 3 in the afternoon (13:00 LT, 14:00 LT, 18:00 LT), and 1 at night (00:00 LT).

5.3 Fluid Dynamics Design

5.3.1 Basic Guidelines

In this section the most relevant parameters related to the design of MicroMED from a fluid dynamics point of view are described and discussed, focusing on the Sampling Head, the Optical Stage and the pump.

The Sampling Head internal diameter must be minimally invasive. An internal tube diameter of 6 mm has been chosen. Aerosol enters the Sampling Head through 4 circular holes, which must be large enough to avoid particle dispersion and impact on walls, but they cannot be too large to prevent sampling of too many particles. A

diameter of 2 mm for the holes has been chosen. A tube length of 245 mm has been chosen to guarantee the probe to be sufficiently far from the EDM platform obstacles to prevent fluid dynamics boundary layer effects and/or contamination from the exhaust jets of the EDM thrusters.

Solutions to match the Sampling Head and inlet duct were investigated numerically in order to find the best performance with respect to particle size (Sect. 5.3.2). In order to control the aerosol flow and confine as much as possible the particles crossing within the sensing region, the internal diameter of the Sampling Head has to be as small as 1-2 mm nearby the Sampling Volume region. Therefore, the flow should pass through a constriction from the Sampling Head to the Sampling Volume region that influences negatively the isokinetic sampling process. This implies that, assuming a stable and known volumetric flow rate, calibrated curves of the sampling efficiency vs. particle size and inertia and environmental conditions are needed to derive the dust particles concentration. Some solutions for the inlet and for the outlet ducts are discussed in Sect. 5.3.2.

A size of 0.3 mm x 0.3 mm x 0.3 mm was chosen for the Sampling Volume, in order to have sufficient power density to detect the smallest particle even with a low power laser source (one order of magnitude lower than for MEDUSA). Nevertheless, the final sizing of the Sampling Volume should depend on the final coupling between the fluid dynamics and optical design and should be verified experimentally. The goal is to have the sampling efficiency (Sect. 3.2.3) as close as possible to 1, for a wide particle size range ($d_p = 0.2\text{-}20\ \mu\text{m}$). The fluid dynamics design should aim to have particles crossing as close as possible to the centroid of the Sampling Volume, while the optical design should aim at maximum uniformity of the laser spot within the sensing region.

Accurate measurements of the particle number density by MicroMED are possible if the flow regime is incompressible. This assumption should facilitate the conversion from mass flow rate to volumetric flow rate and vice versa (Sect. 3.2.3). The Martian atmospheric conditions are quite suitable for incompressible flow, while this hypothesis is verified inside MicroMED if the local Mach number is < 0.3 in each zone of the instrument. For MicroMED, this hypothesis implies that the sections of pipelines should not be too small to cause excessive local acceleration of the fluid at the working pump flow rate. The most critical section of the MicroMED instrument is the inlet duct, as it is

the smallest section along the flow. As said above, the section of the inlet duct should be sufficiently small nearby the Sampling Volume to minimize flow dispersion. Therefore, a design guideline is that the maximum Mach number at the inlet section is below 0.3 (typical Mach number limit for incompressible flows). The mass flow rate (\dot{m}) across a generic section A is given by:

$$\dot{m} = \rho VA \quad (5.1)$$

where ρ is the fluid density and V is the average fluid velocity on the section A . For an ideal gas in a one-dimensional and isentropic flow (Carlomagno, G.M., 2004), the following relationships are applicable between the static quantities (p , T , ρ) and total (stagnation) quantities (p_0 , T_0 , ρ_0):

$$\frac{T}{T_0} = \left(1 + \frac{\gamma-1}{2} M^2\right)^{-1} \quad (5.2)$$

$$\frac{p}{p_0} = \left(1 + \frac{\gamma-1}{2} M^2\right)^{-\frac{\gamma}{\gamma-1}} \quad (5.3)$$

$$\frac{\rho}{\rho_0} = \left(1 + \frac{\gamma-1}{2} M^2\right)^{-\frac{1}{\gamma-1}} \quad (5.4)$$

Considering the equation of state for ideal gases (Eq. (3.35)) and substituting Eqs. (5.2), (5.3) and (5.4) into Eq. (5.1), the following relationship is obtained:


$$\dot{m} = \left(1 + \frac{\gamma-1}{2} M^2\right)^{-\frac{\gamma+1}{2(\gamma-1)}} \frac{\gamma p_0}{(\gamma R T_0)^{1/2}} MA \quad (5.5)$$

Therefore, if the mass flow rate is known from the pump volumetric flow rate and the atmospheric density, Eq. (5.5) gives the relationship between the Mach number M and the section A . The velocity profile at the inlet section is not constant and not one-dimensional, but like a Poiseuille flow (i.e., internal boundary layer in small duct involving a fully-developed viscous flow at low Reynolds number). Therefore, the average fluid velocity is approximately half the velocity along the axis of the section and the maximum average Mach number to be considered for the section is $\sim 0.30/2 = 0.15$.

The pump for MicroMED should work similarly to that considered for MEDUSA. The Gardner Denver Thomas G 6/04 was chosen (Tab. 5.9), which is suitable to have

low volumetric flow rate (1-3 l/min for MicroMED vs. 6 l/min for MEDUSA) and power consumption (~ 0.6 W for MicroMED target vs. ~ 3 W for MEDUSA).

Pump	
Supplier	Gardner Denver Thomas
Model	G 6/04 EB
Part number	50102
Maximum flow rate	4.7 l/min
Maximum intermittent pressure	110 mbar
Maximum continuous pressure	50 mbar
Maximum intermittent vacuum	15%
Maximum continuous vacuum	5%
Motor type	Ironless Core DC
Nominal voltage	6 V DC
Current consumption	0.16-0.48 A
Protection class	IP50
Motor bearing	Ball bearing/sleeve bearing
Operating temperature	-30...+50°C
Weight	100 g



Zeichnung G04-V00
Inches are shown in ()

Befestigungsschelle / Mounting Bracket

Anschlusslitzen Länge ca. 360mm
Position unbestimmt
Lead wire length approx. 360mm
Position undefined

Model	Operation Type	Max. Pressure [mbar]	Max. Vacuum [%]
G 24/04 EB	Continuous	7.0	15
G 12/04 EB	Continuous	6.5	10
G 6/04 EB	Continuous	4.5	10
G 3/04 EB	Continuous	4.5	15
G 24/04 EB	Intermittent	7.0	10
G 12/04 EB	Intermittent	6.5	15
G 6/04 EB	Intermittent	4.5	15
G 3/04 EB	Intermittent	4.5	20

Tab. 5.9: Gardner Denver Thomas G 6/04 pump datasheet.

5.3.2 Computational Fluid Dynamics Analysis

The design of the MicroMED Sampling Head, Optical Stage box, inlet duct and outlet duct was supported by theoretical predictions based on CFD simulations. The CFD simulations were made on the same criteria used for MEDUSA (Sect. 4.5.1). MicroMED working conditions are (as for MEDUSA) low Reynolds number ($Re < 100$), low Mach number ($M < 0.2$), and high local Knudsen number with respect to particles sizes ($Kn_p > 1$). The CFD simulations were performed in typical Martian atmospheric conditions (Tab. 4.15 and Tab. 4.16), injecting Martian dust-like particles of different sizes (Tab. 4.17).

A domain approximating the MicroMED Sampling Head and Optical Stage was considered. The reference frame for the geometry of the CFD model is:

- X Light Trap - Laser Diode direction

- Y Detector - Mirror direction
- Z Flow anti-direction and gravity anti-direction

Different geometrical configurations were taken into account in order to identify a solution able to minimize the particle dispersion and losses from a fluid dynamics point of view and to be compliant with the requirements on the optical elements (Tab. 5.10). The approach started from a solution based on typical assumptions implemented in commercial OPCs, to evidence possible critical aspects. The following critical design parameters were identified and set to reach the purpose:

- Geometrical profile of the Sampling Head tube;
- Diameter of the outflow section of the inlet duct;
- Geometrical profile of the inlet duct;
- Distance between outflow section of the inlet duct and Sampling Volume centroid;
- Diameter of the outlet duct;
- Distance between inflow section of the outlet duct and Sampling Volume centroid;
- Pump volumetric flow rate.

Configuration	MicroMED #1	MicroMED #2	MicroMED #3	MicroMED #4
Geometrical profile of the Sampling Head	Fig. 5.7	Fig. 5.8	Fig. 5.9	Fig. 5.10
Diameter of the outflow section of the inlet duct	2 mm	1.5 mm	0.3 mm	1 mm
Geometrical profile of the inlet duct	Fig. 5.7	Fig. 5.8	Fig. 5.9	Fig. 5.10
Inlet duct - Sampling Volume centroid distance	8 mm	2 mm	2 mm	2 mm
Diameter of the outflow duct	2 mm	1.5 mm	0.3 mm	1 mm
Inlet duct - Sampling Volume centroid distance	8 mm	2 mm	2 mm	2 mm
Pump volumetric flow rate	3 l/min	3 l/min	0.3 l/min	1 l/min

Tab. 5.10: Configurations considered for the MicroMED Sampling Head and Optical Stage.

The geometrical parameters were modified in order to evaluate the effects on the sampling efficiency and velocity of the particles in the Sampling Volume region. The goal was to obtain that most particles cross the Sampling Volume region with a uniform velocity profile. The maximum pump volumetric flow rate was considered 3 l/min. Nevertheless, as explained in Sect. 5.3.1, the value of the volumetric flow rate was also fixed to guarantee that the flow regime should be approximately incompressible.

The different configurations were analysed to maximize the sampling efficiency η_{sample} for $d_p = 0.2-20 \mu\text{m}$. The overall dimensions used for the CFD analysis for all the configurations are reported in Fig. 5.6.

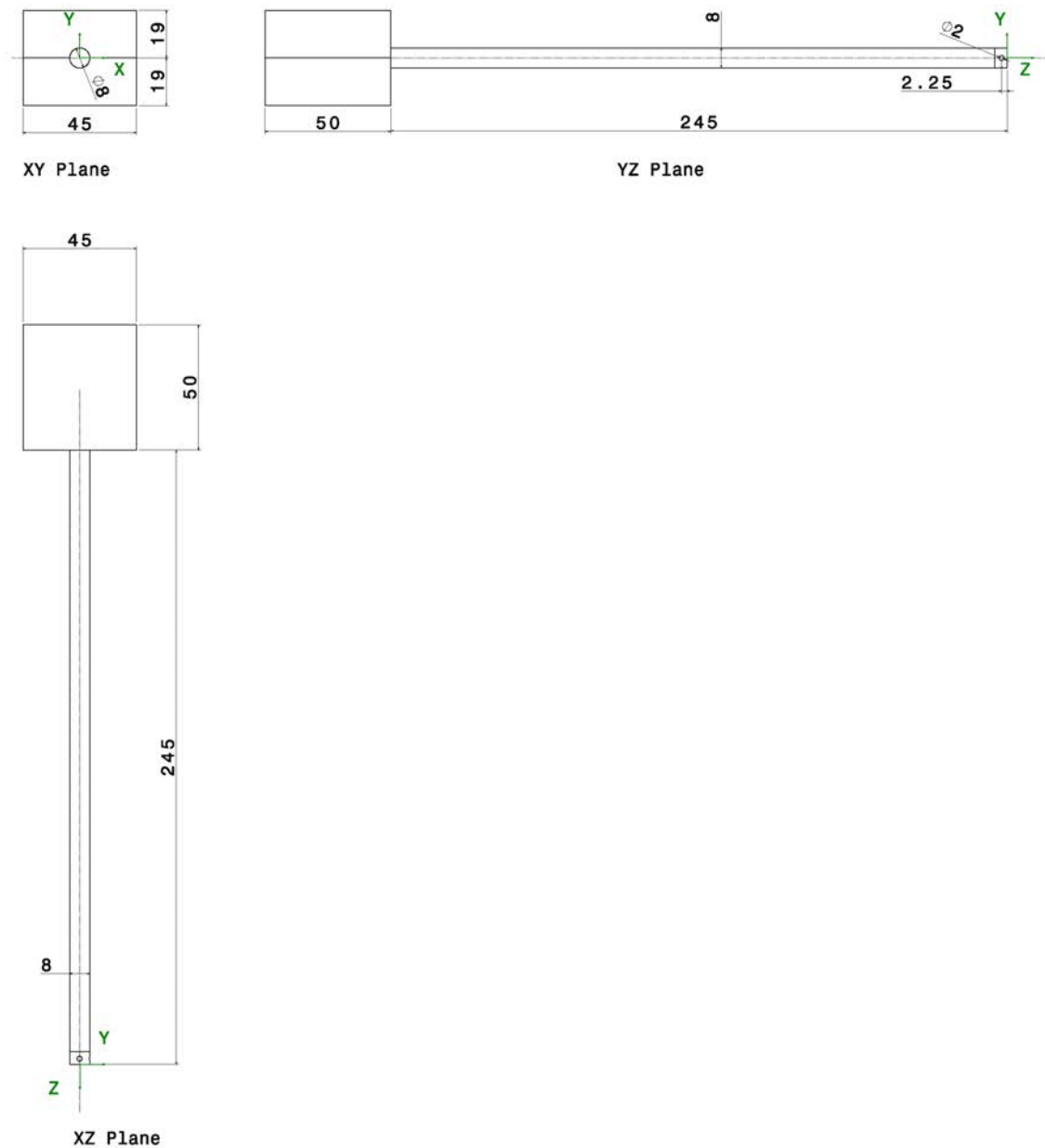


Fig. 5.6: MicroMED Sampling Head and Optical Stage overall dimensions (mm).

The MicroMED geometrical model was simplified including only the relevant parts:

- Sampling Head as a long duct with 4 inlet holes;
- Optical Stage (OS) as parallelepiped case composed by two specular covers;
- Inlet duct inside the OS case as a pipeline axisymmetric nozzle with convergent or constant profile along its axis;
- Outlet duct inside the OS case as a pipeline axisymmetric nozzle with constant profile along its axis;

- The Sampling Volume with ideal size of 0.3 mm x 0.3 mm x 0.3 mm: so it was assumed that the particles should cross the middle plane within a radius of 0.15 mm from the centroid in order to be intercepted by the laser spot.

The only optical element represented in the CFD model is the mirror, which has an envelope of 29 mm diameter and 10 mm height. The mirror dimensions are purely indicative at this stage (Sect. 5.4). The other optical elements, laser diode, collimator lenses, and detector, were not considered in the CFD model as they are far from the Sampling Volume, and, hence, they should not be relevant from a fluid dynamics point of view. The pump, not represented in Fig. 5.6, will be connected at the end of the Optical Stage and with the outlet duct via a proper pipeline (Fig. 5.4).

The MicroMED Configurations #1, #2, #3 and #4 (internal sections) are reported in Fig. 5.7, Fig. 5.8, Fig. 5.9, and Fig. 5.10, respectively. In the OS case of each configuration, the laser beam direction is shown with a blue line and the mirror-photodiode direction is shown with a red line.

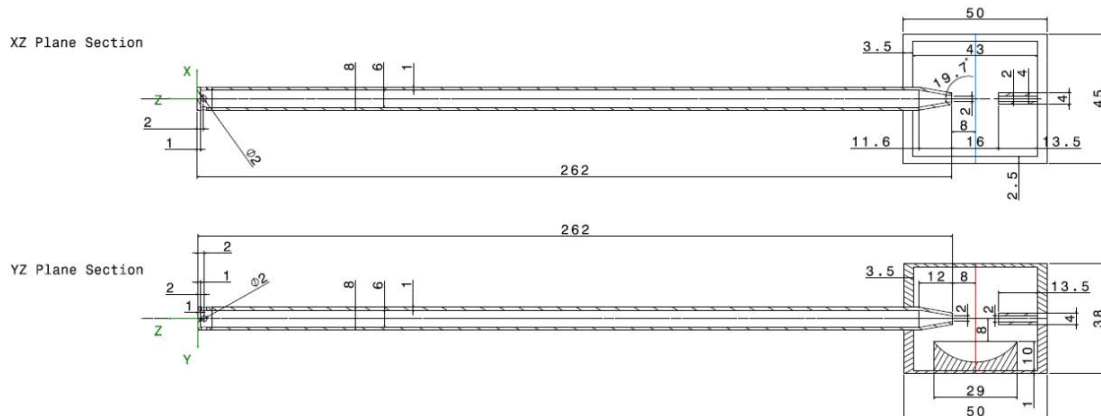


Fig. 5.7: MicroMED Configuration #1 internal sections (mm).

In configuration #1 (Fig. 5.7) the outflow section of the inlet duct has a 2 mm size, which is typical of commercial OPCs. The Sampling Head tube has a constant profile externally, while the inlet duct, extension of the former, has a profile convergent inside the OS case. The distance between the inflow duct and the Sampling Volume centroid is 8 mm in order to be conservative with the optical design, which should require a sufficient free space to avoid laser beam reflections and minimize stray light. The outlet duct has a constant section of the same size of the inlet duct.

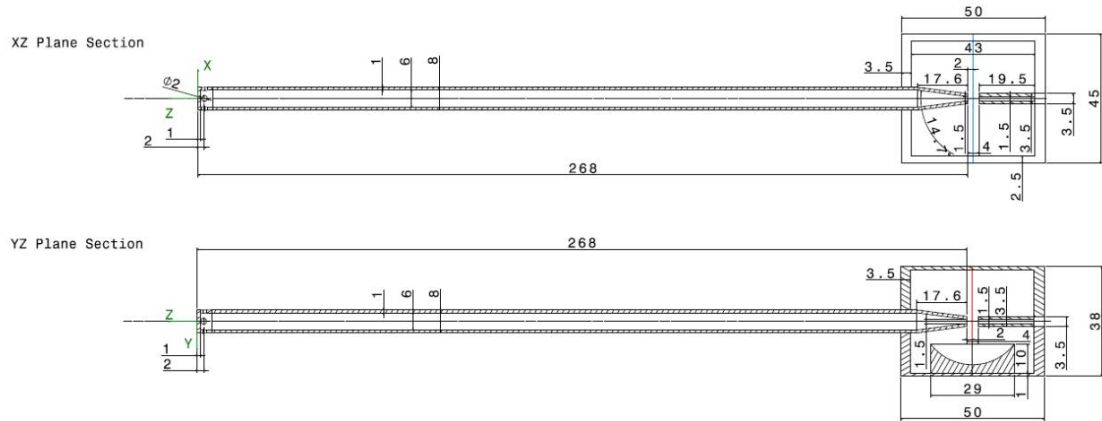


Fig. 5.8: MicroMED Configuration #2 internal sections (mm).

Configuration #2 (Fig. 5.8) has a reduced outflow section of the inlet duct with internal diameter of 1.5 mm to exploit particles inertia in order to make their trajectories closer to the centroid of the Sampling Volume, and the inlet duct is closer to the Sampling Volume centroid (2 mm) in order to reduce the flow dispersion. The inlet duct profile is convergent inside the OS case, while the outlet duct has a constant section with internal diameter of 1.5 mm.

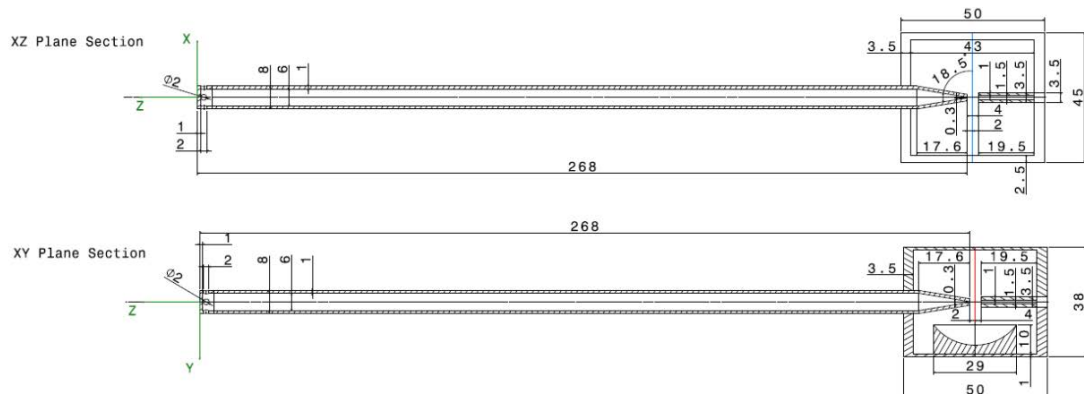


Fig. 5.9: MicroMED Configuration #3 internal sections (mm).

Configuration #3 (Fig. 5.9) has a very small outflow section of the inlet duct with internal diameter of 0.3 mm, and a distance of 2 mm from the centroid of the Sampling Volume. The outlet duct has a constant section with internal diameter of 1.5 mm. Although this configuration should focus better the aerosol stream, it is hardly applicable as the width of the inlet section is too small with respect to particles size, and, would require a too small volumetric flow rate (0.3 l/min) in order to respect the incompressible hypothesis.

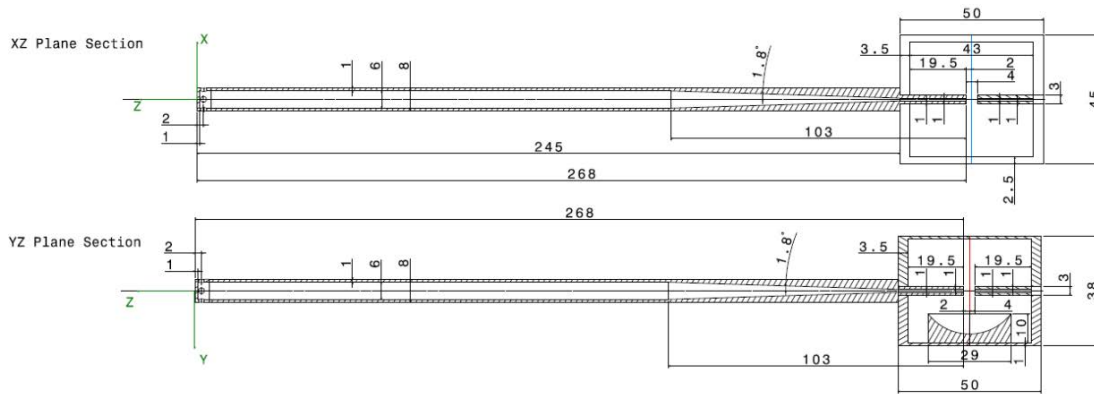


Fig. 5.10: MicroMED Configuration #4 internal sections (mm).

Configuration #4 (Fig. 5.10) is a compromise accounting for fluid dynamics and optical requirements. The envelope inside the OS case is reduced, as the inlet duct has a constant profile with an internal diameter of 1 mm, while a constant + convergent profile is used for the pipeline of the Sampling Head tube, where the internal diameter linearly changes from 6 mm to 1 mm along a distance of 80 mm. The 6 mm size of the pipeline before the OS case is considered to be as minimum value for such component. In fact, a smaller dimension would imply too many impacts of larger particles on walls nearby the inlet holes due to their inertia. The distance from the inlet duct to the Sampling Volume centroid is again set to 2 mm.

In the following, the results of the simulations for the different MicroMED configurations will be shown and discussed.

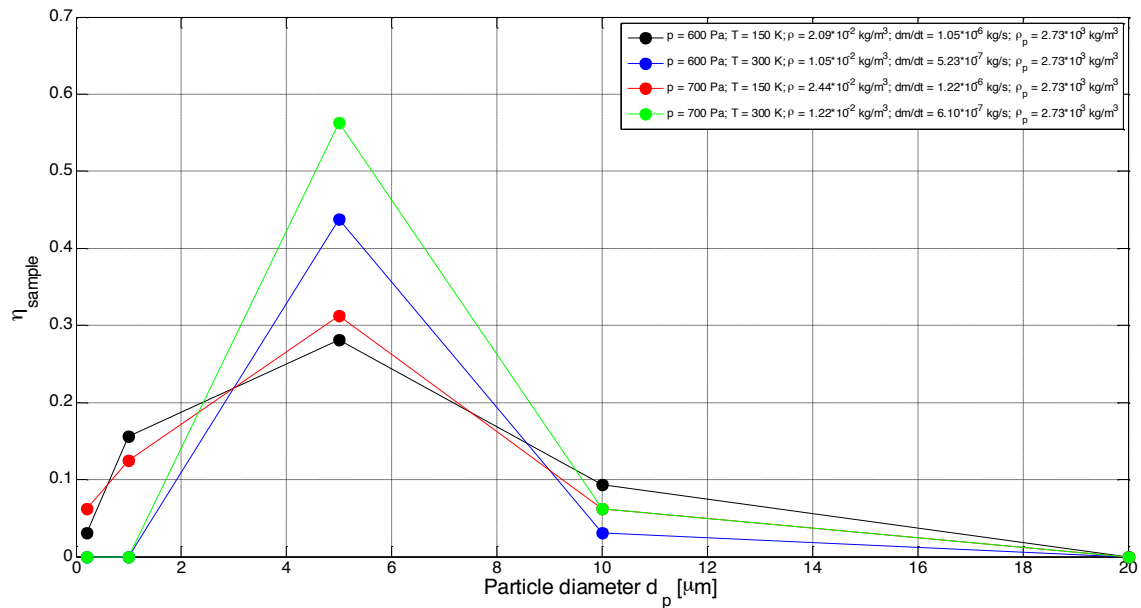


Fig. 5.11: Sampling efficiency (η_{sample}) with respect to particle diameter (d_p) at different boundary conditions for a Sampling Volume of radius 0.15 mm (Configuration #1).

The sampling efficiency (Fig. 5.11), the particles distributions (Fig. 5.12, Fig. 5.14, Fig. 5.16, and Fig. 5.18) and particle axial and radial velocity components (Fig. 5.13, Fig. 5.15, Fig. 5.17, and Fig. 5.19) across the radial coordinate of the Sampling Volume have been evaluated for the Configuration #1 at the boundary conditions discussed above. The sampling efficiency is estimated as the ratio between the number of particles, which were able to cross the Sampling Volume within a distance of 0.15 mm from its centroid, and the total number of particles injected upstream at the MicroMED inlet. The particle distributions are estimated as the ratio between the number of particles with respect to the distance from the centroid of the Sampling Volume and the total number of particles crossing the middle plane of the MicroMED OS, which does not include particle eventually loss upstream.

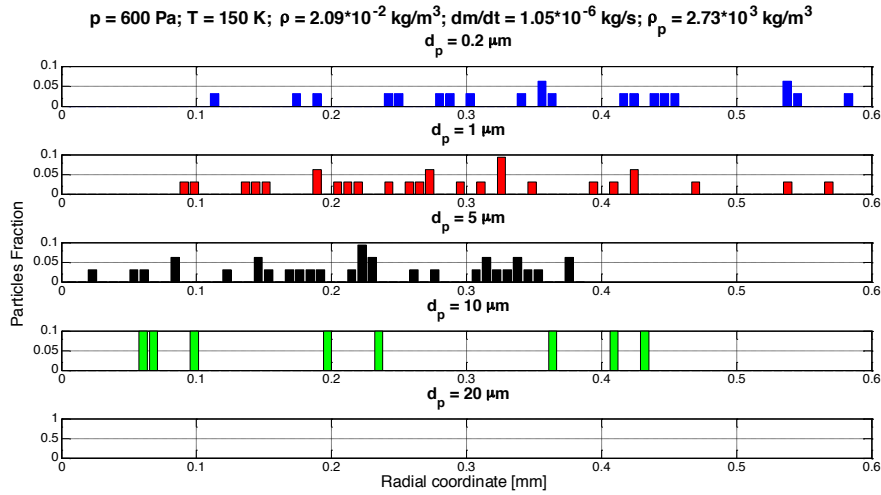


Fig. 5.12: Particle distributions in the middle plane of the Sampling Volume orthogonal to the mainstream ($p = 600 \text{ Pa}$, $T = 150 \text{ K}$, $\rho = 2.09 \cdot 10^{-2} \text{ kg/m}^3$, $\dot{m} = 1.05 \cdot 10^{-6} \text{ kg/s}$, $\rho_p = 2.73 \cdot 10^3 \text{ kg/m}^3$, Configuration #1).

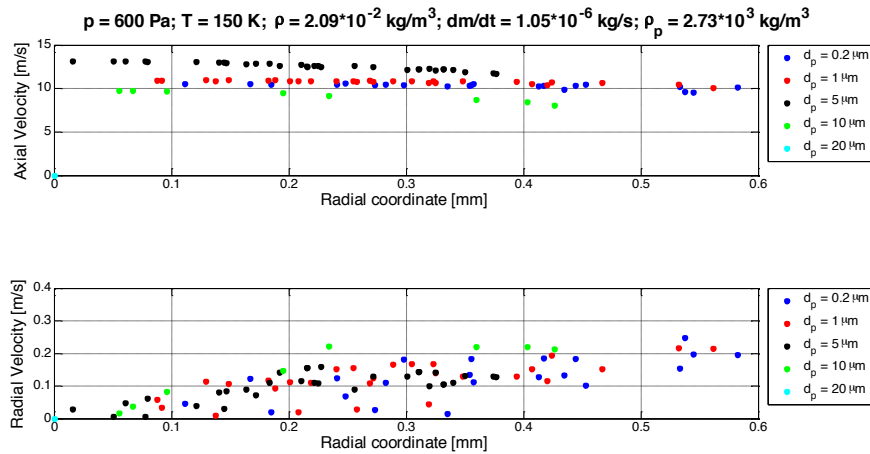


Fig. 5.13: Particle axial and radial velocity components in the middle plane of the Sampling Volume orthogonal to the mainstream ($p = 600 \text{ Pa}$, $T = 150 \text{ K}$, $\rho = 2.09 \cdot 10^{-2} \text{ kg/m}^3$, $\dot{m} = 1.05 \cdot 10^{-6} \text{ kg/s}$, $\rho_p = 2.73 \cdot 10^3 \text{ kg/m}^3$, Configuration #1).

The Configuration #1 is highly conservative from an optical point of view, since the distance between the inlet duct and outlet duct (16 mm) is very large in order to minimize stray light. Nevertheless, from a fluid dynamics point of view, as conceivable, it does not optimize the particle dynamics as trajectories diverge too much at the Sampling Volume. A volumetric flow rate of 3 l/min is suitable to have particles velocity of 10-13 m/s in the Sampling Volume region, which should give response time compatible with the PE performance.

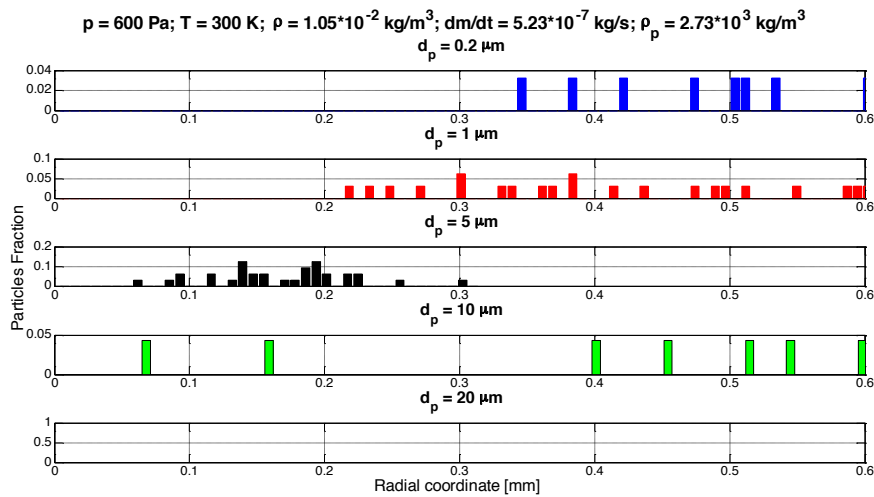


Fig. 5.14: Particle distributions in the middle plane of the Sampling Volume orthogonal to the mainstream ($p = 600$ Pa, $T = 300$ K, $\rho = 1.05 \cdot 10^{-2}$ kg/m³, $\dot{m} = 5.23 \cdot 10^{-7}$ kg/s, $\rho_p = 2.73 \cdot 10^3$ kg/m³, Configuration #1).

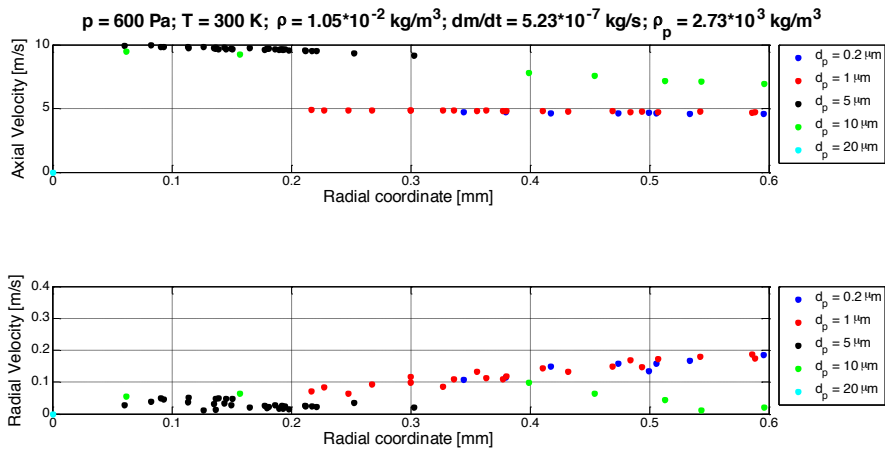


Fig. 5.15: Particle axial and radial velocity components in the middle plane of the Sampling Volume orthogonal to the mainstream ($p = 600$ Pa, $T = 300$ K, $\rho = 1.05 \cdot 10^{-2}$ kg/m³, $\dot{m} = 5.23 \cdot 10^{-7}$ kg/s, $\rho_p = 2.73 \cdot 10^3$ kg/m³, Configuration #1).

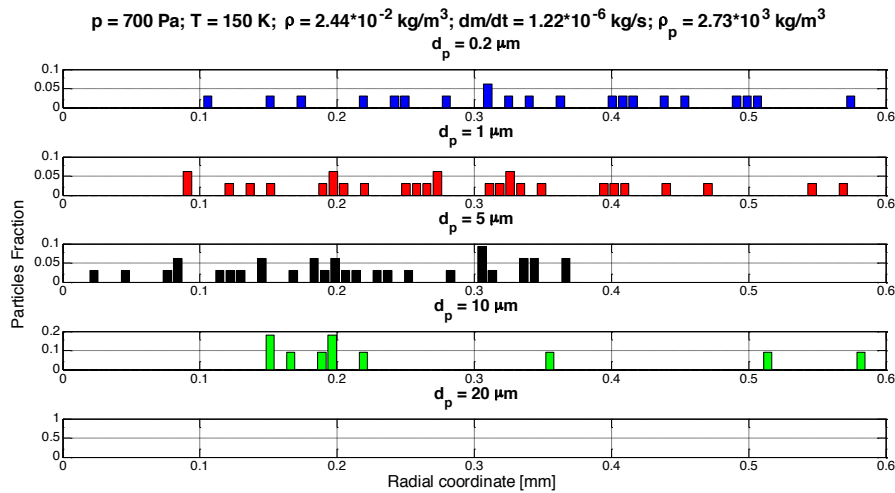


Fig. 5.16: Particle distributions in the middle plane of the Sampling Volume orthogonal to the mainstream ($p = 700 \text{ Pa}$, $T = 150 \text{ K}$, $\rho = 2.44 \cdot 10^{-2} \text{ kg/m}^3$, $\dot{m} = 1.22 \cdot 10^{-6} \text{ kg/s}$, $\rho_p = 2.73 \cdot 10^3 \text{ kg/m}^3$, Configuration #1).

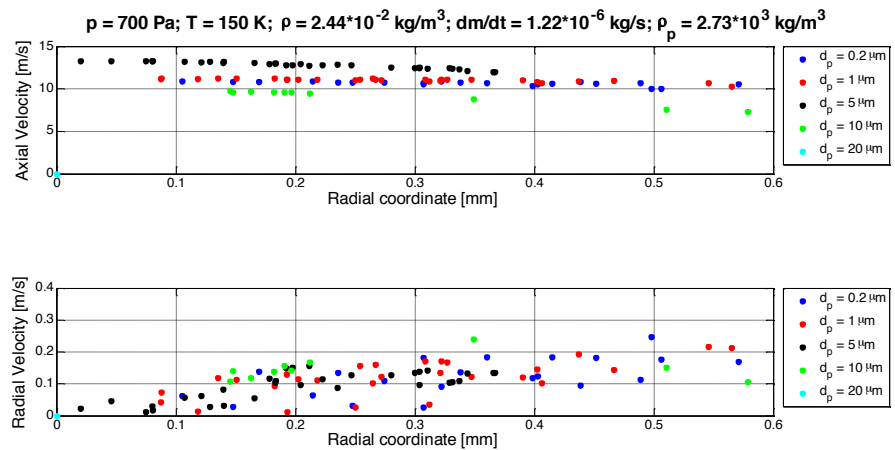


Fig. 5.17: Particle axial and radial velocity components in the middle plane of the Sampling Volume orthogonal to the mainstream ($p = 700 \text{ Pa}$, $T = 150 \text{ K}$, $\rho = 2.44 \cdot 10^{-2} \text{ kg/m}^3$, $\dot{m} = 1.05 \cdot 10^{-6} \text{ kg/s}$, $\rho_p = 2.73 \cdot 10^3 \text{ kg/m}^3$, Configuration #1).

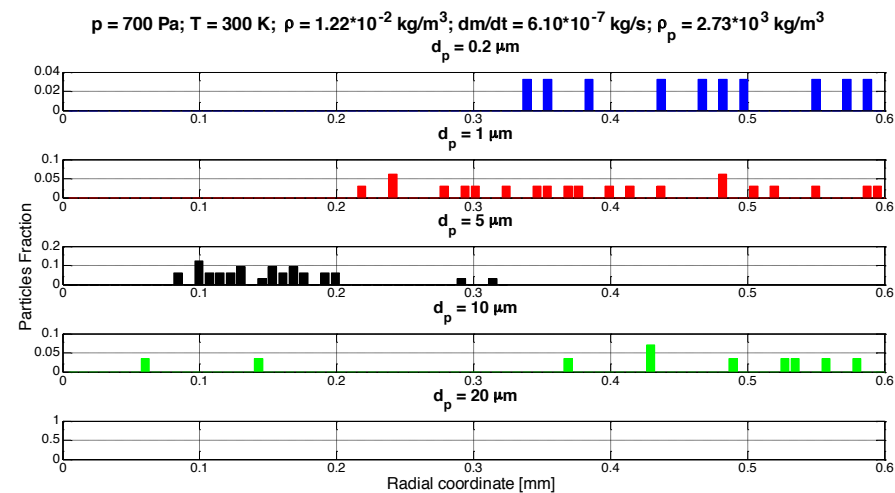


Fig. 5.18: Particle distributions in the middle plane of the Sampling Volume orthogonal to the mainstream ($p = 700 \text{ Pa}$, $T = 300 \text{ K}$, $\rho = 1.22 \cdot 10^{-2} \text{ kg/m}^3$, $\dot{m} = 6.10 \cdot 10^{-7} \text{ kg/s}$, $\rho_p = 2.73 \cdot 10^3 \text{ kg/m}^3$, Configuration #1).

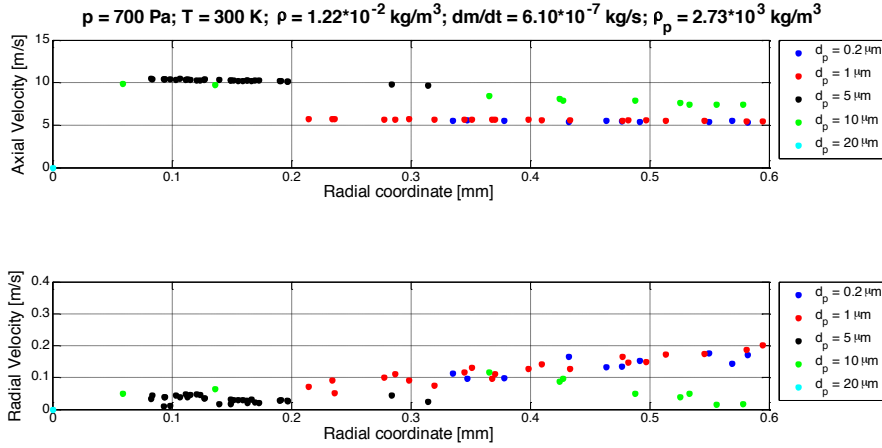


Fig. 5.19: Particle axial and radial velocity components in the middle plane of the Sampling Volume orthogonal to the mainstream ($p = 700$ Pa, $T = 300$ K, $\rho = 1.22 \cdot 10^{-2}$ kg/m³, $\dot{m} = 6.10 \cdot 10^{-7}$ kg/s, $\rho_p = 2.73 \cdot 10^3$ kg/m³, Configuration #1).

d_p (μm)	p (Pa)	T (K)	ρ (kg/m ³)	\dot{m} (kg/s)	$V_{p,a,m}$ (m/s)	$\sigma_{V_{p,a}}$ (m/s)	$V_{p,r,m}$ (m/s)	$\sigma_{V_{p,r}}$ (m/s)
0.2	600	150	$2.09 \cdot 10^{-2}$	$1.05 \cdot 10^{-6}$	-	-	-	-
1					10.95	0.058	0.064	0.045
5					13.06	0.076	0.043	0.029
10					9.73	0.039	0.046	0.034
20					-	-	-	-
0.2	600	300	$1.05 \cdot 10^{-2}$	$5.23 \cdot 10^{-7}$	-	-	-	-
1					-	-	-	-
5					9.80	0.094	0.037	0.013
10					-	-	-	-
20					-	-	-	-
0.2	700	150	$2.44 \cdot 10^{-2}$	$1.22 \cdot 10^{-6}$	10.84	0.030	0.045	0.025
1					11.20	0.052	0.062	0.045
5					13.22	0.072	0.038	0.023
10					9.66	0.082	0.123	0.023
20					-	-	-	-
0.2	700	300	$1.22 \cdot 10^{-2}$	$6.10 \cdot 10^{-7}$	-	-	-	-
1					-	-	-	-
5					10.37	0.061	0.034	0.012
10					9.80	0.122	0.057	0.010
20					-	-	-	-

Tab. 5.11: Particle mean axial velocity ($V_{p,a,m}$) and standard deviation ($\sigma_{V_{p,a}}$) and particle mean radial velocity ($V_{p,r,m}$) and standard deviation ($\sigma_{V_{p,r}}$) in the middle plane of the Sampling Volume orthogonal to the mainstream within a radius of 0.15 mm from the Sampling Volume centroid (Configuration #1).

The mean value and standard deviation of the profiles of the particles axial and radial velocity in the Sampling Volume are reported in Tab. 5.11 for the Configuration #1 at the considered boundary conditions. The statistics were obtained by considering only the particles crossing the Sampling Volume within a radius of 0.15 mm from the centroid. Where the number of the particle crossing the region is insufficient to make a statistical inference, a dash has been put in the table. The value of the particles velocity in the Sampling Volume depends on particles inertia (i.e., mass, density, diameter) and boundary conditions (i.e., fluid mass flow rate, density, pressure) according to the local Stokes number (Eq. (3.83)). The Sampling Volume corresponds to a region where the

fluid flow accelerates (i.e., in the convergent part of the inlet duct), then decelerates in the OS box, and, finally, re-accelerates nearby the outlet duct. From a fluid dynamics point of view this situation is not convenient, but, unfortunately, it is imposed by the optical design requirement of free space for the laser beam. Particles with lower local Stokes number (Eq. (3.83)), i.e., the smaller ones (according to the Stk definition), will follow more strictly the fluid flow velocity changes. This implies that the particle size, which maximizes the velocity in the Sampling Volume is not constant, but depends on the local fluid flow variations, and, hence, on the boundary conditions and geometry, as for the other configurations.

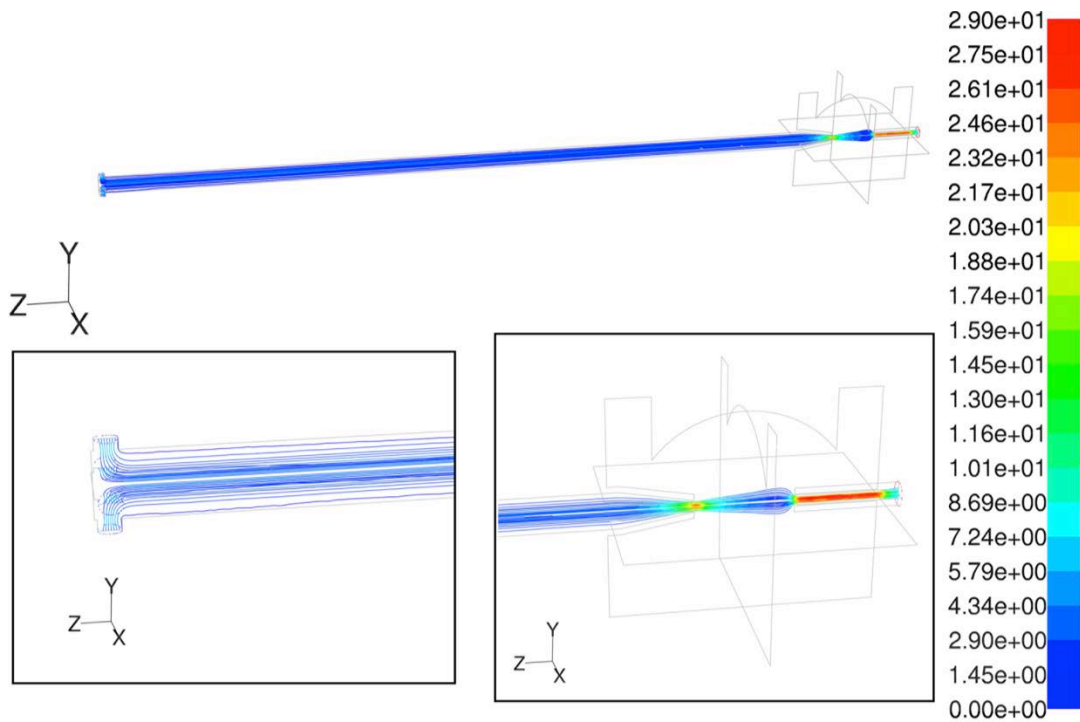


Fig. 5.20: Particle trajectories ($d_p = 0.2 \mu\text{m}$, $\rho_p = 2.73 \cdot 10^3 \text{ kg/m}^3$) coloured with velocity magnitude (m/s) for the Configuration #1 at $p = 600 \text{ Pa}$, $T = 300 \text{ K}$, $\rho = 1.05 \cdot 10^{-2} \text{ kg/m}^3$, $\dot{m} = 5.23 \cdot 10^{-7} \text{ kg/s}$. The figure represents the geometry projected on 3 main planes and the full 3D trajectories.

The sampling efficiency of Configuration #1 is very poor. Very few particles of the injected flow are able to cross the Sampling Volume, while most of them, above all the small ones ($d_p < 1 \mu\text{m}$), cross outside (Fig. 5.20). The most rarefied environment, i.e., $p = 600 \text{ Pa}$, $T = 300 \text{ K}$, $\rho = 1.05 \cdot 10^{-2} \text{ kg/m}^3$, is the most critical case with respect to particle losses, both for small ($d_p < 1 \mu\text{m}$) and large particles ($d_p > 10 \mu\text{m}$) since the fluid control of the particle dynamics depends on the ratio ρ_p/ρ . The large particles ($d_p > 10 \mu\text{m}$) do not have good sampling efficiencies ($\eta_{\text{sample}} < 0.1$) as most of them are lost at the inlet as a result of impacts on the walls of the cylindrical Sampling Head (Fig.

5.21). Nevertheless, the dispersion in the Sampling Volume for the large particles is quite smaller than for the small ones. The best behaviour is for middle size particles ($d_p = 5 \mu\text{m}$) as they have a sufficient low inertia and kinetic energy not to impact on the inlet walls, but they do not have too small inertia to be dispersed away from the Sampling Volume region. Finally, the outlet duct can have a constant section no more than 2 mm and/or of the same size of the inlet duct, but it needs to be closer to the centroid of the Sampling Volume, as the inlet duct. In fact, no significant advantages in the sampling efficiency are introduced by larger diameters and/or convergent profiles of the outlet duct, which, conversely, imply larger mass and/or higher manufacturing complexity.

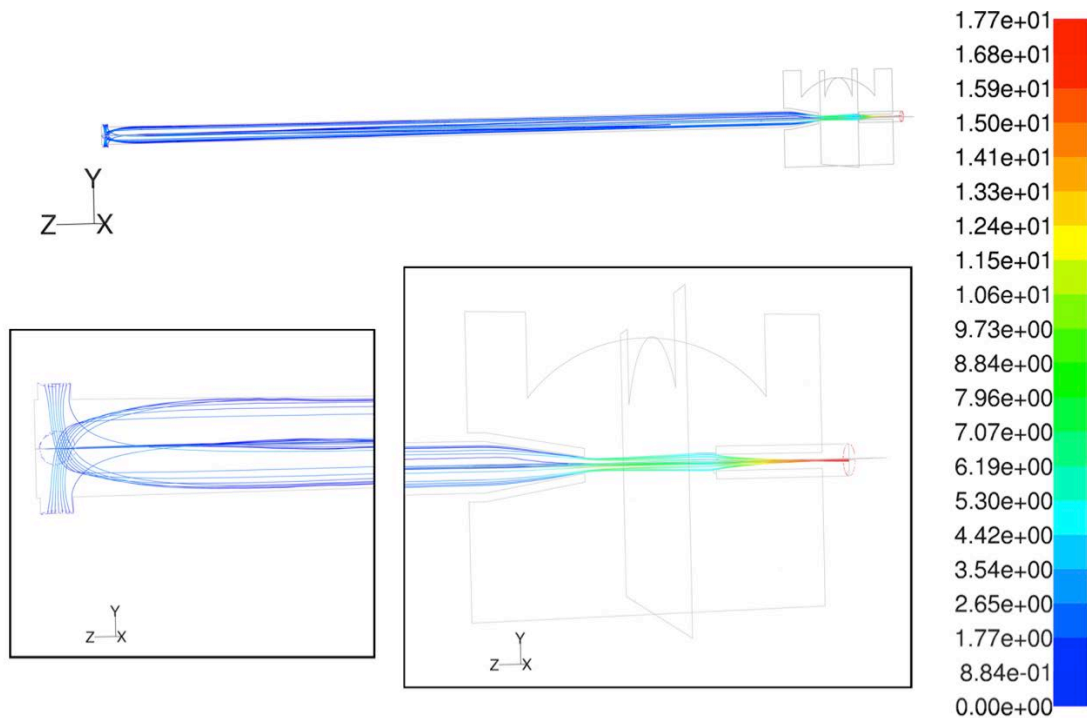


Fig. 5.21: Particle trajectories ($d_p = 10 \mu\text{m}$, $\rho_p = 2.73 \cdot 10^3 \text{ kg/m}^3$) coloured with velocity magnitude (m/s) for the Configuration #1 at $p = 600 \text{ Pa}$, $T = 300 \text{ K}$, $\rho = 1.05 \cdot 10^{-2} \text{ kg/m}^3$, $\dot{m} = 5.23 \cdot 10^{-7} \text{ kg/s}$. The figure represents the geometry projected on 3 main planes and the full 3D trajectories.

The sampling efficiency (Fig. 5.22), the particles distributions (Fig. 5.23, Fig. 5.25, Fig. 5.27, and Fig. 5.29) and the particles axial and radial velocity components (Fig. 5.24, Fig. 5.26, Fig. 5.28, and Fig. 5.30) across the radial coordinate of the Sampling Volume have been evaluated for the Configuration #2 at the boundary conditions discussed above. The mean value and standard deviation of the profiles of the particle axial and radial velocity in the Sampling Volume are reported in Tab. 5.12 for the Configuration #2 at the considered boundary conditions. In the Configuration #2, the

reduction of the distance between the inlet duct and outlet ducts from 16 mm to 4 mm improves the behaviour of the aerosol flow.

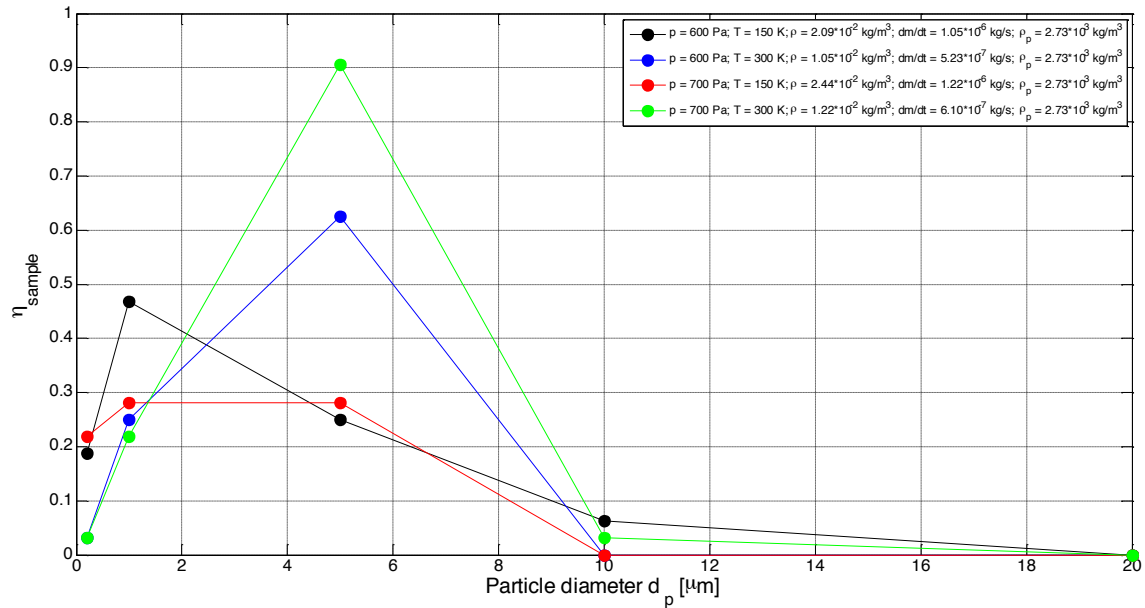


Fig. 5.22: Sampling efficiency (η_{sample}) with respect to particle diameter (d_p) at different boundary conditions for a Sampling Volume of radius 0.15 mm (Configuration #2).

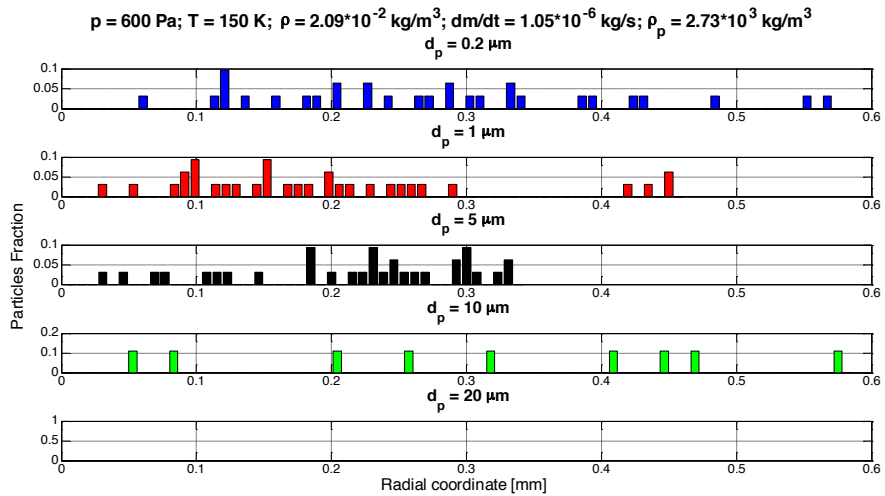


Fig. 5.23: Particle distributions in the middle plane of the Sampling Volume orthogonal to the mainstream ($p = 600 \text{ Pa}$, $T = 150 \text{ K}$, $\rho = 2.09 \cdot 10^{-2} \text{ kg/m}^3$, $\dot{m} = 1.05 \cdot 10^{-6} \text{ kg/s}$, $\rho_p = 2.73 \cdot 10^3 \text{ kg/m}^3$, Configuration #2).

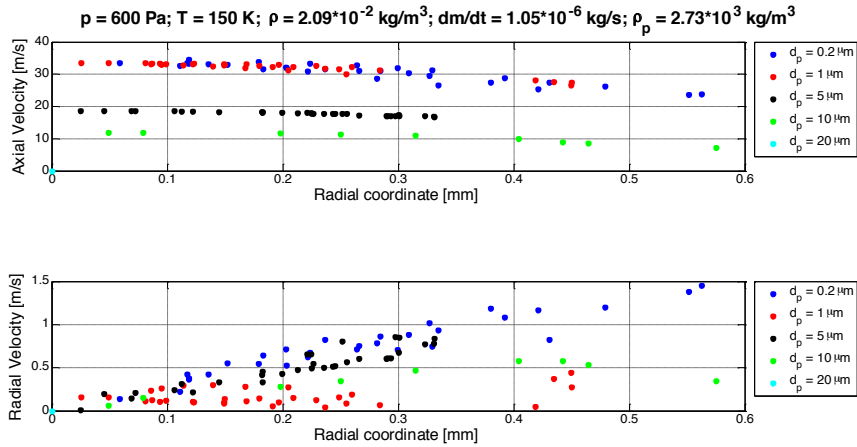


Fig. 5.24: Particle axial and radial velocity components in the middle plane of the Sampling Volume orthogonal to the mainstream ($p = 600 \text{ Pa}$, $T = 150 \text{ K}$, $\rho = 2.09 \cdot 10^{-2} \text{ kg/m}^3$, $\dot{m} = 1.05 \cdot 10^{-6} \text{ kg/s}$, $\rho_p = 2.73 \cdot 10^3 \text{ kg/m}^3$, Configuration #2).

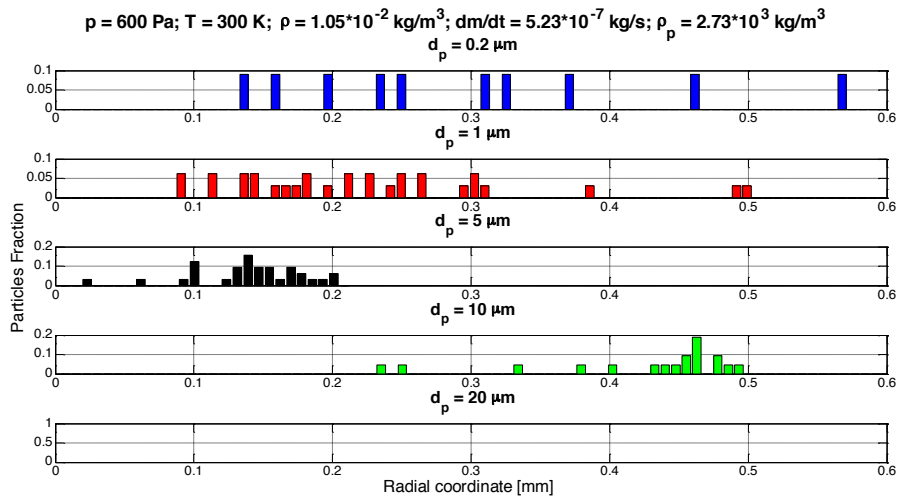


Fig. 5.25: Particle distributions in the middle plane of the Sampling Volume orthogonal to the mainstream ($p = 600 \text{ Pa}$, $T = 300 \text{ K}$, $\rho = 1.05 \cdot 10^{-2} \text{ kg/m}^3$, $\dot{m} = 5.23 \cdot 10^{-7} \text{ kg/s}$, $\rho_p = 2.73 \cdot 10^3 \text{ kg/m}^3$, Configuration #2).

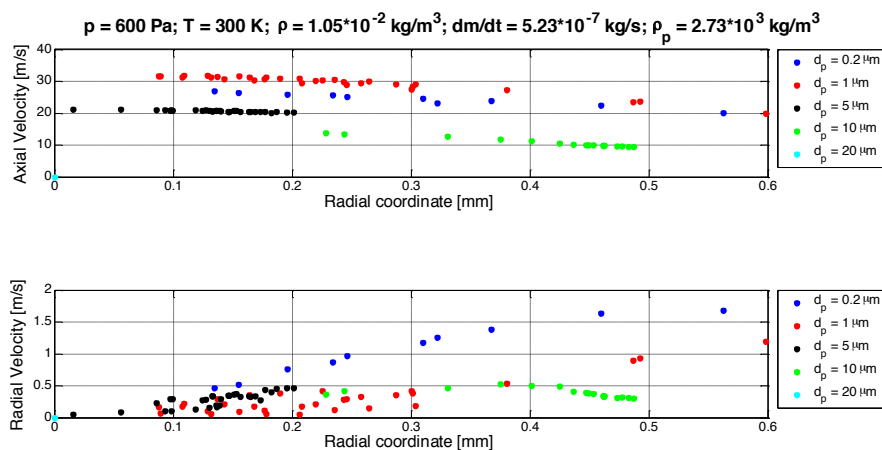


Fig. 5.26: Particle axial and radial velocity components in the middle plane of the Sampling Volume orthogonal to the mainstream ($p = 600 \text{ Pa}$, $T = 300 \text{ K}$, $\rho = 1.05 \cdot 10^{-2} \text{ kg/m}^3$, $\dot{m} = 5.23 \cdot 10^{-7} \text{ kg/s}$, $\rho_p = 2.73 \cdot 10^3 \text{ kg/m}^3$, Configuration #2).

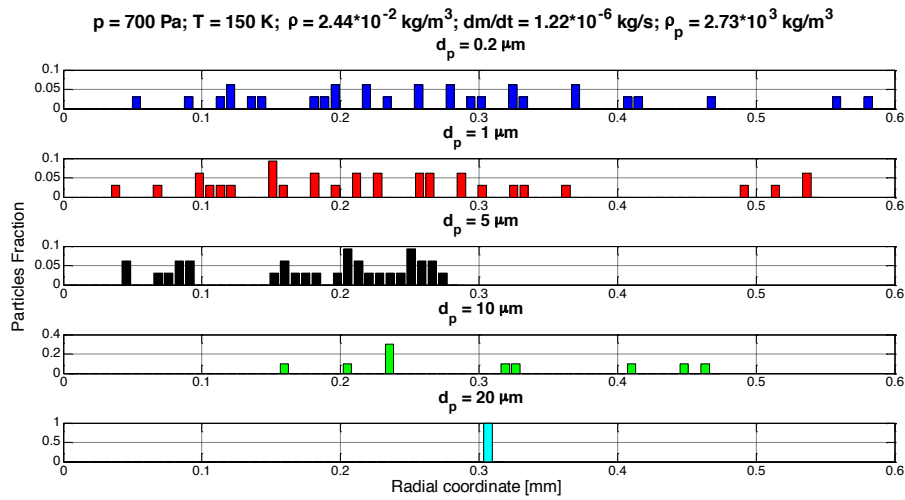


Fig. 5.27: Particle distributions in the middle plane of the Sampling Volume orthogonal to the mainstream ($p = 700 \text{ Pa}$, $T = 150 \text{ K}$, $\rho = 2.44 \cdot 10^{-2} \text{ kg/m}^3$, $\dot{m} = 1.22 \cdot 10^{-6} \text{ kg/s}$, $\rho_p = 2.73 \cdot 10^3 \text{ kg/m}^3$, Configuration #2).

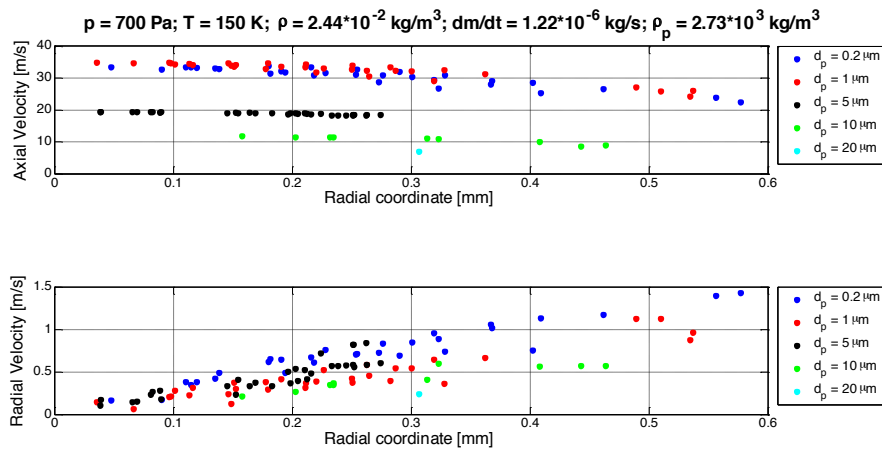


Fig. 5.28: Particle axial and radial velocity components in the middle plane of the Sampling Volume orthogonal to the mainstream ($p = 700 \text{ Pa}$, $T = 150 \text{ K}$, $\rho = 2.44 \cdot 10^{-2} \text{ kg/m}^3$, $\dot{m} = 1.22 \cdot 10^{-6} \text{ kg/s}$, $\rho_p = 2.73 \cdot 10^3 \text{ kg/m}^3$, Configuration #2).

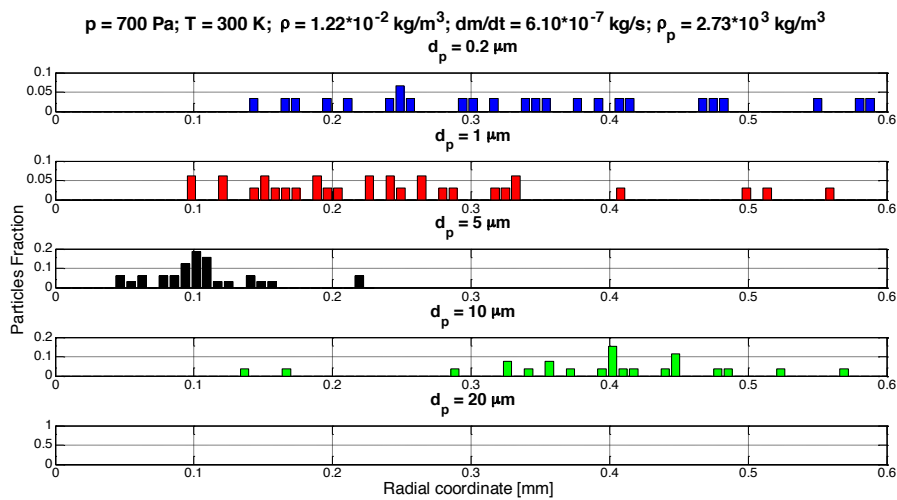


Fig. 5.29: Particle distributions in the middle plane of the Sampling Volume orthogonal to the mainstream ($p = 700 \text{ Pa}$, $T = 300 \text{ K}$, $\rho = 1.22 \cdot 10^{-2} \text{ kg/m}^3$, $\dot{m} = 6.10 \cdot 10^{-7} \text{ kg/s}$, $\rho_p = 2.73 \cdot 10^3 \text{ kg/m}^3$, Configuration #2).

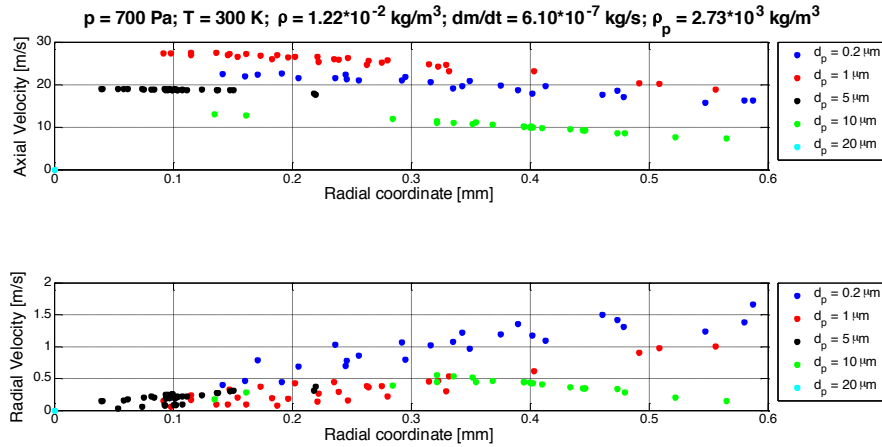


Fig. 5.30: Particle axial and radial velocity components in the middle plane of the Sampling Volume orthogonal to the mainstream ($p = 700 \text{ Pa}$, $T = 300 \text{ K}$, $\rho = 1.22 \cdot 10^{-2} \text{ kg/m}^3$, $\dot{m} = 6.10 \cdot 10^{-7} \text{ kg/s}$, $\rho_p = 2.73 \cdot 10^3 \text{ kg/m}^3$, Configuration #2).

d_p (μm)	p (Pa)	T (K)	ρ (kg/m^3)	\dot{m} (kg/s)	$V_{p,a,m}$ (m/s)	$\sigma_{V_{p,a}}$ (m/s)	$V_{p,r,m}$ (m/s)	$\sigma_{V_{p,r}}$ (m/s)
0.2	600	150	$2.09 \cdot 10^{-2}$	$1.05 \cdot 10^{-6}$	33.46	0.600	0.326	0.119
1					33.12	0.309	0.161	0.073
5					18.54	0.126	0.207	0.101
10					11.81	0.045	0.104	0.065
20					-	-	-	-
0.2	600	300	$1.05 \cdot 10^{-2}$	$5.23 \cdot 10^{-7}$	-	-	-	-
1					31.47	0.332	0.161	0.083
5					20.80	0.232	0.230	0.098
10					-	-	-	-
20					-	-	-	-
0.2	700	150	$2.44 \cdot 10^{-2}$	$1.22 \cdot 10^{-6}$	33.19	0.298	0.336	0.123
1					34.50	0.288	0.202	0.078
5					19.34	0.115	0.208	0.076
10					-	-	-	-
20					-	-	-	-
0.2	700	300	$1.22 \cdot 10^{-2}$	$6.10 \cdot 10^{-7}$	-	-	-	-
1					27.23	0.221	0.161	0.095
5					18.85	0.108	0.183	0.073
10					-	-	-	-
20					-	-	-	-

Tab. 5.12: Particle mean axial velocity ($V_{p,a,m}$) and standard deviation ($\sigma_{V_{p,a}}$) and particle mean radial velocity ($V_{p,r,m}$) and standard deviation ($\sigma_{V_{p,r}}$) in the middle plane of the Sampling Volume orthogonal to the mainstream within a radius of 0.15 mm from the Sampling Volume centroid (Configuration #2).

The sampling efficiency improves from configuration #1 to #2 as it can be seen by comparing Fig. 5.11 and Fig. 5.22. The sampling efficiency of the small particles ($d_p < 1 \mu\text{m}$) slightly increases ($\eta_{\text{sample}} < 0.5$), even if not too much. In fact, a second aspect learnt by comparing configurations #1 and #2 is the influence of the width of the outflow section of the inlet duct. A diameter of 1.5-2 mm of the outflow section of the inlet duct, which is typical of terrestrial OPC, is too large to allow concentration of particles within a radius of 0.15 mm from the Sampling Volume centroid at a volumetric flow rate of 3 l/min (Fig. 5.31). Moreover, a significant loss of large

particles ($d_p > 10 \mu\text{m}$) occurs at the inlet walls as in the Configuration #1. The best sampling efficiency is again for medium sizes ($d_p \approx 5 \mu\text{m}$) as for Configuration #1.

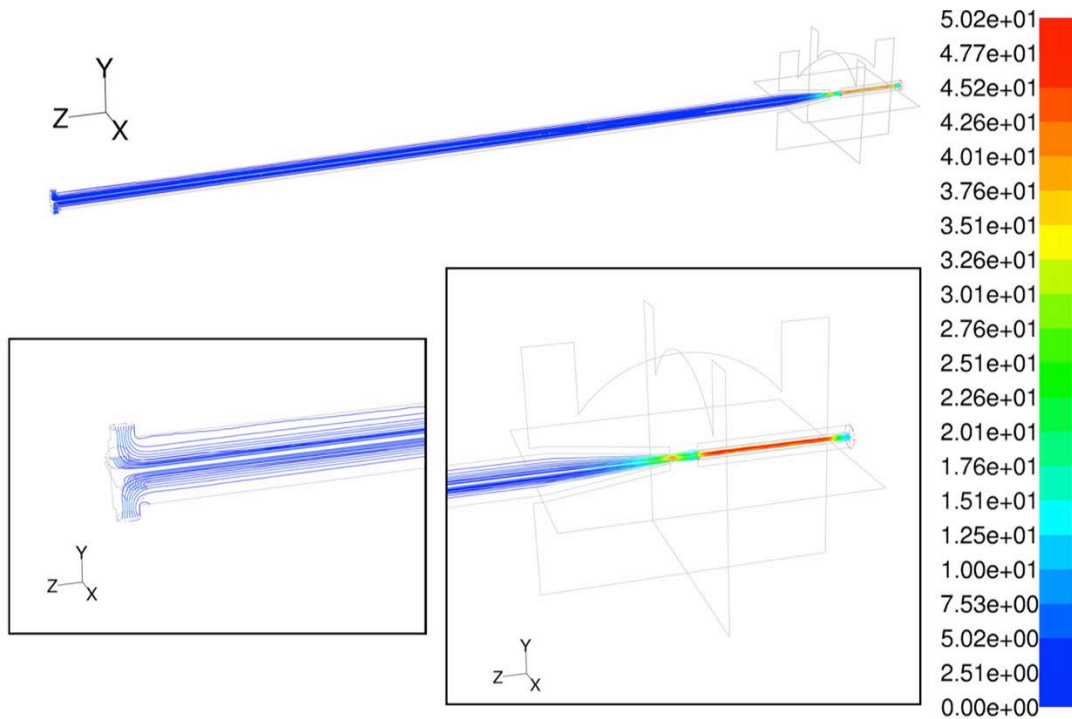


Fig. 5.31: Particle trajectories ($d_p = 0.2 \mu\text{m}$, $\rho_p = 2.73 \cdot 10^3 \text{ kg/m}^3$) coloured with velocity magnitude (m/s) for the Configuration #2 at $p = 600 \text{ Pa}$, $T = 300 \text{ K}$, $\rho = 1.05 \cdot 10^{-2} \text{ kg/m}^3$, $\dot{m} = 5.23 \cdot 10^{-7} \text{ kg/s}$. The figure represents the geometry projected on 3 main planes and the full 3D trajectories.

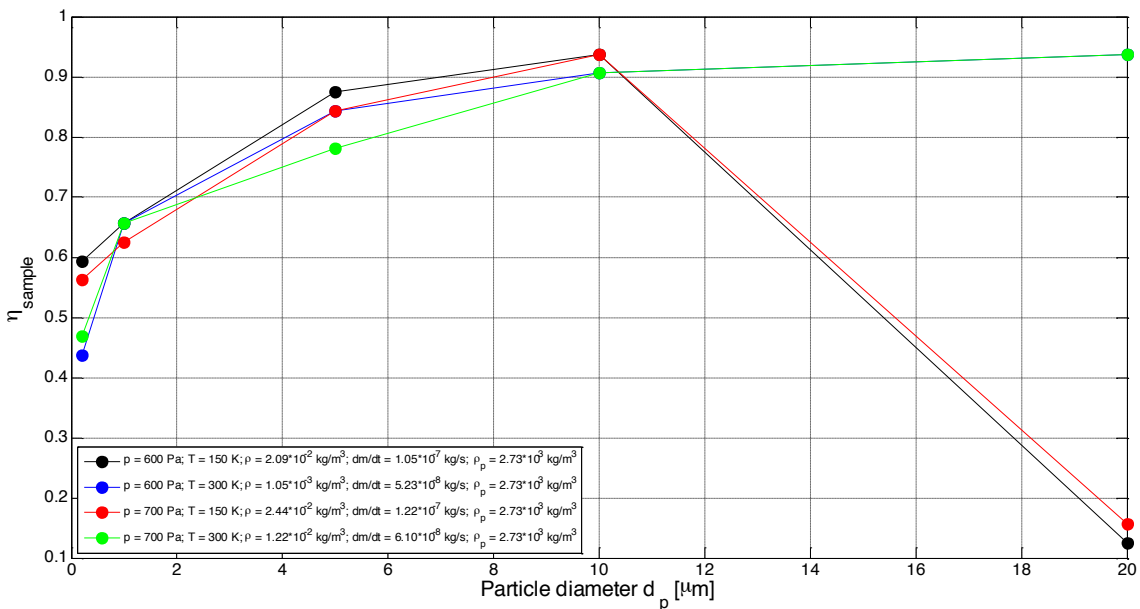


Fig. 5.32: Sampling efficiency (η_{sample}) with respect to particle diameter (d_p) at different boundary conditions for a Sampling Volume of radius 0.15 mm (Configuration #3).

The sampling efficiency (Fig. 5.32), the particle distributions (Fig. 5.33, Fig. 5.35, Fig. 5.37, and Fig. 5.39) and the particle axial and radial velocity components (Fig.

5.34, Fig. 5.36, Fig. 5.38, and Fig. 5.40) across the radial coordinate of the Sampling Volume have been evaluated for the Configuration #3 at the boundary conditions discussed above. The mean value and standard deviation of the profiles of the particles axial and radial velocity in the Sampling Volume are reported in Tab. 5.13 for the Configuration #3 at the considered boundary conditions. In the Configuration #3, the outflow section of the inlet duct is reduced down to 0.3 mm. This also implies to reduce the volume flow rate from 3 l/min to 0.3 l/min in order to have an incompressible flow.

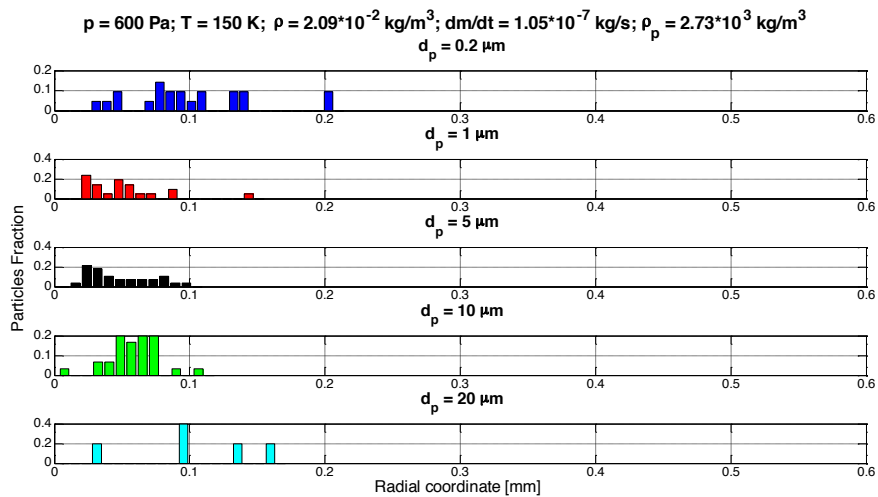


Fig. 5.33: Particle distributions in the middle plane of the Sampling Volume orthogonal to the mainstream ($p = 600 \text{ Pa}$, $T = 150 \text{ K}$, $\rho = 2.09 \cdot 10^{-2} \text{ kg/m}^3$, $\dot{m} = 1.05 \cdot 10^{-7} \text{ kg/s}$, $\rho_p = 2.73 \cdot 10^3 \text{ kg/m}^3$, Configuration #3).

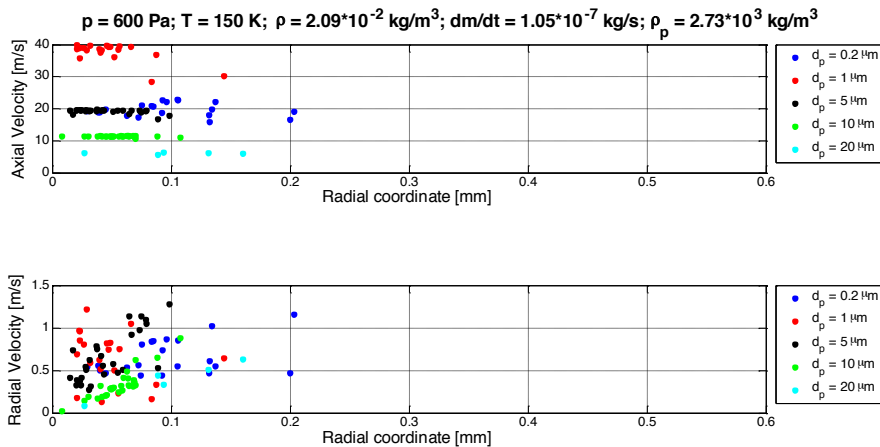


Fig. 5.34: Particle axial and radial velocity components in the middle plane of the Sampling Volume orthogonal to the mainstream ($p = 600 \text{ Pa}$, $T = 150 \text{ K}$, $\rho = 2.09 \cdot 10^{-2} \text{ kg/m}^3$, $\dot{m} = 1.05 \cdot 10^{-7} \text{ kg/s}$, $\rho_p = 2.73 \cdot 10^3 \text{ kg/m}^3$, Configuration #3).

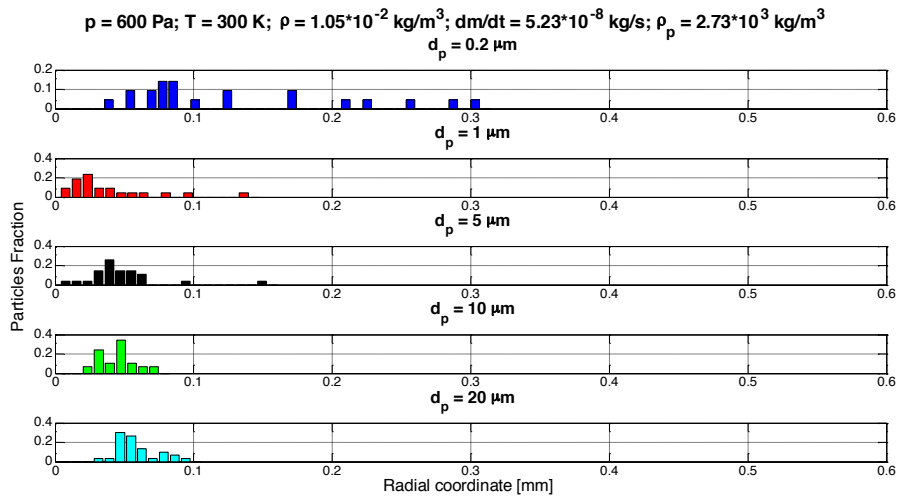


Fig. 5.35: Particle distributions in the middle plane of the Sampling Volume orthogonal to the mainstream ($p = 600 \text{ Pa}, T = 300 \text{ K}, \rho = 1.05 \cdot 10^{-2} \text{ kg/m}^3, \dot{m} = 5.23 \cdot 10^{-8} \text{ kg/s}, \rho_p = 2.73 \cdot 10^3 \text{ kg/m}^3$, Configuration #3).

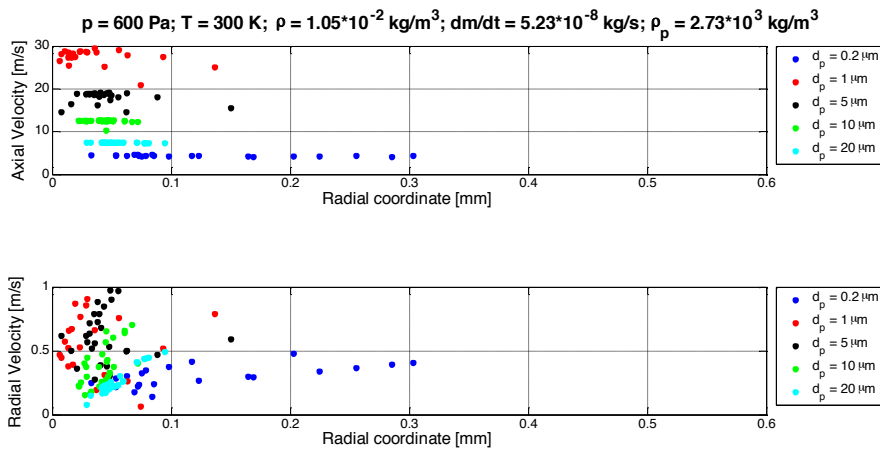


Fig. 5.36: Particle axial and radial velocity components in the middle plane of the Sampling Volume orthogonal to the mainstream ($p = 600 \text{ Pa}, T = 300 \text{ K}, \rho = 1.05 \cdot 10^{-2} \text{ kg/m}^3, \dot{m} = 5.23 \cdot 10^{-8} \text{ kg/s}, \rho_p = 2.73 \cdot 10^3 \text{ kg/m}^3$, Configuration #3).

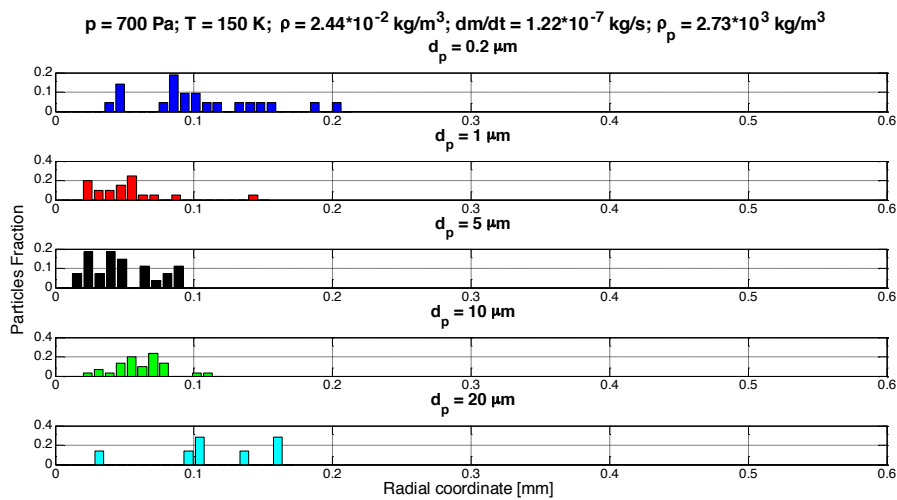


Fig. 5.37: Particle distributions in the middle plane of the Sampling Volume orthogonal to the mainstream ($p = 700 \text{ Pa}, T = 150 \text{ K}, \rho = 2.44 \cdot 10^{-2} \text{ kg/m}^3, \dot{m} = 1.22 \cdot 10^{-7} \text{ kg/s}, \rho_p = 2.73 \cdot 10^3 \text{ kg/m}^3$, Configuration #3).

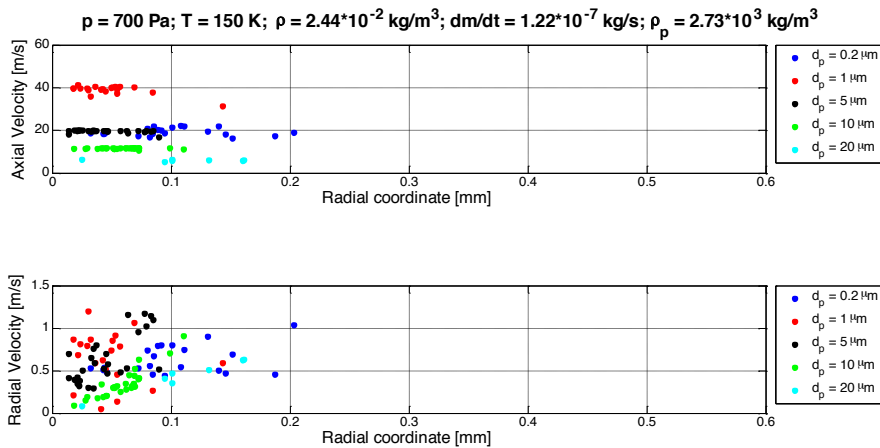


Fig. 5.38: Particle axial and radial velocity components in the middle plane of the Sampling Volume orthogonal to the mainstream ($p = 700 \text{ Pa}$, $T = 150 \text{ K}$, $\rho = 2.44 \cdot 10^{-2} \text{ kg/m}^3$, $\dot{m} = 1.22 \cdot 10^{-7} \text{ kg/s}$, $\rho_p = 2.73 \cdot 10^3 \text{ kg/m}^3$, Configuration #3).

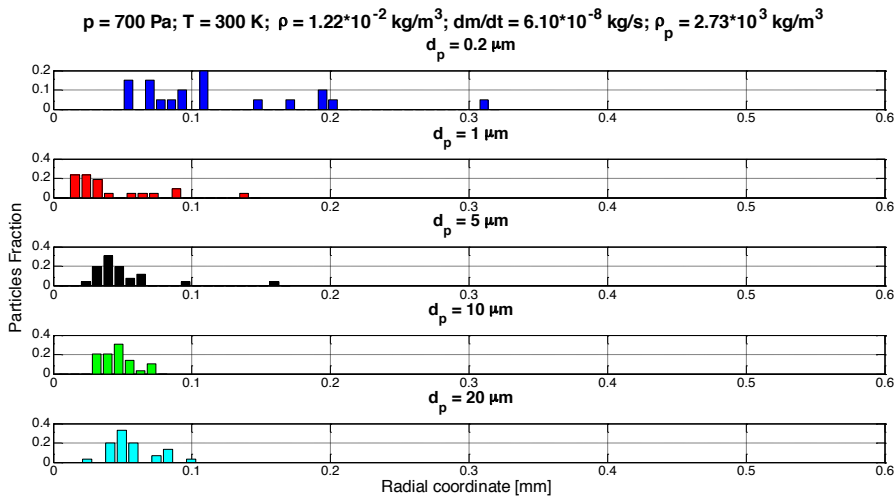


Fig. 5.39: Particle distributions in the middle plane of the Sampling Volume orthogonal to the mainstream ($p = 700 \text{ Pa}$, $T = 300 \text{ K}$, $\rho = 1.22 \cdot 10^{-2} \text{ kg/m}^3$, $\dot{m} = 6.10 \cdot 10^{-8} \text{ kg/s}$, $\rho_p = 2.73 \cdot 10^3 \text{ kg/m}^3$, Configuration #3).

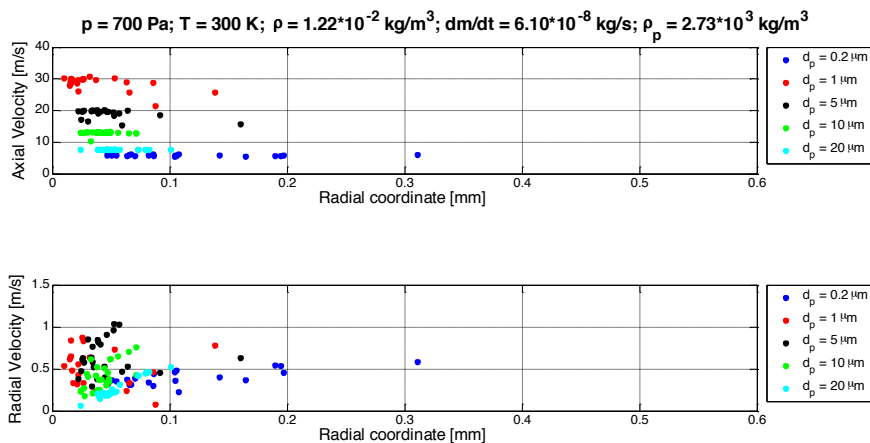


Fig. 5.40: Particle axial and radial velocity components in the middle plane of the Sampling Volume orthogonal to the mainstream ($p = 700 \text{ Pa}$, $T = 300 \text{ K}$, $\rho = 1.22 \cdot 10^{-2} \text{ kg/m}^3$, $\dot{m} = 6.10 \cdot 10^{-8} \text{ kg/s}$, $\rho_p = 2.73 \cdot 10^3 \text{ kg/m}^3$, Configuration #3).

d_p (μm)	p (Pa)	T (K)	ρ (kg/m^3)	\dot{m} (kg/s)	$V_{p,a,m}$ (m/s)	$\sigma_{V_{p,a}}$ (m/s)	$V_{p,r,m}$ (m/s)	$\sigma_{V_{p,r}}$ (m/s)
0.2	600	150	$2.09 \cdot 10^{-2}$	$1.05 \cdot 10^{-7}$	19.95	2.00	0.644	0.178
1					37.68	3.00	0.649	0.307
5					19.21	0.658	0.649	0.292
10					11.39	0.181	0.331	0.164
20					6.11	0.268	0.343	0.187
0.2	600	300	$1.05 \cdot 10^{-2}$	$5.23 \cdot 10^{-8}$	4.42	0.136	0.272	0.076
1					27.48	1.96	0.554	0.233
5					18.11	1.37	0.616	0.198
10					12.48	0.430	0.379	0.161
20					7.45	0.046	0.268	0.105
0.2	700	150	$2.44 \cdot 10^{-2}$	$1.22 \cdot 10^{-7}$	19.69	1.71	0.612	0.146
1					38.95	2.20	0.652	0.307
5					19.61	0.686	0.639	0.282
10					11.56	0.185	0.348	0.170
20					6.00	0.465	0.365	0.169
0.2	700	300	$1.22 \cdot 10^{-2}$	$6.10 \cdot 10^{-8}$	5.86	0.205	0.364	0.068
1					28.60	2.20	0.521	0.225
5					19.27	1.20	0.634	0.222
10					12.97	0.515	0.404	0.162
20					7.67	0.037	0.264	0.116

Tab. 5.13: Particle mean axial velocity ($V_{p,a,m}$) and standard deviation ($\sigma_{V_{p,a}}$) and particle mean radial velocity ($V_{p,r,m}$) and standard deviation ($\sigma_{V_{p,r}}$) in the middle plane of the Sampling Volume orthogonal to the mainstream within a radius of 0.15 mm from the Sampling Volume centroid (Configuration #3).

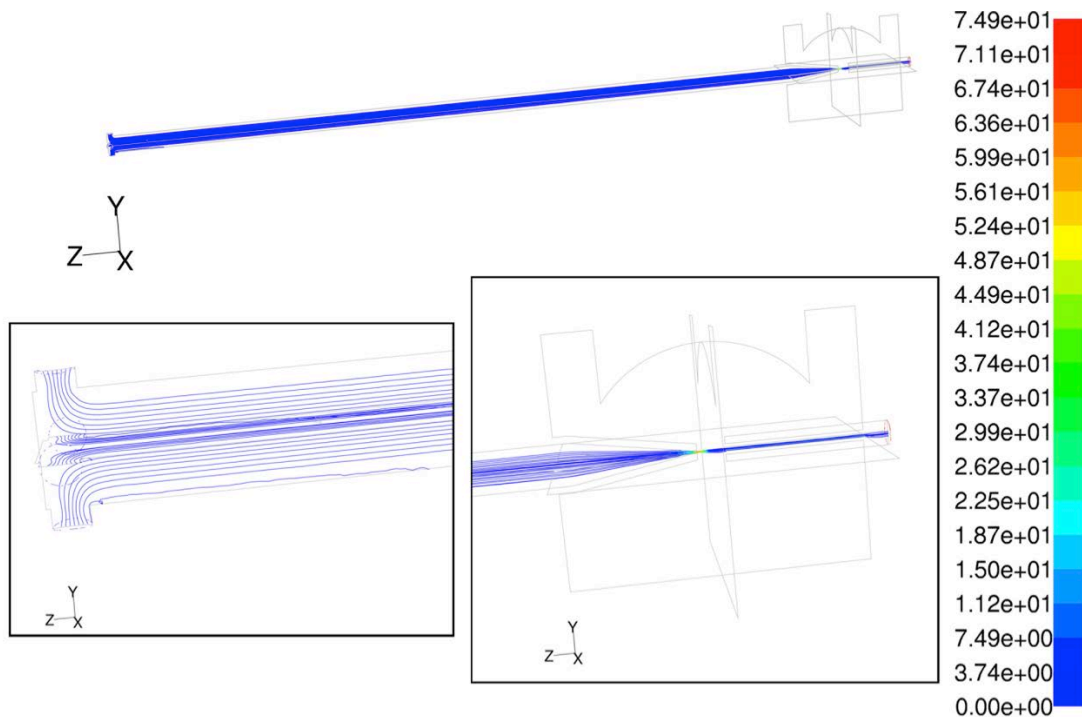


Fig. 5.41: Particle trajectories ($d_p = 0.2 \mu\text{m}$, $\rho_p = 2.73 \cdot 10^3 \text{ kg}/\text{m}^3$) coloured with velocity magnitude (m/s) for the Configuration #3 at $p = 600 \text{ Pa}$, $T = 300 \text{ K}$, $\rho = 1.05 \cdot 10^{-2} \text{ kg}/\text{m}^3$, $\dot{m} = 1.05 \cdot 10^{-7} \text{ kg}/\text{s}$. The figure represents the geometry projected on 3 main planes and the full 3D trajectories.

The sampling efficiency for all particle size improves in Configuration #3. The small particles can reach the Sampling Volume region as they come from a smaller section (Fig. 5.41), while a less amount of medium-sized particles impact on the Sampling Head walls due to the reduction of the volumetric flow rate from 3 l/min to 0.3 l/min.

Fig. 5.32 evidences the influence of the fluid density on the dynamics of the large particles, above all $d_p = 20 \mu\text{m}$, which impact less if the fluid density is lower. The Configuration #3 is better than #1 and #2 from a fluid dynamics point of view, but is considered risky for the higher probability of particle obstruction of the inlet duct. Moreover, the very small volumetric flow rate should not permit to sample a sufficient number of particles with runs of duration of 120-150 s (Sect. 5.4).

The sampling efficiency (Fig. 5.42), the particle distributions (Fig. 5.43, Fig. 5.45, Fig. 5.47, and Fig. 5.49) and the particle axial and radial velocity components (Fig. 5.44, Fig. 5.46, Fig. 5.48, and Fig. 5.50) across the radial coordinate of the Sampling Volume have been evaluated for the Configuration #4 at the boundary conditions discussed above. The mean value and standard deviation of the profiles of the particles axial and radial velocity in the Sampling Volume are reported in Tab. 5.14 for the Configuration #4 at the considered boundary conditions. This configuration has an inlet section of 1 mm, which should compensate the large particle dispersion due to large sections, found with configurations #1 and #2, and the critical aspect of a small section, which was found with configuration #3. In this case a volumetric flow rate of 1 l/min was taken into account.

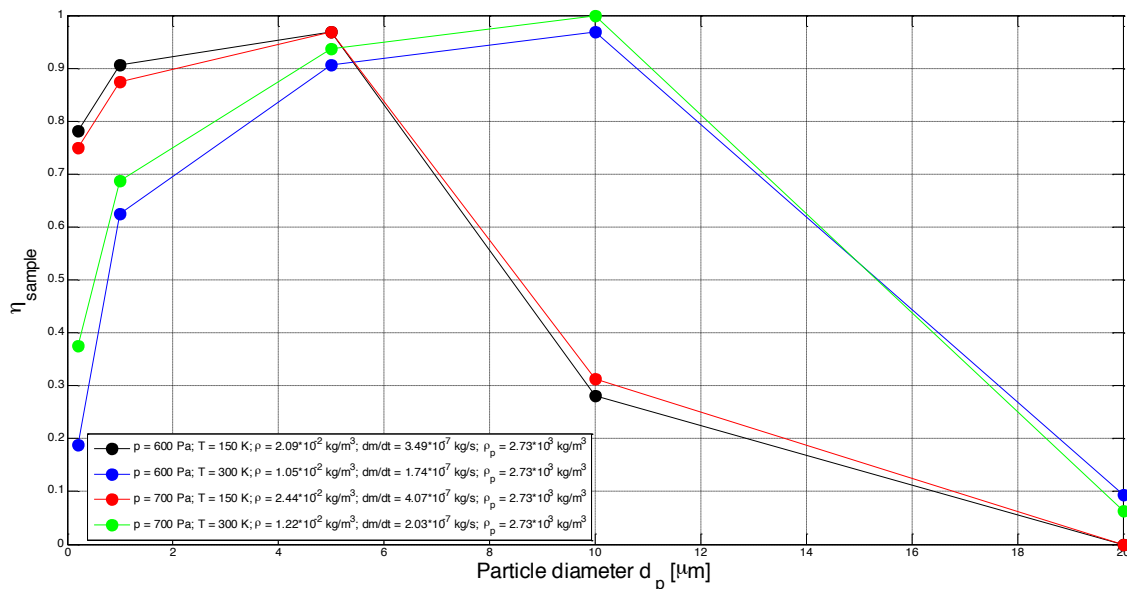


Fig. 5.42: Sampling efficiency (η_{sample}) with respect to particles diameter (d_p) at different boundary conditions for a Sampling Volume of radius 0.15 mm (Configuration #4).

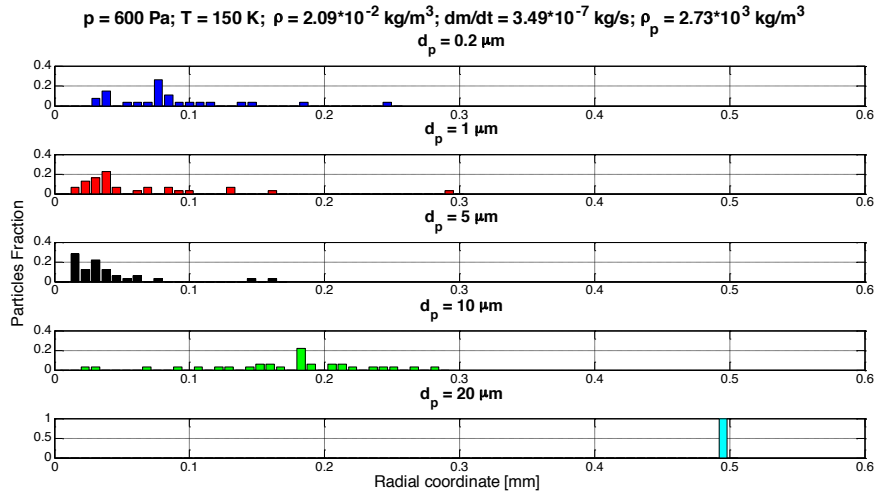


Fig. 5.43: Particle distributions in the middle plane of the Sampling Volume orthogonal to the mainstream ($p = 600 \text{ Pa}$, $T = 150 \text{ K}$, $\rho = 2.09 \cdot 10^{-2} \text{ kg/m}^3$, $\dot{m} = 3.49 \cdot 10^{-7} \text{ kg/s}$, $\rho_p = 2.73 \cdot 10^3 \text{ kg/m}^3$, Configuration #4).

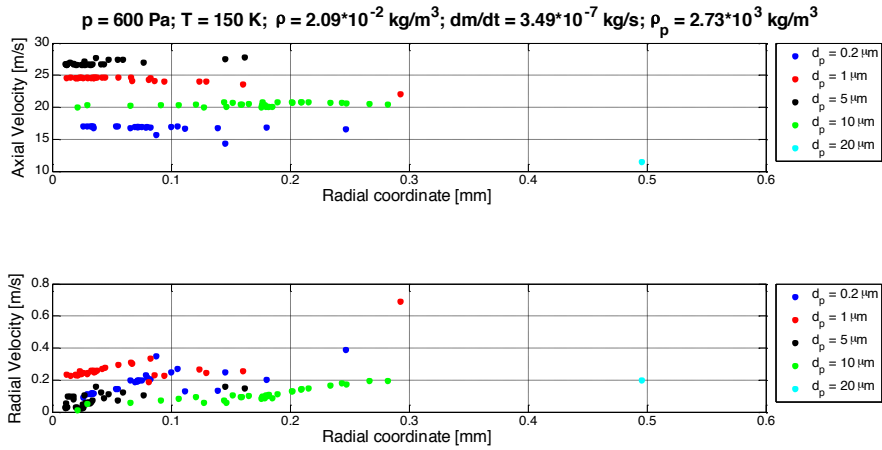


Fig. 5.44: Particle axial and radial velocity components in the middle plane of the Sampling Volume orthogonal to the mainstream ($p = 600 \text{ Pa}$, $T = 150 \text{ K}$, $\rho = 2.09 \cdot 10^{-2} \text{ kg/m}^3$, $\dot{m} = 3.49 \cdot 10^{-7} \text{ kg/s}$, $\rho_p = 2.73 \cdot 10^3 \text{ kg/m}^3$, Configuration #4).

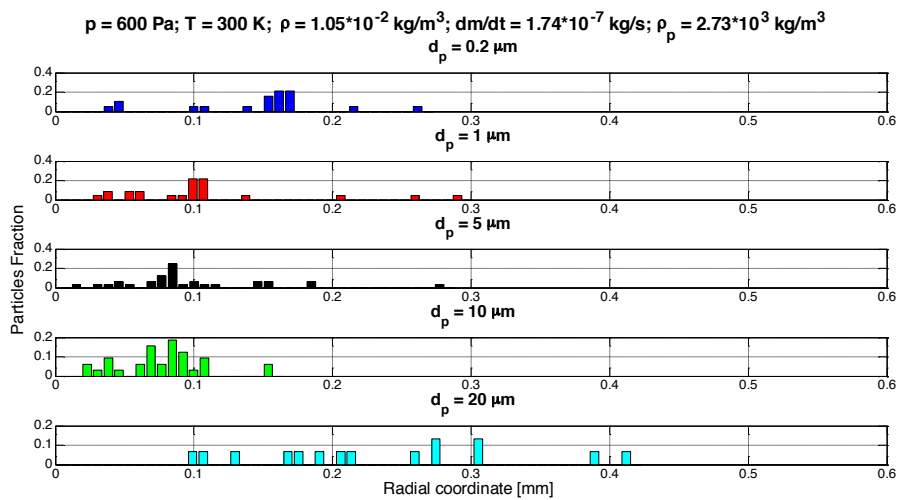


Fig. 5.45: Particle distributions in the middle plane of the Sampling Volume orthogonal to the mainstream ($p = 600 \text{ Pa}$, $T = 300 \text{ K}$, $\rho = 1.05 \cdot 10^{-2} \text{ kg/m}^3$, $\dot{m} = 1.74 \cdot 10^{-8} \text{ kg/s}$, $\rho_p = 2.73 \cdot 10^3 \text{ kg/m}^3$, Configuration #4).

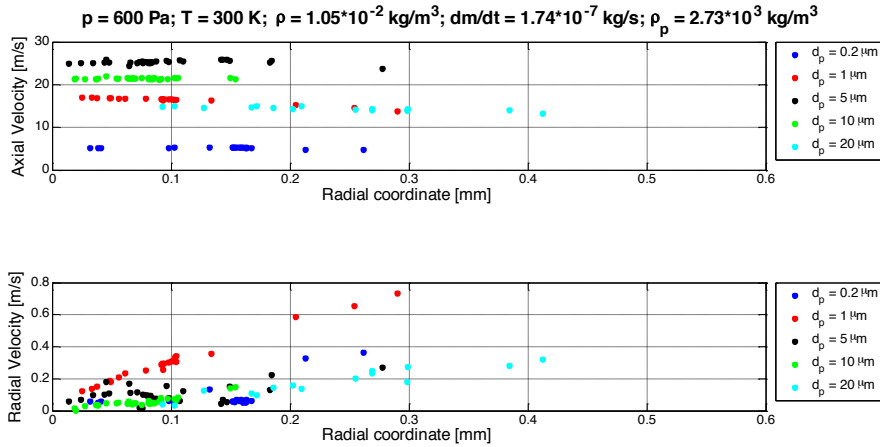


Fig. 5.46: Particle axial and radial velocity components in the middle plane of the Sampling Volume orthogonal to the mainstream ($p = 600$ Pa, $T = 300$ K, $\rho = 1.05 \cdot 10^{-2}$ kg/m³, $\dot{m} = 1.74 \cdot 10^{-7}$ kg/s, $\rho_p = 2.73 \cdot 10^3$ kg/m³, Configuration #4).

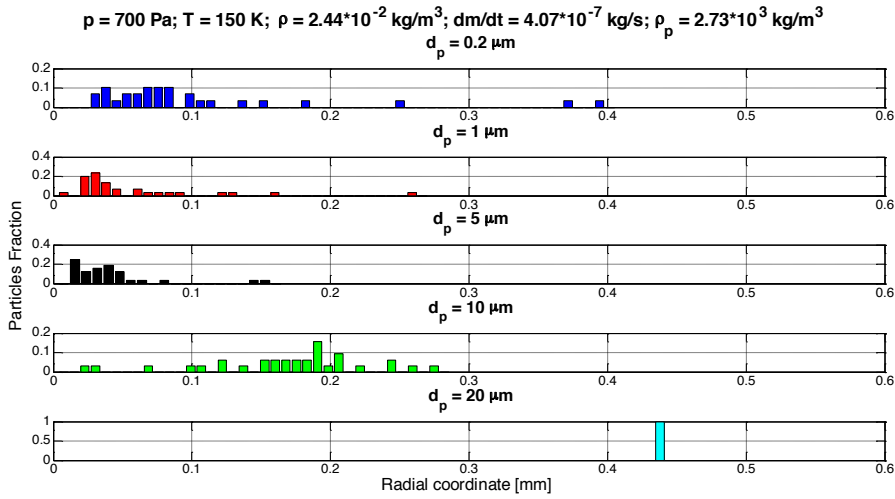


Fig. 5.47: Particle distributions in the middle plane of the Sampling Volume orthogonal to the mainstream ($p = 700$ Pa, $T = 150$ K, $\rho = 2.44 \cdot 10^{-2}$ kg/m³, $\dot{m} = 4.07 \cdot 10^{-7}$ kg/s, $\rho_p = 2.73 \cdot 10^3$ kg/m³, Configuration #4).

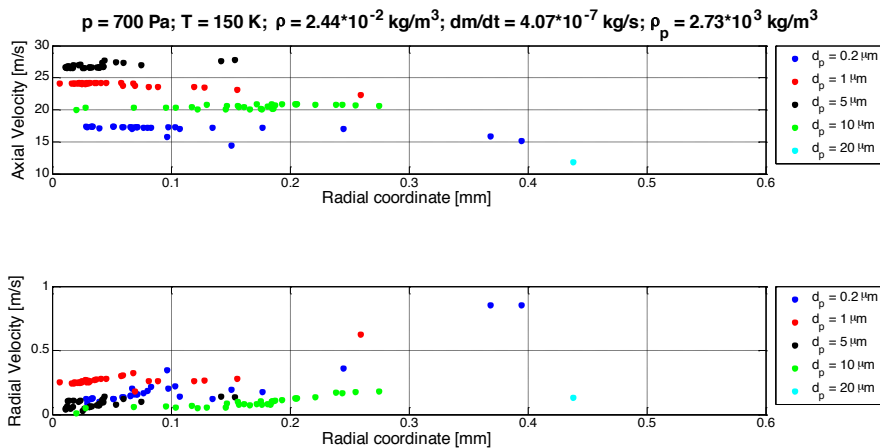


Fig. 5.48: Particle axial and radial velocity components in the middle plane of the Sampling Volume orthogonal to the mainstream ($p = 700$ Pa, $T = 150$ K, $\rho = 2.44 \cdot 10^{-2}$ kg/m³, $\dot{m} = 4.07 \cdot 10^{-7}$ kg/s, $\rho_p = 2.73 \cdot 10^3$ kg/m³, Configuration #4).

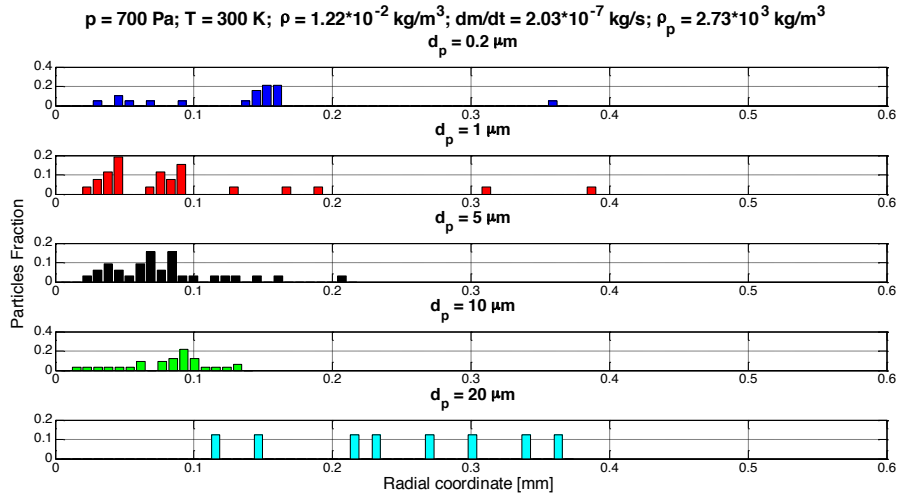


Fig. 5.49: Particle distributions in the middle plane of the Sampling Volume orthogonal to the mainstream ($p = 700 \text{ Pa}$, $T = 300 \text{ K}$, $\rho = 1.22 \cdot 10^{-2} \text{ kg/m}^3$, $\dot{m} = 2.03 \cdot 10^{-7} \text{ kg/s}$, $\rho_p = 2.73 \cdot 10^3 \text{ kg/m}^3$, Configuration #4).

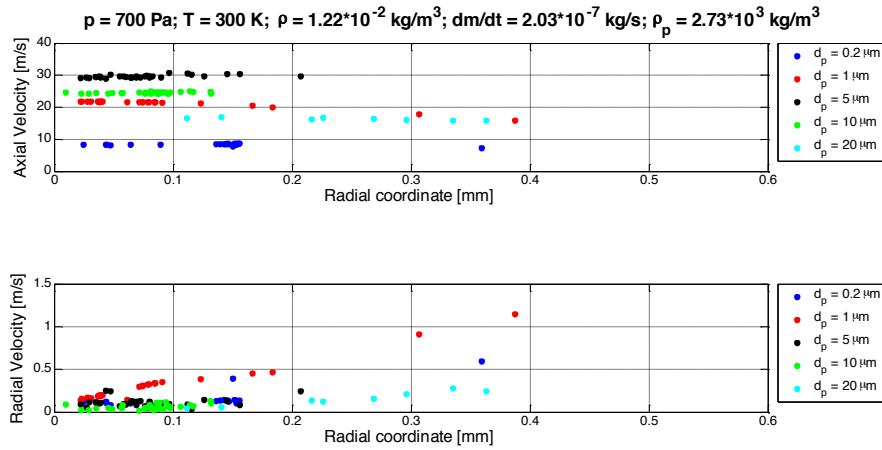


Fig. 5.50: Particle axial and radial velocity components in the middle plane of the Sampling Volume orthogonal to the mainstream ($p = 700 \text{ Pa}$, $T = 300 \text{ K}$, $\rho = 1.22 \cdot 10^{-2} \text{ kg/m}^3$, $\dot{m} = 2.03 \cdot 10^{-7} \text{ kg/s}$, $\rho_p = 2.73 \cdot 10^3 \text{ kg/m}^3$, Configuration #4).

The reduction of the section of the inlet duct from 1.5-2 mm to 1 mm significantly increases the sampling efficiency of the smallest particles. Particles with $d_p = 1 \mu\text{m}$ can reach also $\eta_{sample} \sim 0.8$, while particles with $d_p = 0.2 \mu\text{m}$ show $\eta_{sample} \sim 0.2$ in the worst environmental case. A smaller loss of the large particles ($d_p > 10 \mu\text{m}$) for impacts on the walls is observed with a volumetric flow rate of 1 l/min than with 3 l/min (Configurations #1 and #2). The internal convergent profile of the Sampling Head tube, which starts approximately at middle length, is considered suitable for the application as it does not introduce too much loss due to impacts in the constriction, but many particles with $d_p = 20 \mu\text{m}$ again impact on the walls of the Sampling Volume at the entrance of the Sampling Head.

d_p (μm)	p (Pa)	T (K)	ρ (kg/m^3)	\dot{m} (kg/s)	$V_{p,a,m}$ (m/s)	$\sigma_{V_{p,a}}$ (m/s)	$V_{p,r,m}$ (m/s)	$\sigma_{V_{p,r}}$ (m/s)
0.2	600	150	$2.09 \cdot 10^{-2}$	$3.49 \cdot 10^{-7}$	16.78	0.572	0.183	0.061
1					24.52	0.220	0.254	0.029
5					26.87	0.320	0.070	0.040
10					20.30	0.250	0.063	0.023
20					-	-	-	-
0.2	600	300	$1.05 \cdot 10^{-2}$	$1.74 \cdot 10^{-7}$	5.26	0.064	0.071	0.031
1					16.67	0.189	0.259	0.071
5					25.35	0.332	0.090	0.040
10					21.45	0.156	0.053	0.024
20					14.83	0.272	0.067	0.052
0.2	700	150	$2.44 \cdot 10^{-2}$	$4.07 \cdot 10^{-7}$	17.21	0.315	0.158	0.054
1					24.04	0.227	0.263	0.025
5					26.82	0.333	0.082	0.030
10					20.35	0.260	0.057	0.019
20					-	-	-	-
0.2	700	300	$1.22 \cdot 10^{-2}$	$2.03 \cdot 10^{-7}$	8.41	0.151	0.189	0.024
1					21.67	0.135	0.248	0.082
5					29.65	0.427	0.108	0.047
10					24.55	0.210	0.062	0.030
20					16.76	0.211	0.050	0.006

Tab. 5.14: Particle mean axial velocity ($V_{p,a,m}$) and standard deviation ($\sigma_{V_{p,a}}$) and particle mean radial velocity ($V_{p,r,m}$) and standard deviation ($\sigma_{V_{p,r}}$) in the middle plane of the Sampling Volume orthogonal to the mainstream within a radius of 0.15 mm from the Sampling Volume centroid (Configuration #4).

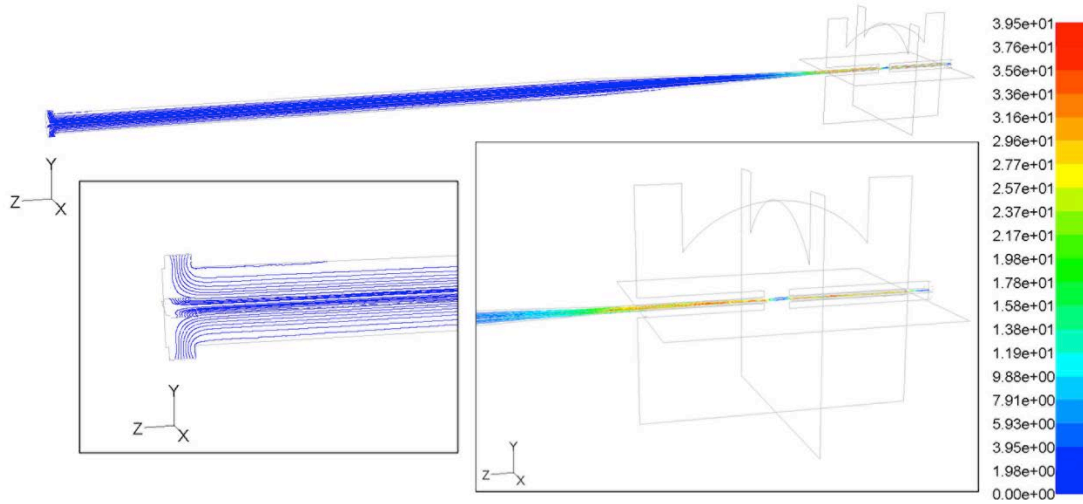


Fig. 5.51: Particle trajectories ($d_p = 0.2 \mu\text{m}$, $\rho_p = 2.73 \cdot 10^3 \text{ kg}/\text{m}^3$) coloured with velocity magnitude (m/s) for the Configuration #4 at $p = 600 \text{ Pa}$, $T = 300 \text{ K}$, $\rho = 1.05 \cdot 10^{-2} \text{ kg}/\text{m}^3$, $\dot{m} = 1.74 \cdot 10^{-7} \text{ kg}/\text{s}$. The figure represents the geometry projected on 3 main planes and the full 3D trajectories.

From the analysis of the four configurations it is clear that the sampling efficiency is best for the medium sized particles ($d_p = 1\text{-}5 \mu\text{m}$).

In order to improve the sampling efficiency of the smallest particles ($d_p < 1 \mu\text{m}$), the Sampling Volume, defined by the optical design, could be slightly enlarged. For instance, by doubling the cross section radius of the Sampling Volume, so that particles are detected if they cross the Sampling Volume within a radius of 0.3 mm from the centroid; in this case the sampling efficiency increases as seen in Fig. 5.42 and Fig. 5.53, while the velocity profiles of the particles preserve an acceptable uniformity since

the mean values decrease by about 2%, even if the standard deviations increase by about 30%.

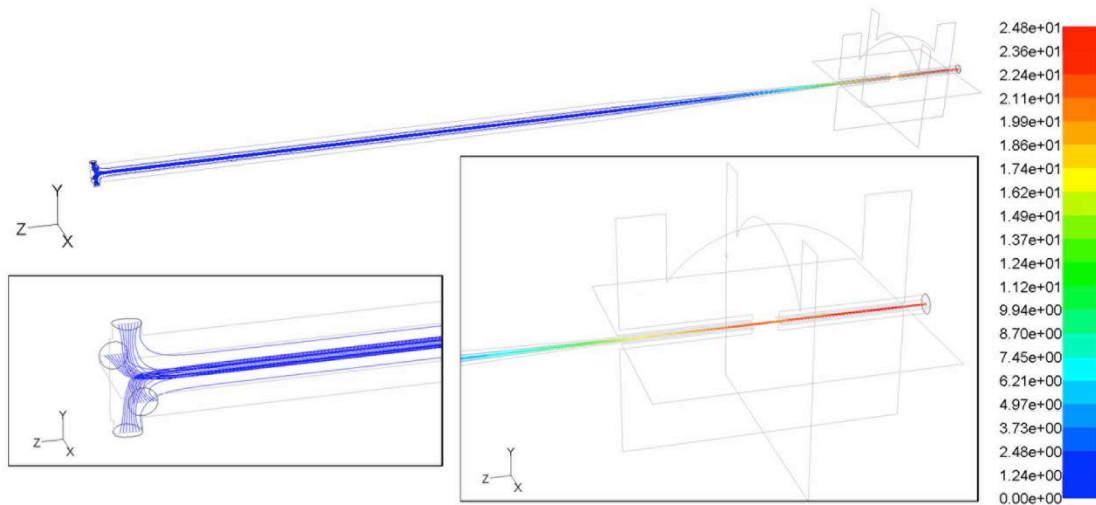


Fig. 5.52: Particle trajectories ($d_p = 10 \mu\text{m}$, $\rho_p = 2.73 \cdot 10^3 \text{ kg/m}^3$) coloured with velocity magnitude (m/s) for the Configuration #4 at $p = 600 \text{ Pa}$, $T = 300 \text{ K}$, $\rho = 1.05 \cdot 10^{-2} \text{ kg/m}^3$, $\dot{m} = 1.74 \cdot 10^{-7} \text{ kg/s}$. The figure represents the geometry projected on 3 main planes and the full 3D trajectories.

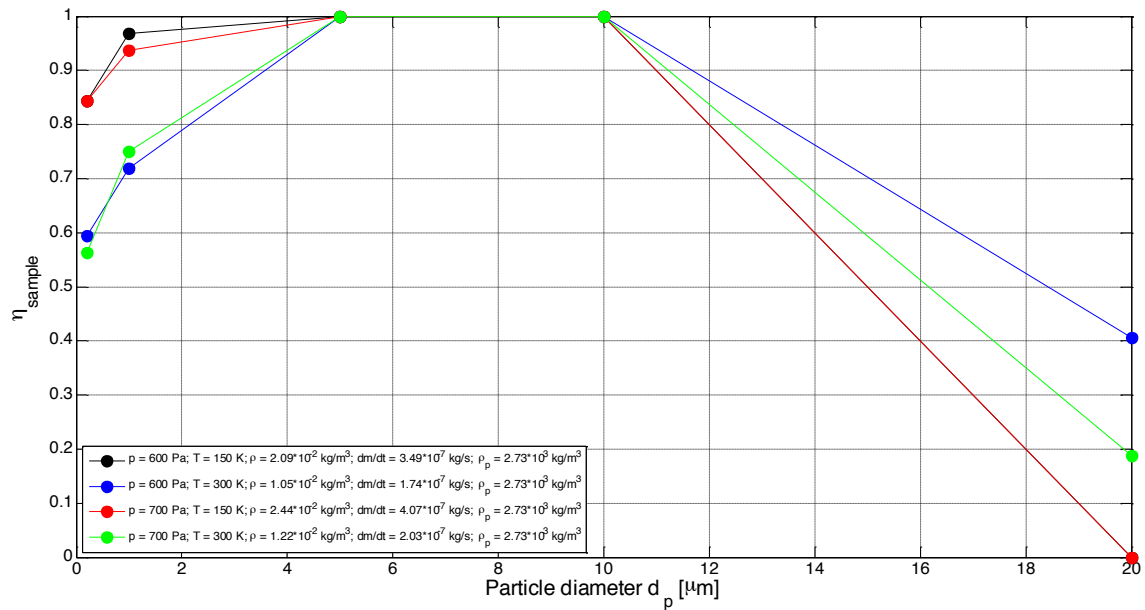


Fig. 5.53: Sampling efficiency (η_{sample}) with respect to particle diameter (d_p) at different boundary conditions for a Sampling Volume of radius 0.30 mm (Configuration #4).

However, an increase in the size of the Sampling Volume should be analysed from an optical point of view. In fact, enlarging the size of the Sampling Volume, the optical density decreases implying a lower sensitivity of the instrument. Moreover, the laser dispersion and stray light increase by defocusing the spot, and, above all, to have a wider spot with uniform light intensity for a source of 100 mW is not simple (a larger Sampling Volume was obtained for MEDUSA with a light source of 1,000 mW and a

large objective system). The choice to consider a larger Sampling Volume in the orthogonal direction to the aerosol mainstream goes beyond the tasks of this fluid dynamics analysis as it depends on the design of the optical components. Anyway, the design guidelines here obtained from the fluid dynamics analysis are still valid also in this case.

All the configurations show low sampling efficiency with particles of $d_p = 20 \mu\text{m}$, which are on the edge of the required measurement range. It is interesting to study deeper the behaviour of these large particles at the entrance of the Sampling Head, where many of them impact on the walls of the tube. The most relevant parameters that determine such behaviour are the fluid density and the fluid mass flow rate, assuming fixed the internal diameter of the Sampling Head duct (6 mm) and the diameter of the entrance holes (2 mm). The large particles have very small settling velocity ($\sim 10^{-5}$ m/s, Tab. 4.17) compared to the local fluid velocity, which implies that their motion in the fluid is quickly balanced, and, hence, an abrupt deviation of the fluid streamlines, which happens at the inlet, is insufficient to overcome the inertial motion of these particles. Moreover, if the fluid density is higher, the aerodynamic drag is higher, and the particles at the Sampling Head inlet are more quickly accelerated, and they are favoured to hit the opposite walls. Moreover, the particles that enter the Sampling Head and then cross transversally the central axis of the tube, due to their inertia, go through a region of the boundary layer, where the fluid velocity decreases approaching the wall down to zero. These particles have, instead, an axial velocity component higher than the local velocity of the fluid, so that they slow down favouring the impact on the walls. These particles can be pushed to follow the mainstream only if their velocity relative to the fluid is sufficiently low, i.e., the fluid locally accelerates or slows a particle depending on its mass.

When a particle is on the wall or quite nearby to the wall, it is in a region of the boundary layer, where fluid velocity is very low, even in rarefied regime. The drag is very small with respect to electrostatic and adhesion forces with the wall surface. Anyway, the particle-wall interaction and related forces should be studied more in depth in order to make more accurate estimation of the effective particles losses on the walls. We recall that in these simulations, walls are considered traps for the impact and an impact means conservatively a loss.

ρ (kg/m ³) \ Q (l/min)	0.3	1.0	3.0
$1.05 \cdot 10^{-2}$	$d_p = 21 \mu\text{m}$	$d_p = 20 \mu\text{m}$	$d_p = 10 \mu\text{m}$
$2.44 \cdot 10^{-2}$	$d_p = 15 \mu\text{m}$	$d_p = 13 \mu\text{m}$	$d_p = 9 \mu\text{m}$

Tab. 5.15: Cut-off diameter for impact on the wall of the Sampling Head tube with respect to volumetric flow rate Q and fluid density ρ .

The impact of the large particles on the wall depends also on the pump volumetric flow rate. The higher the pump volumetric flow rate, the higher the kinetic energy the particles receive at the inlet and the higher the chances to impact on the walls. For instance, at a volumetric flow rate of 0.3 l/min, the percentage of the particles with $d_p = 20 \mu\text{m}$ that do not impact on the wall is about 22% in denser atmosphere ($\dot{m} = 1.22 \cdot 10^{-7} \text{ kg/s}$) and 94% in more rarefied atmosphere ($\dot{m} = 5.23 \cdot 10^{-8} \text{ kg/s}$); at a volumetric flow rate of 1 l/min the non-impacting particles ($d_p = 20 \mu\text{m}$) are 3% in denser atmosphere ($\dot{m} = 4.07 \cdot 10^{-7} \text{ kg/s}$) and 47% in more rarefied atmosphere ($\dot{m} = 1.74 \cdot 10^{-7} \text{ kg/s}$); at a volumetric flow rate of 3 l/min, the non-impacting particles ($d_p = 20 \mu\text{m}$) are less than 3%. In particular, for the Configuration #4, the cut-off diameter, i.e., the diameter at which the transport efficiency is more than 50%, is at $d_p = 13 \mu\text{m}$ in the denser case and at $d_p = 20 \mu\text{m}$ in the more rarefied case (Tab. 5.15). Therefore, the volumetric flow rate can be a parameter to rule the quantity of particles lost for impact on the walls of the Sampling Head tube. At low volumetric flow rate, even if the total number of particles aspirated is lower, the fraction of particles that do not impact on the walls increases. The impact on the wall of the large particles can be reduced with some methods:

- To enlarge the diameter of the Sampling Head tube;
- To make small holes on the upper cover of the Sampling Head;
- To enlarge the entrance holes on the Sampling Head tube.

The enlargement of the Sampling Head tube clearly increases the mass. The internal diameter should be approximately enlarged from 6 mm to 10-12 mm to have a sampling efficiency $\eta_{\text{sample}} > 0.5$ also with particles of $d_p = 20 \mu\text{m}$ in the worst case; this will cause a mass increase of the Sampling Head duct of approximately 67-133%. An alternative solution could be to make some holes on the cover of the Sampling Head with diameter of 0.3-0.5 mm, which can energize the particles giving them additional momentum in the axial direction. Enlarging the size of the current entrance holes on the Sampling

Head tube, at the same flow rate, will reduce locally the particles velocity component orthogonal to the main axis, but also will imply that the number of particles aspirated contemporaneously could become too high. Anyway, to have the sampling efficiency higher than 50%, the diameter of these holes should enlarge from 2 mm to 4 mm ($\eta_{sample} = 0.68, 0.88, 0.51, \text{ and } 0.74$ with $d_p = 20 \mu\text{m}$ at a volumetric flow rate of 1 l/min for the four environmental conditions in Tab. 4.16, respectively).

Anyway, the numerical results should be compared with experimental data to verify quantitatively how many particles could impact on the walls and, then, aspirated and being recirculated under the action of the pump. It is reasonable that a fraction of these particles could be dragged, so slightly increasing the sampling efficiency.

From this theoretical analysis and as also experimentally confirmed (Baron, A., Willeke, K., 2001) it is not trivial to have for an instrument a constant sampling efficiency with respect to the particles size and mass and fluid dynamics variables. Therefore, the adopted design is based on a solution that can minimize the particle losses, and we remark that the CFD analysis here performed is quite conservative for the boundary conditions and hypotheses applied. MicroMED breadboard shall follow the design guidelines of Configuration #4, eventually setting different values for the pump volumetric flow rate. Sampling efficiency should be measured in order to determine more accurately the relationship $\eta_{sample}(d_p, \rho_p, p, T, \dot{m})$. If the environmental conditions are known by other sensors and supposing to have sufficient information about the particles density ρ_p , the sampling efficiency for each particle size can be determined. In this way, the curve $\eta_{sample}(d_p, \rho_p, p, T, \dot{m})$ should be used to correct the count of the particles to have an accurate calculation of the size distribution without errors introduced inevitably by the instrument design.

5.4 Optical Design

5.4.1 Basic Guidelines

In this section the design concept and the steps accomplished for the optical design are described and discussed.

The working principle of the MicroMED *Optical Stage (OS)* is schematized in Fig. 5.54. The scattering angle captured by the detector is wider with respect to the MEDUSA design and centred at 90° from the optical axis. Therefore, MicroMED needs

one collecting mirror and one detector. The laser beam direction is orthogonal to both the aerosol mainstream and mirror-detector direction. The detector and mirror are, therefore, orthogonal both to the laser beam direction and to the mainstream directions.

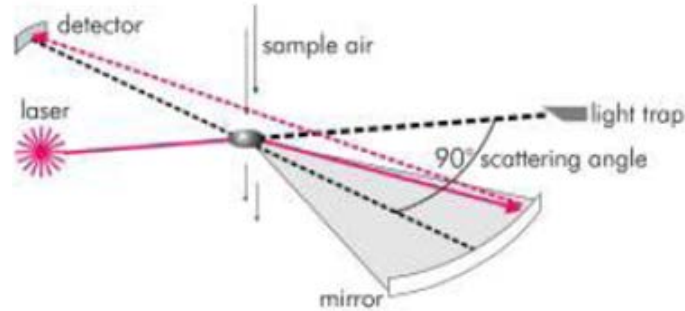


Fig. 5.54: The optical measurement principle implemented in the MicroMED OS (GRIMM Aerosol Technik GmbH & Co. KG).

The *laser diode* selected for MicroMED has a lower optical power (100 mW) than that used for the MEDUSA breadboard (1,000 mW) in order to reduce the power consumption (from to 3.850 W to 0.5 W). The FIDL-100S-850D-60 laser diode by Frankfurt Laser Company was chosen (Tab. 5.16), which is a 850 nm wavelength AlGaAs/GaAs single mode injection laser diode with a built-in monitor photodiode to stabilize the output power. As the laser beam is affected by divergence in the cross-section along two directions (6° and 35°, respectively, from datasheet), a proper objective system is necessary to collimate and focus the beam into a spot in the Sampling Volume region.

Laser Diode	
Supplier	FLC - Frankfurt Laser Company
Model	FIDL-100S-850D-60
Optical Output Power	100 mW (100-110 mW)
Wavelength	850 nm (830-860 nm)
Emitting area	3 μm x 1.5 μm
Threshold Current	30 mA (30-40 mA)
Forward Current	170 mA (170-190 mA)
Forward Voltage	1.9 V (1.9-2.45 V)
Beam Divergence Parallel	6° (4°-8°) FWHM
Beam Divergence Perpendicular	35° (30°-40°) FWHM
Spectral Width (FWHM)	0.5 nm (0.1-1 nm)
Static Alignment	< $\pm 3^\circ$
Positional Accuracy	< $\pm 100 \mu\text{m}$
Mode Structure	SM
Differential Efficiency	0.7 mW/mA (0.5-0.8 mW/mA)
Monitor Photocurrent	0.4 mA (0.2-1.3 mA)
Monitor Diode Voltage	5 V +/- 0.5 V
Wavelength Temperature Drift	< 0.3 nm/°C
Operating Temperature	-60°C \div +60°C

Tab. 5.16: Laser diode FLC FIDL-100S-850D-60 datasheet.

Theoretical predictions based on the Mie theory (see also Sect. 4.5.4 to compare with MEDUSA simulations) show that optical power of 50-100 mW at 850 nm wavelength, focused into a spot of 0.3 mm x 0.3 mm x 0.3 mm (MicroMED Sampling Volume reference size), used for measuring light scattering of particles with refractive index equal to 1.5 collected in an angle of $90^\circ \pm 65^\circ$ with a detector of sensitivity 0.6 A/W and noise level of 10 nA (dark current), should allow detection down to a minimum particle diameter of $\sim 0.4 \mu\text{m}$ (Fig. 5.55 and Fig. 5.56).

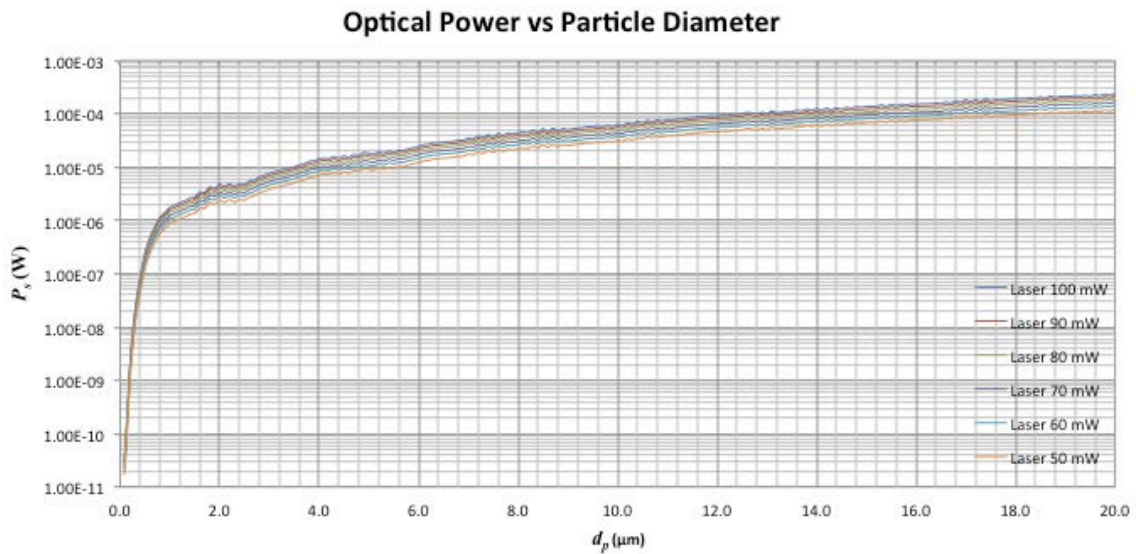


Fig. 5.55: Optical power (P_s) vs. particle diameter detectable by the MicroMED detector as foreseen by the Mie theory.

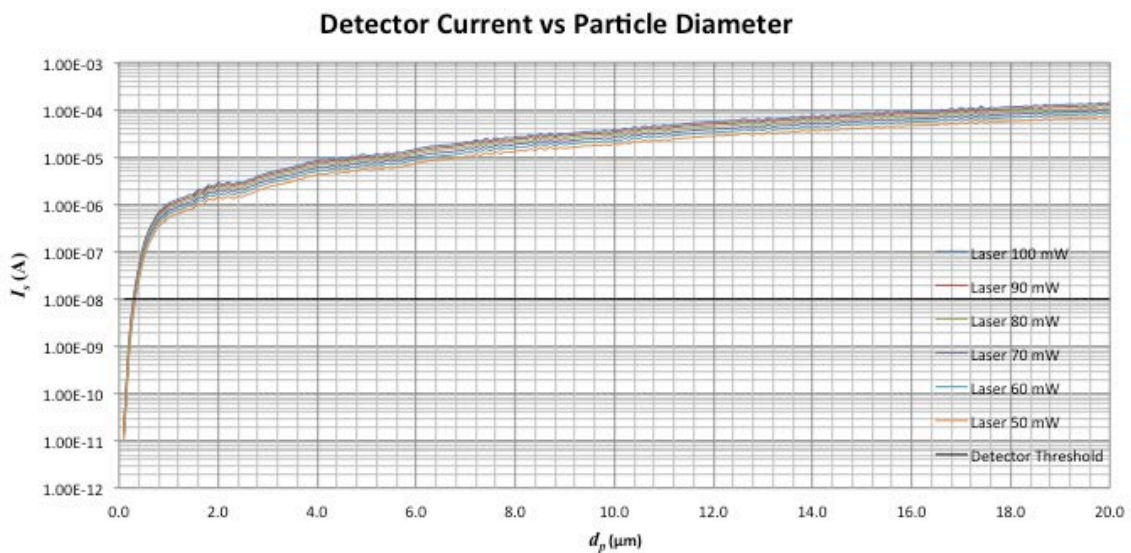


Fig. 5.56: Current intensity (I_s) vs. particle diameter by the MicroMED detector as foreseen by the Mie theory.

The thermal requirements are the most critical issues for the laser diode selection and qualification. The elements on board the EDM Surface Platform Structure (SPS) and EDM Surface Payload (ESP) are required to be able to be compatible with operative temperature range of $-55^{\circ}\text{C} \div +65^{\circ}\text{C}$ and not operative temperature of $-80^{\circ}\text{C} \div +75^{\circ}\text{C}$, with qualification margin of $\pm 10^{\circ}\text{C}$. Specific attention must be taken to decide the accommodation of MicroMED in the platform in order to guarantee that the laser diode works within its tolerable temperature range ($-60^{\circ}\text{C} \div +60^{\circ}\text{C}$).

The MicroMED *Sampling Volume* will be smaller than for MEDUSA in order to optimize particle kinematic uniformity with a stricter cut-off on ambiguous detections and edge effects related to the transit of the particles across the laser spot and to minimize the laser beam non-uniformity. The laser diode will have reduced optical power, and, consequently, reduced power consumption with respect to MEDUSA. The laser beam will be focused into a smaller spot in order to concentrate its optical power and have a power density ($\sim 10^3 \text{ W/cm}^2$), which is sufficient to be used for the scattering analysis. Moreover, as the volumetric flow rate of the MicroMED pump system is lower than for MEDUSA, in order to sample a sufficient number of particles it is also necessary to increase the sampling time. In Tab. 5.17 an approximated estimation of a reference operation is reported, where the data were calculated similarly as done in Sect. 4.3.2.4 for MEDUSA.

Sampling Volume	
Sampling Volume (SV) length in the mainstream direction (X-direction)	$3.00 \cdot 10^{-4} \text{ m}$
Sampling Volume (SV) length in the Y-direction	$3.00 \cdot 10^{-4} \text{ m}$
Sampling Volume (SV) length in the laser beam direction (Z-direction)	$3.00 \cdot 10^{-4} \text{ m}$
Sampling Volume (SV) size (V_s)	$3.44 \cdot 10^{-9} \text{ m}^3$
Inlet duct diameter (D_d)	$1.00 \cdot 10^{-3} \text{ m}$
Inlet duct section (S_d)	$7.85 \cdot 10^{-7} \text{ m}^2$
Pump Volumetric Flow Rate (Q)	$1.67 \cdot 10^{-5} \text{ m}^3/\text{s} = 1 \text{ l/min}$
Sampling time (T_s)	120 s
Dust particles number density (N_p)	$3 \cdot 10^6 \text{ m}^{-3}$ (constant haze)
Dust particles velocity (V_p)	5.31 m/s
Particles residence time in the Sampling Volume (t_s)	$5.65 \cdot 10^{-5} \text{ s}$
Number of particles crossing the SV in T_s (n_c)	$6 \cdot 10^3$
Fraction of coincidence events (F)	$4.05 \cdot 10^{-5}$

Tab. 5.17: Sampling Volume (SV) properties and approximated performance estimations.

The basic elements for the optical design of MicroMED are the working principle (Fig. 5.54), the envelope of the MicroMED Sampling Head and Optical Stage box (Fig. 5.5 and Fig. 5.6), the compatibility with the internal configurations studied for the fluid dynamics design (Fig. 5.7, Fig. 5.8, Fig. 5.9 and Fig. 5.10) of the Optical Stage, and the

laser diode properties (Tab. 5.16). As said in Sect. 5.3, the optical design and the fluid dynamics design work in a combined trade-off in order to find convergence to find the best design solution.

The MicroMED *objective system* should include one or two lenses, placed in front of the laser diode in a protected duct (Fig. 5.4) at sufficient distance from the Sampling Volume centroid in order to focus the light beam into the Sampling Volume providing a suitable correction of the laser beam divergence. The lenses should be less than 6 mm in diameter and the distance between the further lens and the Sampling Volume centroid should be less than 60 mm as a compromise to have small-sized lenses with long focal length. This approach shall guarantee focusing the laser beam into the fixed Sampling Volume sizes, while not exceeding the fixed envelope and keeping the structure compact with a tolerable vibrational behaviour. Since the laser beam has a non-uniform divergence, two kinds of solutions could be considered to correct the astigmatism of the laser beam: an aspherical or toric astigmatic lens with double curvature or two cylindrical lenses with different curvatures.

The MicroMED *collecting mirror* is placed on a lateral OS box wall with its axis normally both to the aerosol mainstream and the laser beam direction, in front of the detector, but on the opposite side with respect to the Sampling Volume centroid (Fig. 5.54). The purpose of the collecting mirror is to collect the light scattered by particles within a wide angle ($90^\circ \pm 65^\circ$). According to the Mie theory and as shown in Fig. 5.55, this angular range centred in a normal scattering direction provides an acceptable solution for the polytonic response, which, as mentioned in Sect. 4.5.4, can be smoothed with wide collection angles (e.g., 130°) and large scattering angle (e.g., 90°). The mirror should have a diameter of 25-34 mm and a FOV of 100° - 130° .

The MicroMED *detector* is a photodiode of the same series of those used for MEDUSA (Sect. 4.3.2.6). The PerkinElmer C30822EH has been preferred for MicroMED as it has a wide field of view (104°), a small diameter of the sensing area (5 mm) and a good responsivity (0.6 A/W). The detector has a length of 5 mm and a diameter of 16 mm. The detector will be placed in front of the mirror on the opposite side with respect to the Sampling Volume centroid (Fig. 5.54). The distance from the wall will depend on the size of the mirror.

Finally, a *light trap* will be placed in front of the laser diode on the opposite side with respect the Sampling Volume, to collect the direct light beam in order to reduce stray light.

5.4.2 Test and Verification of the Laser Diode

The optical power of the laser diode FIDL-100S-850D-60 was tested experimentally in laboratory to verify correspondence with the datasheet specifications. The laser diode performances, i.e., optical power, wavelength and beam divergence angles, are input parameters for the design of the optical system to collimate the light beam into the Sampling Volume. Hence, these physical quantities have been measured and verified in laboratory.



Fig. 5.57: The laser diode in front of the power meter on the optical bench.

The laser diode FIDL-100S-850D-60 was accommodated in a metal support made of Aluminium alloy, which works both as thermal sink and mechanical interface with the optical bench. The laser diode was ruled with the Newport Model 6000 laser controller (Fig. 4.37). A power meter was placed in front of the laser diode and was axially aligned with the laser diode (Fig. 5.57). The distance between the laser diode and the sensing area of the power meter was ruled in order to evaluate the collected optical power vs. distance. This is a basic procedure to evaluate the divergence of the laser beam. The output of the power meter was an analog voltage signal linearly dependent on the optical power after a proper calibration conversion.

The relative position of the laser diode with respect to the sensor was set to several values starting from a minimum obtainable distance ($x_0 = 4.3$ mm) due to the edges of

the mechanical supports. The angular range δ within which the detector can collect the light emitted by the laser diode with respect to their distance is evaluated with:

$$\delta = 2 \tan^{-1} \left(\frac{D_s / 2}{x + x_0} \right) \quad (5.6)$$

where D_s is the diameter of the sensing area, and x is the distance between the laser diode and the sensing area starting from the minimum effective distance x_0 . As the distance between the laser diode and the detector increases, the power collected by the detector decreases as it is collected within a smaller angle.

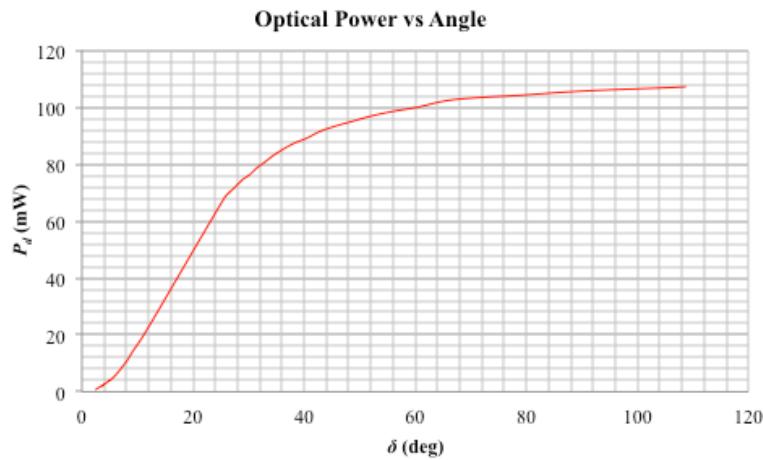


Fig. 5.58: Optical power detected with respect to the angular distance from the laser beam axis ($I_d = 170$ mA).

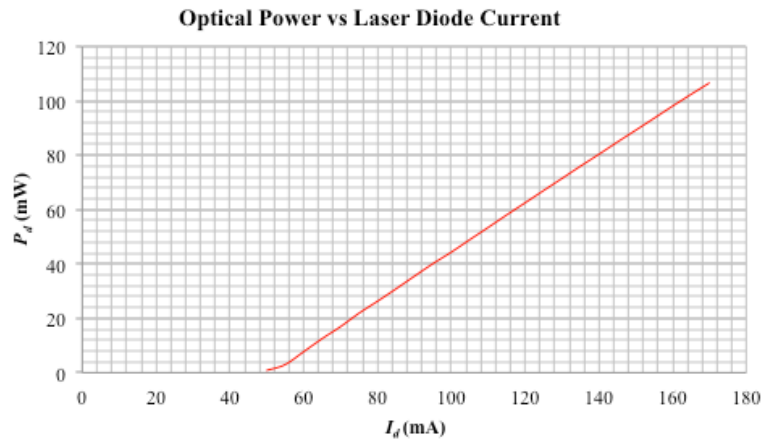


Fig. 5.59: Optical power detected at the minimum distance between the detector and the laser diode with respect to the electrical current supplying the laser diode.

Experimental results show that an optical power of 100 mW, i.e., the nominal optical power from datasheet, is collected within an angle of about 60° (Fig. 5.58). The maximum measured optical power (P_0) is equal to 106.96 mW at a supply current of 170 mA. Nevertheless, this kind of test does not allow us to understand exactly the

divergence of the laser beam along the parallel and perpendicular direction as it gives only the total power collected within a cone with an angle of aperture of about 60° .

The laser diode was also supplied with different current levels to verify the laser response with respect to this parameter. An optical power of 100 mW is obtained for a current (I_d) of at least 165 mA (Fig. 5.59).



Fig. 5.60: (a) The laser diode installed in front of a graduated plane to analyze the beam profile. (b) Image of the laser beam cross section filtered via a red channel.

The profile of the laser beam emitted by the laser diode was determined by analyzing photographs of the laser spot projected onto a graduated surface taken with a Nikon digital camera. The laser diode was installed on a metallic support in front of a graduated plane at a distance of 76 mm (Fig. 5.60). As the laser wavelength (850 nm) is in the infrared range, it was necessary to take the photos with long exposure time (30 s). Moreover, because the images were taken from a lateral view angle with respect to the spot projection due to encumbrance of the experimental setup, so that a correction of the distortion was made via the software ArcGIS in order to have the spot shape as seen from an observer coaxial to the laser beam direction. The background noise was also subtracted to infer the effective light power distribution from the image. ArcGIS allowed us to estimate the spatial distribution of the light intensity normalized to the central maximum.

This procedure allowed us to obtain the power distribution on the cross-section of the laser beam: by calculating the angle between the light source and the projected spot, the divergence angles along the two main directions of the cross-section were extrapolated with respect to specific amount of collected optical power within the spot (Fig. 5.61).

The cross-section of the laser beam has an ellipse-like shape with an axis much longer than the other due to the different divergence angle of the laser beam along the two directions (Fig. 5.60b). It was observed that the laser emits almost all the optical power within 30° in the parallel direction and 105° - 110° in the perpendicular direction. The Full-Width at Half Maximum (FWHM) of the laser beam along the parallel and perpendicular direction are about 13° (4° - 8° from datasheet) and 38° (30° - 40° from datasheet).

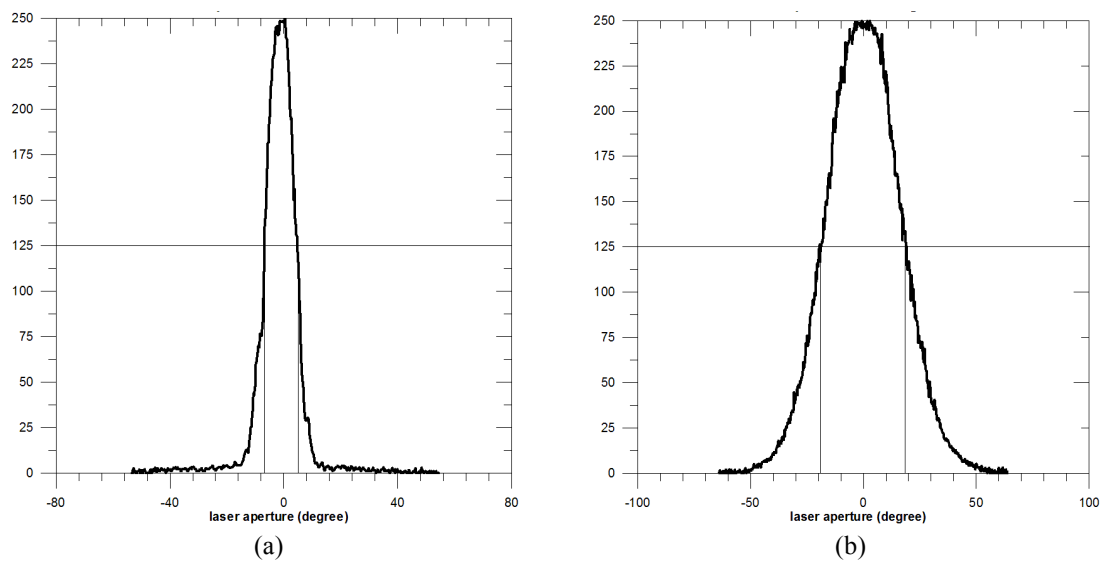


Fig. 5.61: Laser beam profile (image level 0-255) in the parallel (a) and perpendicular direction (b).

5.5 Conclusions about MicroMED

The experience gained with MEDUSA (Chapter 4) was used to develop and improve the miniaturized MicroMED instrument for dust size measurements in the Martian atmosphere. This chapter has described the steps accomplished to go from the MEDUSA to the MicroMED design, also giving numerical estimation of the sampling performance. After re-designing the external envelope and simplifying the working principle with the aim of significantly reducing mass and power consumption, a procedure was achieved to optimize the aerosol flow control and to have an acceptable sampling efficiency.

Among four configurations (Sect. 5.3.2), which were analyzed with CFD analyses, the Configuration #4 (Fig. 5.10) was considered the best to define the internal geometry of the Sampling Head and Optical Stage of MicroMED. The following remarks were inferred:

- The distance from the inlet duct to the outlet duct in the OS box has to be less than 4 mm.
- The internal diameter of the Sampling Head was fixed to 6 mm as a compromise between the mass requirements and the particle sampling efficiency, and it decreases down to 1 mm along its axis as a compromise between minimization of the particle divergent trajectories and minimization of the geometrical disturbance to the optical elements.
- The sampling efficiency for small particles ($d_p < 1 \mu\text{m}$) is < 1 as a result of lateral dispersion in the Sampling Volume, especially if the distance between the inlet duct and the outlet duct is too large and the atmospheric density is low.
- The sampling efficiency of the large particles ($d_p > 10 \mu\text{m}$) is < 1 as a result of impact on the wall of the Sampling Head tube, especially if the atmospheric density is high and pump flow rate is high.
- The diameter of the 4 holes of the Sampling Head, through which the aerosol flow enters, should be set between 2 mm and 4 mm as a compromise between particle aspiration requirement and limitation of impacts and losses of large particles on the tube wall.
- The maximum lateral distance of the particle trajectory from the centroid of the Sampling Volume is 0.5 mm for the Configuration #4 at pump flow rate of 1 l/min, which implies that the Sampling Volume could have a reasonable maximum size below 1 mm.
- The velocity of the particles in the Sampling Volume depends on boundary conditions and particles size and inertia as also observed for MEDUSA.
- The outflow section of the inlet duct should be 1 mm as a compromise between ideal particle trajectories, flow conditions, and manufacturability.

The numerical results, widely discussed in Sect. 5.3, shall be then verified experimentally with a new laboratory model. New breadboards should also verify the optical design in order to reach the goal to have the MicroMED mass below 300 g as required. Finally, the MicroMED design has solved some critical issues found in the MEDUSA design, which should improve the performance in the grains identification:

- The divergence of particle trajectories in the Sampling Volume region is reduced by 70%, and the relative standard deviation of the particle axial velocity distribution in the Sampling Volume is reduced from 4% to less than 1.5%, due to a more compact design including a closer distance between the inlet duct and the outlet duct (4 mm), each ones with a smaller internal diameter (1 mm).
- The polytonic response of the scattering light by particles, mainly at small particle size parameter, foreseen by the Mie theory, is reduced by acquiring the scattering light within a wider collecting angle ($90^{\circ}\pm 65^{\circ}$), even if through one channel.

CONCLUSIONS

This thesis describes the work for the PhD in Aerospace, Naval and Total Quality Management of the University of Naples “Federico II” from 2009 to 2011. The work was mostly performed at National Institute of Astrophysics (INAF) - Astronomical Observatory of Capodimonte, Naples, Italy, and partly at European Space Agency (ESA) - European Space Research and Technology Centre (ESTEC), Noordwijk, The Netherlands. The activities for the present thesis were focused on the investigation of dust in Mars atmosphere. The key subjects covered are:

- Investigation of Mars with the ESA-NASA *ExoMars Programme*;
- Study of the *MEDUSA* experiment for the analysis of dust in the Martian atmosphere at ground level;
- Study of the *MicroMED* instrument, aimed at miniaturizing *MEDUSA* for the *DREAMS* proposal package (ExoMars EDM 2016) or other future mission opportunities.

The work starts with a detailed description of the Martian boundary conditions, based on past exploration missions, with emphasis on properties of grains dispersed in the atmosphere (Chapter 1). This allows us to define the operative scenario for the ExoMars missions, *MEDUSA* and *MicroMED* instruments. The Mars atmosphere is mainly characterized by carbon dioxide (CO_2), which represents about 95% by volume and mass. With respect to Earth, the Martian atmosphere at the surface level has lower pressure (610 Pa on average), lower temperature (215 K on average), and lower density ($2 \cdot 10^{-2} \text{ kg/m}^3$ on average). A feature of Mars is the presence of dust dispersed in the atmosphere. The atmospheric dust content depends on seasonal and daily variations, as well as on global or local events, like dust storms and dust devils. The number density ranges from 1 to 100 particles/cm³, corresponding to a mass concentration of $4.6 \cdot 10^{-11}$ - $4.6 \cdot 10^{-9} \text{ g/cm}^3$, and the average size is about 3 μm . An important feature of the Martian environment is the free molecular path in the rarefied atmosphere at the surface level (about 5 μm) of the same order of magnitude of the dust particle sizes in the atmosphere, which characterizes the models for solving the local fluid dynamics regime.

The original work performed for this thesis is within the ESA-NASA ExoMars Programme, a challenging space project for the exploration of Mars. Tasks have been accomplished on several aspects of the MEDUSA and MicroMED experiments (Chapters 4 and 5), as possible scientific payload of the mission modules foreseen for landing, and on some specific aspects of the ExoMars Programme, during the permanence for a period of 3 months at ESA-ESTEC (Chapter 2).

The ExoMars Programme, in its present configuration, includes a mission in 2016 (EDM, i.e., Entry Descent and Landing Demonstrator Module, and TGO, i.e., Trace Gas Orbiter) and a mission in 2018 (Rover). Some tasks were accomplished at ESA-ESTEC: 1) The preparation of the Announcement of Opportunity (AO) for the selection of the ExoMars EDM 2016 payload by checking the engineering requirements, defined in the EDL Demonstrator Module Payload Experiment Proposal Information Package (E-PIP document, EXM-DM-IPA-ESA-00001); 2) A review of the requirements of the scientific sensors of the Pasteur Payload (PPL) on board the ExoMars Rover allowing the update of the definition of the top level science, measurement, accommodation and deployment requirements, reported in the ExoMars Rover Scientific Payload Requirements Document (SPRD, EXM-PL-RS-ESA-00001); 3) The elaboration of the ExoMars Rover Reference Surface Mission to define the nominal operation scenario of the ExoMars Rover on the surface of Mars by determining the power and energy utilization timelines of the PPL, Drill and Sample Preparation and Distribution System (SPDS) on the basis of the Rover engineering requirements, energetic resources, and SPRD, which was, then, implemented in the ExoMars Rover Reference Surface Mission document (EXM-PL-ES-ESA-00001). These tasks were performed by collaborating mainly with the ExoMars Project Scientist for the EDM and Rover scientific operations, interfacing with the ExoMars Payload and Assembly Integration and Verification (AIV) team and the Rover System Engineers, and allowed to gain a valuable workbench for the scientific operations of the ExoMars Programme.

As a member of the MEDUSA and MicroMED instrument teams, I performed detailed studies on fluid dynamics and light scattering aspects (Chapter 3), relevant for the instrument development. The goals have been to prepare and perform numerical and experimental analyses on the working principle of sensors for aerosol measurements

and, then, to contribute to the design of the two instruments, in particular for fluid dynamics and light scattering aspect.

The MEDUSA instrument (Chapter 4) was designed to accomplish the scientific objectives in the ExoMars Programme relevant to dust investigation; it was selected for the ExoMars Humboldt Payload (HPL) mission. The scientific data measured by MEDUSA are the dust grain sizes, size distribution, concentration, and electrification, and the water vapour abundance at the Martian landing site. The work performed during this thesis has included numerical and experimental activities to characterize the functionality of the MEDUSA breadboard.

A Computational Fluid Dynamics (CFD) analysis was performed to study the fluid flow and particle trajectories inside the MEDUSA Optical Stage (OS). A pre-processor for discretizing the domains and a numerical solver were used (Sect. 4.5.1). The CFD analysis was done by simulating aerosol flows and solving fluid dynamics fields by coupling the Navier-Stokes equations in finite volumes (Eulerian approach) with the dynamics equations for discrete particles phases (Lagrangian approach). The flow regime resulted in low Reynolds number ($Re < 100$), low Mach number ($M < 0.2$), which characterize a laminar incompressible flow, and high local Knudsen number ($Kn_p > 1$) with respect to the interaction between the fluid and the micrometer-sized particles. The latter condition implied that the aerodynamic drag of the particles needed to be evaluated through a corrective coefficient, i.e., the Cunningham correction factor, to take into account the rarefied flow regime. In particular, the CFD analysis for MEDUSA allowed to calculate the particle spatial distributions and the particle velocity profiles in the Sampling Volume, the particle trajectories and sampling efficiency in the MEDUSA OS. The results indicate that: the velocity profiles of the particles in the MEDUSA OS breadboard at the Sampling Volume (1.2 mm x 0.32 mm x 3 mm) have a relative standard deviation (i.e., standard deviation normalized to the mean value of the distribution) of less than 4% with velocity magnitude depending on particles size and inertia and on fluid boundary conditions; the axial velocity distribution of the particles is not monotonic with respect to the particles sizes and/or inertia; small particles ($d_p < 1 \mu\text{m}$) are laterally deviated from the main axis of the instrument in the Sampling Volume showing a maximum radial/axial velocity ratio of 13%; particle recirculation in the OS is expected, especially at lower atmospheric density conditions.

Experimental tests were executed in laboratory simulated Martian conditions on the MEDUSA OS breadboard and its optical components in order to evaluate the validity of the working principle and functionality (Sects 4.5.2, 4.5.3, and 4.5.5). The experimental results suggest that: the MEDUSA breadboard is able to detect dust particles in the range $d_p = 0.4\text{-}20\ \mu\text{m}$ at very low pressure conditions typical of the Martian atmosphere (300-600 Pa); the optical configuration of OS produces a reduction of 16% of the laser optical power emitted by the source (1,000 mW at a wavelength of 808 nm); stray light measurements determined the output threshold levels of the four acquisition channels in order to identify particles crossing the Sampling Volume and underlined the criticality of alignment of the baffles inside the OS.

In the end of 2009 ESA and NASA descope the Humboldt Payload according to a general design review of the ExoMars Programme. Moreover, they decided to re-select the payload, via an Announcement of Opportunity, for a new lander concept, the ExoMars EDM 2016, and fixed a maximum mass for the whole scientific payload of 3 kg. Therefore, a relevant fraction of the work for this thesis was focused on changing from MEDUSA to a new miniaturized and efficient system, called MicroMED, to perform measurements of grain size in the Martian lower atmosphere (Chapter 5).

The baseline design of MicroMED was aimed at simplifying the sub-systems and the working principle of the instrument in order to reduce the resource requirements. The new goal for MicroMED included drastic reduction of the mass from $\sim 3\ \text{kg}$ to less than $0.3\ \text{kg}$, and power consumption from $\sim 21\ \text{W}$ to $1\text{-}1.5\ \text{W}$. Therefore, a simplified optical working principle with a single detection channel collecting light scattered in a wider angle from normal-direction was adopted, instead of four channels (forward and backward direction for scattering detection, each one amplified both with high and low gain) implemented in MEDUSA. The Sampling Volume size was reduced to $0.3\ \text{mm} \times 0.3\ \text{mm} \times 0.3\ \text{mm}$ in order to have sufficient optical power density in the measurement area with a laser diode working at a reduced optical power (100 mW). An accurate fluid dynamics re-design of the instrument was done in this thesis in order to optimize the device functionality, allowing MicroMED to accomplish the same scientific requirements of MEDUSA for what concerns the measurements of the dust grain sizes ($d_p = 0.2\text{-}20\ \mu\text{m}$).

The Sampling Head and the Optical Stage for the MicroMED instrument were re-designed with theoretical provisions also based on CFD analysis (Sect. 5.3). Four configurations (#1, #2, #3 and #4) were investigated for the MicroMED design, which have, in particular, smaller OS and ducts sizes with respect to the MEDUSA design. The CFD analysis allowed us to re-define the internal geometrical configuration of the device and estimate the sampling performance from a fluid dynamics point of view. The MicroMED chosen design (configuration #4) guarantees a dispersion in the non-uniformity of the velocity profiles of the particles in the Sampling Volume reduced with respect to MEDUSA (relative standard deviation less than 1.5%); the trajectory divergence (axial/radial velocity) is reduced of about 70% for all grain sizes from MEDUSA to MicroMED (Tab. 4.18 and Tab. 5.14); the new configuration guarantees an acceptable sampling efficiency (Fig. 5.32). These simulation results will be the ground for the experimental activities on MicroMED to evaluate the sampling efficiency with respect to particle size and inertia in the range $d_p = 0.2-20 \mu\text{m}$. Experiments will have to address issues related to losses of particles for $d_p < 1 \mu\text{m}$ due to dispersion in the Sampling Volume region and for $d_p > 10 \mu\text{m}$ due to impacts on the Sampling Head tube.

The MicroMED fluid dynamics design, accomplished in this thesis, will be the basis, together with a refinement of the optical design to implement a next breadboard and demonstrate the functionality of the new device, in comparison with the theoretical simulations.

Part of the thesis activity was dedicated to the definition and technical organization of the DREAMS package for the ExoMars EDM 2016 mission, which included in its proposed version the MicroMED instrument. The package was proposed in 2011 and a re-scoped DREAMS package was selected by ESA-NASA. In particular, some sensors proposed from the DREAMS payload, including MicroMED, were not included. It is assumed that the work done in this thesis on concept and design of MicroMED will be taken into account for next mission opportunities to investigate the Martian atmospheric dust from the surface, still an open and uncovered issue.

ACRONYMS AND ABBREVIATION

ABL	Atmospheric Boundary Layer
ABP	Aurora Board of Participants
AEP	Advanced Environmental Package
AIT	Assembly Integration and Testing
AIV	Assembly Integration and Verification
ALD	Analytical Laboratory Drawer
AMELIA	Atmospheric Mars Entry and Landing Investigation and Analysis
AO	Announcement of Opportunity
APS	Active Pixel Sensor
APXS	Proton X-ray Spectrometer
ASI/MET	Atmospheric Structure Instrument/Meteorologic Package
ASPERA	Energetic Neutral Atom Analyzer
BB	Breadboard
BD	Blank Dispenser
BED	Basic Experiment Drawer
BSH	Back Shell
BW	Backward scattering direction
BWH	Backward Low Gain Channel
BWL	Backward Low Gain Channel
CAN-bus	Controlled Area Network
CDR	Critical Design Review
CEU	Common Electronics Unit
CFD	Computational Fluid Dynamics
CLUPI	CLose-UP Imager
CM	Carrier Module
CMOS	Complementary Metal Oxide Semiconductor
CNES	Centre National d'Études Spatiales (France)
CNRS	Centre National de la Recherche Scientifique (France)
COSPAR	Committee On SPACE Research
COTS	Commercial Off-The-Shelf
CRISM	Compact Reconnaissance Imaging Spectrometer for Mars
CS	Crushing Station
CSA	Canadian Space Agency
CSTM	Core Sampling Transport Mechanism
CTPU	Central Thermal Power Unit
DAPU	Data Acquisition and Process Unit
DDES	Dust Deposition and Electrification Stage
DHMR	Dry Heat Microbial Reduction
DM	Demonstrator Module
DM	Descent Module
DMC	Descent Module Composite
DMSC	Direct Simulation Monte Carlo
DPM	Discrete Phase Model
DREAMS	Dust characterization, Risk assessment and Environmental Analyzer on the Martian Surface
DS	Dosing Station
E-ICD	Experiment - Interface Control Document
E-IRD	Experiment - Interface Requirements Document
E-PIP	Experiment - Proposal Information Package
EAC	European Astronauts Centre (Cologne, Germany)
EC	Experiment Cycle (ExoMars Rover)
ECSS	European Cooperation for Space Standardization
EDL	Entry, Descend and Landing
EGSE	Electronic Ground Support Equipment
EIP	Entry Interface Point
EM	ElectroMagnetic
EMC	ElectroMagnetic Compatibility
EMCD	European Martian Climate Database
EMCS	ExoMars Climate Sounder
EPF	Emission Phase Function

ESA	European Space Agency
ESAC	European Space Astronomy Centre (Villanueva de la Cañada, Madrid, Spain)
ESOC	European Space Operation Centre (Darmstadt, Germany)
ESP	EDM Surface Platform
ESRIN	European Space Research Institute (Frascati, Rome, Italy)
ESTEC	European Space Research and Technology Centre (Noordwijk, The Netherlands)
EXM	ExoMars
FD	Flattening Device
FM	Flight Model
FMI	Finnish Meteorological Sensor (Finland)
FOV	Field Of View
FPGA	Field Programmable Gate Array
FS	Front Shell
FW	Forward scattering direction
FWH	Forward High Gain Channel
FWHM	Full Width at Half Maximum
FWL	Forward Low gain channel
GCM	Global Climate Model
GCMS	Gas Chromatograph-Mass Spectrometer
GDS	Grain Detection System
GEP	Geophysical and Environment Payload
GIADA	Grain Impact Analyzer and Dust Accumulator
GOA	Geometric Optics Approximation
GSE	Ground Support Equipment
HEPA	High Efficiency Particulate Air
HiRISE	High Resolution Imaging Science Experiment
HiSCI	High-Resolution Stereo Color Imager
HK	Housekeeping
HME	Human Spaceflight and Microgravity
HPL	Humboldt Payload
HRC	High-Resolution Camera
HRSC	High Resolution Stereo Colour Imager
HSF	Human Spaceflight
HW	Hardware
I/F	Interface
IMP	Imager Mars Pathfinder
IMU	Inertial Measurement Unit
IR	Infrared
IRIS	Infrared Interferometer Spectrometer
IRTM	Infrared Radiometers for Thermal Mapping
ISM	Infrared Spectrometer
ISS	International Space Station
JAXA	Japan Aerospace Exploration Agency
JPL	Jet Propulsion Laboratory
KT	Kayser Threde GmbH
LATMOS	Laboratoire Atmosphères Milieux, Observations Spatiale (France)
LDA	Laser Diode Assembly
LEOP	Launch and Early Orbit Phase
LIDAR	Light Detection And Ranging or Laser Imaging Detection And Ranging
LMC	Life Marker Chip
LMD	Laboratoire de Météorologie Dynamique (CNRS, France)
LMST	Local Mean Solar Time
LOCC	Lander Operations Control Centre
LT	Local Time
LTST	Local True Solar Time
Ma_Miss	Mars Multispectral Imager for Subsurface Studies
MAGIE	Mars Atmospheric Global Imaging Experiment
MARCI	Mars Color Imager
MARDI	Mars Descent Imager
MARIE	Martian Radiation Experiment
MaRS	Mars Radio Science Experiment
MARS-XRD	Mineralogy and chemistry analySer - X-Ray Diffractometer
MARSIS	Sub-Surface Sounding Radar Altimeter

MATMOS	Mars Atmospheric Trace Molecule Occultation Spectrometer
MAWD	Mars Atmospheric Water Detection
MB	Mössbauer spectrometer MIMOS II
MBd	Microbalance for dust
MBwv	Microbalance for water vapour
MCS	Mars Climate Sounder
ME	Main Electronics
MECA	Microscopy, Electrochemistry, and Conductivity Analyzer
MEDUSA	Mars Environment Dust Systematic Analyzer
MELACOM	Mars Express Lander Communications
MER	Mars Exploration Rover
MER-A	Mars Exploration Rover-A (Spirit)
MER-B	Mars Exploration Rover-B (Opportunity)
MET	Meteorological Station
MEx	Mars Express
MGCM	Mars General Circulation Model
MGS	Mars Global Surveyor
MGSE	Mechanical Ground Support Equipment
MicrOmega	Micro Observatoire pour la Minéralogie, l'Eau, les Glaces et l'Activité
Mini-TES	Miniature Thermal Emission Spectrometer
MLST	Mars Local Solar Time
MOC	Mars Orbiter Camera
MOd	Mars Odyssey
MOI	Mars Orbit Injection
MOLA	Mars Orbiter Laser Altimeter
MOMA	Mars Organic Molecule Analyzer
MPC	Multiple Particle Counter
MPF	Mars Pathfinder
MRO	Mars Reconnaissance Orbiter
MSL	Mars Surface Level
MSL	Mars Science Laboratory
NA	Numerical Aperture
NASA	National Aeronautics and Space Administration
NEQ	Noise Equivalent Power
NIR	Near Infrared
ODS	Optical Depth Sensor
OGSE	Optical Ground Support Equipment
OM	Orbiter Module
OMEGA	Observatoire pour la Minéralogie, l'Eau, les Glaces et l'Activité
OPC	Optical Particle Counter
OS	Optical Stage
OSIRIS	Optical, Spectroscopic, and Infrared Remote Imaging System
PA	Product Assurance
PBL	Planetary Boundary Layer
PCB	Printed Circuit Board
PCDE	Power Control and Distribution Electronics
PCR	Payload Confirmation Review
PDA	Phase Doppler Analyzer
PDR	Preliminary Design Review
PE	Proximity Electronics
PFM	Proto-Flight Model
PFS	Planetary Fourier Spectrometer
PHX	Phoenix
PI	Principal Investigator
PIV	Particle Velocimetry Imaging
PL	Payload
PM	Particulate Matter
PM	Project Manager
PP	Planetary Protection
PPL	Pasteur Payload
PS	Project Scientist
PSE	Payload Support Equipment
PSHS	Powder Sample Handling System

PSU	Power Supply Unit
QCM	Quartz Crystal Microbalance
RA	Robotic Arm
RAC	Robotic Arm Camera
RAT	Rock Abrasion Tool
RC	Refillable Container
RDA	Radar-Doppler Altimeter
RF	Radio Frequency
RH	Relative Humidity
RHU	Radioisotope Heating Unit
RLS	Raman Laser Spectrometer
RM	Rover Module
ROCC	Rover Operations Control Centre (ALTEC, Turin, Italy)
RSA	Russian Federal Space Agency (Roscosmos)
RSM	Reference Surface Mission
RTPU	Remote Terminal and Power Unit
S/C	Spacecraft Composite
SEM	Scanned Electron Microscope
SHARAD	Shallow Subsurface Radar
SM	Structural Model
SOC	Science Operation Centre
SOIR/NOMAD	Nadir Occultation for Mars Discovery / Solar Occultation InfraRed
SoP	System on Package
SPC	Single Particle Counter
SPDS	Sample Preparation & Distribution System
SPICAM	Ultraviolet and Infrared Atmospheric Spectrometer
SPL	Surface Payload
SPR	Scientific Payload Requirements
SRE	Science and Robotic Exploration
STM	Structural Thermal Model
STP	Standard Temperature Pressure
SV	Sampling Volume
SVM	Service Module
SW	Software
TAS-F	Thales Alenia Space France
TAS-I	Thales Alenia Space Italy
TC	Telecommands
TCS	Thermal Control Sub-system
TEC	Thermoelectric Cooler
TECP	Thermal and Electrical Conductivity Probe
TEGA	Thermal and Evolved Gas Analyzer
TES	Thermal Emission Spectrometer
TGO	Trace Gas Orbiter
THEMIS	Thermal Emission Imaging System
TM	Telemetries / Thermo-Mechanical
TM	Thermal Model
TM	Traceability Matrix
TN	Technical Note
TRL	Technology Readiness Level
TT&C	Telemetry Telecommand and Control
TVC	Thermal Vacuum Chamber
UCZ	Ultra Clean Zone
UMST	Universal Martian Solar Time
VIS	Vidicon Camera for Images
VIS	Visible
VL	Viking Lander
VO	Viking Orbiter
VS	Vertical Survey
WAC	Wide-Angle Camera
WISDOM	Water Ice and Subsurface Deposit Observation on Mars

SYMBOLS

a	Speed of sound
B	Particle mechanical mobility
C	Peculiar or diffusion velocity
\overline{C}_c	Cunningham slip correction factor
C_D	Aerodynamic drag coefficient
c_p	Fluid specific heat at constant pressure
\overline{C}_p	Particle settling velocity
c_{pp}	Particle heat capacity
c_v	Fluid specific heat at constant volume
D	Diffusion coefficient or diffusivity
d_M	Molecule diameter
dm/dt	Mass flow rate
d_p	Particle diameter
$D_{T,p}$	Thermophoretic coefficient
E	Electrical field
\bar{e}	Electron charge ($e = 1.609 \cdot 10^{-19}$ C)
e_n	Normal coefficient of restitution
e_t	Tangential coefficient of restitution
F	Coincidence probability, i.e., fraction of coincidence events
f	Probability distribution function
g	Gravity acceleration
G	Geometric cross-sectional area of particles per unit volume
h	Fluid specific enthalpy
h_c	Convective heat transfer coefficient
i	Imaginary unit
I_d	Laser diode current
\underline{J}_k	k -th species mass diffusive flux
\underline{J}_p	Particle diffusive flux
\underline{J}_t	Thermal diffusive flux
k	Fluid thermal conductivity
k_B	Boltzmann constant ($1.380 \cdot 10^{-23}$ J/K)
Kn	Knudsen number
k_p	Particle thermal conductivity
l	Mean free molecular path
l_r	Mean free molecular path at reference condition ($p = 1.013 \cdot 10^5$ Pa, $T = 293$ K)
L_S	Areocentric solar longitude
M	Mach number
m	Mass of a molecule
\dot{m}	Mass flow rate
m_0	Molar mass
N	Number density
n	Complex refractive index ($n_r - in_i$)
N_A	Avogadro's number ($N_A = 6.022 \cdot 10^{23}$ mol ⁻¹)
n_e	Number of electrical charges
n_i	Imaginary part of the complex refractive index
n_p	Number of particles
N_p	Particle number density, i.e., number of particles per unit volume
n_r	Real part of the complex refractive index
Nu	Nusselt number ($Nu = hd_p/k$)
p	Fluid static pressure
p_0	Fluid total (stagnation) pressure
P_0	Maximum optical power
P_k^+	k -th species mass source
Pr	Prandtl number ($Pr = \mu c_p/k$)
P_s	Power scattered by a particle over 4π steradians solid angle
$P_{s,0+\Delta\theta}$	Power scattered by a particle between the angles θ and $\theta+\Delta\theta$
Q	Volumetric flow rate
q	Electrical charge
\overline{Q}_s	Scattering efficiency
q_s	Saturation charge level
\underline{Q}_s	Scattering efficiency
\underline{r}	Position vector
R	Gas constant
Re	Reynolds number
r_{eff}	Effective particle radius
r_g	Mean geometric particle radius
r_m	Mean particle radius
r_{md}	Modal particle radius

r_p	Particle radius
r_{pmed}	Mass median radius
r_s	Mean particle radius for scattering
S	Sutherland constant
s_d	Stopping distance
S_{eff}	Effective particle skewness
$S_{n,ij}$	Spectral intensity
s_{rms}	Root mean square distance
Stk	Particle Stokes number
T	Fluid static temperature
T_0	Fluid total (stagnation) temperature
T_p	Particle temperature
t_r	Relaxation time
T_s	Sampling time
t_s	Particle residence time in the sampling volume
U	Fluid velocity x-component
U_0	Asymptotic gas velocity
U_s	Mean sampling velocity
u_w	Slip velocity
u_τ	Threshold friction velocity
v	Molecule velocity vector
\underline{V}	Fluid mass velocity vector ($\underline{V} = (U, V, W)$)
V	Fluid velocity y-component
V_p	Particle velocity vector
$V_{p,a,m}$	Particle mean axial velocity
$V_{p,r,m}$	Particle mean radial velocity
V_s	Sampling volume
V_{ts}	Particle terminal settling velocity
W	Fluid velocity z-component
x	Distance
x_0	Reference distance
x_i	Mole fraction
y^+	Dimensionless wall distance
z_0	Equivalent roughness height
Z_p	Particle electrical mobility
α	Particle size parameter
α_k	Thermal diffusion coefficient
γ	Ratio between the fluid specific heat at constant pressure and the specific heat at constant volume
γ_s	Surface energy of adhesion
δ	Boundary layer thickness
Δ	Optical power density
δ	Angular range
δ_M	Mean molecular spacing
δ_s	Shape factor
Δt	Time interval
ε	Surface roughness
ε_0	Permittivity of free space ($\varepsilon_0 = 8.85 \cdot 10^{-12}$ F/m)
ε_p	Particle emissivity
ε_r	Relative permittivity
η_{asp}	Aspiration efficiency
η_{inlet}	Inlet efficiency
η_{sample}	Sampling efficiency
η_{trans}	Transmission efficiency
θ	Scattering angle
θ_c	Far field divergence half-angle
θ_R	Radiation temperature
λ	Wavelength
μ	Fluid viscosity
v_{eff}	Effective particle variance
ζ	Number of degree of freedom for a molecule
ρ	Fluid static density
ρ_0	Fluid total (stagnation) density
σ	Stefan-Boltzmann constant ($\sigma = 5.670 \cdot 10^{-8}$ W/m ² /K ⁴)
σ	Standard deviation
σ_g	Standard deviation of the geometric particle radius
σ_M	Total collision cross-section
σ_s	Scattering cross-section
$\sigma_{V_{p,a}}$	Particle axial velocity standard deviation
$\sigma_{V_{p,r}}$	Particle radial velocity standard deviation
$\underline{\tau}$	Stress tensor
τ	Optical depth
τ_w	Wall stress
Ω	Solid angle

BIBLIOGRAPHY

- Abramowitz, M., Stegun, I.A., *Handbook of Mathematical functions* - Dover, New York, 1972.
- Agarwal, A., Prabhu, S.V., *Deduction of Slip Coefficient in Slip and Transition Regimes from Existing Cylindrical Couette Flow Data* - Experimental Thermal and Fluid Science, Vol. 32, pp. 991–996, 2008.
- Aitken, R.J., et al., *Aerosol Inhalability in Low Air Movement Environments* – Journal of Aerosol Science, Vol. 30, pp. 613-626, 1999.
- Allen, M.D., Raabe, O.G., *Re-Evaluation of Millikan's Oil Drop Data for the Motion of Small Particles in Air* - Journal of Aerosol Science, Vol. 13, N. 6, pp. 537-547, 1982.
- Anderson Jr, J.D., *Hypersonic and High Temperature Gas Dynamics* - McGraw-Hill, 1989.
- Anderson, E.M., Leovy, C.B., *Mariner 9 Television Limb Observations of Dust and Ice Hazes on Mars* - Journal of Atmospheric Science, Vol. 35, pp. 723-734, 1978.
- Atreya, S.K. et al., *Oxidant Enhancement in Martian Dust Devils and Storms: Implications for Life and Habitability* - Astrobiology, Vol. 6, pp. 439-450, 2006.
- Atreya, S.K., Mahaffy, P.R., Wong, A.-S., *Methane and related Trace Species on Mars: Origin, Loss, Implication for Life, and Habitability* - Planetary and Space Science, Vol. 55, pp. 358-369, 2007.
- Bada, J.L., *How Life Began on Earth: a status report* - Earth and Planetary Science Letters, Vol. 226, pp. 1-15, 2004.
- Bagnold, R.A., *The Physics of Blown Sand and Desert Dunes* - London: Methuen, 1941.
- Balme, M., Hagermann, A., *Particle Lifting at the Soil–Air Interface by Atmospheric Pressure Excursions in Dust Devils* - Geophysical Research Letters, Vol. 33, 2006.
- Balme, M.R., Whelley, P.L., Greeley, R., *Mars: Dust Devil Track Survey in Argyre Planitia and Hellas Basin* - Journal of Geophysical Research, Vol. 108, N. E8, 2003.
- Barber, P.W., Hill, S.C., *Light Scattering by Particles: Computational Methods*, Word Scientific, 1990.
- Barker, E.S., et al., *Mars Detection of Atmospheric Water Vapor during the Southern Hemisphere Spring and Summer Season* - Science, Vol. 170, pp. 1308-1310, 1970.
- Barnes, J.R., *Time Spectral Analysis of Midlatitude Disturbances in the Martian Atmosphere* - Journal of Atmospheric Science, Vol. 37, pp. 2002-2015, 1980.
- Baron, A., Willeke, K., *Aerosol Measurement – Principles, Techniques, and Applications* – Wiley-Interscience, 2001.
- Batt, R.G., Peabody, S.A., *Threshold Friction Velocities for Large Pebble Gravel Beds* – Journal of Geophysical Research, Vol. 104, N. 24, pp. 273-279, 1999.
- Bell III, J.F., et al., *Mineralogic and Compositional Properties of Martian Soil and Dust* - Journal of Geophysical Research, Vol. 105, pp. 1721-1755, 2000.
- Bell III, J.F., Savransky, D., Wolff, M.J., *Chromaticity of the Martian Sky as Observed by the Mars Exploration Rover Pancam Instruments* - Journal of Geophysical Research, Vol. 111, N. E12S05, 2006.
- Belyaev, S.P., Levin, L.M., *Investigation of Aerosol Aspiration by Photographing Particles Tracks under Flash Illumination* – Journal of Aerosol Science, Vol. 3, pp. 127-140, 1972.
- Belyaev, S.P., Levin, L.M., *Techniques for Collection of representative Aerosol Samples* – Journal of Aerosol Science, Vol. 5, pp. 325-338, 1974.
- Berthelier, A., et al., *The effect of the east-west component of the interplanetary magnetic field on magnetospheric convection as deduced from magnetic perturbations at high latitudes.* – Journal of Geophysical Research, Vol. 79, pp. 3187-3192, 1974.
- Berthelier, J.J. et al., *ICE, the electric field experiment on DEMETER* - Planetary and Space Science, Vol. 54, Issue 5, pp. 456-471, 2006.
- Berthelier, J.J., et al., *GPR, a ground-penetrating radar for the Netlander mission* - Journal of Geophysical Research, Vol. 108, pp. 8027, 2003.
- Biener, K.K., et al., *Observations of Dust Devils in MOC Wide Angle Camera Images* - Lunar Planetary Science XXXIII, Abstract N. 2004, 2002.

- Bird, G.A., *Molecular Gas Dynamics and the Direct Simulations of Gas Flows* - Oxford Science Publications, 1994.
- Bjoraker, G.L., Mumma, M.J., Larson, H.P., *Isotropic Abundance Ratios for Hydrogen in the Martian Atmosphere* - Bulletin of American Astronomy Society, Vol. 21, pp. 991, 1989.
- Bohren, C.F., Huffman, D.R., *Absorption and Scattering of Light by Small Particles*, John Wiley, New York, 1998.
- Böttger, H.M., et al., *The Effects of the Martian Regolith on GCM Water Cycle Simulations* - Icarus, Vol. 177, pp. 174–189, 2005.
- Bougher, S.W. et al., *Comparative terrestrial planet thermospheres 2. Solar cycle variation of global structure and winds at equinox* - Journal of Geophysical Research, Vol. 104, pp. 16591-16611, 1999.
- Bryson, K.L. et al., *Stability of ice on Mars and the water vapor diurnal cycle: Experimental study of the sublimation of ice through a fine-grained basaltic regolith* – Icarus, Vol. 196, pp. 446-458, 2008.
- Bussoletti, E., Colangeli, L., Lopez Moreno, J.J., et al., *The GIADA Experiment for Rosetta Mission to Comet 46P/Wirtanen: Design and Performance* – Advances in Space Research, Vol. 24, N. 9, 1999.
- Cantor, B.A., et al., *Observations of the Martian Atmosphere by MRO-MARCI, an Overview of 1 Mars Year* - Mars Atmosphere: Modeling and Observations, 2008.
- Cantor, B.A., Kanak, K.M., Edgett, K.S., *Mars Orbiter Camera Observations of Martian Dust Devils and their Tracks (September 1997 to January 2006) and Evaluation of Theoretical Vortex Models* - Journal of Geophysical Research, Vol. 111, N. E12002, 2006.
- Cao, B.Y., Chen, M., Guo, Z.Y., *Effect of Surface Roughness on Gas Flow in Microchannels by Molecular Dynamics Simulation* - International Journal of Engineering Science, Vol. 44, pp. 927–937, 2006.
- Cao, B.Y., Chen, M., Guo, Z.Y., *Temperature Dependence of the Tangential Momentum Accommodation Coefficient for Gases* - Applied Physics Letters, Vol. 86, 091905, 2005.
- Carlomagno, G.M., *Fluidodinamica* – Liguori Editore, 2004.
- Chapman, S., Cowling, T.G., *The Mathematical Theory of Non-Uniform Gases* - Cambridge University Press, 1952.
- Chen, T., et al., *Performance Evaluation of the Sampling Head and Annular Kinetic Impactor in the Savannah River Site Alpha Continuous Air Monitor* - Aerosol Science and Technology, Vol. 31, pp. 24-38, 1999.
- Cheng, W., Dunn, P.F., Brach, R.M., *Surface Roughness Effects on Microparticle Adhesion* – Journal of Adhesion, Vol. 78, pp. 929-965, 2002.
- Chicarro, A.F., *Mars Express – Science Summary after Five Years in Orbit* - 40th Lunar and Planetary Science Conference, 2009.
- Cho, A.W.H., *Contact Charging of Micron-Sized Particles in Intense Electric Fields* – Journal of Applied Physics, Vol. 35, N. 9, pp. 2561-2564, 1964.
- Chylek, P., Grams, G.W., *Scattering by Nonspherical Particles and Optical Properties of Martian Dust* - Icarus, Vol. 36, pp. 198-203, 1978.
- Clancy, R.T., et al., *A New Model for Mars Atmospheric Dust Based upon Analysis of Ultraviolet through Infrared Observations from Mariner 9, Viking and Phobos* - Journal of Geophysical Research, Vol. 100, pp. 5235-5250, 1995.
- Clancy, R.T., et al., *Mapping Mars Water Vapor with the Very Large Array* - Icarus, Vol. 100, pp. 48-59, 1992.
- Clancy, R.T., et al., *Water Vapor Saturation at Low Altitudes around Mars Aphelion: A Key to Mars Climate?* - Icarus, Vol. 122, pp. 36-62, 1996.
- Clancy, R.T., Lee, S.W., *A New Model for Mars Atmospheric Dust Based upon Analysis of Ultraviolet through Infrared Observations from Mariner 9, Viking and Phobos* - Icarus, Vol. 93, pp. 135-158, 1991.
- Clancy, R.T., Wolff, M.J., Christensen, P.R., *Mars Aerosol Studies with the MGS TES Emission Phase Function Observations: Optical Depths, Particle Sizes, and Ice Cloud Types versus Latitude and Solar Longitude* - Journal of Geophysical Research, Vol. 108, N. E9, 2003.
- Clancy, R.T., Wolff, M.J., Christensen, P.R., *Types, Sizes, Shapes and Distributions of Mars Ice and Dust Aerosols from the MGS TES Emission Phase Function Observations* - American Geophysical Union,

- Fall Meeting 2001, Abstract #P42A-0542, 2001.
- Colangeli, L., et al., *MEDUSA: The ExoMars Experiment for in-situ Monitoring of Dust and Water Vapour* - Planetary and Space Science, Vol. 57, Issue 8-9, pp. 1043-1049, 2009.
- Colangeli, L., *GIADA: The Grain Impact Analyzer and Dust Accumulator for the Rosetta Space Mission* – Advances in Space Research, Vol. 39, pp. 446-450, 2007.
- Colangeli, L., Mazzotta Epifani, E., Palumbo, P., *The New Rosetta Targets – Observations, Simulations, and Instrument Performances* – Kluwer Academic Publishers, 2004.
- Colburn, D., et al., *Diurnal Variations in Optical Depth at Mars* - Icarus, Vol. 79, pp. 159-189, 1989.
- Colver, G.M., *Dynamic and Stationary Charging of Heavy Metallic and Dielectric Particles against a Conducting Wall in the Presence of a DC Applied Electric Field* - Journal of Applied Physics, Vol. 47, N. 11, pp. 4839-4849, 1976.
- Conrath, B.J., *Thermal Structure of the Martian Atmosphere during the Dissipation of the Dust Storm of 1971* - Icarus, Vol. 24, pp. 36-46, 1975.
- Corn, M., *The Adhesion of Solid Particles to Solid Surfaces* - Journal of Air Pollution Control Association, Vol. 11, pp. 566, 1961.
- Crane, R.L., Evans, R.L., *Inertial Deposition of Particles in a Bent Pipe* – Journal of Aerosol Science, Vol. 8, pp. 161-170, 1977.
- Cunningham, E., *On the Velocity of Steady Fall of Spherical Particles through Fluid Medium* - Proceedings of the Royal Society, Vol. 83, p. 357, 1910.
- Curle, N., *The influence of solid boundaries upon aerodynamic sound* - Proc. R. Soc. London, Ser. A, 231, pp. 505-514, 1955.
- Daley, P.S., Lundgren, D.A., *The Performance of Piezoelectric crystal sensors concentrations* - American Industrial Hygiene association Journal, Vol. 35, pp. 518, 1975.
- Davies, C.N., *Definitive Equations for the Fluid Resistance of Spheres* - Proceedings of the Physical Society, Vol. 57, pp. 18, 1945.
- Davies, C.N., *The Entry of Aerosols into Sampling Tubes and Heads* – British Journal of Applied Physics, Vol. 21, pp. 921-932, 1968.
- Davies, D.W., *The Mars Water Cycle* - Icarus, Vol. 45, pp. 398-414, 1981.
- Davies, D.W., *The Vertical Distribution of Mars Water Vapor* - Journal of Geophysical Research, Vol. 84, pp. 2875-2880, 1979.
- Davy, R., et al., *A Model of Dust in the Martian Lower Atmosphere* - Journal of Geophysical Research, Vol. 114, N. D04108, 2009.
- Delory, G.T., et al., *Oxidant Enhancement in Martian Dust Devils and Storms: Storm Electric Fields and Electron Dissociative Attachment* – Astrobiology, Vol. 6, pp. 451-462, 2006.
- Dickinson C., et al., *Lidar Atmospheric Measurements on Mars and Earth* - Planetary and Space Science, 2010.
- Drossart, P., et al., *Martian Aerosol Properties from the Phobos/ISM Experiment* - Annales Geophysicae, Vol. 9, pp. 754-760, 1991.
- Durham, M.D., Lundgren, D.A., *Evaluation of Aerosol Aspiration Efficiency as a Function of Stokes Number, Velocity Ratio and Nozzle Angle* - Journal of Aerosol Science, Vol. 11, pp. 179-188, 1980.
- Ellehöj, M.D., et al., *Dust Devils And Vortices at the Phoenix Landing Site on Mars* - 40th Lunar and Planetary Science Conference, 2009.
- Encrenaz, T. et al., *The Solar System* - Springer, 2003.
- Encrenaz, T., et al., *A Study of the Martian Water Vapor over Hellas Using OMEGA and PFS Aboard Mars Express* - Astronomy & Astrophysics, Vol. 484, pp. 547–553, 2008.
- Encrenaz, T., *Searching for Water in the Universe* - Springer, 2007.
- Encyclopedia of Astronomy and Astrophysics - Nature Publishing, 2001.
- Esposito, F., *Il Sensore d’Impatto dello Strumento GIADA per la Misura della Quantità di Moto di Grani Cometari della Sonda Spaziale ESA “ROSETTA”*, PhD Thesis, University of Naples “Federico II”, 2001.
- Farmer, C.B., et al., *Mars: Water Vapor Observations from the Viking Orbiters* - Journal of Geophysical

- Research, Vol. 82, pp. 4225-4278, 1977.
- Farrell, W.M. et al., *A model of the ULF magnetic and electric field generated from a dust devil* - Journal of Geophysical Research, Vol. 111, E11004, 2006.
- Farrell, W.M., et al., *A simple electrodynamic model of a dust devil* - Geophysical Research Letters, Vol. 30, pp. 2050, 2003.
- Farrell, W.M., et al., *Electric and magnetic signatures of dust devils from the 2000-2001 MATADOR desert tests* - Journal of Geophysical Research, Vol. 109, E03004, 2004.
- Fedorova, A.A., et al., *Solar Infrared Occultation Observations by SPICAM Experiment on Mars-Express: Simultaneous Measurements of the Vertical Distributions of H₂O, CO₂ and Aerosol* - Icarus, Vol. 200, pp. 96–117, 2009.
- Ferri, F., et al., *Dust Devils as Observed by Mars Pathfinder* - Journal of Geophysical Research, Vol. 108, N. E12, pp. 5133, 2003.
- Ferzinger, J.H., Peric, M., *Computational Methods for Fluid Dynamics* - Springer, 2002.
- Fluent 6.3 User's Guide - Fluent Inc., 2006.
- Forget, F., *Alien Weather at the Poles of Mars* – Science, Vol. 306, 2004.
- Forget, F., Costard, F., Lagnonné, F., *Planet Mars - Story of Another World* - Springer, 2006.
- Formisano, V., et al., *Detection of Methane in the Atmosphere of Mars* – Science, Vol. 306, pp. 1758-1761, 2004.
- Formisano, V., et al., *Detection of Methane in the Atmosphere of Mars* - Science, Vol. 306, pp. 1758-1747, 2004.
- Formisano, V., et al., *IRIS Mariner 9 Data Revisited: Water and Dust Daily Cycles* - Planetary Space Science, Vol. 49, pp. 1331-1346, 2001.
- Friedlander, S.K., *Smoke, Dust, and Haze* - New York, John Wiley & Sons, 1977.
- Fuchs, N.A., Thomas, J.W. – Journal of Air Pollution Control Association, pp. 8-32, 1958.
- Goldsmith, P., May, F.G., *Diffusiophoresis and Thermophoresis in Water Vapor Systems* – Aerosol Science, C.N. Davies, New York, Academic Press, pp. 163-194, 1966.
- Golombek, M.P., et al., *Constraints on ripple migration at Meridiani Planum from Opportunity and HiRISE observations of fresh craters* - Journal of Geophysical Research, Vol. 115, E00F08, 2010.
- Golombek, M.P., et al., *Erosion rates at the Mars Exploration Rover landing sites and long-term climate change on Mars* - Journal of Geophysical Research, Vol. 111, E12S10, 2006.
- Google Mars, <http://www.google.com/mars/>.
- Gormley, P.G., Kennedy, M., *Diffusion from a Stream Flowing through a Cylindrical Tube* – Proceedings of the Royal Irish Academy, Vol. 52A, pp. 163-169, 1949.
- Grard, R., *Electrostatic charging processes of balloon and gondola surfaces in the Earth atmosphere* - Journal of Geophysical Research, Vol. 103, 23315-23320, 1998.
- Greeley, R., et al., *Active Dust Devils in Gusev Crater, Mars: Observations from the Mars Exploration Rover, Spirit* - Journal of Geophysical Research, Vol. 111, N. E12S09, 2006.
- Greeley, R., et al., *Martian Dust Devils: Laboratory Simulations of Particle Threshold* - Journal of Geophysical Research, Vol. 108, N. E5, 2003.
- Greeley, R., Iversen, J.D., *Wind as a Geological Process on Earth, Mars, Venus and Titan* - Cambridge Planetary Science Series, 1985.
- Greeley, R., Leach, R., White, B.R., *Threshold Windspeeds for Sand on Mars: Wind Tunnel Simulations* - Geophysical Research Letters, Vol. 7, pp. 121-124, 1980.
- Grinshpun, S., Willeke, K., Kalatoors, S., *A General Equation for Aerosol Aspiration by Thin Walled Sampling Probes in Calm and Moving Air* - Atmospheric Environment, Vol. 27A, pp. 1459-1470, 1993.
- Guo, X., et al., *Numerical and Experimental Study of Gas Flows in 2D and 3D Microchannels* - Journal of Micromechanics and Microengineering, Vol. 18, 2008.
- Haberle, R.M., et al., *Interannual Variability of Global Dust Storms on Mars* - Science, Vol. 234, pp. 459-461, 1986.
- Haberle, R.M., Greeley, R., *Sand and Dust on Mars* - NASA CP Vol. 10074, p. 36, 1991.

- Hamilton, K., Garcia, R.R., *Theory and Observations of the Short-Period Normal-Mode Oscillations of the Atmosphere* - Journal of Geophysical Research, Vol. 91, pp. 11867-11875, 1986.
- Hangal, S., Willeke, K., *Aspiration Efficiency: Unified Model for all forward Sampling Angles* - Environment Science Technology, Vol. 24A, pp. 688-691, 1990.
- Hangal, S., Willeke, K., *Overall Efficiency of Tubular Inlets Sampling at 0-90 Degrees from Horizontal Aerosol Flows* - Environment Science Technology, Vol. 24A, pp. 2379-2386, 1990.
- Hansen, J.E., Travis, L.D., *Light Scattering in Planetary Atmospheres* - Space Science Reviews, Vol. 16, pp. 527-610, 1974.
- Heyder, J., Gebhart, J., *Gravitational Deposition of Particles from Laminar Aerosol Flow through Inclined Circular Tubes* - Journal of Aerosol Science, Vol. 8, pp. 289-295, 1977.
- Holman, J.P., *Heat Transfer* - New York, McGraw-Hill, 1972.
- Holstein-Rathlou, C., et al., *Winds at the Mars Phoenix Landing Site* - 40th Lunar and Planetary Science Conference, 2009.
- Holve, D., Self, S.A., *Optical particle sizing for in situ measurements - Part 2* - Applied Optics, Vol. 18, No. 10, pp. 1646-1652, 1979
- Holve, D., Self, S.A., *Optical particle sizing for in situ measurements - Part 1* - Applied Optics, Vol. 18, No. 10, pp. 1632-1645, 1979
- Holzworth, R.H., Bering, E.A. III, *Ionospheric electric fields from stratospheric balloon-borne probes* - Measurement Techniques in Space Plasmas - Fields, edited by R. F. Pfaff, J.E. Borovsky, and D.T. Young, AGU Monograph 103, 1998.
- Horne, D., Smith, M.D., *Mars Global Surveyor Thermal Emission Spectrometer (TES) Observations of Variations in Atmospheric Dust Optical Depth over Cold Surfaces* - Icarus, Vol. 200, pp. 118-128, 2009.
- Hudson, T.L., et al., *Near-Surface Humidity at the Phoenix Landing Site as Measured by the Thermal and Electrical Conductivity Probe (TECP)* - 40th Lunar and Planetary Science Conference, 2009.
- Hutchins, D.K., Harper, M.H., Felder, R.L., *Slip Correction Measurements for Solid Spherical Particles by Modulated Dynamic Light Scattering* - Aerosol Science and Technology, Vol. 22, Issue 2, p. 202, 1995.
- Iversen, J.D., Greeley, R., Pollack, J.B., *Windblown Dust on Earth, Mars and Venus* - Journal of the Atmospheric Sciences, Vol. 33, N. 12, pp. 2425-2429, 1976.
- Iversen, J.D., White, B.R., *Saltation Threshold on Earth, Mars and Venus* - Sedimentology, Vol. 29, pp.111-119, 1982.
- Jakosky, B.M., Barker, E.S., *Comparison of ground-based and Viking Orbiter Measurements of Martian Water Vapor: Variability and Seasonal Cycle* - Icarus, Vol. 57, pp. 322-334, 1984.
- Jakosky, B.M., Farmer, C.B., *The Seasonal and Global Behaviour of Water Vapor in the Mars Atmosphere: Complete Global Results of the Viking Atmospheric Water Vapor Detector Experiment* - Journal of Geophysical Research, Vol. 87, pp. 2999-3019, 1982.
- Jakosky, B.M., Haberle, R.M., *The Seasonal Behaviour of Water on Mars* - The University of Arizona Press, pp. 969-1016, 1992.
- Jakosky, B.M., Haberle, R.M., *Year to Year Instability of the Mars South Polar Cap* - Journal of Geophysical Research, Vol. 95, pp. 1359-1365, 1990.
- Jakosky, B.M., *The Role of Seasonal Reservoirs in the Mars Water Cycle - I Seasonal Exchange of Water with the Regolith* - Icarus, Vol. 55, pp. 1-18, 1993.
- Jakosky, B.M., *The Role of Seasonal Reservoirs in the Mars Water Cycle - II Coupled Models of the Regolith, the Polar Caps, and Atmospheric Transport* - Icarus, Vol. 55, pp. 19-39, 1983.
- Jakosky, B.M., *The Seasonal Cycle of Water on Mars* - Space Science Reviews, Vol. 41, pp. 131-200, 1985.
- Jakosky, B.M., Zurek, R.W., La Pointe, M.R., *The Observed Day-To-Day Variability of Mars Atmospheric Water Vapor* - Icarus, Vol. 73, pp. 80-90, 1988.
- James, P.B., et al., *Monitoring Mars with the Hubble Space Telescope: 1990-1991 Observations* - Icarus, Vol. 109, pp. 79-101, 1994.
- James, P.B., *The Martian Hydrological Cycle: Effects of CO₂ Mass Flux on Global Water Distribution* - Icarus, Vol. 64, pp. 249-264, 1985.

- Jensen, L.L., et al., *A Facility for Long-Term Mars Simulation Experiments: the Mars Environmental Simulation Chamber (MESCH)* - *Astrobiology*, Vol. 8, N. 3, 2008..
- Jones, K.L., et al., *One Mars year: Viking Lander Imaging* - *Science*, Vol. 204, pp. 799-806, 1979.
- Kahn, R.A., et al., *The Martian Dust Cycle* - The University of Arizona Press, pp. 1017-1053, 1992.
- Kahn, R.A., *Ice Haze, Snow, and the Mars Water Cycle* - *Journal of Geophysical Research*, Vol. 95, pp. 14677-14693, 1990.
- Kieffer, H.H., *Mars South Polar Spring and Summer Temperatures - A Residual CO₂ Frost* - *Journal of Geophysical Research*, Vol. 84, pp. 8263-8288, 1979.
- Kok, J.F. Renno, N.O., *Electrification of wind-blown sand on Mars and its implications for atmospheric chemistry* - *Geophysical Research Letters*, Vol. 36, L05202, 2009.
- Kok, J.F., *Difference in the Wind Speeds Required for Initiation versus Continuation of Sand Transport on Mars: Implications for Dunes and Dust Storms* - *Physical Review Letters*, Vol. 104, Issue 7, 2010.
- Korablev, O.I., et al., *Vertical Structure of Martian Dust Measured by Solar Infrared Occultation from Phobos Spacecraft* - *Icarus*, Vol. 102, pp.76-87, 1993.
- Krasnopolsky, M.J., Maillard, J.P., Owen, T.C., *Detection of Methane in the Martian Atmosphere: Evidence for Life?* - *Icarus*, Vol. 172, pp. 537-547, 2004.
- Laktionov, A.B., *Aspiration of an Aerosol into a Vertical Tube from a Flow Transverse to it* – *Fizika Aerozoley*, Vol. 7, pp. 83-87, 1973.
- Landis, G.A., et al., *Development of a Mars dust characterization instrument* - *Planetary and Space Science*, Vol. 44, pp. 1425, 1996.
- Landis, G.A., et al., *Measurement of the Settling Rate of Atmospheric Dust on Mars by the MAE instrument on Mars Pathfinder* - *Journal of Geophysical Research*, Vol. 105, N. 1855, 2000.
- Leach, R., Greeley, R., *Saltation Thresholds and Entrainment of Fine Particles at Earth and Martian Pressures* - NASA Technical Memorandum, TM-102193, pp. 43, 1989.
- Lee, K.W. Gieseke, J.A., *Deposition of Particles In Turbulent Pipe Flows* - *Journal of Aerosol Science*, Vol. 25, pp. 699-709, 1994.
- Lefèvre F., Forget, F., *Observed variations of methane on Mars unexplained by known atmospheric chemistry and physics* – *Nature*, Vol. 460, pp. 720-723, 2009.
- Leovy, C., et al., *The Martian Atmosphere: Mariner 9 Television Experiment Progress Report* - *Icarus*, Vol. 17, pp. 373-393, 1972.
- Leovy, C., *Weather and climate on Mars* – *Nature*, Vol. 412, pp. 245-249, 2001.
- Li, A., Ahmadi, G., *Dispersion of Spherical Particles from Point Sources in a Turbulent Channel Flow* – *Aerosol Science and Technology*, Vol. 16, pp. 209-226, 1992.
- Liu, B.Y.H., Agarwal, J.K., *Experimental Observation of Aerosol Deposition in Turbulent Flow* - *Journal of Aerosol Science*, Vol. 5, pp. 145-155, 1974.
- Liu, B.Y.H., Pui, D.Y.H., *Aerosol Sampling Inlets and Inhabitable Particles* – *Atmospheric Environment*, Vol. 15, pp. 589-600, 1981.
- Liu, B.Y.H., Zhang, Z.Q., Kuehn, T.H., *A Numerical Study of Inertial Errors in Anisokinetic Sampling* - *Journal of Aerosol Science*, Vol. 20, pp. 367-380, 1989.
- Määttänen, A., et al., *A Study of the Properties of a Local Dust Storm with Mars Express OMEGA and PFS Data* - *Icarus*, Vol. 201, pp. 504–516, 2009.
- Maguire, W.C., *Martian Isotropic Ratios and Upper Limits for Possible Constituents as Derived from Mariner 9 Infrared Spectrometer Data* - *Icarus*, Vol. 32, pp. 85-97, 1977.
- Malin, M.C., Edgett, K.S., *Mars Global Surveyor Mars Orbiter Camera: Interplanetary Cruise through Primary Mission* - *Journal of Geophysical Research*, Vol. 101, N. E10, pp. 23429-23570, 2001.
- Maltagliati, L., et al., *Observations of Atmospheric Water Vapor above the Tharsis Volcanoes on Mars with the OMEGA/MEx Imaging Spectrometer* - *Icarus*, Vol. 194, pp. 53–64, 2008.
- Markiewicz, W.J., et al., *Optical Properties of the Martian Aerosols as Derived from Imager for Mars Pathfinder Midday Sky Brightness Data* - *Journal of Geophysical Research*, Vol. 104, pp. 9009-9017, 1999.
- Marple, V.A., Rubow, K.L., *An Aerosol Chamber for Instrument Evaluation and Calibration* – American

- Industrial Hygiene Association Journal, Vol. 44, pp. 361-367, 1983.
- Mars Climate Database*, <http://www-mars.lmd.jussieu.fr/>.
- Marticorena, B., Bergametti, G., *Modeling the atmospheric dust cycle: 1. Design of a soil-derived dust emission scheme* - Journal of Geophysical Research, Vol. 100, Issue D8, pp. 16415-16430, 1995.
- Martin, T.Z., Richardson, M.I., *New Dust Opacity Mapping from Infrared Thermal Mapper Data* - Journal of Geophysical Research, Vol. 98, pp. 10941-10949, 1993.
- Martin, T.Z., *Thermal Infrared Opacity of the Mars Atmosphere* - Icarus, Vol. 66, pp. 2-21, 1986.
- Maugis, D., *Adhesion of Spheres: The JKR-DMT Transition Using a Dugdale Model* - Journal of Colloid and Interface Science, Vol. 150, N. 1, pp. 243-269, 1991.
- Maynard, A.D., Kenny, L.C., *Sampling Efficiency Determination for Three Models of Personal Cyclones* - Journal of Aerosol Science, Vol. 26, pp. 671-684, 1995.
- McCord, T.B., Huguenin, R.L., Johnson, G.L., *Photometric Imaging of Mars during the 1973 Opposition* - Icarus, Vol. 31, pp. 293-314, 1977.
- Mehta, K.T. et al., *Hubble Space Telescope Observations of the Quasar PKS 0637-752: Equipartition Electron-Proton Jet from the Most Complete Spectral Coverage to Date* - The Astrophysical Journal, Vol. 690, pp. 1706-1714, 2009.
- Melchiorri, R., et al., *OMEGA/Mars Express: South Pole Region, Water Vapor Daily Variability* - Icarus, Vol. 201, pp. 102-112, 2009.
- Melchiorri, R., et al., *Water Vapor Mapping on Mars Using OMEGA/Mars Express* - Planetary and Space Science, Vol. 55, pp. 333-342, 2007.
- Melnik, O. Parrot, M., *Electrostatic discharge in Martian dust storms* - Journal of Geophysical Research 103, 29107-29118, 1998.
- Merrison, J.P., et al., *A Forthcoming European Mars Simulation Wind Tunnel Facility* - 40th Lunar and Planetary Science Conference, 2009.
- Merrison, J.P., et al., *Simulation of the Martian Dust Aerosol at Low Wind Speeds* - Journal of Geophysical Research, Vol. 107, N. E12, pp. 5133, 2002.
- Metzger, S.M., et al., *Dust Devil Vortices Seen by the Mars Pathfinder Camera* - Geophysical Research Letters, Vol. 26, pp. 2781, 1999.
- Metzger, S.M., *Feeding the Mars Dust Cycle: Surface Dust Storage and Dust Devil Entrainment* - 30th Annual Lunar and Planetary Science Conference, 1999.
- Michaux, C.M., Newburn, R.L., *Mars Scientific Model* - JPL Document, 1972
- Millikan, R.A., *Coefficients of Slip in Gases and the Law of Reflection of Molecules from the Surfaces of Solids and Liquids* - Physical Review, Vol. 21, pp. 217, 1923.
- Mischna, M.A., et al., *An Intercomparison of PFS and MCS Temperature Profiles in Support of Mars Phoenix EDL* - Mars Atmosphere: Modeling and Observations, 2008.
- Molfese, C., *Stray Light Compensation for Dust Analysers based on Light Scattering* - Proc. SPIE, Vol. 7726, 2010.
- Monti, R., Zuppari, G., *Elementi di Aerodinamica Ipersonica* - Liguori Editore, 2007.
- Moroz, V.I., et al., *Aerosol Vertical Profile on Mars from the Measurements of Thermal Radiation near the Limb* - Kosmochenkie Issled, Vol. 31, pp. 102-122, 1993.
- Moroz, V.I., Petkova, E.V., Ksanfomality, L.V., *Spectrophotometry of Mars in KRFM Experiment of the Phobos Mission: Some Properties of the Particles of Atmospheric Aerosols and the Surface* - Planetary Space Science, Vol. 41, pp. 565-585, 1993.
- Mozer, F.S., *Balloon measurements of vertical and horizontal atmospheric electric fields* - Pure Applied Geophysics, Vol. 84, pp. 32, 1971.
- Mumma, M.J., et al., *A Sensitive Search for Methane on Mars* - American Astronomical Society, DPS Meeting, Vol. 35, pp. 14-18, 2003.
- Mumma, M.J., et al., *Strong Release of Methane on Mars in Northern Summer 2003* - Science, Vol. 323, pp. 1041-1045, 2009.
- Muyshondt, A, Mc Farland, A.R., Anand, N.K., *Turbulent Deposition of Aerosol Particles in Large Transport Tubes* - Aerosol Science Technology, Vol. 24, pp. 107-116, 1996.

- NASA, *Mars Fact Data Sheet*, Nov. 2007 <http://nssdc.gsfc.nasa.gov/planetary/factsheet/marsfact.html>.
- Newman, C.E., et al. *Modeling the Martian dust cycle 2. Multiannual radiatively active dust transport simulations* - Journal of Geophysical Research, Vol. 107, pp. 5124, 2002.
- Newman, C.E., et al., *Modeling the Martian dust cycle, 1. Representations of dust transport processes* - Journal of Geophysical Research, Vol. 107, pp. 5123, 2002.
- Nier, A.O., McElroy, M.B., *Composition and Structure of Mars' Upper Atmosphere - Results from the Neutral Mass Spectrometers on Viking 1 and 2* - Journal of Geophysical Research, Vol. 82, pp. 4341-4349, 1977.
- Nogami, K., et al., *Development of the Mercury Dust Monitor (MDM) onboard the BepiColombo Mission* - Planetary and Space Science, Vol. 58, Issue 1-2, pp. 108-115, 2010.
- Nørnberg, P., et al., *Salten Skov I: A Martian Magnetic Dust Analogue* - Planetary and Space Science, Vol. 57, pp. 628-631, 2009.
- Novick, V.J., Hummer, C.R., Dunn, P.F., *Minimum dc Electric Field Requirements for Removing Powder Layers from a Conductive Surface* - Journal of Applied Physics, Vol. 65, pp. 3242, 1989.
- Nye, J.F., *The Instability of a South Polar Cap on Mars Composed of Carbon Dioxide* - Icarus, Vol. 144, pp. 456-472, pp. 449-455, 2000.
- Okazaki, K., Wiener, R.W., Willeke, K., *Isoaxial Aerosol Sampling; Non Dimensional Representation of Overall Sampling Efficiency* - Atmospheric Environment, Vol. 21, pp. 178-182, 1987.
- Okazaki, K., Wiener, R.W., Willeke, K., *Non Axial Aerosol Sampling: Mechanism Controlling the Overall Sampling Efficiency* - Atmospheric Environment, Vol. 21, pp. 183-187, 1987.
- Okazaki, K., Wiener, R.W., Willeke, K., *The Combined Effect of Aspiration and Transmission on Aerosol Sampling Accuracy for Horizontal Isoaxial Sampling* - Atmospheric Environment, Vol. 21, pp. 1181-1185, 1987.
- Olasen, J.B., Dunn, P.F., *Dispensing Particles under Atmospheric and Vacuum Conditions using an Electrostatic Device* - Journal of Applied Physics, Vol. 66, pp. 6098-6109, 1989.
- Owen, T., *The Composition and Early History of the Atmosphere of Mars* - The University of Arizona Press, pp. 818-834, 1992.
- Palomba, E., et al., *Performance of Micro-balances for dust flux measurement*. Advanced in Space Research, Vol. 29, Issue 8, pp. 1155-1158, 2002.
- Palomba, E., et al., *Microbalances for dust flux measurement* - Advances in Space Research, Vol. 29, pp. 1155, 2002.
- Pang, K., et al., *Complex Refractive Index of Martian Dust - Mariner 9 Ultraviolet Observations* - Icarus, Vol. 27, pp. 55-67, 1976.
- Panizza, A., *Analisi Numerica della Dinamica dell'Aerosol in uno Strumento per il Campionamento In Situ delle Polveri Atmosferiche Marziane*, PhD Thesis, University of Naples "Federico II", 2004.
- Patel, M.R., et al., *Seasonal and Diurnal Variations in Martian Surface Ultra-violet Irradiation: Biological and Chemical Implications for the Martian Regolith* - International Journal of Astrobiology, Vol. 2, pp. 21-34, 2003.
- Pathak, J., et al., *Simulating Martian Boundary Layer Water Ice Clouds and the Lidar Measurements for the Phoenix Mission* - Journal of Geophysical Research, Vol. 113, N. E00A05, 2008.
- Pogoda de la Vega, U., Rettberg, P., Reitz, G., *Simulation of the Environmental Climate Conditions on Martian Surface and its Effect on Deinococcus Radiodurans* - Advances in Space Research, Vol. 40, pp. 1672-1677, 2007.
- Pollack, J.B., et al., *Properties and Effects of Dust Particles Suspended in the Martian Atmosphere* - Journal of Geophysical Research, Vol. 84, pp. 2929-2945, 1979.
- Pollack, J.B., et al., *Properties of Aerosols in the Martian Atmospheres as Inferred from Viking Lander Imaging Data* - Journal of Geophysical Research, Vol. 82, pp. 4479-4496, 1977.
- Pollack, J.B., Ockert, M.E., Shepard, M.K., *Viking Lander Image Analysis of Martian Atmospheric Dust* - Journal of Geophysical Research, Vol. 100, pp. 5235-5250, 1995.
- Pope, S.B., *Turbulent Flows* - Cambridge University Press, 2000.
- Pozzi, A., *Lezioni di Gasdinamica* - Dept. of Aerospace Engineering, University of Naples Federico II,

- 2003.
- Pui, D.Y.H., Romay-Novas, F., Liu, B.Y.H., *Experimental Study of Particle Deposition in Bends of Circular Cross Sections* – Aerosol Science Technology, Vol. 7, pp. 301-315, 1987.
- Rader, D.J., Marple, V.A., *A Study of the Effect of Anisokinetic Sampling* - Aerosol Science Technology, Vol. 8, pp. 283-299, 1988.
- Rader, D.J., O'Hern, T.J., *Optical Direct-Reading Techniques: In Situ Sensing* - in Baron, P.A., Willeke, K., 2001.
- Renno, N.O. et al., *Electrical discharges and broadband radio emission by Martian dust devils and dust storms* - Geophysical Research Letters, Vol. 30, pp. 2140, 2003.
- Renno, N.O. et al., *MATADOR 2002: A pilot field experiment on convective plumes and dust devils* - Journal of Geophysical Research, Vol. 109, E07001, 2004.
- Renno, N.O., Kok, J.F., *Electrical Activity and Dust Lifting on Earth, Mars, and Beyond* - Space Science Reviews, Vol. 137, Issue 1-4, pp. 419-434, 2008.
- Ringrose, T.J., Towner, M.C., Zarnecki, J.C., *Convective Vortices on Mars: A Reanalysis of Viking Lander 2 Meteorological Data, Sols 1-60* - Icarus, Vol. 163, pp. 78-87, 2003.
- Ruff, S.W., Christensen, P.R., *Bright and Dark Regions on Mars: Particle Size and Mineralogical Characteristics Based on Thermal Emission Spectrometer Data* - Journal of Geophysical Research, Vol. 107, N. E12, pp. 5127, 2002.
- Rupprecht, E., Meyer, M., Pataschnick, H., *The Tapered Element oscillating Microbalance as a tool for measuring ambient particulate concentration in real time* – Journal of Aerosol Science, Vol. 23, Suppl. 1, pp. 635-638, 1992.
- Ryan, J.A., Henry, R.M., *Mars Atmospheric Phenomena during Major Dust Storms as Measured at the Surface* - Journal of Geophysical Research, Vol. 84, pp. 2821-2829, 1979.
- Ryan, J.A., Lucich, R.D., *Possible Dust Devils, Vortices on Mars* - Journal of Geophysical Research, Vol. 88, N. C15, pp. 11005-11011, 1983.
- Santee, M., Crisp, D., *Thermal Structure and Dust Loading of the Martian Atmosphere during Late Southern Summer: Mariner 9 Revisited* - Journal of Geophysical Science, Vol. 98, pp. 3261-3279, 1993.
- Sauerbrey, G. *Verwendung von Schwingquarzen zur Wägung dünner Schichten und zur Mikrowägung* - Zeitschrift für Physik, Vol. 155, pp. 206–222, 1959.
- Schmid, O., et al., *Sizing of Aerosol in Gases other than Air Using a Differential Mobility Analyzer* - Aerosol Science and Technology, Vol. 36, pp. 351-360, 2002.
- Schwendiman, L.C, Stegen, G.E., Glissmeyer, J.A., *Report BNWL-SA-5138* - Richland, WA, Battelle Pacific Northwest Laboratory, 1975.
- Shao, Y., Raupach, M.R., Leys, J.F., *A Model for Predicting Aeolian Sand Drift and Dust Entrainment on Scales from Paddock to Region* - Australian Journal of Soil Research. Vol. 34, pp. 309-342, 1996.
- Shelton, H., Hendricks, C.D., Wuerker, R.F., *Electrostatic Acceleration of Microparticles to Hypervelocities* - Journal of Applied Physics, Vol. 31, p. 1243, 1960.
- Sinclair, P.C., *General Characteristics of Dust Devils* - Journal of Applied Meteorology, Vol. 8, pp. 32-45, 1969.
- Sleep, N.H., *Martian Plate Tectonics* - Journal of Geophysical Research, Vol. 99, pp. 5,639-5,655, 1994
- Smith, D.E., et al., *Mars Orbiter Laser Altimeter (MOLA): Experiment Summary after the First Year of Global Mapping of Mars* - Journal of Geophysical Research, Vol. 106, pp. 23,689-23,722, 2001.
- Smith, M.D., et al., *Compact Reconnaissance Imaging Spectrometer Observations of Water Vapor and Carbon Monoxide* - Journal of Geophysical Science, Vol. 114, N. E00D03, 2009.
- Smith, M.D., *Interannual Variability in TES Atmospheric Observations of Mars during 1999–2003* - Icarus, Vol. 167, pp. 148-165, 2004.
- Smith, M.D., *The Annual Cycle of Water Vapor on Mars as Observed by the Thermal Emission Spectrometer* - Journal of Geophysical Research, Vol. 107, N. E11, 5115, 2002.
- Smith, P.H., Lemmon, M., *Opacity for the Martian Atmosphere Measured by the Imager for Mars Pathfinder* - Journal of Geophysical Research, Vol. 104, pp. 8975-8985, 1999.
- Soderblom, J.M., et al., *Temporal Variations in The Size Distribution of Martian Atmospheric Dust from*

- Mars Exploration Rover Navcam Observations* - Lunar and Planetary Science XXXIX, 2008.
- Sorensen, C.M., Wang, G.M., *Note on the Correction for Diffusion and Drag in the Slip Regime* - Aerosol Science and Technology, Vol. 33, pp. 353-356, 2000.
- Stanzel, C., et al., *Dust Devil Speeds, Directions of Motion and General Characteristics Observed by the Mars Express High Resolution Stereo Camera* - Icarus, Vol. 197, pp. 39-51, 2008.
- Sullivan, R. et al., *Results of the Imager for Mars Pathfinder Windssock Experiment* – Journal of Geophysical Research, Vol. 105, N. E10, pp. 24547-24562, 2000.
- Sullivan, R., et al., *Wind-driven Particle Mobility on Mars: Insights from Mars Exploration Rover Observations at the "El Dorado" and Surroundings at Gusan Crater* - Journal of Geophysical Research, Vol. 113, N. E06S07, 2008.
- Szarek, T.R., Dunn, P.F., *An Apparatus to Determine the Pull-Off Force of a Conducting Microparticle from a Charged Surface* - Aerosol Science and Technology, Vol. 41, pp. 43-50, 2007.
- Talbot, L., et al., *Thermophoresis of Particles in a Heated Boundary Layer* – Journal of Fluid Mechanics, Vol. 101, pp. 737-758, 1980.
- Tampari, L.K., et al., *Phoenix and MRO Coordinated Atmospheric Science* - 40th Lunar and Planetary Science Conference, 2009.
- Taylor, P.A., et al., *Modeling Dust Distributions in the Atmospheric Boundary Layer on Mars* - PBL/ARW Special Issue Manuscript, 2007.
- Taylor, P.A., et al., *Phoenix: Summer Weather in Green Valley (126W, 68N on Mars)* - Mars Atmosphere: Modeling and Observations, 2008.
- Tillman, J.E., et al., *The Martian Annual Atmospheric Pressure Cycle - Years without Great Dust Storms* - Journal of Geophysical Research, Vol. 104, pp. 9019-9026, 1993.
- Tillman, J.E., *Mars Global Atmospheric Oscillations - Annually Synchronized, transient normal-mode Oscillations and the Triggering of Global Dust Storms* - Journal of Geophysical Research, Vol. 93, pp. 9433-9451, 1988.
- Tillman, J.E., *Martian Meteorology and Dust Storms from Viking Observations* - The Case for Mars II, San Diego, CA, Univelt, Inc., pp. 333-342, 1985.
- Titov, D.V. et al., *Evidences of the regolith-atmosphere water exchange on Mars from the ISM (Phobos-2) infrared spectrometer observations* - Advances in Space Research, Vol. 16, No. 6, pp. (6)23-(6)33, 1995.
- Titov, D.V., et al., *Measurements of the Atmospheric Water Vapor on Mars by the Imager for Mars Pathfinder* - Journal of Geophysical Research, Vol. 104, pp. 8987-9007, 1999.
- Titov, D.V., et al., *Observations of Water Vapor Anomaly above Tharsis Volcanoes on Mars in the ISM (Phobos-2) Experiment* - Planetary Space Science, Vol. 42, pp. 1001-1010, 1994.
- Titov, D.V., *Water Vapor in the Atmosphere of Mars* - Advances in Space Research, Vol. 29, pp. 183-191, 2002.
- Tomasko, M.G., et al., *Properties of Dust in the Martian Atmosphere from the Imager on Mars Pathfinder* - Journal of Geophysical Research, Vol. 104, pp. 8987-9007, 1999.
- Toon, O.B., Pollack, J.B., Sagan, C., *Physical Properties of the Particles Composing the Martian Dust Storm of 1971-1972* - Icarus, Vol. 30, pp. 663-696, 1977.
- Towner, M.C., et al., *The Beagle 2 environmental sensors: science goals and instrument description* - Planetary and Space Science, Vol. 52, Issue 13, pp. 1141-1156, 2004.
- Van Zuilen, M., *Stable Isotope Ratios as a Biomarker on Mars* - Space Science Reviews, Vol. 135, No. 1-4, pp. 221-232, 2008.
- Waldman, L. Schmitt, K.H., *Thermophoresis and diffusiophoresis of Aerosols* – Aerosol Science, C.N. Davies, New York, Academic Press, pp. 137-162, 1966.
- Waller, D., et al., *Near-Surface Wind Speeds Inferred from Movement of Sand Grains Observed by Spirit in Gusev Crater, Mars* - Lunar and Planetary Science XXXIX, pp. 2218, 2008.
- Wennmacher, A., et al., *A Search for Dust Devils on Mars* - Lunar Planetary Science XXVII, Abstract N. 1417, 1996.
- White, B.R., *Soil transport by winds on Mars* – Journal of Geophysical. Research, Vol. 84, pp. 4643-4651, 1979.

- White, F.M., *Viscous Fluid Flow* - McGraw-Hill, Inc., 1991.
- Whiteway, J., et al., *Lidar on the Phoenix Mission to Mars* - Journal of Geophysical Research, Vol. 113, N. E00A08, 2008.
- Whiteway, J., et al., *Phoenix Lidar Observations of Dust, Clouds, and Precipitations on Mars* - 40th Lunar and Planetary Science Conference, 2009.
- Wilhelms, D.E., Squyres, S.W., *The Martian Hemispheric Dichotomy May Be Due to a Giant Impact* - Nature, Vol. 309, pp. 138-140, 1984.
- Williams, J.-P., *Acoustic environment of the Martian surface* - Journal of Geophysical Research, Vol. 106, pp. 5033-5042, 2001.
- Williams, M.M.R., Loyalka, S.K., *Aerosol Science Theory and Practice* - Pergamon Press, 1991.
- Wilson, A. M., *The occurrence and chemical implications of geothermal convection of seawater in continental shelves* - Geophysical Research Letters, Vol. 30, pp. 2127, 2003.
- Wise, D.U., Golombek, M.P., McGill, G.E., *Tectonic Evolution of Mars* - Journal of Geophysical Research, Vol. 84, pp. 7934-7939, 1979.
- Wise, D.U., Golombek, M.P., McGill, G.E., *Tharsis Province of Mars - Geologic Sequence, Geometry, and a Deformation Mechanism* - Icarus, Vol. 38, pp. 456-472, 1979.
- Wolff, M.J., Clancy, R.T., *Constraints on the Size of Martian Aerosols from Thermal Emission Spectrometer Observations* - Journal of Geophysical Research, Vol. 108, N. E9, pp. 5097, 2003.
- Wolff, M.J., et al., *1995 Observations of Martian Dust Storms Using the Hubble Space Telescope* - Journal of Geophysical Research, Vol. 102, pp. 1679-1691, 1977.
- Wolff, M.J., et al., *Constraints on Dust Aerosols from the Mars Exploration Rovers using MGS Overflights and Mini-TES* - Journal of Geophysical Research, Vol. 111, N. E12S17, 2006.
- Wolkenberg, P., et al., *Simultaneous Observations of the Martian Atmosphere by Planetary Fourier Spectrometer on Mars Express and Miniature Thermal Emission Spectrometer on Mars Exploration Rover* - Journal of Geophysical Research, Vol. 114, N. E04012, 2009.
- Wolkenberg, P., et al., *Simultaneous Observations of the Martian Atmosphere by Planetary Fourier Spectrometer on Mars Express and Miniature Thermal Emission Spectrometer on Mars Exploration Rover* - Journal of Geophysical Research, Vol. 114, N. E04012, 2009.
- Xu, R., *Particle Characterization: Light Scattering Methods* - Kluwer Academic Press, 2001.
- Ye, Y., Pui, D.Y.H., *Particle Deposition in a Tube with an Abrupt Contraction* - Journal of Aerosol Science, Vol. 21, pp. 29-40, 1990.
- Zender, C., *Natural Aerosols in the Climate System* - Dept of Earth System Science, University of California, Irvine, 2008.
- Zent, A.P., et al., *A Coupled Subsurface Boundary Layer Model of Water on Mars* - Journal of Geophysical Research, Vol. 98, pp. 3319-3337, 1993.
- Zhang, G., et al., *Continuum-Based Slip Model and its Validity for Micro-Channel Flows* - Chinese Science Bulletin, Vol. 51, No. 9, pp. 1130-1137, 2006.
- Zuber, M.T., et al., *Dynamics of the Atmosphere of Mars* - The University of Arizona Press, pp. 835-933, 1992.
- Zuppardi, G., *Direct Simulation Monte Carlo - Unique Solution of the Transitional Regime* - Dept. of Science and Space Engineering Luigi G. Napolitano, University of Naples Federico II, 2001.
- Zureck, R.W. et al., *Dynamics of the Atmosphere of Mars* - The University of Arizona Press, pp. 835-933, 1992.
- Zureck, R.W., *Diurnal Tide in the Martian Atmosphere* - Journal of Atmospheric Science, Vol. 33, pp. 321-337, 1992.
- Zureck, R.W., et al., *Comparative Aspects of the Climate of Mars: An Introduction to the Current Atmosphere* - The University of Arizona Press, pp. 835-933, 1992.
- Zureck, R.W., *Free and Forced Modes in the Martian Atmosphere* - Journal of Geophysical Research, Vol. 93, pp. 9452-9462, 1988.
- Zureck, S.K., Chicarro, M.A., *Final Report from the 2016 Mars Orbiter Bus Joint Instrument Definition Team (JIDT)* - ESA-ESTEC, 2009.

TECHNICAL DOCUMENTS

- DREAMS Proposal - ExoMars Entry Descent and Landing Demonstrator Module (EDM), DREAMS Proposal Team, 01/03/2011.
- EXM-DM-IPA-ESA-00001, Issue 1, Rev. 0 - ExoMars EDL Demonstrator Module Surface Payload Experiment Proposal Information Package - ESA, 08/11/2010.
- EXM-ME-GA-RP-001, Issue 1, Rev 1 - ExoMars MEDUSA Design Report, Selex Galileo, 16/02/2009.
- EXM-ME-GA-RP-006, Issue 1, Rev. 0 - ExoMars MEDUSA Carbon Vane Micro-Pump - Performances in Mars Environment - Selex Galileo, 16/02/2009.
- EXM-ME-GA-TR-003, Issue 1, Rev. 0 - ExoMars MEDUSA Breadboard Test Report - Selex Galileo, 10/04/2009.
- EXM-MS-PL-ESA-00002, Issue 5, Rev. 4 - ExoMars Science Management Plan - ESA, 12/02/2010.
- EXM-MS-RS-ESA-00001, Issue 6, Rev. 0 - ExoMars Mission and Systems Requirements Document - ESA, 15/02/2010.
- EXM-MS-SSR-AI-0013, Issue 4 - Thermal Environment and Test Requirements Specification - Thales Alenia Space, 15/10/2010.
- EXM-OM-IPA-ESA-00001, Issue 1, Rev. 1 - ExoMars Orbiter Experiment Proposal Information Package - ESA, 11/01/2010.
- EXM-PL-ICD-ESA-00006, Issue 1, Rev. 2 - ExoMars MEDUSA Experiment Interface Control Document (MEDUSA E-ICD) - ESA, 05/02/2009.
- EXM-PL-IRD-ESA-00001, Issue 7, Rev. 0 - ExoMars Pasteur Payload Experiment Interface Requirements Document (PPL E-IRD) - ESA, 05/10/2010.
- EXM-PL-RS-ESA-00001, Issue 3, Rev. 0 - ExoMars Scientific Payload Requirements - ESA, 25/04/2008.
- EXM-PL-RS-ESA-00001, Issue 3, Rev. 4 - ExoMars Rover Scientific Payload Requirements Document (SPRD) - ESA, 08/10/2010.
- EXM-PL-RS-ESA-00002, Issue 4, Rev. 0 - ExoMars Reference Surface Mission - ESA, 04/10/2010.
- EXO-MED-TN-002, Issue 3, Rev. 0 - MEDUSA Design Report and Test Plane - INAF-OAC, 31/03/2006.
- MARS-TS-00-003-JOINT, Issue 4, Rev. 0 - Mars Environment Specification, CNES ESA NASA, 15/05/2004.
- MED-RP-001, Issue 2, Rev. 0 - Definition of Boundary Operative Conditions at Mars Relevant for the MEDUSA Experiment - INAF-OAC, 29/11/2002.
- MED-RP-002, Issue 1, Rev. 0 - Definition of Technical Characteristics of Sensors and Resources for the MEDUSA Experiment - INAF-OAC, 29/11/2002
- Ventura, S., Sergio Ventura's Training Report - ESA-ESTEC - Sept-Dec 2010, 10/12/2010.
- EXO-MED-TN-006, Issue 1, Rev. 0 - INAF-OAC, 26/02/2007.
- ECSS-E-10-30A - Space Engineering - Testing - European Cooperation for Space Standardization (ECSS), 15/02/2002.